UNIVERSITÀ
DEGLI STUDI
DI PADOVA

**University Centre of Studies and Activities for Space**

**"Giuseppe Colombo"- CISAS**

**University of Padova, Italy**

---

Course: Space Science Technology and Measurement (STMS)

Curriculum: Mechanical Measurements for Engineering and Space (MMIS)

Cycle: XXIX °

# Dynamic Wireless Charging of Electric Vehicle

School director: Prof. Giampiero Naletto

Supervisor: Prof. Giuseppe Buja

Co-supervisor: Prof. Stefano Debei

PhD student

**Hemant Kumar Dashora**

Metricola: 1086858

UNIVERSITÀ
DEGLI STUDI
DI PADOVA

Sede Amministrativa: Università degli Studi di Padova

Centro di Ateneo di Studi e Attività Spaziali "Giuseppe Colombo" - CISAS_

---

CORSO DI DOTTORATO DI RICERCA IN: Scienze, Tecnologie e Misure Spaziali

CURRICOLO: Misure Meccaniche per l'Ingegneria Spaziali

CICLO: 29°

# Dynamic Wireless Charging of Electric Vehicle

**Coordinatore:** Prof. Giampiero Naletto _____

**Supervisore:** Prof. Giuseppe Buja _____

**Co-Supervisore:** Prof. Stefano Debei _____

**Dottorando:**

**(Hemant Kumar Dashora)**

_____

# Abstract

Wireless battery charging (WBC) is an attracting solution to promote electric vehicles (EVs) in the market, which may provide superior charging infrastructure and unlimited driving range. The most suitable technique to implement WBC is inductive power transfer (IPT) with a coupling established between two distant coils, one buried into the road and another installed in EV, and the power transferred from the buried coil to that onboard EV through a high-frequency oscillating magnetic flux. WBC can be carried out with EV that is either standing (while parked) or moving (on the road); the two WBC modes are termed static wireless charging (SWC) and dynamic wireless charging (DWC), respectively. However, this thesis focusses on the DWC, where an IPT track is buried into the road whilst the coil onboard EV, commonly termed pickup, remains coupled with the track to get power while moving on the road.

The in-moving vehicle charging has been researched and demonstrated by some institutes across the world using two possible track arrangements: stretched and lumped coil track. The former one is composed of a single elongated coil, much longer than the pickup size, and the later one is an arrangement of multiple coils placed one next to the other, the length of them being comparable to the pickup size. A lumped track permits activation/deactivation only of the coil interacting with a pickup. This ability is called segmentation and is very important for DWC to reduce the losses and to avoid exposing the people to electromagnetic radiations; therefore, a lumped track has been dealt with in this thesis.

The contactless power transfer at large airgap is possible with high frequency (in kHz) and high-magnitude current supply of the track coils; as increasing supply frequency improves power transfer efficiency. Apart from the supply characteristics and the coil dimensions, power transfer capabilities of a the system depend upon the coupling properties of the coil pairs, thus a pair polarized coils (also called DD coils) has been found more suitable for DWC due to its coupling merits at misalignment. Considering a lumped track composed of equally distant several DD coils, power and energy transfer to an EV moving on the track have been analyzed. Based on that, lumped track layout and its design procedure have been discussed in detail with an example of an EV.

Segmentation of a DWC track is very important function, as mentioned above, which can be obtained by various methods and one of them is using the impedance reflected into a track coil from the coupled pickup. In this way, four compensation topologies have been discussed to investigate their reflexive properties (resistance and reactance) when they are deployed in a pickup circuit. Summarizing the outcomes and comparing their behavior, two topologies have been found useful for the track segmentation. Considering them, further analysis has been done to obtain and discuss their performance figures.

This thesis also discusses about the power converters in both track side and pickup side circuit. The track side power converters include rectifier, power factor correction circuit and inverter, which extract power from the supply grid and transform into the appropriate form to realize efficient WBC. Converter arrangement in the pickup circuit includes rectifier and chopper to charger a battery using the received power.

# Sommario

La ricarica della batteria senza fili (dall'inglese *Wireless Battery Charging* - WBC) è una soluzione attraente per la possibile diffusione dei Veicoli Elettrici (VE) nel mercato. Essa può fornire infrastrutture di ricarica migliori e un' autonomia del veicolo praticamente illimitata. La tecnica più adatta per attuare il WBC è il trasferimento di potenza induttivo (*Inductive Power Transfer* - IPT), il quale sfrutta l'accoppiamento magnetico tra due bobine, una posizionata sotto il manto stradale e l'altra installata a bordo di un veicolo elettrico, e la potenza viene trasferita dalla bobina interrata a quella di bordo attraverso un flusso magnetico oscillante alta frequenza. Il WBC può essere effettuato con un VE fermo (parcheggiato) o in movimento sulla strada; le due modalità di WBC sono chiamate ricarica senza fili statica (*Static Wireless Charging* - SWC) e ricarica senza fili dinamica (*Dynamic Wireless Charging* - DWC), rispettivamente. Tuttavia, questa tesi si concentra sulla DWC, dove una bobina trasmittente, chiamata *track*, è interrata sotto la strada, mentre la bobina a bordo del VE, comunemente chiamata *pickup*, rimane accoppiata con il track per ricevere la potenza mentre il VE è in movimento.

La ricarica di un VE in movimento è stata studiata e dimostrata da alcuni istituti di tutto il mondo i quali hanno adottato due differenti strutture di bobina trasmittente: track allungato e track concentrato. La prima struttura è formata da una singola bobina allungata, molto più lunga del pickup, mentre la seconda struttura è una disposizione di più bobine posizionate una dopo l'altra, la cui lunghezza è paragonabile alle dimensioni pickup. La struttura con track concentrato consente l'attivazione/disattivazione della sola bobina interagente con il pickup. Questa capacità è chiamata segmentazione ed è molto importante per DWC perché consente di ridurre le perdite e di evitare l'esposizione delle persone a radiazioni elettromagnetiche; di conseguenza, in questa tesi è stata trattata la soluzione con track concentrato.

Il trasferimento della potenza senza fili con un elevato traferro è possibile solo con un'alta frequenza (dell'ordine dei kHz) ed un'alta intensità della corrente di alimentazione delle bobine del track; poiché l'aumento della frequenza di alimentazione migliora l'efficienza di trasferimento della potenza. Oltre alle caratteristiche di alimentazione e le dimensioni delle bobine, le capacità di trasferimento di potenza di un sistema dipendono dalle proprietà di accoppiamento delle bobine stesse, così una coppia di bobine polarizzate (chiamate anche bobine DD) è stata trovata essere la soluzione più adatta per il DWC grazie al suo elevato valore di accoppiamento quando track e pickup sono disallineati. Considerando un track concentrato composto da diverse bobine DD equamente distribuite, sono state analizzate la potenza e l'energia trasferite al VE in movimento. Sulla base di questo, la struttura del track concentrato e la sua procedura di progettazione sono stati discussi in dettaglio per un particolare caso di studio.

Come detto precedentemente, la segmentazione del track è una funzione molto importante. Essa può essere ottenuta con vari metodi e uno di questi utilizza l'impedenza riflessa del pickup in una bobina del track. Così, quattro topologie di compensazione del circuito di pickup sono state investigate per studiarne le differenti impedenze riflesse. Riassumendo i risultati e confrontando il loro comportamento, solo due topologie sono state trovate utili per la

segmentazione del track. Considerando quest'ultime, ulteriori analisi sono state fatte per ottenere e discutere le loro prestazioni.

Questa tesi tratta anche i convertitori di potenza utilizzati sia nel track che nel pickup. I convertitori di potenza del track includono un raddrizzatore, un circuito di correzione del fattore di potenza (PFC) e un inverter, i quali sfruttano l'energia prodotta dalla rete di alimentazione e la convertono nella forma più appropriata per realizzare efficienti WBC. Nella bobina di pickup il circuito di condizionamento è formato dalla cascata di un raddrizzatore e un chopper che permettono di ricaricare la batteria di bordo utilizzando la potenza ricevuta.

Dedicated to my family

# Acknowledgement

I would like to express my deepest gratitude to each and every one who helped me with their constant support and motivation during my doctoral program. At first, I would like to thank my supervisor Professor Giuseppe Buja for his supervision and experienced guidance. His continuous support and encouragements gave me more confidence in my research and successful accomplishment of the course. I would also like to thank Professor Manuele Bertoluzzo for his valuable guidance, cooperation, constructive discussions and support that enriched my knowledge and skills.

I am grateful to my supervisor Prof. Buja and thank him once again who ensured full funding for all three years during my stay in Padova and provided hassle-free economic environment. In this order, I would like to acknowledge *Fodezione Ing. Algo Gini* for the research grant and university of Padova for the research fellowship.

This journey would have not been pleasant without my friends and fellows, in this way I would like to thank Carolliane for her immense care and companion; and I show my gratitude in the same way to my lab colleagues Kishore, Rupesh, Christian, Mattia and Stefano for their help and creating healthy work environment.

At last but not the least, I always remember my family which is my biggest support and source of motivation. I am grateful and would like to thank my parents to promote me to enhance my career, and many thanks to my sisters Sudha, Komal and brother Harsh for their moral support.

# Table of Contents

# Abbreviations and Acronyms

AC- Alternating current.
BEV- Battery electrical vehicle.
BR- Basic restriction.
CAD- Computer aided design.
CAE- Computer aided engineering.
CCps- Capacitor-capacitor in parallel-series.
CCsp- Capacitor-capacitor in series-parallel.
CLsp- Capacitor-inductor in series-parallel
CN- Compensation network.
CSM- Charge sustaining mode.
DC- Direct current.
DD- Double-D shape.
DDP- Double-D pad.
DDQ- DD with a quadrature coil in middle.
DWC- Dynamic wireless charging.
DWPT- Dynamic wireless power transfer.
EMF- Electromagnetic field.
emf- Electromotive force.
EMI- Electromagnetic interference.
ENEA- An Italian research organization named "Energia Nucleare e Energia Alternative"
EV- Electric vehicle.
FEA- Finite element analysis.
FEM- Finite element method.
Fig. - Figure.
HF- High frequency.
ICES- International committee on electromagnetic safety
ICNIRP- International commission on non-ionizing radiation protection
IEEE- Institute of electrical and electronics engineers.
IGBT- Insulated-gate bipolar transistor.
IPT- Inductive power transfer.
JMAG- A simulation software for the development and design of electrical devices
KAIST- Korea advance institute of science and technology.
KVL- Kirchhoff's voltage law.
LCR meter- An instrument to measure inductance, capacitance, and resistance.
LCsp- Inductor-capacitor in series-parallel.
MATLAB- A mathematical analysis tool.
MOSFET- Metal-oxide-semiconductor field-effect transistor
OFC- Overlapped flux coverage (of two coils)
OFC1- OFC situation with discontinuous conduction of rectifier in pickup circuit.
OFC2- OFC situation with continuous conduction of rectifier in pickup circuit.
OLEV- Online electric vehicle.
PDE- Partial differential equation.
PFC- Power factor correction.
PS- Parallel series topology of compensation.
PSIM- Tool to simulate power electronic-circuit
PWM- Pulse width modulation.
rms- root mean square.
RPEV- Roadway powered electric vehicle.
RRR- Reflected resistance ratio.
SAE- Society of automotive engineers.
SEPIC- Single-ended primary-inductor converter.
SFC- Separate flux coverage (of two coils)
SiC- Silicon carbide.
SP- Series-parallel topology of compensation.
SR- Segmentation ratio (actually current gain)
UDD- Unequal-double-D coil.
USA- United States of America.
WPT- Wireless power transfer.
ZCS- Zero current switching.
ZVS- Zero voltage switching.
2D- Two dimensional.
3D- Three dimensional.

## Chapter 1

# Introduction

Over the past 100 years, we have become increasingly dependent on our cars for meeting life's most basic needs. In most of the world, getting to and from work and holidays, bringing food home from the grocery store, or going to the doctor means using one's car. This reliance on the automobile and on the petroleum-powered internal combustion engine, in particular, comes with significant costs. Our dependence on oil makes our overall economy and household budgets highly vulnerable to volatile oil prices. The pollutant emissions from our vehicles contribute to unhealthy air and global climate change.

Vehicles powered by electricity have the potential to reduce many of these problems. In most places, electric drive lowers the smog-forming and global warming pollution associated with vehicle use, and when powered by renewable resources, electric vehicles can nearly eliminate such pollution from vehicular operation. Electric vehicles powered by a clean electricity grid offer a key pathway to achieve the greater-than-80-percent reduction in global warming pollution we need by mid-century to avoid the worst consequences of climate change. Powered by domestically produced electricity, electric vehicles (EVs) could be a significant part of reducing our oil dependence.

Electric vehicles (EV) are propelled by an electric motor that is supplied with power from a rechargeable battery. The required performance characteristics of an EV must compete with the conventional vehicle; therefore battery capacity and charging facility should be acceptable in the market. There are various technologies for the battery charging circuit like on board and off board charging. On board charging circuit is meant to be a compact system on the vehicle itself which can be connected to grid during charging but off board charging system is established at the charging station which provides appropriate form of power to be fed the battery. In recent years because of many unwanted precautions and massy arrangement of wired charging, the options of wireless charging are being investigated. The idea of wireless charging is to transfer power from grid to vehicle fully contactless. There are various concepts of contactless energy transfer like microwave, light, capacitive, inductive, radiative etc. however inductive power transfer among them is preferred technology for vehicular application.

## 1.1 Background of Inductive Power transfer

The history of the wireless power transfer began in 1891 when Nikola Tesla invented his famous Tesla coil or magnifying transmitter. The system contains two loosely coupled and tuned resonant circuits: a primary and a secondary. The coils were built using large, single-layer solenoids, which significantly reduces the coil resistance and increases the quality factor. The primary and secondary coils were tuned using an external capacitor and the parasitic self-capacitance, respectively. Periodic spark gap discharges were used to short out the primary resonant circuit and initiate the power transfer. Even with the significant spark losses, the Tesla coil was able to transfer power with 85% efficiency. The power transfer is carried out with flux coupling between two coils therefore it's also termed as inductive power transfer (IPT). The IPT technique for wireless power transfer is the most convenient in implementation and suitable approach for high power. An IPT system is able to work with relatively less voltage and current rated devices compared to other methods (e.g. capacitive, radiative) for the same amount of power transfer [9]. In this way the responsible coils (primary and secondary) can carry high power which is required for the charging EV batteries. More recently applications for IPT have been spread to the automotive industries where in the push for electrification of personal transportation systems IPT can offer some highly attractive possibilities. This idea leads to the system where a vehicle can be charged contactless, convenient, hassle-free, clean and safe.

The inductive power transfer consists of a pair of inductively coupled coils, one is primary coil or transmitting coil another is secondary or pickup coil. The transmitting coil is fixed and connected to the grid through required power converters and the pickup captures power inductively and delivers to the battery load. The main requirement of power supply to feed primary coil is high frequency (in kHz) for high efficiency in power transfer. In this system the inductive counterpart is pickup or receiving coil which is placed at the vehicle chassis. During power transfer, both transmitting and pickup coils are magnetically coupled to each other. The secondary coil is associated with on-board charging system for the vehicle battery. There is a large air-gap between primary and secondary coils in such system, so coupling coefficient ($k$) remains very small.

The IPT based contactless chargers are more easily accessible as the users can get rid of the electric plugs, their connections, and massy wires. These chargers can be deployed at any of the places where a car can interact to them and get charged. There are two most possible places a car can collect charge i.e. parking lot and road. Considering the possibility of presence of the EVs, there can be two type of wireless charging methods: one is in stationary condition

which is called static power transfer and another one is on-road battery charging, that is dynamic wireless power transfer.

### *1.1.1 Static Wireless Charging*

Static wireless power transfer refers to the power transfer in stationary condition where both the coupled coils are fixed and aligned to each other. This technique is applicable in many application like charging of mobile phone, biomedical implants and electric vehicles etc. In case of vehicles, the WPT setup can be installed at the parking lots or charging station where EVs stay for long and can get charged. The transmitting coil along with its power supply arrangement is installed under the ground surface and fed by the grid. The power supply can be operated based on the availability or coupling level of a receiver coil. The receiving coil is mounted in the chassis of an electric vehicle to capture the power transferred by the inductively coupled transmitting coil. This coil feed the captured power to the onboard charging circuit installed in the vehicle. This kind of charging stations are being implemented many places where a vehicle remains stationary at defined position and WPT coils get coupled. This method provides nice facility at charging station without any manual connections which is safe and hassle free in all weather conditions. The mentioned convenience of wireless charging promotes the use of EVs in market, but static wireless charging also consumes the same charging time the conventional wired charging does.

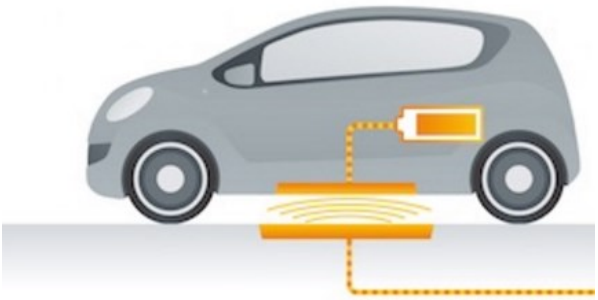

Fig. 1.1 Static wireless charging.

There are some cars available in the market with the wireless charging setup, for example Chevrolet Volt, Nissan Leaf and Cadillac ELR. There is also a partnership between German vehicle manufacturer Daimler AG and telecommunications chipmaker Qualcomm for developing wireless charging technologies both for in-car applications as well as for recharging electric vehicles without plugging the car into an electrical outlet. Another German vehicle and engine manufacturer BMW AG is developing a wireless inductive charger for its batteries that could be installed in the floor of a garage.

### *1.1.2 Dynamic Wireless Charging*

Wireless charging gives much comfort and flexibility to replace oil fueled transport with the electric vehicles; but even after the static charging technology, electric vehicles still face some important difficulties to grow in the market. Along with the charging issues, a considerable factor which discourages EVs is their battery due to its size, weight and cost. The major contribution in the price of an electric vehicle is its big size battery which is important and essential for the required driving range. Advancements in battery technology helped to reduce the battery size with better energy density but still it's affecting EV sell. In order to defeat conventional vehicles, EVs need to improve its recharging time which should be as convenient as refueling a car. At the existing EV charging stations the vehicles have to be parked and the driver has to pass the time being idle. Batter infrastructure and fast charging techniques may help to address this issue at some extent but difficult to compete the existing refueling system.

All the mentioned hitches can be resolved if it's possible to acquire charge for the battery wherever the EV goes. This facility can eliminate the range anxiety which is associated with the small size of battery. An electric vehicle most of the time stays in parking area and moving on the road. During its parked, its battery can get charged by wired or wireless charging being in stationary condition and propel with the acquired charge when the vehicle is away. In another scenario when vehicle is moving on the road, if battery can be charged simultaneously, there is no reason of range anxiety. Even in this case the required battery size is also smaller, that is also just for creating energy reserve and power continuity. The on road charging or in-moving charging is termed as dynamic wireless charging of future electric vehicles.

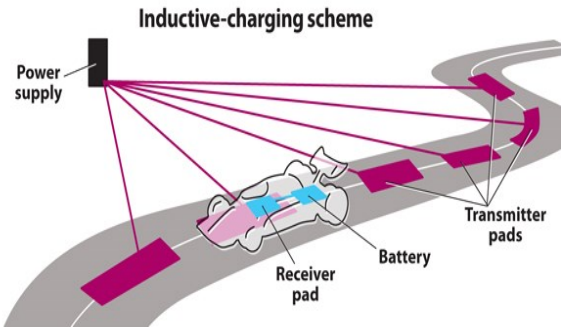

Fig. 1.2 On-road charging for EVs

The inductive power transfer is the most suitable technique to implement on road charging. For this the required infrastructure is a special track (i.e. WPT track) where many magnetic coils are placed under the road surface to generate flux for power transfer. An EV moving on the same track can capture the transmitted power inductively, using a receiving coil attached under the vehicle chassis. The coils associated in the WPT track are fed with high frequency supply withdrawn from the power grid. The high frequency supply is required for

the sake of efficiency and power transfer. In this arrangement vehicle moves on the road and gets power from the road surface to charge its battery. For the power transfer at high level, the flux density should also be high. This high electromagnetic field (EMF) is not acceptable on the part of the road where vehicle is not available because it's harmful for the animals and people walking along the road. Therefore only the part of road track should transmit high flux where a vehicle is available to receive the flux, rest of the part should have flux below defined safe limit. This strategy is called segmentation to switch on and switch off a particular part of the transmitting track.

To implement DWPT, few design solutions are proposed by some researchers across the globe. Those solution can basically be classified in two categories based on the track design. One is having a track which is built with a single coil spread across a long distance, therefore this type of track is called stretched coil track. Korea Advanced Institute of Science and Technology (KAIST) developed a DWPT system using such track and achieved significant progress towards technology evolution. This system is robust in design and simple in construction but constantly energised coil on the road is unfavourable for efficiency and safety reasons. Another category of DWPT incorporate a track with multiple coils connected in series/parallel or individually fed. All the track coil can be energised independently based on the coupling state with a pickup coil. This type of track called segmented coil track or lumped coil track. DWPT systems using lumped coil track are suggested by some researchers from USA and New Zealand. This type of system is more complex and costly but it gives flexibility of operating track partially for safety from EMF.

## 1.2 Objective of the Thesis

Electric vehicle is now well focused emerging technology and future means of transport, therefore wireless charging has become quite necessary for EVs while parked as well as moving. Considering present need and future aspects, the objective of this research project is to contribute in developing a viable concepts of on-road charging which can be accepted world-wide. Bearing this in mind, this thesis focusses on the following goals:

- To understand and carry out a critical review of existing technologies for dynamic wireless charging. In this preliminary research the thesis will summarize the work done by other researchers.

- To understand and analyse different coil structures usable for static and dynamic wireless power transfer. The appropriate coil design can be chosen based on the power transfer capacity, size and cost etc.
- To carry out power and energy analysis for the entire coupled system to understand energy requirements for a vehicle and scope of optimizing the system. This analysis focusses on the movement of a vehicle over the WPT track.
- To investigate the concepts of reflexive segmentation of a WPT track and find the scope of improvement. In this technique the reactance of a track coil can be compensated using the coupled pickup. Therefore the goal is to analyse various compensation topologies and find an appropriate method to implement the reflexive segmentation.
- To define the specifications and design the power supply for the WPT track.
- To develop a prototypal system to experimentally prove the analytical findings obtained by Simulation.

## 1.3 Thesis Structure

The thesis is organized in eleven chapters including the introduction. Although it focuses on DWPT, however, asserting from basic to advance aspects of WPT the thesis outline is mentioned below.

*Chapter 2*

Introducing the concept of on-road charging and its evolution, this chapter gives a state of art about inductive power transfer, dynamic charging and its main system requirements. There are some primary configurations of the DWPT system and power supply discussed at introductory level.

*Chapter 3*

Starting with the basics of inductive coils, this chapter discusses about coils for WPT applications. It illustrates various types and shapes of coils, and amongst them a polarized coil, which is also called DD coil, is elaborated more with its utility in DWPT system.

*Chapter 4*

Finding the lumped-coil track arrangement the best suitable for DWPT, this chapter presents a detailed energy analysis while vehicle is moving on a WPT enabled road and getting

the required tractive power. Considering DD coils in the track as well as in vehicles, coil placement on the road has been proposed that can fulfill the energy requirement of a vehicle.

*Chapter 5*

Taking forward the analysis of chapter 4, this chapter consists a proposal of a special DD coil that is called unequal-DD (UDD) coil for DPWT. UDD coil provides longer opportunity of capturing power by a pickup while moving, thus system rating and number of track coils come down for the same energy transfer. All the analysis is explained with a case study.

*Chapter 6*

In this thesis many of the analysis are supported with numerical data and other simulations. Therefore this chapter presents general idea of finite element methods (FEM) and power electronics simulations, for that JMAG and PSIM are mainly used tools, respectively.

*Chapter 7*

One of the main requirements of DWPT for vehicle charging is track segmentation and its operation. For that, this chapter introduces reflexive segmentation which is automation and exploits the reflected impedance of pickup into a track coil. Therefore, pickup compensation with topologies have been analyzed and evaluated for such segmentation.

*Chapter 8*

Amongst various compensation topologies discussed in chapter 7 for pickup circuit, two topologies, having two capacitors, are found suitable for reflexive segmentation. Therefore this chapter elaborates the analysis of performance figures for both of the mentioned topologies.

*Chapter 9*

This chapter of the thesis deals with the power supply and applied converters in both track and pickup side. It summarizes about high frequency power supply for track, compensation networks to get constant current/voltage, and converters in pickup side to charge the battery.

*Chapter 10*

All the analysis done in previous chapters related to coil and track design is implemented and elaborated with a case study. Apart of DD coil design for a particular vehicle, this chapter also includes a discussion of core selection and core material optimization.

*Chapter 11*

This chapter talks about the beginning of experimental setup, mainly the realization of DD coils and investigation of their coupling parameters.

# Chapter 2

# Dynamic Wireless Power Transfer for EV Battery Charging

Vehicles powered by electricity have the potential to reduce many of environmental and economic problems. Wireless power transfer technique has provided huge confidence to get rid of the perplexities and hurdles in charging of electric vehicles (EVs), and to rise EVs in our lives. As introduced in the previous chapter the wireless charging can be realized with stationary as well as moving EVs. Paying attention on in-moving wireless charging which is also called dynamic wireless charging (DWC), this chapter is going to present a state of the art about the subject, comprising an introduction to the technology and its evolution, basic principle, main system requirements, and primary configuration to implement the system.

## 2.1 Introduction

Electric-powered vehicles have evolved significantly over the fifteen years since they were first introduced in the United States. Development efforts are proceeding on all-electric vehicles nowadays. These battery electric vehicles (BEVs) are powered exclusively by rechargeable battery systems and do not include a conventional internal combustion engine. Energy is transferred to a vehicle either by plugging it into an electric supply to charge the battery or exchanging the spent/discharged battery with a charged one. The latter method which involves battery-exchange cannot be admitted as a nice solution due to many reasons like battery aging, their size and shape etc. that vary vehicle to vehicle. Therefore charging of installed batteries is adopted to provide energy for EVs. The EV batteries require a proper system of electrical and electronic components to collect power from grid and feed to the vehicle. The system can provide the required power to recharge EVs in two ways: on-board i.e. on the vehicle and off-board which is installed at charging station. These on-board and off-board systems and components must be designed to integrate seamlessly with one another to ensure a safe, convenient and trouble-free experience for consumers. So while looking for a good charging technology wireless power transfer (WPT) come in attention of researchers as an exciting solution for future electric vehicles. In WPT, two coils get inductively coupled to transfer power from one to another, and when they are at resonance with the supply frequency, this is called resonant coupling that makes rise in power transfer efficiency. Since the resonant inductive coupling is more efficient than inductive coupling, the term inductive power transfer (IPT) is usually referred to the resonant inductive coupling.

### *2.1.1 On-Road Charging: Need and Expectation*

The main difficulties of EV technology to get success in the market are battery size, battery cost, battery life, lass driving range, charging infrastructure, long charging time etc. The effective solution suggested for all these issues is on-road charging of EV batteries when vehicle is moving on the road. In order to achieve the feature of on-road charging, the wireless power

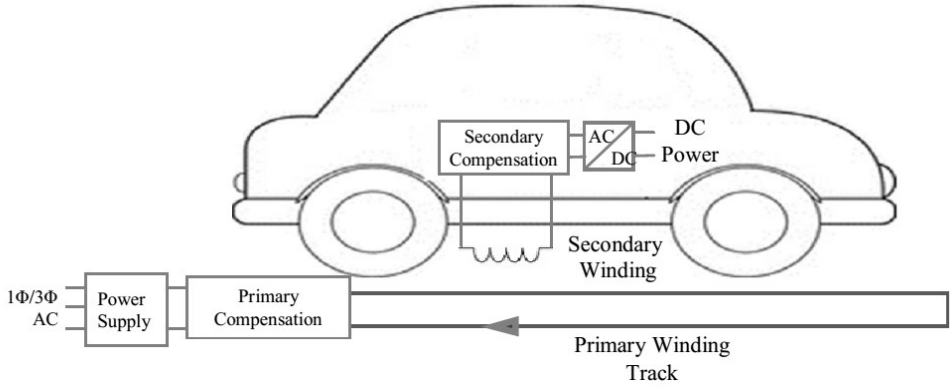


Fig. 2.1 On-road charging of vehicle.

transfer is an exciting technique in consideration. This is called dynamic wireless charging of electric vehicles. In this technique, one coil is buried in the pavement of the roads and is fed by the mains whilst the other one is embedded into the vehicle chassis, takes power from the first one and delivers energy to the EV batteries. Each coil is equipped with a proper power converter and control system for power conditioning purposes.

Static wireless charging has a constraint to keep vehicle stationary at the charging station and the driver has to wait for the charging duration. Instead, with the dynamic charging, the driver does not need to wait for the charging time. Furthermore, the amount of batteries required on board the EVs is much less than with the static charging as the charging process takes place with continuity on the road. Since it is expected that the roads are equipped with the coil all along their length, EV-onboard batteries are still necessary to operate as a temporary energy buffer, but this can significantly reduce battery size in EVs.

Dynamic wireless power transfer (DWPT) has more challenges in the operation than the static charging, like vehicle position with respect to the charging track, transmitter-receiver coil shapes and power converter topologies along the road. There are various solutions proposed by researchers to optimize the system design and improve the performance and efficiency, discussed in further sections of this chapter.

### *2.1.2 Technology Evolution*

The evolution of wireless power transfer started in 1891, when Nikola Tesla invented his famous Tesla Coil or magnifying transmitter. The system contains two loosely coupled and tuned resonant circuits: a primary and a secondary. The coils were built using large, single-layer solenoids, which significantly reduces the coil resistance and increases the quality factor. The tesla coil was able to transfer power with 85% efficiency [3]. Tesla's experiment demonstrates the majority of modern IPT design concept.

The next milestone in vehicle dynamic charging took place in 1894, when Hutin and Leblanc filed a patent that describes a transformer for powering streetcars without contact. The proposed system included a single-wire elongated primary coil carrying 2 kHz AC and coupled by multiple secondary windings. They used ferromagnetic materials and suspension systems that lower the receivers to increase the coupling. Although the proposed topology has some similarities to modern solutions (described in later section of this chapter), because of component limitations at the time, the system was not a commercial success.

In the 1990s, researchers at the University of California, Berkeley, built a complete infrastructure of roadway-powered electric bus [3]. There was a 213m long test track with two 120m powered sections. The bipolar primary track was supplied with 1200 A, 400 Hz AC current and coupled to a receiver. The system efficiency was around 60%. These results proved the potential of the technology but were limited by the size of the system due to the very low operating frequency. After that, researchers at Auckland University laid the theoretical groundwork in the 1990s for much of the research that is presently ongoing in the design of wireless chargers and they have developed an optimal design of stationary wireless charging pad for EVs with efficiency more than 90% at a distance of 20 cm [2], [3].

Starting in 2008, researchers at the Korea Advanced Institute of Science and Technology (KAIST) have built several prototypes of roadway powered EVs, which they named online EVs or OLEV. In this way, six generations of IPT systems have been developed, and tested upon various vehicles, with system efficiency peaking at about 80% [13].

## 2.2 Basics of Wireless Power Transfer

As introduced before, there are two loosely coupled inductive coils in such wireless power transfer (WPT) as shown in Fig. 2.2; one is transmitting coil which is fixed under the ground surface and connected to the power supply. There is a set of power converters in power supply side to draw the required power from the grid and convert to an appropriate form to feed the transmitting coil. In the WPT system another coil is receiving coil or pickup coil which is attached in the vehicle chassis and connected to the on board battery charging system of the vehicle. During power transfer, both transmitting and receiving coils get magnetically coupled to each other. Here in the figure, $L_T$ and $L_R$ are the self-inductances of transmitting and receiving coils respectively and the mutual inductance between them is denoted by $M$. A general relation among the inductances of two coupled coils is written as

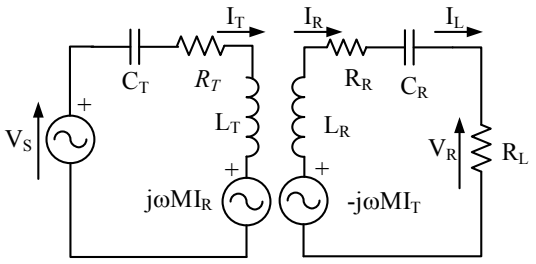

Fig. 2.2 Equivalent circuit of WPT transformer.

$$M = k\sqrt{L_T L_R} \qquad (2.1)$$

where $k$ is coupling coefficient which varies between 0 and 1 according to the coupling level. Since there is a large airgap between two IPT coils, the coupling factor $k$ is very small for such system. The induced voltage in coupled receiving circuit due to the current in the transmitting coil is

$$V_R = j\omega M I_T \qquad (2.2)$$

where $\omega$ is the supply frequency and $I_T$ is supply current in the transmitting coil and $V_R$ is the induced voltage across the receiving coil.

Basically the inductive power transfer is possible only if the transmitting coil is supplied with an alternating current source and angular frequency of the supply is denoted by $\omega$ for the circuit mentioned above. In such situation, the power source has to deliver apparent power higher than transferred active power due to highly inductive nature of the circuit. The reactive power is unnecessary extra burden on the utility which causes more losses and affects the power factor as well. In order to address such issues, an appropriate compensation is provided in either side of the circuits. The compensation helps to improve the IPT performance in many aspects which will be discussed more in further chapters. As of now while going through the basics of

IPT system, a simple series-capacitor compensation is used in Fig. 2.2 in both side to cancel the reactance of the coils. There are some resistances shown in the same figure like $R_T$ and $R_R$ which denote parasitic resistances of the coils and $R_L$ is the load equivalent resistance of the charging circuit. In coupled circuit, current flowing in one circuit induces voltage in the next circuit which depends upon the amount of current, mutual inductance between them and angular frequency of the current. There are two induced voltage sources which are depicted in Fig. 2.2, in series with the coils; they are dependent of the current in the coupled circuit. If $I_T$ current flows in transmitter coil and $I_R$ in receiver coil then Kirchhoff's voltage equations for both the sides can be written as

$$V_s = \left(\frac{1}{j\omega C_T} + j\omega L_T + R_T\right) I_T - j\omega M I_R \qquad (2.3)$$

$$0 = j\omega M I_T - \left(\frac{1}{j\omega C_R} + j\omega L_R + R_{R1}\right) I_R \qquad (2.4)$$

where $V_s$ is supply voltage, $R_T$ is primary coil resistance and $R_{RI}$ is the total resistance of secondary side i.e. coil plus load resistance $R_{RI} = R_R + R_L$. From (2.3) and (2.4) we can rearrange for the current in the secondary circuit

$$I_R = \frac{j\omega M}{\left(R_T + \frac{1}{j\omega C_T} + j\omega L_T\right) \times \left(R_{R1} + \frac{1}{j\omega C_R} + j\omega L_R\right) + \omega^2 M^2} V_s \qquad (2.5)$$

At the perfect resonant conditions of two circuits, the tuning of the capacitances in primary and secondary circuits should meet the following

$$\frac{1}{j\omega_0 C_T} + j\omega_0 L_T = 0$$

$$\frac{1}{j\omega_0 C_R} + j\omega_0 L_R = 0$$

where $\omega_o$ is the resonance frequency. The delivered power to the secondary circuit, $P_R$, and, hence, the transfer efficiency $\eta$, at the resonance frequency can be obtained as follows in

$$\eta = \frac{P_R}{P_T} = \frac{Re\{V_R . I_R^*\}}{Re\{V_S . I_T^*\}} \qquad (2.6)$$

Here '*' means the complex conjugate. By simplifying the (2.6) using (2.3), (2.4) and (2.5) the transfer efficiency can be written as following

$$\eta = \frac{(j\omega_0 M I_T).\left(\frac{-j\omega_0 M}{R_T . R_{R1} + \omega_0^2 M^2} V_s\right)}{V_s I_T}$$

$$\eta = \frac{\omega_0^2 M^2}{R_T . R_{R1} + \omega_0^2 M^2} = \frac{1}{1 + \frac{R_T R_{R1}}{\omega_0^2 M^2}} \qquad (2.7)$$

Here, we can see the efficiency depends upon the denominator term $\frac{R_T R_{R1}}{\omega_0^2 M^2}$ of (2.7). Considering the resistance terms $R_T$ & $R_{R1}$ constant; the term $\frac{R_T R_{R1}}{\omega_0^2 M^2}$ becomes smaller with increase in $\omega_o$ or M or both. Thus efficiency of wireless power transfer is improved with increasing operating frequency or mutual inductance. For a stationary coupling between two coils where coils are fixed, therefore $M$ is constant, then for very high values of $\omega_o$ the term $\frac{R_T R_{R1}}{\omega_0^2 M^2} \ll 1$. In this situation the power transfer efficiency tends to unity.

## 2.3 Main System Requirements

An inductively coupled WPT system is capable of delivering power from a stationary primary source to a fixed or mobile receiver over a relatively large air gap. This way of power transfer is similar to the transformer action but the primary and secondary coils are loosely coupled because of the airgap. The airgap leads the coupling coefficient very low and thus characteristics of these transformers are very different from conventional transformers. In such situation, a WPT system needs extra dedicated arrangements to achieve desired power transfer wirelessly with acceptable efficiency. There are few fundamental and crucial requirements mentioned below to realize an inductive wireless power transfer system.

### *2.3.1 High Frequency*

The power transfer from the primary and secondary coil of a transformer can be achieved through a narrow air gap at low frequencies of 50 Hz or 60 Hz. This phenomenon has been called as strongly coupled near-field inductive power transfer. In another case, if the operating frequency is high enough that the inductive coupling between two circuits can be stronger, due to the rapid change of the magnetic field, then power transfer across a big airgap is also possible [5]. As discussed in the previous section, and according to the expression (2.7) the WPT efficiency for higher operating frequency gets improved [5-7].

The analytical expression can also be understood physically by considering the same voltage and current in the transmitting coil; the induced voltage and respective current in receiving side will be higher for higher operating frequency according to (2.2). Hence the power transfer is higher for the same input with higher frequency and efficiency as well. Therefore this is a main requirement wireless power transfer to keep operating frequency high; and normally for vehicular application this is kept in kHz.

### *2.3.2 Limit of unwanted EMF*

Electromagnetic field (EMF) exposure is a major concern for wireless charging for EVs. EMF exposure need to be rigorously analyzed to be within acceptable level specified by safety standards, both under normal conditions as well as unusual conditions such as during abnormal operation, under vehicle presence of a human, or intended wickedness, etc. [8]. Apparently, the most hazardous radiation zone is right between the two coils, and secondary hazardous zone is around the coils (not right over the coils but still under the vehicle). These areas are the most hazardous zones but it is noted that they are not directly exposed to humans or animals at all time. After considering these under-vehicle areas, another important hazardous zone in need of consideration is near the charger (the power supply) and around the vehicle (not under the body), which exposes to the general public directly. This area along with the two hazardous areas under the vehicle body needs to be considered during the design cycle.

There are two international groups that set standards/guidelines for human exposure to electromagnetic field (EMF): one is the International Committee on Electromagnetic Safety (ICES) under the Institute of Electrical Electronic Engineers (IEEE), and the other one is International Commission on Non-ionizing Radiation Protection (ICNIRP) [9]. There are different types of recommendations given by ICES (IEEE) and ICNIRP both, where the main is expressed in terms of basic restrictions (BRs).The ICNIRP has only one general limit for BR, but the ICES has multiple limits for different parts of body tissue such as brain, heart and other tissues. The ICNIRP-2010 reference level for general public exposure to time-varying electric and magnetic fields is 27μT which is much lower than the ICES level [8].


Fig. 2.3. WPT track and its segmentation.

To maintain the EMF safe limit for human exposure in WPT system, there are some methods identified for EMF cancellation. This is an idea to cancel or suppress the incident magnetic field using auxiliary field. The auxiliary magnetic field can be generated with separate source or using the same incident field. Based on the varieties of technique, the EMF cancellation is basically categorized in three classes: passive EMF cancellation, active EMF cancellation and reactive EMF cancellation. Another important way for EMF safety is track segmentation which is especially implementable for Dynamic WPT system. Since in the

dynamic WPT there is a long track to provide magnetic flux and its most of the part is open and unsafe, therefore EMF safety becomes crucial in such situation.

### *2.3.3 Track Segmentation*

In dynamic wireless charging application of EVs, a special track is required to be built under the road surface. This track can be called WPT track which carries power supply and generates magnetic field. During the charging, vehicle pickup/receiving coil interacts with the track and extracts the required power transmitted by the track and from the road. If the track generates magnetic field and transmits all along the road then it's inefficient and can be harmful for humans and animals exist close to the active WPT coil. Being adequate in power transfer for charging EVs, the flux density needs to be high; subsequently the track may exceed the safety limit. To transfer the require power being confined in the safe boundary, the WPT track must be operated part wise. In order to attain such operability the track can be divided in several small parts or segments to be controlled individually. The transmitting parts of the track should be activated when vehicles are on the road but they should be deactivated to prevent humans or animals from potentially harmful electromagnetic field (EMF) when no vehicles are there on the road. Dividing the track into segments and independently turning them on and off according to vehicle position is called segmentation.

The segmentation of track can be visualized using certain arrangement of switches and sensors, so that according to vehicle position track activation process is done. The segmentation also helps to reduce electric and magnetic losses in the track and unnecessary heating during idle time.

## 2.4 Primary Configurations

The main challenge for the development of a dynamic WPT system is the track and pickup design. The track should be built in such a way that it can feed multiple pickups and well segmented throughout its length to fulfill required technical and safety criteria. Therefore the WPT track should have the following features:

- Simple in construction for ease of maintenance.
- Good field focusing towards pickup for good efficiency.
- Ability of self-compensation with multiple pickups.
- EMF should be under defined limit in idle situation.
- Less overall cost including cable, switches and sensors.

In order to achieve the mentioned important features, various solutions are suggested by different researchers across the world which are discussed the next chapter. The WPT track is a network of electrically connected coils to transfer energy to the vehicle passing over it. The basic element of a WPT track is a coil and there are many proposals of the coil design based on shape, size, length, core etc. Therefore the WPT track can be classified in two categories based on the coil type.

### *2.4.1 Stretched coil track*

The first roadway powered electric vehicle (RPEV) developed by the Lawrence Berkeley National Laboratory in 1976 and OLEV developed by KAIST Korea, both concepts are based on stretched coil WPT track. In this type of track the coil length is much longer than the embedded pickup coil in the vehicle. This is also called single coil track where only one coil is disseminated along the road for a long distance and supplied by a single inverter. In recent OLEV designs the coil conductors are not just placed as a rail but they are organized in twisted pattern to suppress the leakage inductance of the track circuit [12], [13]. The twisting of conductors frames several loops which can be considered as individual poles (or small coils). These small coils are made of a single conductor and apparently connected in series.

Since the stretched coil track uses just one conductor wire to construct the track for long distance so the design is simple, robust and cost effective. The possible design of narrow track and wide pickup coil may allow good lateral displacement of vehicle without much compromising the power transfer and efficiency. Looking aside all the benefits, the whole track is constructed of several small-small series connected coils which can be turned on and off together. Therefore in this kind of track design it's difficult to control a part of the track, so being the full track on, this design may violate the safety constraints.

### *2.4.2 Lumped coil track*

In some research organizations in USA, Europe and New Zeeland, another kind of track is proposed which is made of several individual coils placed on the road. The size of each track coil is comparable to the size of pickup coil in the vehicle and each coil can be controlled independently based on the vehicle position. The pickup coil interacts with a track coil then the particular coil starts transferring power and rest of the track coils remain off ideally. The power transfer process shifts to the next track coil as a vehicle moves on the road. In this concept each track coil behaves like a segment of the track which can be independently controlled so this

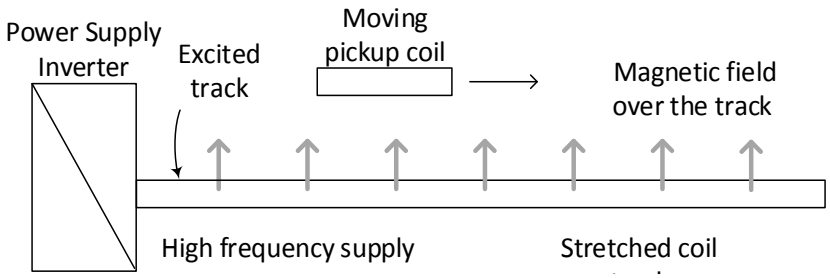


Fig. 2.4 Conceptual layout of the stretched coil track.

kind of track design is called segmented coil track. Since the switching on and off control is independent for individual coils so they must be connected in parallel to each other.

The segmented coil tracks are proposed to achieve segmentation in WPT track and it's one of the most important requirement in dynamic WPT. So this can fulfill safety constraints as required but these coil are individually controlled using some switching arrangement. The construction of the track, required switching arrangement and its control may make the system expensive.

Since the lumped coil track consists of multiple coils then the size of each coil and spacing between them becomes very important consideration. Each coil is designed for a particular power transfer capability that is defined based on the mutual inductance with a pickup coil in perfectly aligned condition. In dynamic WPT system, the pickup coil remains perfectly aligned with a track coil very rare due to movement. The misalignment of coils in the direction of

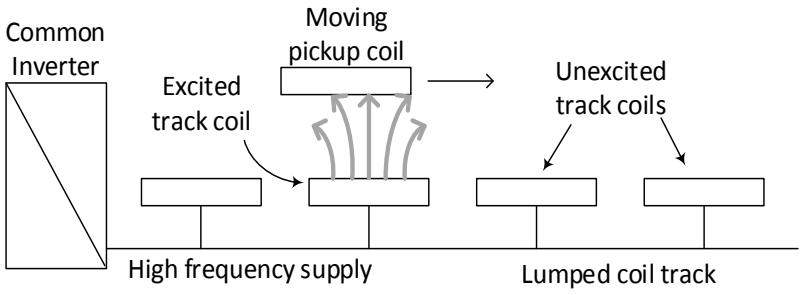


Fig. 2.5 Conceptual layout of the lumped coil track.

motion is inevitable but the lateral misalignment from the track should be minimized because it slashes down the power transfer and efficiency a lot. The ability of transferring power in laterally misaligned condition is called lateral misalignment tolerance. The coil size also affect the lateral misalignment tolerance while a vehicle moves over the track; narrow coils have

smaller misalignment tolerance. The track is composed of several identical coils in a series but the distance between each coil is very important parameter for energy transfer. In other words, required number of coils in a certain distance of the track is very important in the track design to fulfill the energy requirement of a vehicle. This kind of analysis in detail is discussed in chapter 4 and lumped coil track design is considered in further chapters.

## 2.5 Power Supply System for the WPT track

A WPT track is constructed to continuously provide power to the electric vehicles (EVs) moving on the road and is constituted of one or several coils that are supplied by high frequency voltage or current. There can be many EVs on the road, interacting with the WPT track, but usually most of the track remains uncoupled and not shielded by the vehicle chassis. A fully energized and exposed track implies high magnetic losses and constitutes a hazard to the people and the environment. In order to face this issue the track is divided in short segments and only those segments covered by a pickup are energized to operate the power transfer. The track segmentation can be conveniently implemented in lumped coil track which consists several individually controllable coils. A string of track coils is then deployed on the road and the power supply to each coil is controlled according to the vehicle position.

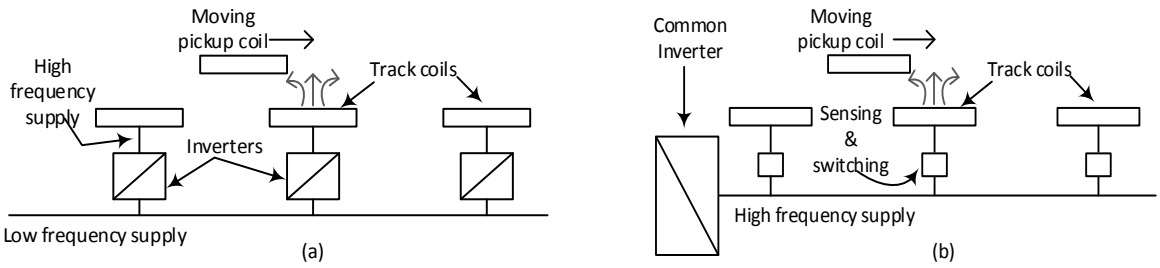


Fig. 2.6 Different ways to supply WPT track.

There are basically two ways to implement segmentation; one straight forward method is to use individual inverters for each track coil, as shown in Fig. 2.6(a), which is turned on and off according to the presence of a pickup [2]. In this arrangement, low power inverters are required to feed a single track coil and separate compensation of each coil may improve reliability and performance. The drawback of this approach that increases the installation cost is the request of a large number of inverters independently controlled. The second way to implement segmentation is to supply the string of coils with a common inverter and to make recourse to sensing & switching devices that connect to the inverter output only the track coil,

or coils, that is actually coupled with a pickup, as illustrated in Fig. 2.6(b). Centralization of the inverter and the use of cost effective sensing & switching devices are the assets of this approach.

The inductive way of wireless power transfer (IPT) is now recognized as a convenient and acceptable technique to transfer power through an air-gap with a weak magnetic coupling. Although the demand for high power IPT systems is growing, the implementation of such IPT systems is severely hampered by the limitations of voltage and current ratings of available semiconductor devices. While using dynamic WPT track, multiple vehicles may be available to get charged at a time on road. In such situation the WPT track must carry adequate power to satisfy the charging requirement of all the vehicles coupled with the track. For high power systems, it is therefore preferable the track current to be sufficiently high, which is produced with high voltage, and unfortunately it cannot be achieved using currently available semiconductor devices. Considering the device limitation and power requirement some researchers proposed possible ideas of power supply using a combination of inverters [17].

## References


[1] I.S. Suh and J. Kim, "Electric vehicle on-road dynamic charging system with wireless power transfer technology" Proc. of IEEE International Electric Machines & Drives Conference (IEMDC), 2013, pp. 234 - 240.

[2] G.A. Covic and J.T. Boys, "Inductive power transfer", Proc. of IEEE, vol. 101, no. 6, pp.1276-1289, June 2013.

[3] S. Lukic and Z. Pantic, "Cutting the Cord: static and dynamic inductive wireless charging of electric vehicles", Proc. of IEEE Electrification Magazine, vol. 1, no. 1, 2013, pp. 57- 64.

[4] N. Rauh, T. Franke, and J.F. Krems, "Understanding the impact of electric vehicle driving experience on range anxiety", Proc. of The Journal of the Human Factors and Ergonomics Society, available: http://hfs.sagepub.com

[5] W. Zhang, S.C. Wong, C.K. Tse, and Q. Chen, "Design for efficiency optimization and voltage controllability of series-series compensated inductive power transfer systems", *IEEE Transactions on Power Electronics*, vol. 29, no. 1, pp. 191- 200, January 2014.

[6] J.L. Villa, J. Sallán, A. Llombart, and J.F. Sanz, "Design of a high frequency Inductively Coupled Power Transfer system for electric vehicle battery charge", Proc. of Science Direct Journal on Applied Energy, vol. 86, 2009, pp. 355–363.

[7] J.L. Villa, A. Llombart, J.F. Sanz, and J. Sallan, "Development of an inductively coupled power transfer system (ICPT) for electric vehicles with a large air gap", Proc. of IEEE International Symposium on Industrial Electronics, 2007, pp. 1219 - 1223.

[8] H. Jiang, P. Brazis, M. Tabaddor, and J.Bablo, "Safety considerations of wireless charger for electric vehicles - a review paper", UL LLC 2013, available: http://newscience.ul.com/wp-content/uploads/sites/30/2014/04/Safety_Considerations_of_Wireless_Charger_for_Electric_Vehicles.pdf

[9] International Commission on Non-Ionizing Radiation Protection (ICNIRP) Guidelines [Online]. Available: www.icnirp.de/documents/emfgdl.pdf

[10] S. Lee, J. Huh, C. Park, N.S. Choi, G.H. Cho, and C.T. Rim, "On-line electric vehicle using inductive power transfer system", Proc. of IEEE Energy Conversion Congress and Exposition (ECCE), 2010, pp. 1598-1601.

[11] J. Huh, S.W. Lee, W.Y. Lee, G.H. Cho, and C.T. Rim, “Narrow-width inductive power transfer system for online electrical vehicles”, *IEEE Transactions on Power Electronics*, vol. 26, no. 12, pp. 3666 - 3679, 2011.

[12] J. Huh, W. Lee, S. Choi, and C.T. Rim, “A new cross-segmented power supply rail for roadway powered electric vehicles”, IEEE International Symposium on Power Electronics for Distributed Generation Systems (PEDG), 2012, pp. 291-296.

[13] S. Choi, J. Huh, W.Y. Lee, S.W. Lee, and C.T. Rim , “New cross-segmented power supply rails for roadway-powered electric vehicles”, *IEEE Transactions on Power Electronics*, vol.28, no. 12, pp. 5832 - 5841, 2013.

[14] K. Lee, Z. Pantic, and S.M. Lukic, “Reflexive field containment in dynamic inductive power transfer systems”, *IEEE Transactions on Power Electronics*, vol. 29, no. 9, pp. 4592 - 4602, 2014.

[15] J.A. Russer, M. Dionigi, M. Mongiardo, and P. Russer, “A moving field inductive power transfer system for electric vehicles”, Proc. of European Microwave Conference (EuMC), 2013, pp. 519 - 522.

[16] J.A. Russer and P. Russer, "Design considerations for a moving field inductive power transfer system," in IEEE International Wireless Power Transfer Conference Perugia WPTC, May 15 – 16, 2013, pp. 1 - 4.

[17] U.K. Madawala and D.J. Thrimawithana, “A ring inductive power transfer system”, Proc. of International Conference on Industrial Technology (ICIT), 2010, pp. 667 – 672.

# Chapter 3

# Coils for Wireless Power Transfer

The inductive power transfer technique made wireless charging convenient for stationary vehicles as well as implementable for moving vehicles. For an IPT system three parts are essential: power supply, WPT coils (or pad) and pickup converter. The WPT coils are physically isolated with a certain air gap but gets coupled magnetically during power transfer. Their shape, size, winding structure, air gap etc. define the coupling coefficient between two coupled coils. Getting into the depth this chapter mainly focusses on the WPT coils and their coupling behavior which is responsible for the power transfer without contacts and efficiency.

## 3.1 Basics of Inductive Coils

Coil is a two terminal mechanical structure made of a conductor which shows magnetic properties when supplied by an electric source or influenced by an external magnetic field. Here magnetic properties refers to the phenomenon of flux generation due to current in the coil and conversely current generation due to flux. The electromagnetic behavior of such an element can be understood by the Maxwell's equations. Since the coils are equipped in the systems which operate with AC supply therefore their inductive nature is more dominant. However in an electric circuit a coil can be represented with two parameters: resistance and inductance. The former one is known as parasitic resistance of the coil due to lossy conductive material. The inductance of the coil is due to associated flux i.e. either because of the current flowing in itself or possibly another source or both. Considering the flux linkage with a coil, the inductance can be categorized into two types: Self-inductance and mutual inductance.

In a WPT system two or more coils get coupled but for the sake of simplicity, as of now, considering two coil system, their self and mutual inductances are deliberated. Here assuming that both the coils are identical in respect of shape, size and number of turns. The self-inductance of a coil refers to the phenomenon of resisting the supply current by the coil due to its own magnetic flux. This is well known as Lenz's law. In a separate and isolated coil when it's supplied, the voltage across the terminals can be written as

$$V = L\frac{di_1}{dt} \tag{3.1}$$

where $L$ is the self-inductance of the coil and $i_1$ is supply current.

In a case when two coils are magnetically connected which means their associated flux link each other, mutual inductance is also observed. Similarly the self-inductance, the mutual inductance is also a phenomenon to resist the supply current in a coil but in this case it's due to the current flown into another coil. If one of the two magnetically coupled, adjacent coil is supplied then an induced voltage is developed across the terminals of another coil. The mutually induced voltage in first coil due to the current in second coil can be written as

$$V_{12} = M_{12}\frac{di_2}{dt} \qquad (3.2)$$

where $M_{12}$ is the mutual inductance between two coils and $i_2$ is current in the second coil.

The current flowing in coil one sets up a magnetic field around itself with some of these magnetic field lines passing through coil two giving us mutual inductance. The flux linking coil one when a current flows around coil two is exactly the same as the flux linking coil two when the same current flows around coil one above, then the mutual inductance of coil one with respect of coil two is defined as $M_{21}$. This mutual inductance is true irrespective of the size, number of turns, relative position or orientation of the two coils. Because of this, we can write the mutual inductance between the two coils as:

$$M_{12} = M_{21} = M \qquad (3.3)$$

Then we can see that self-inductance characterizes an inductor as a single circuit element, while mutual inductance signifies some form of magnetic coupling between two inductors or coils, depending on their distance and arrangement. In a situation when two identical coils are coupled so close that their flux link to each other completely then mutual inductance can be same as the self-inductance of one coil. If coils are not identical and coupling is imperfect then the mutual inductance can be given by

$$M = \mathrm{k}\sqrt{L_1 L_2} \qquad (3.4)$$

where $L_1$, $L_2$ are self-inductances of two coupled coil and $k$ is coupling coefficient. Generally, the amount of inductive coupling that exists between the two coils is expressed as a fractional number between 0 and 1 instead of a percentage (%) value, where 0 indicates zero or no inductive coupling, and 1 indicates full or maximum inductive coupling. In other words, if $k=1$ the two coils are perfectly coupled, if $k>0.5$ the two coils are said to be tightly coupled and if $k<0.5$ the two coils are said to be loosely coupled. All the applications based on wireless power transfer consist loos coupling because in such cases the coupled coils stay apart with a significant airgap. The presence of airgap allows just a small part of the generated flux by the

transmitting coil to reach the receiving one which consequences lower coupling coefficient. Other than the air gap between two coupled coils, coupling coefficient also depends upon the coil design. Various coil designs are proposed by different researchers and some of the important of them are discussed in the next section.

## 3.2 Coil Types and Shapes

Implementation of wireless power transfer to charge battery of an electric vehicles needs a pair of coupled inductive coils with an airgap large enough to ensure the required ground clearance under the vehicle. Back and forth of the ground clearance the WPT coils are placed, it means one coil is on the ground and another under vehicle. According to space optimization, planner form of the WPT coils is the most appropriate structure both in stationary and in-moving wireless power transfer. Planner coils are more convenient in installation and keeps better misalignment tolerance in comparison of helical or cylindrical coils. Before discussing about the types of coil and their suitability in WPT applications, basic required features of the pair of the coil can be defined. The WPT coil should have

- Higher coupling coefficient.
- Good misalignment tolerance.
- Adequate power capacity.
- Simple structure.

The mutual inductance between two coils basically depends upon airgap, number of turns and area of the coil. In vehicular application the airgap is fixed then mutual inductance can be enhanced having more number of turns or coil area. Therefore a loop of coil with maximum possible area deployable under the car and multiple turns can be equipped to get higher mutual inductance. Considering the wire radius for a coil winding if all the turns are placed at the periphery of the coil than the coil will be no more planner but will be helix structure. Also in such coil the magnetic field doesn't remain uniform over the face of the coil.

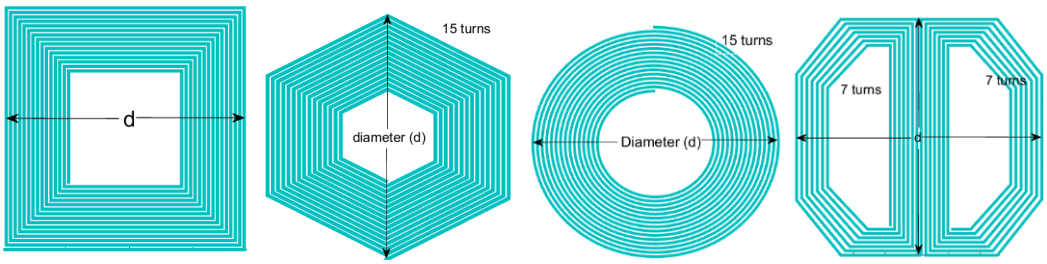


Fig. 3.1 Square, hexagonal, circular and DD shapes of spiral coils.

There is another way to construct the coil with multiple turns is in spiral pattern. The spiral coil is planner and has almost uniform magnetic flux density over its face. Comparing helical and spiral coils, it's observed which is obvious also that helical coil has higher self and mutual inductance because average area of each turn is higher in helix. Despite of lower inductance values than helical coil, the spiral structure holds higher coupling coefficient [6], [7].

Keeping this conclusion in mind and considering the required features of the WPT coils some coil structures in spiral patterns are brought into attentions. Fig. 3.1 shows the diagrams of square, hexagonal, circular and a double-D kind of coil structures. In coupled condition of such coils with 15 turns and airgap between two coils is 15 cm, their self and mutual inductances are obtained using finite element methods with COMSOL-Multiphysics tool. Here in the figure

Table 3.1 Coupling parameters of various coils.

| Indices/Shapes | Square | Hexagonal | Circular | DD shape |
|---|---|---|---|---|
| Self-inductance (μH) | 86.03 | 58.82 | 73.67 | 53.45 |
| Mutual-inductance (μH) | 17.16 | 8.89 | 12.20 | 9.55 |
| Coupling Coefficient | 0.199 | 0.151 | 0.166 | 0.179 |

shown, square, hexagon and circle are ordinary geometry in construction and flux pattern as well but the double-D has different characteristics which is called polarized coil and discussed more in the next section. In the numerical computation dimensions of all the coils are adopted such that all the coil can be deployed in the area available under vehicle body. For this comparison study 40x40 $cm^2$ area is considered deployable. The numerical analysis is carried for the mentioned coils to find out their inductive parameters and the results are reported in Table 3.1. This analysis does not consider any core associated with the coils.

The study found that self and mutual inductances of a square coil is the maximum which is justified also because for the given deployable area the square coil have maximum coil area than hexagonal and circular. In this study the DD coil is not directly comparable because it has different turn arrangement but still the coupling coefficient is observed higher than circular and hexagonal. That creates scope of more investigation which is discussed in the next section.

### 3.3 Polarized coils for WPT

Coils can be divided into two main classes: non-polarized and polarized. Non-polarized coils are characterized by the presence of only one magnetic pole in each coil face and are often

used in static WPT. These coils are fabricated with simple topologies, such as spirals of circular, square etc. shapes as discussed in the last section. The flux lines in non-polarized coils leave the coil face where the north-pole lays and reach to another face where south-pole exists, moving around the coils edges.

Polarized coils have a more complex topology where north and south magnetic poles together appear in both the faces of the coil. In this case, the flux lines leave the faces of the coil from the region corresponding to the north-pole and reach the region of the south-pole on the same face of the coil. Flux lines are hence confined in the space over (and under) the coil while magnetic flux density is low around the coil edges. These effects are further increased by the employment of flat ferrite cores and metallic shields that help in confining the flux lines in the volume between the transmitting and the pickup coils. This kind of a coil incorporates two sub-coils attached to each other and current direction in them decides the magnetic polarity over the face of a sub-coil. This type of polarized coil is also referred to double-D coil or DD coil in short form. As shown in Fig. 3.2, a DD coil is formed by two D-shaped sections that are placed back-to-back in the same plane. The two sections are electrically connected to produce, when supplied, opposite magnetic polarities over the coil faces so that, when the pickup coil is superimposed on a track coil, the flux generated by each section of the track coil links the corresponding section of the pickup coil and the voltage at the pickup coil terminals results in the sum of the voltages induced in its two sections.

The track on the road surface for dynamic wireless power transfer as discussed in the previous chapter can be realized with two types of track configuration: lumped coil track and stretched coil track. This thesis deals more about the lumped one and a lumped WPT track consists of several coils placed along the road with a certain displacement to inductively transfer

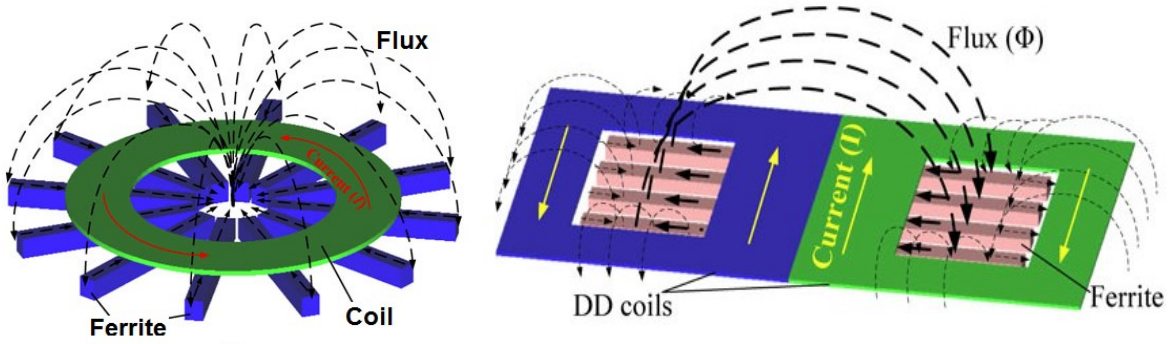


(a) (b)

Fig. 3.2 Coil structure and flux pattern (a) for Non-polarized and (b) for polarized coils.

power to the vehicle moving on the road. These track coils can be supplied by a common or individual power sources when a pickup coil gets coupled with one of them. The coupling coefficient between track and pickup coils is a very important factor in determining the efficiency and the power transfer capability of the WPT system; it depends not only on the coils alignment and spacing but also on the design and shape of the coupled coils. In order to achieve required coupling coefficient for the given airgap, the circular coils must have bigger diameter according to the concept of fundamental flux path height [2], [3] as the height is roughly proportional to one quarter of the coil diameter. This means that to increase the airgap by 10 mm, diameter of a circular coil must be increased by 40 mm. This is not suitable for dynamic wireless power transfer, as several coils need to be placed along the road. The double-D (DD) coil configuration is proposed in [3], [4] to overcome the drawbacks of the conventional coil designs. The DD coil has a bipolar configuration, as shown in Fig. 3.2 (b), and is constructed of two D-shaped back-to-back coils, placed in the same plane and electrically connected such that they have opposite magnetic polarities over their faces when supplied. During coupling of track and pickup DD coils, flux generated from one D section of the track coil passes through the pickup DD set and returns back to the other D section of the same track coil. The DD coil is only designed to generate and couple parallel flux polarized along the length of the pad while the circular coil is only designed to generate and couple perpendicular flux. This can be identified by looking into the same figure and supposing another coil is being coupled over the first one. In the circular coil flux lines travel perpendicularly upward but in the DD coil flux lines travels parallel through the pickup coil. In this way flux lines link with the pickup in parallel fashion and the flux path height is almost double then the circular coil coupler [3].

### 3.4 Misalignment and Coupling Coefficient

Coupling coefficient during misalignment or mutual inductance profile is very important consideration in dynamic WPT, because most of the time a pickup remains misaligned from any of the track coil while moving on the road. Coupling between two planner coils is found the best when both the coupled coils are same in size and perfectly aligned to each other. The

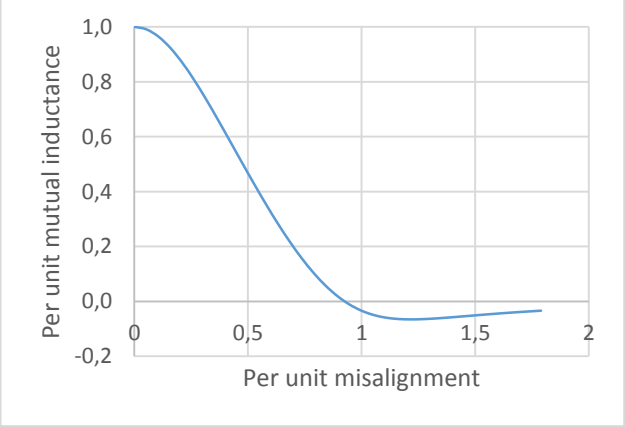


Fig.3.3. Mutual inductance vs. misalignment in circular

alignment can be classified in two types: angular alignment and displacement alignment where the former one is perfect when both the planer coils are parallel to each other and its mostly maintained in WPT for vehicular application. The displacement alignment is the major concern in vehicle charging because of the difficulty to control the vehicle position accurately over a transmitting WPT track. The displaced or misaligned pickup coil from a transmitting coil has to pay by reducing coupling coefficient. For a given airgap between two coupled coils, their mutual inductance is maximum when they are perfectly aligned angularly and laterally. Since this thesis deals about wireless charging for EVs where both the coupled coils are laid under the vehicle body and parallel to each other, therefore angular misalignment remains zero and not discussed. The misalignment which is only considered is about the displacement from the position of the stationary coil.

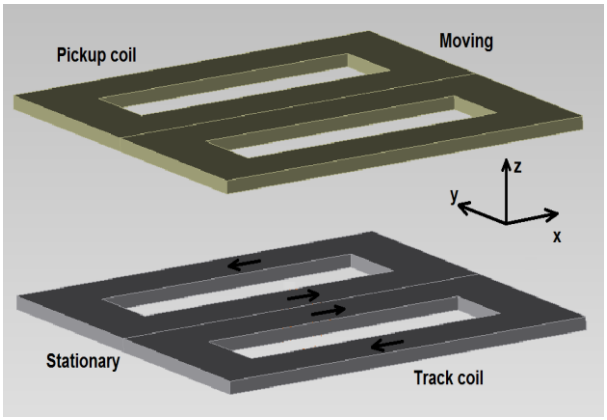

Fig.3.4. Misalignment directions in DD coils.

The effect on mutual inductance due to misalignment, sometimes depends upon the direction of the displacement also if the coil shape is not symmetric. The asymmetry in coil shape causes asymmetry in magnetic field with respect to directions, consequently the mutual inductance profile is found different in the displacement in different directions. A planner circular WPT pad has got symmetry around any radial direction therefore mutual inductance doesn't get affected by the direction of misalignment. A mutual inductance profile for a circular coil is shown on per-unit scale in Fig. 3.3; where x-axis represents the displacement of the coil center from the center of another coil. The base value to represent per unit distance is the radius of the coil and the base value for mutual inductance is its maximum value when perfectly aligned. The mutual inductance is maximum when two coils are perfectly aligned and decreases to zero with the displacement from the center point.

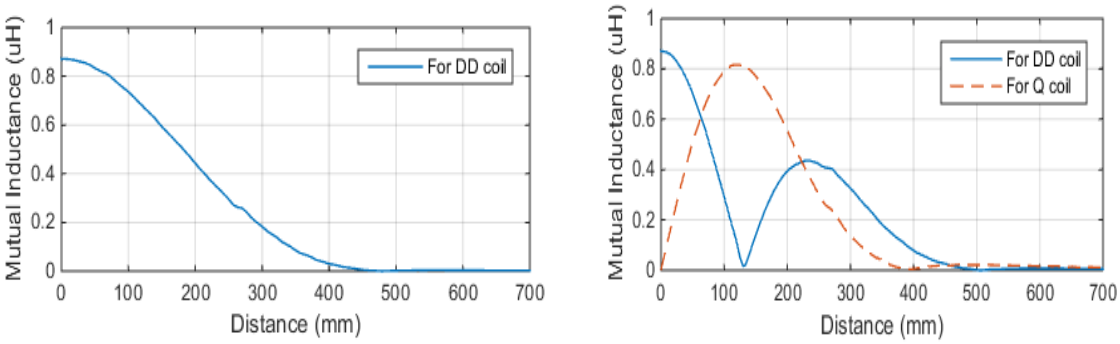


Fig. 3.5. Mutual inductance plots: (a) displacement in x-direction, (b) displacement in y-direction.

Instead, in DD coil coupler the mutual inductance profile is not same in all misalignment directions. There are mainly two orthogonal directions considered: one is the direction along which the pickup coil passes over different DD coils with alternate polarity, it is orthogonal to the back-to-back axis of the DD coil and is denoted as y-direction in Fig. 3.4; the other direction, along which the pickup coil passes over the parallel pair of DD coils, is parallel to the back-to-back axis of the DD coils and is denoted as x-direction. The mutual inductance along the x-direction has smoothly varying profile as shown in Fig. 3.5(a), similar to circular or square etc., which varies from maximum value to zero value. The mutual inductance along the y-direction has a different behavior, as shown in Fig. 3.5(b) blue line; it exhibits a dip that nearly reaches zero even if the pickup coil is still over the DD coils. At this particular position, flux links with the pickup perpendicularly so that it enters and exits from the same D coil of the pickup and the induced voltage is zero in pickup DD set. At this position, power transfer between track coil and pickup becomes zero, therefore it is called power null point. In order to avoid this point an additional coil as shown in Fig. 3.6, is placed in the center of the pickup structure such that it can capture flux around power null point. This coil is called quadrature (Q) coil [3]; it is independently tuned and the induced voltage across its terminals is rectified by a separate power converter before adding its output power to the output of the DD set. The dashed line shown in Fig. 3.5(b) is the mutual inductance curve of Q-coil which is maximum when there is a dip in mutual inductance of DD coil

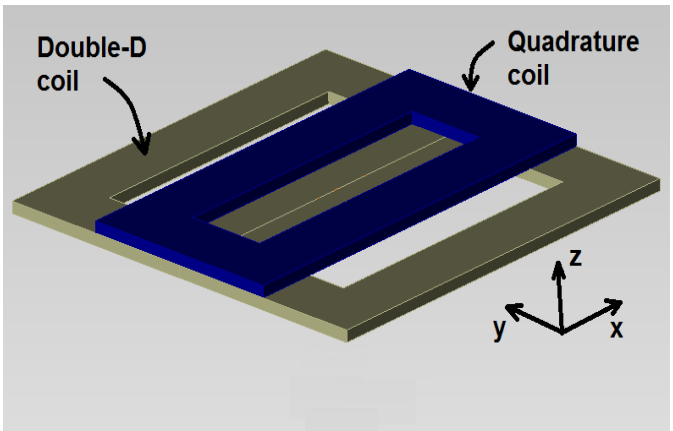


Fig.3.6. Misalignment directions in DD coils.

(solid line). Therefore a combination of DD and Q-coil can improve the coupling performance of WPT track. The DDQ configuration is only applied in pickup side and the track coil remains the same DD shown in Fig. 3.4. For dynamic WPT the DD coils are recognized more suitable for the track than the circular coils which is more discussed in the next section.

## 3.5 Comparison of Coils for Dynamic WPT

There are various types of coils proposed by many researchers as discussed earlier for wireless power transfer where each type has its pros and cons. Since the pair of coil shows better coupling when the coupled coils are identical and well aligned to each other, so this pair can be considered as a single unit and called WPT coupler. Among the various designs of the coils, appropriate coil can be chosen based on the required features. A WPT planner coil should be as thin as possible for ground clearance and fitting, operate with a large air gap (~150-200mm), be lightweight to minimize vehicle energy requirements and have good tolerance to misalignment to allow easier parking or tranquil driving over the road. Considering these basic requirements, circular and double-D coils with spiral winding pattern are chosen for a comparison. The comparison between these coils is more focused to identify better candidature in the implementation for dynamic WPT.

The most common coupler designs use a circular coil and that is being well implemented in static WPT systems. It has been noted that regardless of how optimized a design is, the fundamental flux paths in a circular coil remain relatively unchanged. The height of the flux path above the coil determines the coupling between pads and clearly higher paths are favorable. For a circular coil, the fundamental height of the flux path is roughly proportional to one quarter of the diameter as shown by the dashed line on a cut plane through the center of a track pad in Fig. 3.2 (a). This means in order to achieve required coupling coefficient for the given airgap, the circular coils must have bigger diameter according to the concept of fundamental flux path height [2], [3]. To increase the airgap by 10 mm, diameter of a circular coil must be increased by four time (i.e. 40 mm) to increase the fundamental flux path height. This is not suitable for dynamic wireless power transfer, as several coils need to be placed along the road. In other hand the DD coil is found with better fundamental flux path height than circular one with the same dimensions. This phenomenon can be understood by looking at the mutual inductance profile when the airgap is varied. Considering the same square area where a coil can be placed, pair of circular coils and DD coils is modelled in JMAG Designer. Same

square means if a circular coil is mounted in that place then diameter of the circle is equal to the length of a side of the square.

Considering a square area of 0.6x0.6 $m^2$ which is dedicated to place a circular coil and a DD coil, FEM models are created for the pair of coils of the same kind. For simplicity there is a single turn in each coil where wire diameter is kept 5 mm. Both the pairs (one circular and another DD coil pair) are fully covered by the magnetic cores of equal thickness and the same material at the top and bottom most layer of the pairs. In order to see the effect of fundamental flux path height, number of parametric simulation are carried out to obtain coupling coefficient with various airgap between two coupled coils. Fig. 3.7 illustrates the behavior of the coupling coefficient in circular coil (red line) and DD coil (blue line). This shows that pair DD coils is much better in coupling than the pair of circular coils for smaller airgap, but they behave almost same beyond a certain airgap. By this analysis it's clear that DD coil has superior coupling properties.

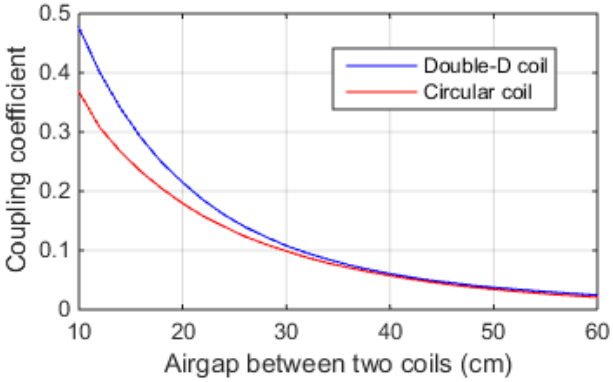

Fig.3.7. Airgap vs. coupling coefficient.

Recently, it has been shown in [3] that a polarized coil design using a DDQ receiver and a DD transmitter provides a charge zone five times larger than that of the non-polarized coil design comprising identical circular receiver and transmitter with a similar material cost and a smaller size. Fig. 3.8 illustrates a comparison of charge zone of circular and DD coil-set, where the coil dimensions are kept same, 260 mm diameter for circular and equivalent for DD. The DD pair has larger charge zone than circular coils. In case of using additional coil (i.e. Q-coil) the charge zone can be enhanced in transverse direction of the coils, shown in the same figure. Further it can also be observed that a DDQ receiver is not only increases the charge zone significantly (almost 3 times

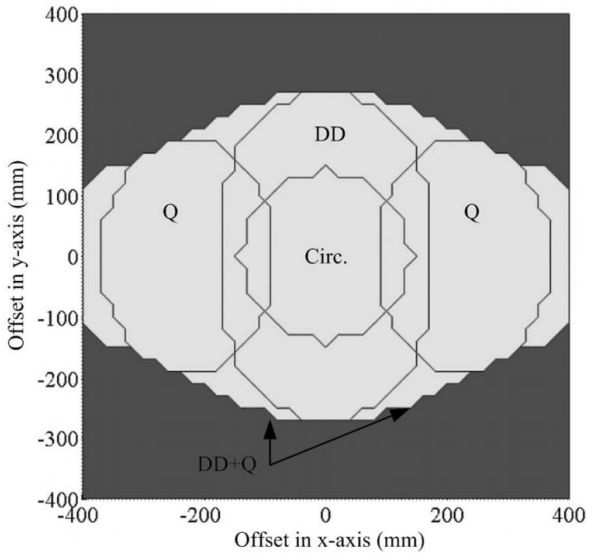

Fig. 3.8. Airgap vs. coupling coefficient.

larger) than that of a circular transmitter/ receiver system but actually it is completely interoperable with a circular transmitter. During perfectly aligned condition of circular transmitter and DDQ pickup, the net induced voltage in DD coil would be zero but not in the Q-coil, because this behaves as non-polarized one. Due to polarized nature of DD and non-polarized nature of Q-coil, the DDQ coil becomes the best choice with respect to better charge zone and interoperability.

## References


[1] L. Chen, G.R. Nagendra, J.T. Boys, and G.A. Covic, "Double-Coupled Systems for IPT Roadway Applications," IEEE Journal of Emerging and Selected Topics in Power Electronics, vol.3, no.1, pp.37-49, March 2015.

[2] M. Budhia, G. Covic, J. Boys, "A new IPT magnetic coupler for electric vehicle charging systems," proc. of IEEE Industrial Electronics Conference (IECON), 2010, pp.2487-2492.

[3] M. Budhia, J.T. Boys, G.A. Covic, and C.Y. Huang, "Development of a Single-Sided Flux Magnetic Coupler for Electric Vehicle IPT Charging Systems," IEEE Transactions on Industrial Electronics, Vol.60, No.1, pp.318-328, Jan. 2013.

[4] A. Zaheer, H. Hao, G.A. Covic, D. Kacprzak, "Investigation of Multiple Decoupled Coil Primary Pad Topologies in Lumped IPT Systems for Interoperable Electric Vehicle Charging," IEEE Transactions on Power Electronics, Vol.30, No.4, pp.1937-1955, April 2015.

[5] M. Budhia, G. A. Covic, J. T. Boys, and C.-Y. Huang, "Development and evaluation of single sided flux couplers for contactless electric vehicle charging," in Energy Conversion Congress and Exposition (ECCE), 2011 IEEE, 2011, pp. 614-621.

[6] M. Teng, W. Chenyang, W. Kai, and L. Ping, “Design of Multilayer Flat Spiral Inductive Coil for Wireless Power Transfer,” IEEE Global Conference on Consumer Electronics, 2016, pp. 1-2.

[7] Z. Kehan, D. Luona, “Comparison of Spiral Circular Coil and Helical Coil Structures for Wireless Power Transfer System,” World Academy of Science, Engineering and Technology (WASET) International Journal of Electronics and Communication Engineering Vol. 4, No. 1, pp. 752, 2017.

Chapter 4

# Analysis of Vehicle Movement over a Lumped Coil Track

In dynamic wireless charging (DWC) there is a pickup coil in the vehicle chassis which gets coupled with the track and receives power [1]-[2]. As discussed in Chapter 2, in power transmitting side the track can be constructed of two types: a long distant single coil that is called stretched coil track and a set of several small size coils that is called segmented coil track [3]-[6]. Since the stretched coil is spread along the road and its size is not equivalent to the pickup coil so this is not good in segmentation. Another track type is constructed of several individual coils which can be controlled individually to generate magnetic field according to requirement. As a vehicle moves on the track current flow is transferred to next coil and previous coil can be shut off. In this way segmentation can be easily achieved in lumped coil track to avoid EMI hazards. Research on the stretched tracks has led to the development of the OLEV prototype by KAIST [7] while research on lumped tracks has been initiated by a research group of Auckland University [8]. The lumped track lends itself to the supply of only the track portion actually coupled with a pickup coil; this supply solution, commonly termed as segmentation, is useful both to increase the DWC efficiency and to avoid the radiation of electromagnetic fields from the non-coupled track portions [9].This chapter refers the lumped coil track for more discussion.

## 4.1 Lumped Coil Track

DWC is a situation where the pickup coil interacts with different coils placed on the road to form a WPT track. These coils are called track coils. Every track coil can be considered as source of wireless power and when a pickup coil is perfectly aligned with a pole, maximum power is transferred inductively. The mutual inductance between two coaxial planner coils is maximum and it falls down when the distance between their axis increases [10]-[12]. Therefore the power captured by the pickup coil varies as vehicle moves over the WPT track. The power captured is also affected by lateral misalignment because it effectively increases the axis distance of two coils. So the peaks of power transfer in moving condition are periodic and intermittent that is only in perfectly aligned condition. The periodic variation of power which oscillates between zero and the peak value as vehicle moves and the frequency of power peaks depends upon the vehicle velocity. This document is about a study of energy captured by pickup with different vehicle speed.

In a DWC system, the movement of the pickup coil while EV moves along the road, exemplified by axis *x* in Fig. 4.1. Both track coils and pickup coil are usually compensated by capacitors with the end of increasing efficiency and power transfer capability of the DWC system [14], [15]. Here a series-connected capacitor is used for the pickup coil while it is not of importance in this chapter the compensation topology used for the track coils.

Design of the lumped track layout is carried out under the following hypotheses:

i) The track coils are deployed at a constant distance $D$ from one another, where $D$ is long enough so that, when the pickup coil is exactly aligned on the top of a track coil, the mutual inductances of the pickup coil with the previous and next track coils are irrelevant.

ii) The track coils are supplied with the same sinusoidal current $i_t$ having constant peak magnitude $I_t$ and angular frequency $\omega_s$.

iii) EV moves along the line passing through the track coil centres. This is omitted in a later stage where a motion with a lateral displacement along axis *y* of Fig. 4.1 is evaluated.

iv) The EV speed $U$ is constant.

v) EV travels a distance during one period of the supply current is much shorter than $D$.

vi) Track and pickup coils are equal and of core-type; the coils have two axes of symmetry that are directed along the directions *x* and *y*.

Under hypothesis i), when the pickup coil moves between the two track coils as illustrated in Fig. 4.1, the voltage induced in the pickup coil is

$$v_p = -\frac{d\lambda_b}{dt} - \frac{d\lambda_a}{dt} \qquad (4.1)$$

where $\lambda_b$ is the flux linkage originated by the track coil behind the pickup coil (coil $b$) and $\lambda_a$ is the flux linkage originated by the track coil ahead it (coil $a$).

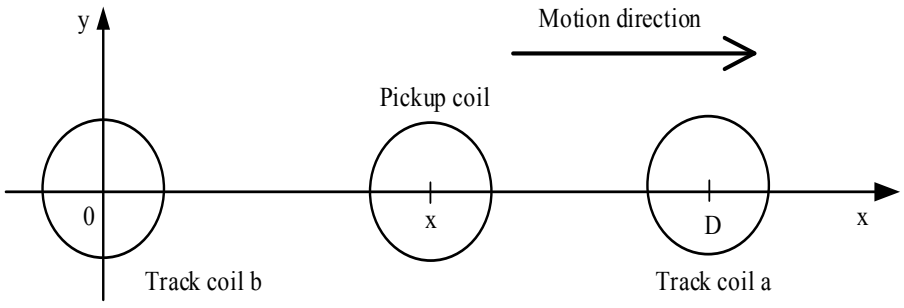


Fig. 4.1. Top view of a moving pickup coil along a lumped track.

Under hypothesis ii), eq. (4.1) can be rewritten as

$$v_p = -[M_b(x) + M_a(x)]\frac{di_t}{dt} - \frac{d[M_b(x)+M_a(x)]}{dt} i_t \qquad (4.2)$$

where $M_b(x)$ and $M_a(x)$ are the mutual inductances between the pickup coil at the position $x$ and the coils $b$ and $a$, respectively. As emphasized in (4.2), they depend on the pickup coil position $x$. The first term on the right hand side of (4.2) is the transformer voltage proper of any static wireless charging system. The second term is the motional voltage that arises in the pickup coil of a DWC system because of its motion with respect to the track coils. Hereafter, this term is disregarded since its amplitude is much less than the first term, as demonstrated in Section 4.4.

Under the hypotheses from i) to iii), the first term of (4.2) has a sinusoidal waveform with peak magnitude $V_I$ given by

$$V_I = \omega_s I_t [M_b(x) + M_a(x)] \qquad (4.3)$$

An equivalent schematic of the DWC system is shown in Fig. 4.2, where $L_p$ is the self-inductance of the pickup coil, $L_t$ is the self-inductance of the track coils, $i_p$ is the current in pickup, $C_p$ is the compensation capacitor and $R_L$ is the pickup load resistance. Capacitor $C_p$ is selected in order to resonate with $L_p$ at the supply angular frequency; resistor $R_L$ represents the battery resistance referred to the pickup coil terminals, henceforth termed as battery equivalent load.

As shown later on, cored track and pickup coils have self-inductances that vary with the pickup coil position. To simplify the design, such a variation, in particular that one of $L_p$, is ignored in the designed stage, leaving to the computer-assisted analysis in Section 4.5 to check its relevance. Further to this simplification, the series branch $L_p$, $C_p$ resonates for any position $x$ of the pickup so that the voltage across the branch is zero, and the peak magnitude of the current flowing in $R_L$ is

$$I_p = \frac{V_I}{R_L} = \frac{\omega_s I_t [M_b(x)+M_a(x)]}{R_L} \qquad (4.4)$$

Under hypothesis v), the change of the mutual inductances due to the EV motion in one

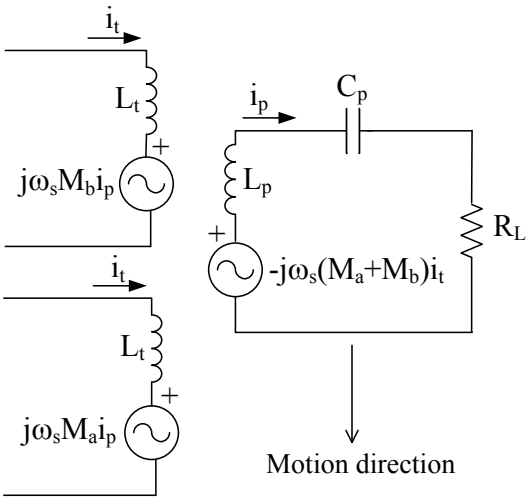


Fig. 4.2. DWC system equivalent schematic.

period of the track coil supply current can be disregarded and the average power transferred to $R_L$ in the period is

$$P_L = \frac{1}{2} I_p^2 R_L = \frac{1}{2} \frac{\omega_s^2 I_t^2 [M_b(x) + M_a(x)]^2}{R_L} \qquad (4.5)$$

Let $T_D$ be the time taken by EV to cover the distance $D$. The energy transferred to $R_L$ during $T_D$ is given by

$$E = \int_0^{T_D} P_L(t)\, dt \qquad (4.6)$$

Further to hypothesis iv), it is

$$dt = \frac{1}{U} dx \qquad (4.7)$$

and (4.6) can be expressed as

$$E = \frac{1}{U} \int_{x(0)}^{x(0)+D} P_L(x)\, dx \qquad (4.8)$$

where *x(0)* is the EV position along the axis *x* at *t*=0. By (4.5), (4.8) can be rewritten as

$$E = \frac{1}{U} K \int_{x(0)}^{x(0)+D} [M_b(x) + M_a(x)]^2 dx \qquad (4.9)$$

where $K$ is given by (4.10) and it accounts for the track coils supply current and the battery equivalent load

$$K \triangleq \frac{1}{2} \frac{\omega_s^2 I_t^2}{R_L} \qquad (4.10)$$

Further to hypothesis vi), the following relations hold for the mutual inductances:

$$M_a(x) = M_a(-x), \;\; M_b(x) = M_b(-x) \qquad (4.11)$$

$$M_a(x) = M_b(x - D) \qquad (4.12)$$

thus (4.9) can be simplified as

$$E = \frac{1}{U} K \int_0^D [M_b(x) + M_a(x)]^2 dx \qquad (4.13)$$

If the track coils are deployed all along a certain EV route, the number of track coils coupled with the pickup coil in a given time interval is proportional to the EV speed; on the other hand, according to (4.13), the energy transferred to the pickup coil between two track coils is inversely proportional to the speed. Consequently, the total energy transferred to the pickup coil in a given time interval does not depend on the EV speed.

## 4.2 Coils for WPT Track

The mutual inductance *M* between track and pickup coils is a key factor in setting efficiency and power transfer capability of any DWC system; it depends not only on the relative coil position, which varies during the EV motion, but also on the shape of the coils. In recent year the so-called DD coils have been proposed [11], [16]. They are conveniently used for the pickups of both stretched and lumped track DWC systems and, in the latter case, they are used also in the track [17]. In Fig. 4.3 a pair of DD coils, one for the track and the other one for the pickup, is drawn. The coils are made of two D sections placed back-to-back in the same plane. The two sections are electrically connected to produce, when they are supplied, opposite magnetic polarities over the coil faces so that, when the pickup coil is superimposed on a track coil, the flux generated by each section of the track coil links the corresponding section of the pickup coil and the voltage at the pickup coil terminals is the sum of the voltages induced in its two sections.

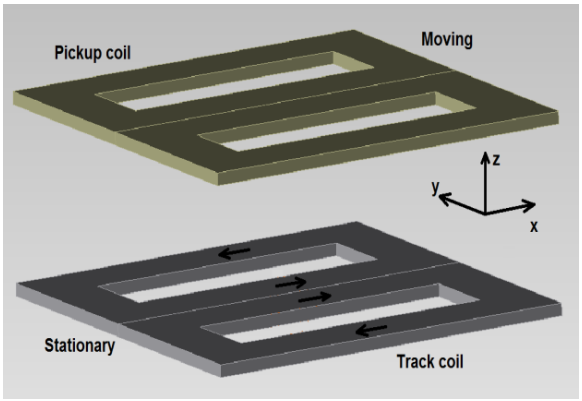


Fig. 4.3. DD coil set.

A FEM code in JMAG environment has been drawn up to evaluate the dependence of the mutual and self-inductances of the DD coils on the pickup position *x*, also termed as longitudinal displacement. Four different pairs of DD coils with the dimensions X (longitudinal) and Y (lateral) reported in Table 4.1 have been examined. Each pair is made of two equal coils having one wire turn and placed on parallel planes set 0.2 m apart. Both the coils have planar ferrite cores leant on their external faces so that most of the flux lines are confined in the volume between the two coils. The longitudinal displacement has been increased from 0, where the coils are aligned, up to a distance where their mutual inductances falls below 1% of their maximum value.

Table 4.1

Coil Pair Parameters

| Coil pair | X dimension [m] | Y dimension [m] | $M_0$ [μH] | $L_0$ [μH] | $k_0$ |
|---|---|---|---|---|---|
| #1 | 2.5 | 1.5 | 16.6 | 34.0 | 0.487 |
| #2 | 1.5 | 1.5 | 9.7 | 21.1 | 0.460 |
| #3 | 1.0 | 1.5 | 6.3 | 17.7 | 0.428 |
| #4 | 1.5 | 1.0 | 5.8 | 16.4 | 0.357 |

The resultant dependence of the mutual inductances is plotted in Fig. 4.4, where the lines marked with x, o, □, and * refer to coil pair #1, #2, #3,

and #4 in Table 4.1, respectively. The plots show that the mutual inductances varies with $x$ in a nearly linear way, decreasing from the maximum value $M_0$ to about zero in a space interval $S$ a little longer than the longitudinal dimension of the coils. Such a dependence of the mutual inductance with the longitudinal displacement is typical of the DD coils and is supported by the experiments in chapter 11. Coils with other shapes have a mutual inductance that decreases with the longitudinal displacement in a different way; for example, the circular coils exhibit a parabolic decrease [18]. The results obtained for coil pairs #2 and #4 put in evidence that the length of the space interval $S$ is not affected by the lateral dimension of the coils, at least for the examined dimension range. Instead, the maximum mutual inductance $M_0$ is affected by both the longitudinal and lateral dimensions of the coils. Regarding the self-inductance of the coils, it changes with the longitudinal displacement because the coils are endowed with ferrite cores, otherwise it would remain constant. As shown in Fig. 4.5, the self-inductance reaches its maximum value $L_o$ when the coils are aligned and then decreases as the longitudinal displacement increases. In accordance with the simplification posed for the design stage, $L_p$ is taken constant, equal to its value $L_o$ in aligned conditions.

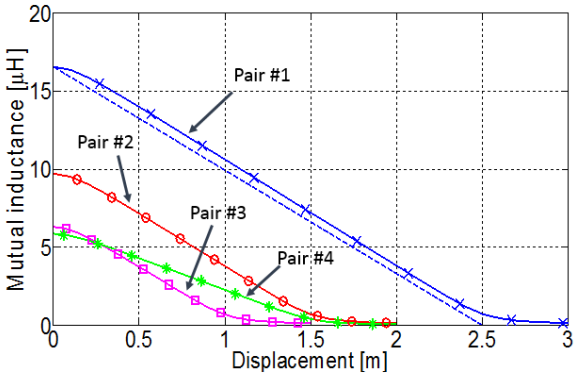


Fig. 4.4. Mutual inductance vs. longitudinal displacement.

Maximum values of the mutual and self-inductances as well as the corresponding coupling coefficients are reported in the right side columns of Table 4.1.

Figs. 4.4 and 4.5 refer to the inductive parameters of a coil pair made of the pickup coil and one track coil. In real DWC systems, however, the track is made of a string of coils, whose existence could influence the self-inductance of the pickup coil and its mutual inductance with the track coils, especially if the latter ones are deployed at short distance from each other. This influence has been also evaluated by a

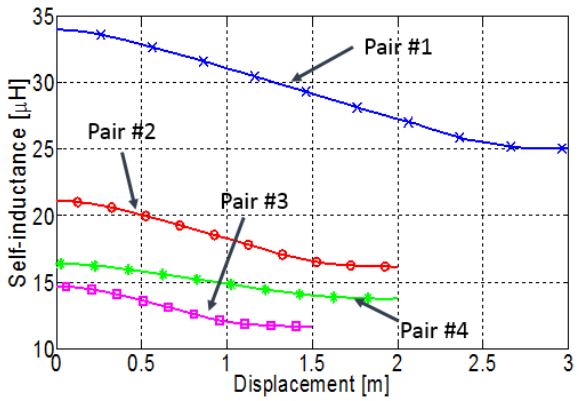


Fig. 4.5. Self-inductance (b) vs. longitudinal displacement.

FEM analysis, for pickup and track coils having the dimensions of coil pair #1 and for a track section of three coils. Mutual inductance and self-inductance have been worked out from the results of the FEM analysis for five different distances $D$, namely $D=X$ (i.e. with track coils in contact each other), $D=1.25X$, $D=1.5X$, $D=1.75X$ and $D=2X$ (i.e. with a gap between two subsequent track coils equal to the coil length). Longitudinal displacement of the pickup coil with respect to the central track coil has been increased from 0 to $D/2$ and then, by exploiting the symmetry of the track layout, inductive parameters have been found for a longitudinal displacement increasing up to $D$. The profiles of the mutual inductance for the five values of $D$ are traced in Fig.4.6. They are almost superimposed, and their values coincide with those in Fig. 4.4 so that it can be concluded that the mutual inductance is unaffected by $D$. Instead, the self-inductance of the pickup coil changes with respect to Fig. 4.5: it gets higher values and its profile becomes flatter. Such a change is more sensible when D is small and the longitudinal displacement is large. The extreme condition is reached for $D=X$, where the self-inductance is constant over $D$.

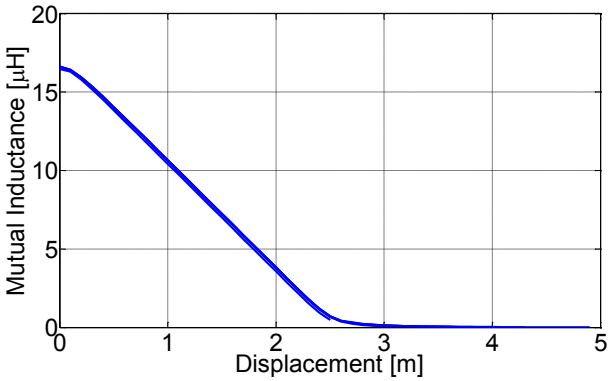

Fig. 4.6. Mutual inductance vs. longitudinal displacement for different track coil distance.

In order to more simplify (4.13) and to find a relation in pole distance and energy transferred, the plot of mutual inductance can be approximated. As shown in Fig. 4.4, mutual inductance is maximum at the pole faces that is $M_0$ which decreases with distance apart from a pole and becomes zero (or negligible) after $\sigma$ distance. The distance $\sigma$ can be called as magnetic flux coverage of a coil. All the track coils are placed on the road such that their mutual coupling is negligible. The energy analysis is done considering two situations: when flux coverages of two consecutive coils don't intersect each other and another when flux coverages are overlapped; this is more discussed in the next section.

### 4.3 Transferred Power and Energy in Track with DD Coils

On the basis of the outcomes of the previous section, the dependence of $M_a$ and $M_b$ on the longitudinal displacement is approximated with a line as exemplified in Fig. 4.4 for coil pair #1; note that the line is a bit lower than the actual mutual inductance profile all along the

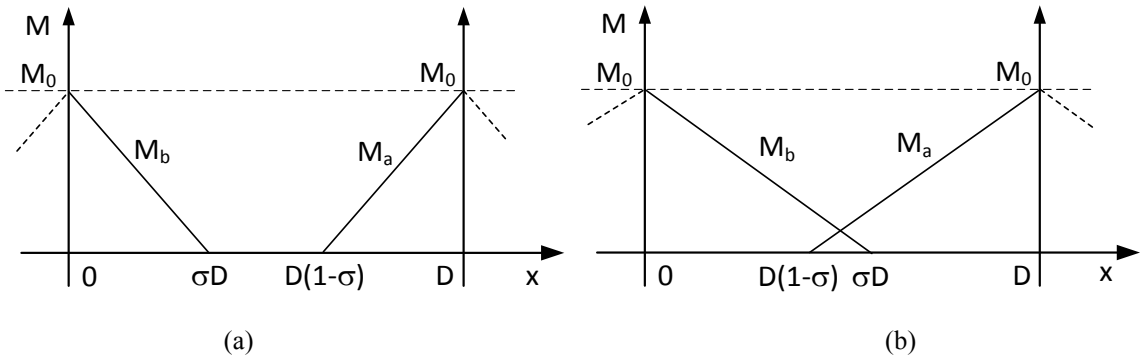


(a) (b)

Fig. 4.7. Profile of the mutual inductances along the direction x and different coverage situations: (a) separate flux coverage, and (b) overlapped flux coverage.

displacement. By hypothesis vi) in Section 4.1, the profiles of $M_a$ and $M_b$ along the axis $x$ are as traced in Fig. 4.7.

The parameter $\sigma$, denoted as track flux coverage, is introduced in Fig. 4.7. By referring to coil $b$, $\sigma$ is defined as the ratio between the position $x$ at which $M_b$ becomes equal to zero and the track coil distance $D$. According to hypothesis i) in Section 4.1, it is $\sigma<1$. From an inspection of Fig. 4.4, it emerges that, with good approximation, $\sigma D$ is equal to the longitudinal dimension of the coil. Consequently, for a track of a given length, $\sigma$ represents the portion of track populated with coils and, hence, it gives a useful index of cost of the DWC system.

Depending on the distance of the track coils and their longitudinal dimension, $M_b$ could become zero before or after that $M_a$ becomes greater than zero; the first situation, designated with "separate flux coverage" (SFC), is represented in Fig. 4.7 (a) and occurs for $\sigma<1/2$ while the second one, designated with "overlapped flux coverage" (OFC), is represented in Fig. 4.7 (b) and occurs for $\sigma>1/2$.

By the linear approximation, $M_b$ and $M_a$ can be expressed as in (4.14) and (4.15), respectively; the expressions are given as a function of $x/D$ in order to make the subsequent analysis parametric.

$$\begin{cases} M_b\left(\frac{x}{D}\right) = M_0\left(1 - \frac{1}{\sigma}\frac{x}{D}\right), & \frac{x}{D} \in [0, \sigma] \\ M_b\left(\frac{x}{D}\right) = 0, & \frac{x}{D} \in [\sigma, 1] \end{cases} \tag{4.14}$$

$$\begin{cases} M_a\left(\frac{x}{D}\right) = 0, & \frac{x}{D} \in [0, (1-\sigma)] \\ M_a\left(\frac{x}{D}\right) = M_0\left[1 + \frac{1}{\sigma}\left(\frac{x}{D} - 1\right)\right], & \frac{x}{D} \in [(1-\sigma), 1] \end{cases} \tag{4.15}$$

*4.3.1 Power and energy analysis under SFC (σ<1/2)*

Under SFC, the power transferred to the pickup coil while EV moves from track coil *b* to track coil *a* is obtained by substituting (4.14) and (4.15) in (4.5). The expression of the transferred power is

$$\begin{cases} P_{L,SFC}\left(\frac{x}{D}\right) = KM_0^2\left(1-\frac{1}{\sigma}\frac{x}{D}\right)^2, & \frac{x}{D}\in[0,\sigma] \\ P_{L,SFC}\left(\frac{x}{D}\right) = 0, & \frac{x}{D}\in[\sigma,(1-\sigma)] \\ P_{L,SFC}\left(\frac{x}{D}\right) = KM_0^2\left[1+\frac{1}{\sigma}\left(\frac{x}{D}-1\right)\right]^2, & \frac{x}{D}\in[(1-\sigma),1] \end{cases} \quad (4.16)$$

By (4.13)-(4.15), the energy transferred to EV is

$$E_{SFC} = \frac{\mathrm{D}}{U}K\left\{\int_0^{\sigma} M_b^2\left(\frac{x}{D}\right)d\frac{x}{D} + \int_{(1-\sigma)}^{1} M_a^2\left(\frac{x}{D}\right)d\frac{x}{D}\right\} \quad (4.17)$$

Solving (4.17) yields

$$E_{SFC} = 2\sigma D\frac{KM_0^2}{3U} \quad (4.18)$$

Eq. (4.18) points out that the energy transferred to EV is proportional to $2\sigma D$, i.e. to the length of the two fractions of the track coil distance where either $M_a$ or $M_b$ are greater than zero. The remaining part of $D$ does not enter in the expressions of $P_{L,SFC}$ and $E_{SFC}$ because there is no any power transfer within it.

*4.3.2 Power and energy analysis under OFC (σ>1/2)*

Under OFC, the expression of the power transferred to the pickup coil while EV moves from track coil *b* to track coil *a* is

$$\begin{cases} P_{L,OFC}\left(\frac{x}{D}\right) = KM_0^2\left(1-\frac{1}{\sigma}\frac{x}{D}\right)^2, & \frac{x}{D}\in[0,(1-\sigma)] \\ P_{L,OFC}\left(\frac{x}{D}\right) = KM_0^2\left(2-\frac{1}{\sigma}\right)^2, & \frac{x}{D}\in[(1-\sigma),\sigma] \\ P_{L,OFC}\left(\frac{x}{D}\right) = KM_0^2\left[1+\frac{1}{\sigma}\left(\frac{x}{D}-1\right)\right]^2, & \frac{x}{D}\in[\sigma,1] \end{cases} \quad (4.19)$$

By (4.13)-(4.15), the energy transferred to EV is

$$E_{OFC} = \frac{D}{u}K\left\{\int_0^{(1-\sigma)} M_{\mathrm{b}}^2\left(\frac{x}{D}\right)d\frac{x}{D} + \int_{(1-\sigma)}^{\sigma}\left[M_b\left(\frac{x}{D}\right)+M_a\left(\frac{x}{D}\right)\right]^2 dx + \int_{\sigma}^{1} M_a^2\left(\frac{x}{D}\right)d\frac{x}{D}\right\} \quad (4.20)$$

The latter expression, rewritten as

$$E_{OFC} = E_{SFC} + \frac{\mathrm{D}}{u}K2\int_{(1-\sigma)}^{\sigma} M_b\left(\frac{x}{D}\right)M_a\left(\frac{x}{D}\right)d\frac{x}{D} \quad (4.21)$$

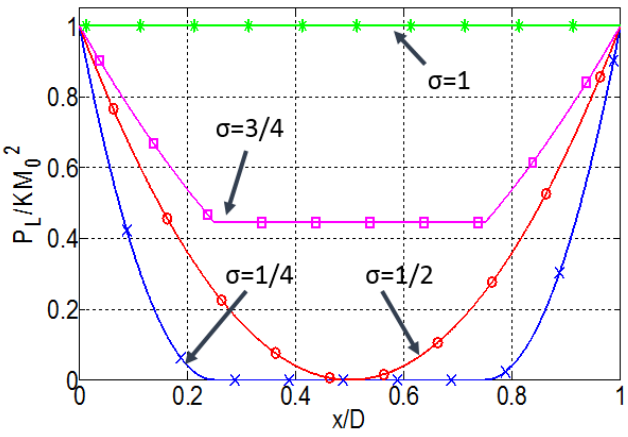


Fig. 4.8. Normalized transferred power vs. $x/D$ for $\sigma$=1/4 (x), $\sigma$=1/2 (o), $\sigma$=3/4 (□) and $\sigma$=1 (*).

emphasizes that the transferred energy under OFC is higher than under SFC because in the interval $[D(1-\sigma), \sigma D]$ both the track coils $b$ and $a$ contribute to the transfer of power, as described by the second of (4.19). After simple manipulations, the expression of $E_{OFC}$ can be rewritten as

$$E_{OFC} = 2\sigma D \frac{KM_0^2}{3U}\left(5 + \frac{3}{\sigma^2} - \frac{1}{2\sigma^3} - \frac{6}{\sigma}\right) \qquad (4.22)$$

Eq. (4.22) highlights that $E_{OFC}$ depends on the product of two terms, one is $2\sigma D$ like for $E_{SFC}$, and the other one is a non-linear function of $\sigma$.

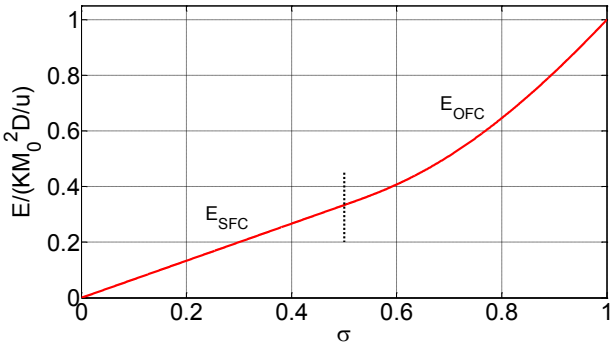


Fig. 4.9. Normalized transferred energy vs. σ.

The transferred power as a function of $x/D$ and for four values of $\sigma$ is traced in Fig. 4.8, where the power is normalized to $KM_0^2$. The trace marked with crosses refers to SFC with $\sigma$=1/4; the trace marked with circles refers to $\sigma$=1/2, which is the boundary condition between SFC and OFC; the traces marked with squares and stars refer to OFC with $\sigma$=3/4 and $\sigma$=1, respectively. The traces points out that OFC is more effective than SFC in transferring power to the pickup coil.

The transferred energy as a function of $\sigma$ is traced in Fig. 4.9, where the energy is normalized to $KM_0^2 D/U$. As expected, $E_{OFC}$ is larger than $E_{SFC}$ and increases more than in linear way with $\sigma$.

## 4.4 Effect of Motion upon Voltage

The voltage induced in the pickup coil because of its motion with respect to the track coils is composed by sine waves; they have the same angular frequency as the track supply current and peak magnitude that varies as given by

$$V_M = \left|\frac{d[M_b(x)+M_a(x)]}{dt}\right| I_t = \left|\frac{d[M_b(x)+M_a(x)]}{dx}\right| UI_t \qquad (4.23)$$

Under linear profiles of $M_a$ and $M_b$, the expression of $V_M$ for both SFC and OFC is given by

$$\begin{cases} V_M\left(\frac{x}{D}\right) = M_0 I_t f_D \frac{1}{\sigma}, & \frac{x}{D} \in [0, \sigma] \\ V_M\left(\frac{x}{D}\right) = 0, & \frac{x}{D} \in [\sigma, (1-\sigma)] \\ V_M\left(\frac{x}{D}\right) = M_0 I_t f_D \frac{1}{\sigma}, & \frac{x}{D} \in [(1-\sigma), 1] \end{cases} \qquad (4.24)$$

where $f_D$=1/$T_D$.

By substituting (4.14) and (4.15) in (4.3), the expressions of the peak magnitude $V_I$ of the transformer voltage for SFC and OFC become

$$\begin{cases} V_{I,SFC}\left(\frac{x}{D}\right) = I_t \pi f_s M_0 \left(1 - \frac{1}{\sigma}\frac{x}{D}\right), & \frac{x}{D} \in [0, \sigma] \\ V_{I,SFC}\left(\frac{x}{D}\right) = 0, & \frac{x}{D} \in [\sigma, (1-\sigma)] \\ V_{I,SFC}\left(\frac{x}{D}\right) = I_t \pi f_s M_0 \left[1 + \frac{1}{\sigma}\left(\frac{x}{D} - 1\right)\right], & \frac{x}{D} \in [(1-\sigma), 1] \end{cases} \qquad (4.25)$$

$$\begin{cases} V_{I,OFC}\left(\frac{x}{D}\right) = I_t \pi f_s M_0 \left(1 - \frac{1}{\sigma}\frac{x}{D}\right), & \frac{x}{D} \in [0, (1-\sigma)] \\ V_{I,OFC}\left(\frac{x}{D}\right) = I_t \pi f_s M_0 \left(2 - \frac{1}{\sigma}\right), & \frac{x}{D} \in [(1-\sigma), \sigma] \\ V_{I,OFC}\left(\frac{x}{D}\right) = I_t \pi f_s M_0 \left[1 + \frac{1}{\sigma}\left(\frac{x}{D} - 1\right)\right], & \frac{x}{D} \in [\sigma, 1] \end{cases} \qquad (4.26)$$

where the frequency $f_s$=$\omega_s$/2$\pi$ is introduced in place of $\omega_s$ to facilitate the comparison between $V_I$ and $V_M$.

If such a comparison were performed at $\frac{x}{D} = \sigma$ or at $\frac{x}{D} = (1-\sigma)$, the results would be not significant because the linear approximations of $M_a$ and $M_b$ have cusps in those positions that originate discontinuities in $V_M$. Indeed, the effective profile of the mutual inductances decay to zero smoothly and $V_M$ does not have any discontinuity. The same would occur at $\frac{x}{D} = 0$ or at $\frac{x}{D} = 1$. For this reason, $V_M$ and $V_I$ are compared at $\frac{x}{D} = \frac{\sigma}{2}$. From (4.23), (4.25) and (4.26), one obtains for SFC and OFC, respectively

$$\begin{cases} \frac{V_M\left(\frac{\sigma}{2}\right)}{V_I\left(\frac{\sigma}{2}\right)} = \frac{f_D}{f_S}\frac{2}{\pi\sigma}, & \sigma \in \left[0, \frac{2}{3}\right] \\ \frac{V_M\left(\frac{\sigma}{2}\right)}{V_I\left(\frac{\sigma}{2}\right)} = \frac{f_D}{f_S}\frac{1}{\pi(2\sigma-1)}, & \sigma \in \left[\frac{2}{3}, 1\right] \end{cases} \quad (4.27)$$

The supply frequency $f_s$ of the DWC systems has been fixed at 85 kHz by SAE International J2954 Task Force; the frequency $f_D$, in turn, does not exceed 10 Hz. With these frequency values, the first equation of (4.27) states that $V_M$ has a magnitude as high as to $V_I$ only if $\sigma$ is about $75 \cdot 10^{-6}$, i.e. only if 75 mm of coil are deployed for every km of track. And additionally, the second equation of (4.27), calculated for $\sigma$=2/3, states that $V_I$ is more than 8900 times greater than $V_M$. Further to these data, it can be concluded that in a practical DWC system the motional voltage is negligible compared to the transformer voltage and, hence, it can be disregarded in designing the track layout.

## 4.5 Case Study and Sizing of Track Layout

As a study case, a compact C-class car moving at high speed for a long distance, for instance in the highways, is considered. The main characteristics of the car are reported in Table 4.2. The DWC system is required to transfer to EV all the energy spent for its motion so that the charge level of the battery when EV leaves the highway is the same as when it was entering (transferred energy balance requirement).

The power needed to run a car at constant speed $U$ on a horizontal road is

$$P = (F_d + F_{roll})U \quad (4.28)$$

where $F_d$ is the air drag force and $F_{roll}$ is the rolling resistance force. The air drag force is expressed as

$$F_d = \frac{1}{2} C_d \rho_{air} A_f U^2 \quad (4.29)$$

where $C_d$ is the air drag coefficient, $A_f$ is the front area of the car and $\rho_{air}$ is the air density, set at 1.167 kg/m$^3$. The rolling resistance force is expressed as

$$F_{roll} = K_{rf} mg \quad (4.30)$$

Table 4.2
Reference Car Parameters

| Quantity | Symbol | Values |
|---|---|---|
| Mass | $m$ | 1475 kg |
| Width | $l$ | 1.77 m |
| Wheelbase | $h$ | 2.7 m |
| Maximum speed | $U$ | 140 km/h |
| Air drag coefficient | $C_d$ | 0.28 |
| Front area | $A_f$ | 2.23 m2 |
| Rolling friction coefficient | $K_{rf}$ | 0.01 |
| Nominal battery voltage | $V_B$ | 365 V |
| Nominal battery charging power | $P_N$ | 50 kW |
| Pulse battery charging power | $P_{pk}$ | 70 kW |

where $K_{rf}$ is the rolling friction coefficient, $m$ is the mass of the car and $g$ is the gravitational acceleration.

An overall efficiency of 80% is assumed for the EV powertrain, which goes from the DC bus to the wheels and includes the traction inverter, the traction motor and a reduction gear. By help of (4.28)-(4.30), the average power $P_{avg}$ that must be entered into the DC bus of the powertrain is 34 kW, corresponding to an energy $E_{km}$=874 kJ/km. These data represent the need of power and energy to be transferred from the DWC system to the pickup coil.

By assuming, for simplicity, that the DC bus voltage is equal to the nominal battery voltage, the EV powertrain appears at the terminals of the compensated pickup coil as an average equivalent load of about

$$R_L = \frac{8}{\pi^2}\frac{V_B^2}{P_{avg}} \cong 3.2\Omega \qquad (4.31)$$

### *4.5.1 Track Layout Sizing*

Being the longitudinal dimension of the track coils much smaller than 1 km, the number of coils deployed in 1 km of track can be approximated with 1000/$D$. By (4.18), (4.22) and (4.10), the following equations of $E_{km}$ apply for SFC and OFC, respectively:

$$E_{km} = \frac{1000}{3U}\frac{\omega_s^2 I_t^2 M_0^2}{R_L}\sigma,\ \sigma \in \left[0, \frac{1}{2}\right] \qquad (4.32)$$

$$E_{km} = \frac{1000}{3U}\frac{\omega_s^2 I_t^2 M_0^2}{R_L}\sigma\left(5 + \frac{3}{\sigma^2} - \frac{1}{2\sigma^3} - \frac{6}{\sigma}\right),\ \sigma \in \left[\frac{1}{2}, 1\right] \qquad (4.33)$$

For given values of $E_{km}$, $\omega_s$, $U$ and $R_L$, (4.32) and (4.33) establish a relationship between $I_t$, $M_0$ and $\sigma$. It is represented by the diagrams of Fig. 4.10 for three values of the track supply

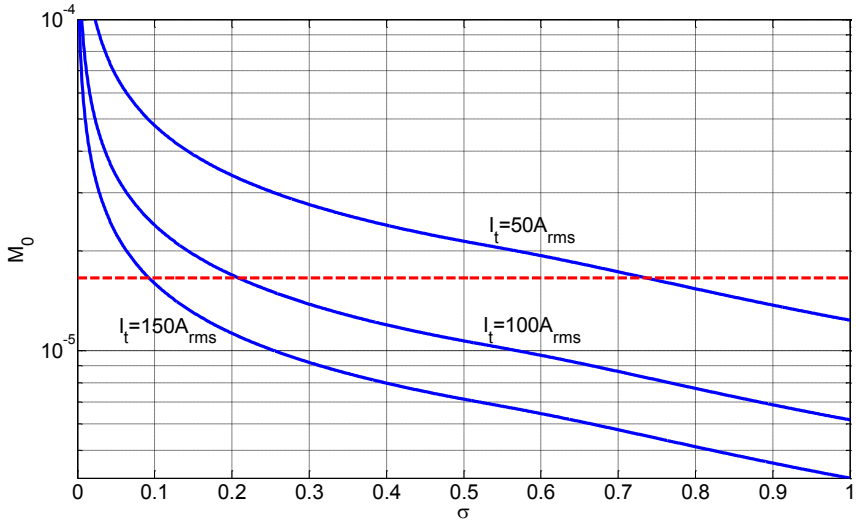


Fig. 4.10. Mutual inductance vs. $\sigma$ for various track currents ($E_{km}$ =874 kJ/km).

currents: 50 $A_{rms}$, 100 $A_{rms}$ and 150 $A_{rms}$. The diagrams give a guideline to size the track layout. As a matter of fact, they permit to find out $M_0$ once $\sigma$ is set or, conversely, to find out $\sigma$ once $M_0$ is known. As an example, for coil pair #1 (horizontal line in Fig. 4.10 with $M_0$=16.6 μH) the value of $\sigma$ is 0.736 for a track supply current of 50 $A_{rms}$, 0.208 for 100 $A_{rms}$, and 0.093 for 150 $A_{rms}$.

Table 4.3

Track Layout Parameters

| **Coil pair** | **Current [$A_{rms}$]** | **σ** | **D [m]** | **n [coil/km]** |
|---|---|---|---|---|
| #1 | 50 | 0.736 | 3.39 | 294 |
| | 100 | 0.208 | 11.99 | 83 |
| | 150 | 0.093 | 26.98 | 37 |
| #2 | 50 | n.a. | n.a. | n.a. |
| | 100 | 0.595 | 2.52 | 397 |
| | 150 | 0.269 | 5.57 | 179 |
| #3 | 50 | n.a. | n.a. | n.a. |
| | 100 | 0.981 | 1.01 | 981 |
| | 150 | 0.623 | 1.60 | 623 |
| #4 | 50 | n.a. | n.a. | n.a. |
| | 100 | n.a. | n.a. | n.a. |
| | 150 | 0.683 | 2.19 | 455 |

Inspection of Fig. 4.10 shows that an increase in the supply current allows the deployment of track coils with a smaller $\sigma$. However, for a fixed increment in the supply current, the reduction of $\sigma$ results lower at high supply currents; moreover, the advantage of increasing the supply current is greater when coils with lower $M_0$ are employed.

As an example, the diagram can be used to find $\sigma$ for the four coil pairs in Table 4.1. Being the longitudinal dimension of the coils about equal to $\sigma D$, the number of coils to be deployed for each km of track is readily obtained. The results are summarized in Table 4.3, where n.a. stands for not applicable and means that there is no intersection of the $M_0$ line with the specified track supply current.

It is worth to notice that the procedure followed in deriving (4.32) and (4.33) is based on the hypothesis of a linear profile of the mutual inductance, rounding down their actual values. Therefore, expressions (4.32) and (4.33) are conservative for the transferred energy. On the other hand, expressions (4.4) and (4.5) for $I_p$ and $P_L$ have been found in the hypothesis of resonance of the couple $L_p$-$C_p$, which requires that $L_p$ is constant. Actually, $L_p$ is subjected to a decrease as a function of the longitudinal displacement so that the impedance of the $L_p$-$C_p$-$R_L$ series branch gets a reactive component that causes $I_p$, and hence $P_L$, to decrease. This reduces, or nullifies, the design safety margin in the transferred power given by the defect approximation of the mutual inductance.

Equations (4.32) and (4.33) point out that the transferred energy is proportional to $M_0^2$. It is known that if the coil dimensions and distance are kept fixed, $M_0$ is nearly proportional to the square of the turn number of the coils. Therefore, the mutual inductances of coil pairs with the dimensions of those considered till now, but made of two or three turns are obtained by multiplying by 4 or 9 the values reported in Table 4.1.

The resultant values of $M_0$ and, in correspondence, of $\sigma$, obtained from (4.32) or (4.33) or by using the diagrams of Fig. 4.10, are reported in Table 4.4 together with those of the coil pairs with one turn. Inspection of the table shows that a greater turn number rewards for smaller coil dimensions. As an example, coil pair #4 with 2 turns requires a smaller $\sigma$ than coil pair #1 with one turn, thus satisfying the transferred energy balance requirement by means of a tack made of smaller track coils, which is less expensive to be manufactured and installed.

Table 4.4

Track Parameters & Turn Number

| Coil pair | 1 Turn | 2 Turns | 3 Turns |
|---|---|---|---|
| #1 | $M_0$=16.6 μH | $M_0$=65.1 μH | $M_0$=0.38mH |
| | σ=0.208 | σ=0.013 | σ=0.0026 |
| #2 | $M_0$=9.72 μH | $M_0$=38.1 μH | $M_0$=0.22 mH |
| | σ=0.595 | σ=0.039 | σ=0.0075 |
| #3 | $M_0$=6.29 μH | $M_0$=24.6 μH | $M_0$=0.14 mH |
| | σ=0.981 | σ=0.090 | σ=0.0178 |
| #4 | $M_0$=5.86 μH | $M_0$=22.9 μH | $M_0$=0.13 mH |
| | σ=n.a. | σ=0.104 | σ=0.0206 |

On the other hand, transfer of the required energy $E_{km}$ using a lower number of track coils leads to an increase of the power sizing of both the coils and the power converters, whether they are used to supply the track coils or to condition the power received by the pickup. Moreover, for given values of the peak charging power of the EV battery and of the power needed to move EV, the transferred power should be limited to their sum; otherwise an auxiliary storage system, for example based on supercapacitors, must be installed on-board EV to absorb the peaks of the transferred power and to gradually release the stored energy to move EV in the portion of the track coil distance where the transferred power is not sufficient.

### *4.5.2 Sizing Validation*

Sizing of the track layout has been checked against a numerical analysis carried out in the MATLAB environment with the data obtained by the FEM analysis for the mutual and self-inductances of the track and the pickup coils, and reported in Figs. 4.4 and 4.5.

Coil pair #1 with one turn and a supply current of 100 $A_{rms}$ has been examined. By Table 4.3, the required $\sigma$ is of 0.208 with a corresponding coil distance of 12 m. On account of the

large distance between the track coils and according to Figs. 4.4 and 4.5, the mutual inductance $M_b$ becomes zero before $M_a$ starts to increase and, at the same way, the pickup coil self-inductance $L_p$ reaches its minimum and maintains it for a comparatively long distance before increasing again with a symmetric behaviour around the position $x=D/2$.

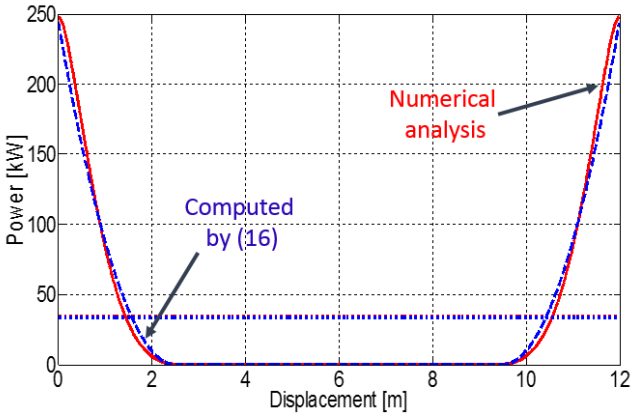

Fig. 4.11. Transferred power computed by (16) (dashed blue line) and by numerical analysis (solid red line) for coil pair #1.

The profile of the power transferred from the track coils to the pickup coil is shown in Fig. 4.11. The dashed curve represents (4.16) whilst the solid line is found by the numerical analysis. When the pickup moves from 0 to about 1m or from 11 to 12 m, the power calculated by (4.16) is lower because, when $L_p$ is around its nominal value, (4.16) gives a defect approximation of the transferred power. When EV moves from 1 to 2 m or from 10 to 11 m, the power calculated by (4.16) is higher because of the variation of $L_p$ that causes the loss of the resonance with $C_p$. In the central part of the interval between two track coils there is no power transfer because both $M_a$ and $M_b$ are zeroed. The horizontal dotted line in Fig. 4.11 represents the average transferred power. From the numerical analysis it results in 34.55 kW while from (4.16) it results in 34.01 kW, i.e. the two data are almost coincident. By numerical analysis, the transferred energy per km is 888 kJ, which is about 1.6% higher than the specified one. Peak of the transferred power is about 250 kW so that an auxiliary storage system on-board EV is required with this track layout.

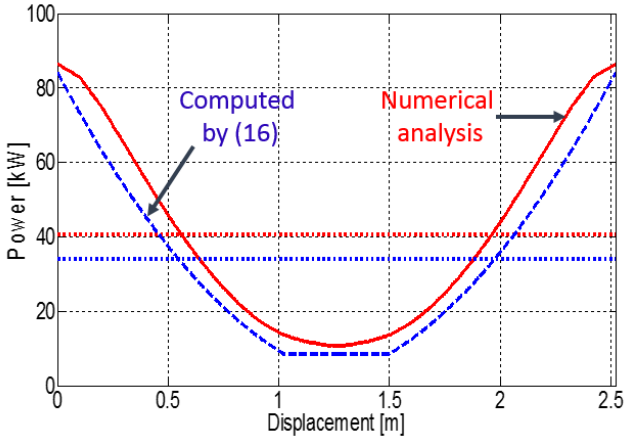

Fig. 4.12. Transferred power computed by (16) (dashed blue line) and by numerical analysis (solid red line) for coil pair #2.

When the track coils are set at a shorter distance, because of the combined effects of the cores of the track coils just ahead and behind the pickup, the self-inductance of the pickup coil is near to its maximum along the full EV route. In this case the transferred power given by (4.16) results lower than the actual one. As an example, let us consider pair coil

#2 with one turn and a track supply current of 100 $A_{rms}$. By Table 4.3, the required $\sigma$ is of 0.595 with a corresponding coil distance of 2.52 m. The profile of the power transferred with this track layout is reported in Fig. 4.12. From numerical analysis the average transferred power results in 40.78 kW while from (4.16) it results in 34.03 kW. The transferred energy per km is 1.05 MJ, which is about 20% higher than that estimated by (4.33). Peak of the transferred power is about 86 kW so that there is no need of any additional storage system on-board EV.

## 4.6 Conclusion

This chapter has dealt with the design of the layout of a lumped track for a DWC system. To this purpose, the power transferred from the track coils to the pickup coil, both with DD shape, has been modeled along the EV route for different coil dimensions. Model equations have been worked out from the profile of the coil mutual inductances along their longitudinal displacement, as obtained by a FEM analysis. Then, the energy requirement has been determined for a compact C-class car to move at high speed along the route. By help of the above results, a sizing procedure has been arranged to compute the track coil distance. The sizing procedure has been validated by a computer-assisted analysis, which proves that requisite energy is transferred to the moving pickup coil with the proposed design.

## References


[1] M.P. Kazmierkowski and A.J. Moradewicz, "Unplugged But Connected: Review of Contactless Energy Transfer Systems," *IEEE Industrial Electronics Magazine*, vol. 6, nº 4, pp. 47-55, 2012.

[2] G.A.Covic and J.T.Boys, "Inductive Power Transfer," *IEEE Proceedings*, vol. 101, nº 6, pp. 1276-1289, 2013.

[3] G.A. Covic and J.T. Boys, "Modern Trends in Inductive Power Transfer for Transportation Applications," *IEEE Journal of Emerging and Selected Topics in Power Electronics*, vol.1, nº 1, pp. 28-41, 2013.

[4] S.Y. Choi, B.W. Gu, S.Y. Jeong, and C.T. Rim, "Advances in Wireless Power Transfer Systems for Roadway-Powered Electric Vehicles," *IEEE Journal of Emerging and Selected Topics in Power Electronics*, vol.3, nº.1, pp.18-36, March 2015.

[5] S. C. Moon and G-W Moon, "Wireless Power Transfer System with an Asymmetric 4-Coil Resonator for Electric Vehicle Battery Chargers," in Proc. IEEE Applied Power Electronics Conference and Exposition (APEC), 2015, pp. 1650 - 1657.

[6] T. Sun, X. Xie, G. Li, Y. Gu, Y. Deng, and Z. Wang, "A Two-Hop Wireless Power Transfer System With an Efficiency-Enhanced Power Receiver for Motion-Free Capsule Endoscopy Inspection," *IEEE Transactions on Biomedical Engineering*, vol. 59, nº 11, pp. 3247–3254, 2012.

[7] J. Shin, S. Shin, Y. Kim, S. Ahn, S. Lee, G. Jung, S.-J. Jeon, and D.-H. Cho, "Design and implementation of shaped magnetic-resonance-based wireless power transfer system for roadway-powered moving electric vehicles," *IEEE Transactions on Industrial Electronics*, vol. 61, nº 3, pp. 1179-1192, 2014.

[8] J.T. Boys and G.A. Covic, "The Inductive Power Transfer Story at the University of Auckland," *IEEE Circuits and Systems Magazine*, vol. 15, nº 2, pp.6-27, 2015.

[9] K. Lee, Z. Pantic, and S. M. Lukic, "Reflexive Field Containment in Dynamic Inductive Power Transfer Systems", *IEEE Transactions on Power Electronics*, vol. 29, nº 9, pp. 4592 – 4602, 2014.

[10] G.R Nagendra, G.A. Covic, and J.T Boys, “Determining the Physical Size of Inductive Couplers for IPT EV Systems,” IEEE Journal of Emerging and Selected Topics in Power Electronics, vol. 2, no 3, pp. 571-583, 2014.

[11] T.D. Nguyen, S. Li, W. Li, and C.C. Mi, “Feasibility study on bipolar pads for efficient wireless power chargers,” in Proc. IEEE Applied Power Electronics Conference and Exposition (APEC), 2014, pp. 1676-1682.

[12] W. Zhang, S.C. Wong, C.K. Tse, and Q. Chen, "An Optimized Track Length in Roadway Inductive Power Transfer Systems," *IEEE Journal of Emerging and Selected Topics in Power Electronics*, vol.2, nº 3, pp. 598-608, 2014.

[13] Z. Zhang and K. Chau, "Homogeneous Wireless Power Transfer for Move-and-Charge," *IEEE Transactions on Power Electronics*, vol.30, nº 11, pp. 6213-6220, 2015.

[14] W. Li, H. Zhao, S. Li, J. Deng, T. Kan, and C.C. Mi, “Integrated Compensation Topology for Wireless Charger in Electric and Plug-in Electric Vehicles,” *IEEE Transactions on Industrial Electronics*, vol. 62, nº 7, pp. 4215-4225, 2015

[15] L. Chen, S. Liu, Y.C. Zhou, and T.J. Cui, “An optimizable circuit structure for high-efficiency wireless power transfer,” *IEEE Transactions on Industrial Electronics*, vol. 60, nº 1, pp. 339-349, 2013.

[16] M. Budhia, J.T. Boys, G.A. Covic, and C.Y. Huang, "Development of a Single-Sided Flux Magnetic Coupler for Electric Vehicle IPT Charging Systems," *IEEE Transactions on Industrial Electronics*, vol. 60, nº 1, pp. 318-328, 2013.

[17] A. Zaheer, G.A. Covic, and D. Kacprzak, "A Bipolar Pad in a 10-kHz 300-W Distributed IPT System for AGV Applications," *IEEE Transactions on Industrial Electronics*, vol.61, nº 7, pp. 3288-3301, 2014.

[18] J. Acero, C. Carretero, I. Lope, R. Alonso, O. Lucia, and J.M. Burdio, "Analysis of the Mutual Inductance of Planar-Lumped Inductive Power Transfer Systems," *IEEE Transactions on Industrial Electronics*, vol.60, nº 1, pp. 410-420, 2013.

[19] V. Prasanth and P. Bauer, “Distributed IPT Systems for Dynamic Powering: Misalignment Analysis,” *IEEE Transactions on Industrial Electronics*, vol. 61, nº 11, pp. 6013-6021, 2014.

[20] Q. Zhu, Y. Guo, L. Wang, C. Liao, and F. Li “Improving the Misalignment Tolerance of Wireless Charging System by Optimizing the Compensate Capacitor, “*IEEE Transactions on Industrial Electronics*, vol. 62, nº 8, pp. 4832-4836, 2015.

[21] S. Raabe and G.A. Covic, "Practical Design Considerations for Contactless Power Transfer Quadrature Pick-Ups," *IEEE Transactions on Industrial Electronics*, vol.60, nº 1, pp. 400-409, 2013.

[22] H. Matsumoto, Y. Neba, K. Ishizaka, and R. Itoh, "Comparison of Characteristics on Planar Contactless Power Transfer Systems," *IEEE Transactions on Power Electronics*, vol.27, nº 6, pp. 2980-2993, 2012.

[23] A. Zaheer, H. Hao, G.A. Covic, and D. Kacprzak, "Investigation of Multiple Decoupled Coil Primary Pad Topologies in Lumped IPT System for interoperable electric vehicle charging,” *IEEE Transactions on Industrial Electronics*, vol. 30, nº 4, pp. 1937-1955, 2015.

[24] J. Deng, W. Li, T.D. Nguyen, S. Li, and C.C. Mi, "Compact and Efficient Bipolar Coupler for Wireless Power Chargers: Design and Analysis," *IEEE Transactions on Power Electronics*, vol. 30, nº 11, pp. 6130-6140, 2015.

## Chapter 5

# DWC System with Unequal DD Coil-set

For dynamic DWC, various coil configurations have been investigated, also making recourse to additional resonant coils [19], and among them the double-D (DD) shape showed the most suited coupling properties [20], [21]. This chapter is concerned with the geometrical design of a DD coil set for a lumped track where the pickup coil is sensibly longer than the track coils as shown in Fig. 5.1, and demonstrates that this configuration assures better power transfer continuity and lower cost of the track deployment with respect to the coil sets where the pickup and the track coils have about the same length. A procedure is developed that determines both the length of the track coils and the distance between them; differently from the works found in the literature, the track coil sizing procedure takes as inputs the characteristics and the requirements of the EV battery and the pickup coil length. The theoretical basis of the sizing procedure are validated by the experimental results taken from a

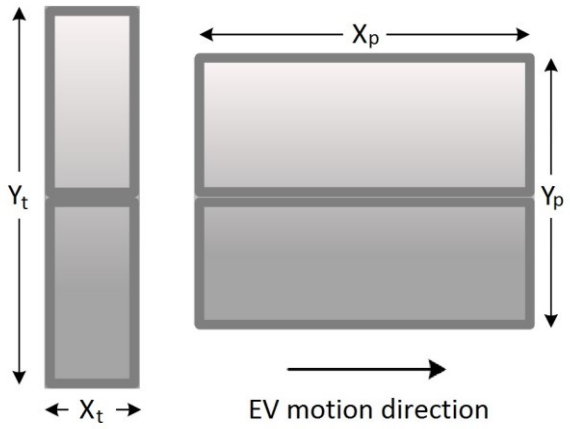


Fig. 5.1. DD coil set (track coil on the right and pickup coil on the left).

scaled down prototype of the coil set. The procedure is then applied to size the coil set of a DWC system devoted to supply a commercially available electric mini car, chosen as case study EV. Finally, the effectiveness of the sizing procedure is checked by simulating in the PSIM environment the full DWC system, confirming the theoretical findings.

### 5.1 DWC System Operation with DD Coils

DD coils are conveniently used in the pickups of DWC systems having distributed track and both in pickups and track in DWC systems with lumped track [22]. When both track and pickup coils have the same dimensions, the profiles of the mutual inductances $M_b(x)$ and $M_a(x)$ can be approximated with the triangular waveforms of Fig. 5.3, where $M_0$ denotes the maximum value of $M$, reached when the pickup coil is perfectly aligned with the track coil [24].

$$V_p = \omega_s I_t [M_b(x) + M_a(x)] \qquad (5.1)$$

When $X_t<D/2$, as shown in Fig. 5.3, the profiles of $M_a$ and $M_b$ are separated by a space interval where both of them are zero; this condition is denoted as Separate Flux Coverage

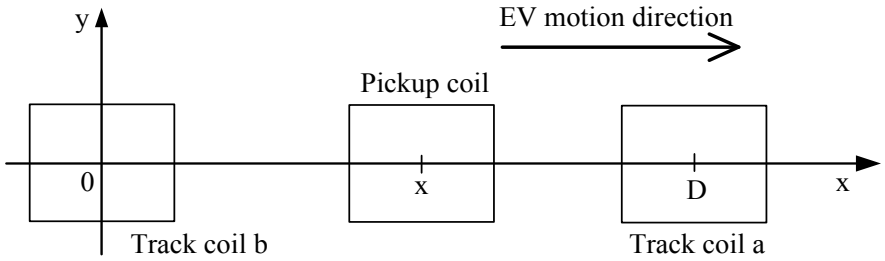


Fig. 5.2. Top view of a moving pickup coil along a lumped track.

(SFC). In SFC, following from (5.1), $V_p$ has the same triangular profile of $M_a$ and $M_b$. Instead, when $X_t>D/2$, the profiles of Ma and $M_b$ overlap and a space interval exists where the pickup coil is supplied simultaneously by track coil a and b and, by (5.1), $V_p$ is constant; this condition is denoted as Overlapped Flux Coverage (OFC).

A schematic of a DWC system is shown in Fig. 5.4 where, in order to simplify the description, coupling between the pickup coil and only one track coil is considered. In DWC systems, the coils are usually connected to compensation networks (CN), to increase the

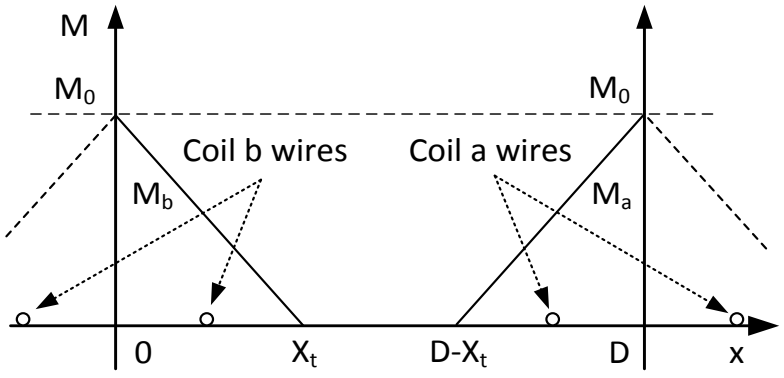


Fig. 5.3. Profile of the mutual inductances along the x-direction in SFC.

capability and the efficiency and the system [25], [26]. The CN of the pickup coil is assumed to be formed by the series-connected capacitor $C_{CN}$ that resonates with the coil inductance at the supply frequency; instead, no assumptions are made about the topology of the CN connected to the track coils. In order to simplify the analysis, parasitic resistances of CNs components, of the coil set and of the power switches are disregarded.

The filtering effect of the CNs makes the current in the coils nearly sinusoidal so that only the first harmonic of alternate quantities is considered in the following discussion; this simplification implies that the voltage supplying the track coils and the voltage at the input of the diode rectifier are modeled with sinusoidal signals even if they actually have a semi-square and a square waveform, respectively [27].

Voltage supplying the CN of the track coils has amplitude $V_s$ and is controlled so that amplitude $I_t$ of the current flowing in the track coils is kept constant despite the load variation. Losses and possibly harmful leakage flux are reduced by implementing the segmentation of the track: each track coil is supplied only when it is coupled with a pickup coil, otherwise it is turned off. Taking Fig. 5.2 as a reference, it means that if $0<x<D$, both coils *a* and *b* are supplied, but as soon as *x* exceeds *D*, coil *b* is turned off and the coil on the right of *a* is turned on.

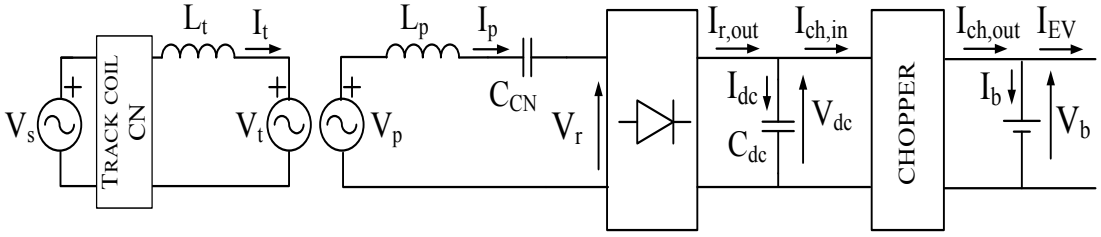


Fig. 5.4. Schematic of a DWC system.

The capacitor $C_{dc}$ at the output of the rectifier sustains the voltage $V_{dc}$ of the DC bus at the input of the chopper. The current $I_{ch,out}$ at the output of the chopper is divided into two components: $I_{EV}$ supplies the propulsion drive while $I_b$ charges the battery; if the DWC system operates in charge sustaining mode (CSM) the latter component is equal to zero when $OFC_2$ condition, described in Section V, is enforced.

Proper operation of the chopper is possible only if $V_{dc}$ exceeds a minimum threshold voltage $V_m$. In the following analysis, a buck chopper is considered so that $V_m$ must be greater or at least equal to the chopper output voltage $V_b$, which corresponds to the battery voltage.

If the vehicle speed *U* and the chopper output power are constant, the operations of the DWC system evolve periodically with period *D* along the track. Let suppose the DWC system operating in SFC, the DC bus voltage being $V_m$ and the EV approaching coil *b* from the left. In this condition, induced voltage and current in the pickup coil are drawn in the leftmost side of Fig. 5.5, where the blue solid line marked with circles is the waveform of $V_p$ and red solid line marked with star is waveform of $I_p$, both as a function of the EV position over the track coil *b*. While the pickup lays in the interval $[-D, -X_t]$ $V_p$ is zero and diode rectifier does not conduct.

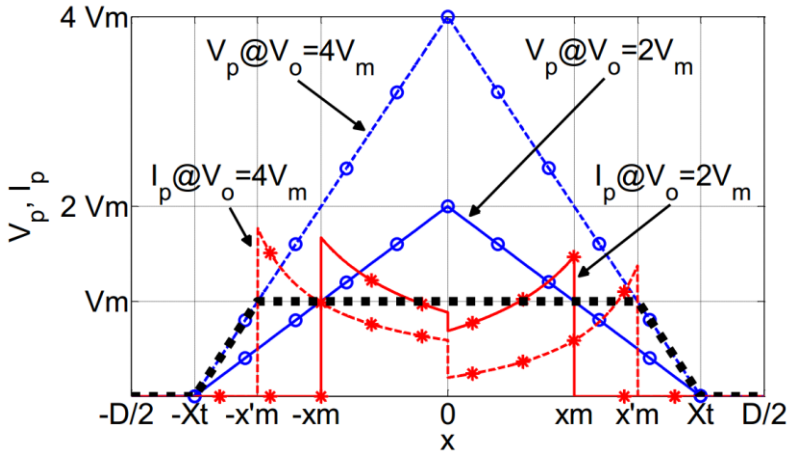


Fig.5.5. Profile of the induced voltage vs. pickup coil position.

Being the vehicle moving rightward, at position $-X_t$ $V_p$ begins increasing linearly and as soon as it exceeds $V_m$ the diode rectifier starts conducting; this happens at position $-x_m$, laying in the interval $[-X_t, 0]$. Once the diode rectifier is in continuous conduction mode, the voltage $V_r$ found at its input equals $V_p$ because the voltage drop across the resonating $L_p$-$C_{CN}$ series is zero and (5.2) can be written.

$$V_r = V_p = \frac{4}{\pi} V_{dc} \qquad (5.2)$$

From here on, $V_{dc}$ increases proportionally to $V_p$ till position 0 is reached, where $V_p$ takes its maximum value $V_0$, which in this case is equal to twice $V_m$ Then $V_p$ decreases and $C_{dc}$ is discharged through the chopper to maintain the diode rectifier in conduction and to allow a continuous power transfer to the EV. Finally, at position $x_m$, $V_{dc}$ drops below $V_m$ and both the chopper and the diode rectifier cease to operate.

A proper sizing of $C_{dc}$ makes negligible the effects on $V_{dc}$ of the high frequency component of the rectifier output current; hence, the DWC system operations are analyzed considering only its average value $I_{r,out}$, computed over one supply period. Being $I_p$ sinusoidal, it is related to $I_{r,out}$ by

$$I_p = \frac{\pi}{2} I_{r,out} \qquad (5.3)$$

From the schematic of Fig. 5.4, $I_{r,out}$ results the sum of the two currents $I_{dc}$, which charges (or discharges) $C_{dc}$, and $I_{ch,in}$, which enters the chopper. From (5.3), it results

$$I_p = \frac{\pi}{2}\left(I_{dc} + I_{ch,in}\right) = \frac{\pi}{2}\left(C_{dc}\frac{dV_{dc}}{dt} + \frac{V_b}{V_{dc}} I_{ch,out}\right) \qquad (5.4)$$

By (5.2), $I_p$ is rewritten as a function of $V_p$ in the form

$$I_p = C_{dc}\frac{\pi^2}{8}\frac{dV_p}{dt} + 2\frac{V_b}{V_p}I_{ch,out} \qquad (5.5)$$

In the interval [$X_t$, 0], while $C_{dc}$ is charged, $I_p$ is expressed as

$$I_p = C_{dc}\frac{\pi^2}{8}V_0\frac{U}{X_t} + 2\frac{P_{ch,out}}{V_p} \qquad (5.6)$$

obtained observing that the chopper output power is

$$P_{ch,out} = V_b I_{ch,out} \qquad (5.7)$$

Current $I_p$ takes the qualitative profile reported by the solid line marked with stars in Fig. 5.5. The figure shows that $I_p$ reaches the maximum value as soon as the rectifier starts conducting, then decreases as $V_p$ increases, has a step drop at position 0 when the capacitor starts being discharged, and finally increases again until the rectifier stops conducting.

From the above description, it results that only half of the interval [-$X_t$, $X_t$] is exploited to supply the EV. The track coils would be more effectively exploited selecting a higher $V_0$; for example, increasing $V_0$ to four times $V_m$, as shown by the blue dashed line marked with circles of Fig. 5.5, conduction takes place from -$x'_m$ to $x'_m$ and the interval available to transfer power to the EV lengthens to 3/2 $X_t$. If $V_0$ is set to 4 $V_m$ the graph of $I_p$ changes into that one denoted with the red dashed line marked with stars; as it can be seen on the left side of the figure, the increase of $V_0$ leads to a higher peak value of $I_p$, this effects being stronger for higher values of $C_{dc}$.

It can be concluded that the increase of $V_0$ widens the interval available for power transfer and hence it has a positive effect on the amount of energy supplied to the EV while it moves between two track coils; on the other side, having higher $V_0$ forces the chopper to operate over a larger input voltage swing and requires the diode rectifier to sustain higher voltage and current, thus decreasing the efficiency of the power converters and increasing their cost.

A way to circumvent these issues consists in changing the waveform of $V_p$ to the trapezoidal profile highlighted with the black dotted line in order to achieve the advantage of operating at higher voltage, transferring power to the EV for a larger fraction of the [-$X_t$, $X_t$] interval, without the need of increasing the sizing voltage and current of the DWC system components.

## 5.2 Unequal DD Coils

Induced voltage $V_p$ has the same profile as the mutual inductance between the track and pickup coils; consequently, it can be forced to the trapezoidal waveform of Fig. 5.5 by re-designing the coil set to suitably tune the profile of their mutual inductance. The coil set presented in this chapter holds the same flux coupling principle as DD coils, but the pickup coils are longer than the track coils; for this reason this arrangement is denoted as unequal double-D coils or UDD coils. An example of UDD coils is shown in Fig. 5.1.

Fig. 5.6. Case study mini car

Research activity on UDD coils has been focused on sizing a DWC system able to charge the battery of the case study mini car Birò, produced by Estrima, shown in Fig.5.6 and having the characteristics reported in Table 5.1.

### *5.2.1 FEM analysis of UDD coils*

The coupling characteristics of the UDD coil has been studied on sets of UDD coils having lateral dimensions $Y_t$ and $Y_p$ equal to 0.95 m, i.e. the maximum allowable by the EV body, and length $X_t$ and $X_p$ initially set at 0.4 m; the coil airgap has been fixed to 0.17 m. At first, effect of pickup coil length $X_p$ over the mutual inductance has been investigated positioning the pickup coil exactly centered over the track coil and performing a number of FEM analysis in the JMAG environment increasing step by step the pickup length $X_p$. Obtained mutual inductance is reported as a function of the coils length ratio with the blue line marked by dots in Fig. 5.7. Inspection of the graph shows that the mutual

Table 5.1

Parameters of mini car Birò

| Quantity | Symbol | Values |
|---|---|---|
| Mass (with driver) | $m$ | 600 kg |
| Front area | $A_f$ | 1.9 m$^2$ |
| Ground clearance | $g_c$ | 0.17 m |
| Maximum pickup coil x-dimension | $X_{P,M}$ | 1.2 m |
| Maximum pickup coil y-dimension | $Y_{P,M}$ | 0.95 m |
| Maximum speed | $U$ | 50km/h |
| Air drag coefficient | $Cd$ | 0.28 |
| Rolling friction coefficient | $K_{rf}$ | 0.01 |
| Powertrain efficiency | $\eta_{PT}$ | 0.82 |
| Full charge battery voltage | $V_{b,M}$ | 56 V |
| Max charging current | $I_{b,M}$ | 10 A |

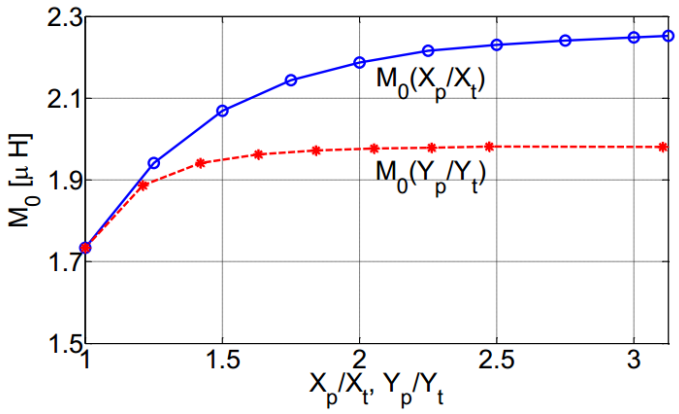


Fig. 5.7. Mutual inductance vs. length and width ratio of the coils.

inductance initially increases with $X_p/X_t$ but once $X_p$ is about $2.25X_t$ this effect becomes negligible.

The same approach has been applied to investigate the effect of the pickup lateral dimension. Pickup length has been again set at 0.4 m while its width $Y_p$ has been increased up to about three times $Y_t$. The mutual inductances obtained by FEM analysis as a function of the coils width ratio are reported in Fig. 5.7 with the red line marked by stars. Also in this case, the mutual inductance increases with the dimension of the pickup coil, but this effect becomes negligible when the $Y_p/Y_t$ ratio is about 1.5. Comparison of the two plots shows that for a given value of $X_p/X_t$ and $Y_p/Y_t$, the coil set with the longer pickup has a higher mutual inductance than the pair with wider pickup. Considering that functional parameters of DWC system are strictly related to their mutual inductance, and that the mini car does not offer room to increase the pickup width, the subsequent analysis has been focused on coil sets with pickup coil longer than track coil.

Table 5.2

Coil pair parameters

| Coil pair | $X_p$ [m] | $Y_p$ [m] | $L_t$ [μH] | $L_p$ [μH] | $M_0$ [μH] | $k_0$ | $\sigma_1$ [m] | $\sigma_2$ [m] |
|---|---|---|---|---|---|---|---|---|
| #1 | 0.4 | 0.950 | 6.02 | 6.01 | 1.73 | 0.29 | 0 | 0.4 |
| #2 | 0.8 | 0.720 | 5.98 | 8.93 | 1.73 | 0.24 | 0.2 | 0.6 |
| #3 | 1.0 | 0.706 | 5.97 | 10.65 | 1.73 | 0.22 | 0.3 | 0.7 |
| #4 | 1.2 | 0.700 | 5.97 | 12.79 | 1.73 | 0.20 | 0.4 | 0.8 |

A second series of tests investigated the combined effects on the coupling coefficient of the pickup length and of its position $x$. Four different pickups have been analyzed, having $X_p$ equal to 0.4 m, 0.8 m, 1.0 m and 1.2 m, which is the maximum allowed by the mini car dimension. The pickup coils lateral dimension $Y_p$ has been adjusted according to the values reported in Table 5.2 in order to obtain the same mutual inductance $M_0$ when the pickup is

centered over the track coil. Track coil dimensions $X_t$ and $Y_t$ have been maintained at 0.4 m and 0.95 m, respectively for each considered coil set. Both track and pickup coils are endowed with a planar core to increase the coupling coefficient and, consequently, the power transfer efficiency of the DWC system. The presence of the core explains the slight dependence of the self-inductance of the track coil on the dimension of the pickup coil, reported in the fourth column of Table 5.2.

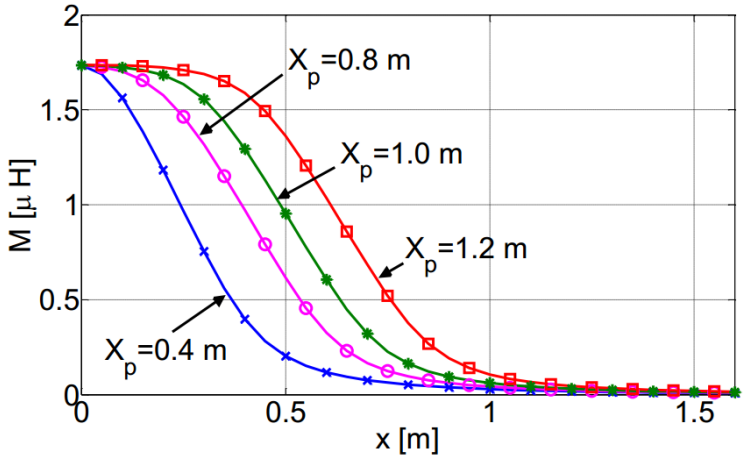


Fig. 5.8. Mutual inductance profile obtained by numerical analysis.

The mutual inductance as a function of pickup coil position is reported in Fig. 5.8 for the four coil arrangement. The trace marked with crosses is drawn for pickup coil length 0.4 m, the circles, stars and squares mark the traces relevant to 0.8 m, 1 m and 1.2 m coil length, respectively. As expected, the mutual inductance is maximum when the pickup coil is centered over the track coil, then, while the pickup coil covers completely the track coil, it remains about constant despite the increasing distance between the coil centers, and finally drops almost linearly while the pickup leaves the track coil. Note that the case of $X_p$=$X_t$=0.4 m corresponds to a conventional DD coils set and the relevant profile of the mutual inductance resembles a triangle, as stated in the previous section.

### *5.2.2 Experimental validation*

A set of UDD coils made of one turn have been built following the proportion of coil set #4 with a reduction ratio of 3 with respect to the dimensions reported in Table 5.2. The coils have been set apart of 1/3 of the ground clearance $g_c$ reported in Table 5.1 and leant against two planar ferrite cores having dimension 0.4 m x 0.4 m available in the lab. The mutual inductance have been measured at different relative positions $x$ using the LCR meter LCR-819 of inSTECK Company, and compared with the results of FEM analysis. Experimental results are denoted in

Fig. 5.9 with the blue circles while the red line represents the FEM analysis outcomes, after scaling down their maximum value and the pickup position in order to comply with the dimensions of the prototype. As can be seen, experimental results match almost perfectly with that of the FEM analysis confirming the validity of the trapezoidal approximation used for the mutual inductance.

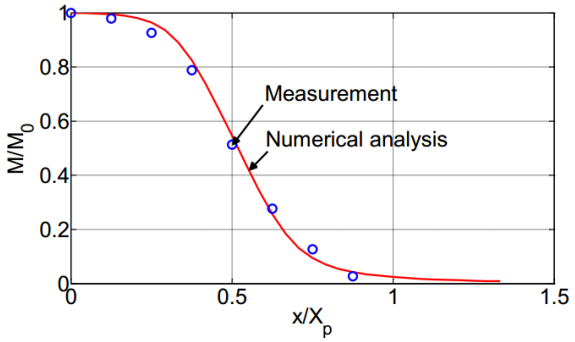


Fig. 5.9. Mutual inductance samples obtained by measurement (blue circles), and by numerical analysis (red line).

### 5.3 Pickup coil voltage and current with UDD coils

The mutual inductance profiles of Fig. 5.8 are approximated by trapezoidal profiles of Fig. 5.10. Mutual inductance $M_b(x)$ has been sketched exploiting its even symmetry, given by the geometry of the coils, around position $x$=0, while $M_a(x)$ has been obtained by translating on the right the profile of $M_b(x)$ of the distance $D$. Mutual inductance $M_b(x)$ is constant and equal to $M_0$ for an interval having width equal to $2\sigma_1$ while it increases and decreases linearly from 0 to $M_0$ and from $M_0$ to 0, respectively, in two separate intervals having width equal to $\sigma_2$-$\sigma_1$.

Considering the motion direction and the coil arrangement of Fig. 5.2, $\sigma_1$ is the position where the rear edge of the pickup coil is placed exactly on the left edge of track coil $b$ while $\sigma_2$ is the position where the rear edge of the pickup coil corresponds to the right edge of track coil $b$. The parameters $\sigma_1$ and $\sigma_2$ are defined by

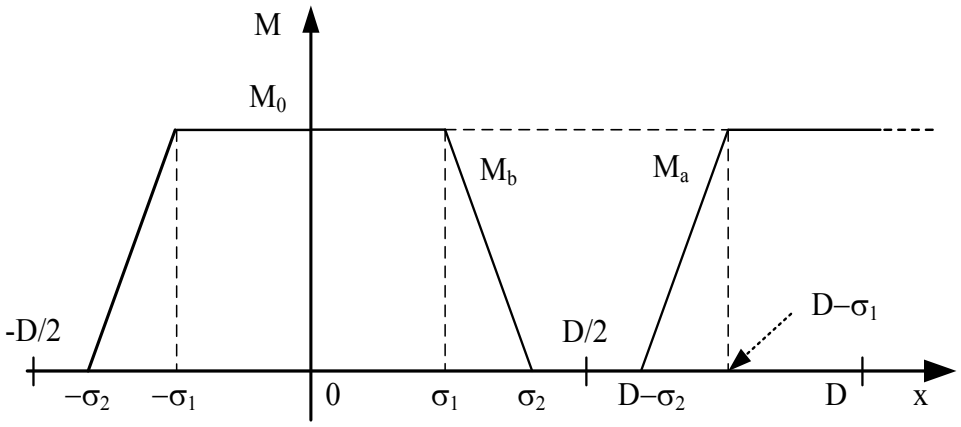


Fig. 5.10. Approximate profile of mutual inductance vs. the position of the pickup coil.

$$\begin{cases} \sigma_1 \triangleq \frac{X_p - X_t}{2} = \frac{\lambda - 1}{2} X_t \\ \sigma_2 \triangleq \frac{X_p + X_t}{2} = \frac{\lambda + 1}{2} X_t \end{cases} \quad (5.8)$$

where the length ratio $\lambda = X_p/X_t$ discriminates between DD coils, where $\lambda=1$, and UDD coils, where $\lambda>1$. The values $\sigma_2$ and $\sigma_1$ for each coil pair analyzed by FEM are reported in the rightmost columns of Table 5.2.

SFC and OFC can be defined also for UDD coils; the first situation is represented in Fig. 5.10 and occurs for $\sigma_2<D/2$ while the second one occurs when $(D-\sigma_1)>\sigma_2>D/2$. A third situation happens if

$$\sigma_2 > (D - \sigma_1) \Rightarrow X_t > \frac{D}{\lambda} \;\Rightarrow\; X_p > D \quad (5.9)$$

In this case, $M_a$ starts increasing while $M_b$ is still at maximum and, by (5.1), $V_p$ reaches its maximum while the pickup lays between two track coils. This condition is not considered in the following discussion because it requires to deploy a large number of track coils one close to the others, thus increasing the overall cost of the track and vanishing the advantages of using UDD coils.

The piecewise linear approximation of $M_b(x)$ in the interval [-D/2, *0*] is expressed by (5.10)

$$\begin{cases} M_b(x) = 0, & x \in \left[-\frac{D}{2}, -\sigma_2\right] \\ M_b(x) = \frac{M_0}{\sigma_2 - \sigma_1}(x + \sigma_2), & x \in [-\sigma_2, -\sigma_1] \\ M_b(x) = M_0, & x \in [-\sigma_1, 0] \end{cases} \quad (5.10)$$

### *5.3.1 Voltage and current analysis under SFC ($\sigma_2<D/2$)*

Under SFC, $V_p$ is proportional to (5.10) according to (5.11), written recognizing that $V_0=\omega_s I_t M_0$. The profile $V_p(x)$ in the interval [-*D*/2, *0*] is depicted in Fig. 5.11, drawn considering $V_0=2V_m$.

$$\begin{cases} V_p(x) = 0, & x \in \left[-\frac{D}{2}, -\sigma_2\right] \\ V_p(x) = \frac{V_0}{\sigma_2 - \sigma_1}(x + \sigma_2), & x \in [-\sigma_2, -\sigma_1] \\ V_p(x) = V_0, & x \in [-\sigma_1, 0] \end{cases} \quad (5.11)$$

Following from the analysis of Section 5.1, power transfer takes place only when $V_p$ exceeds $V_m$, i.e. while EV moves in interval [$-x_m$, $x_m$]. Actual value of $x_m$ depends on the parameters of the DWC system and whether it operates in SFC or OFC.

For SFC, $x_m$ is easily worked out solving the second of (5.11) setting $V_p(-x_m)=V_m$, and results in

$$x_m = \left[\sigma_2\left(1-\frac{V_m}{V_0}\right)+\sigma_1\frac{V_m}{V_0}\right] \qquad (5.12)$$

By manipulating (5.12) using definitions (5.8), $x_m$ can be expressed also in the form

$$x_m = X_t\left(\frac{\lambda+1}{2}-\frac{V_m}{V_0}\right) \qquad (5.13)$$

that highlights the dependence of $x_m$ on the dimensions of the track and pickup coils.

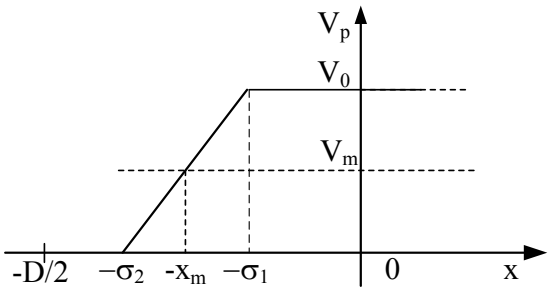


Fig. 5.11. Waveform of $V_p$ under SFC.

Analysis of (5.12) shows that when $V_m/V_0$ is small, $x_m$ is about proportional to $\sigma_2$, so that, according to (5.8), the interval available to transfer energy increases of the same amount whether the pickup or track coil is lengthened. Instead, when $V_m/V_0$ approaches 1, $x_m$ is about proportional to $\sigma_1$, and the interval available to transfer energy increase when pickup coil is lengthened or track coil is shortened, which is the design solution adopted for the UDD coils. This consideration suggests that UDD coils are best exploited when $V_0$ is not much higher than $V_m$.

Current in the pickup coil is obtained from (5.5) and (5.11) in the form

$$\begin{cases} I_p(x) = 0, & x \in \left[-\frac{D}{2}, -x_m\right] \\ I_p(x) = V_0\frac{\pi^2}{8}C_{dc}\frac{U}{(\sigma_2-\sigma_1)} + 2\frac{P_{ch,out}}{V_0}\frac{(\sigma_2-\sigma_1)}{(x+\sigma_2)}, & x \in [-x_m, -\sigma_1] \\ I_p(x) = 2\frac{P_{ch,out}}{V_0}, & x \in [-\sigma_1, 0] \end{cases} \qquad (5.14)$$

The first term in the second of (5.14) is the component of $I_p$ that charges the capacitor $C_{dc}$ while the second one accounts for the power delivered by the chopper. Using (5.8) and the second of (5.11) they can be rewritten as in (5.6), confirming that thanks to UDD coils energy is transferred to the EV for a wider interval without increasing the maximum pickup current.

Obviously, the component of $I_p$ that charges $C_{dc}$ does not appear in the third of (5.14) because in that interval $V_p$, and hence $V_{dc}$, are constant. In the interval $[\sigma_1, x_m]$, the current component charging $C_{dc}$ has the same amplitude as in (5.14) but with a negative sign because $V_{dc}$ is decreasing and the capacitor discharges through the chopper. This entails that while the pickup

coil is leaving the track coil, a lower $I_p$ is required to obtain the same power at the chopper output.

The qualitative waveforms of the ratios $V_p/V_0$ and $I_p/I_0$, where $I_0$ is the current given by the third of (5.14), are shown in Fig. 5.12. They are drawn with blue line marked by circles and red line marked by stars, respectively, and have been obtained using $\sigma_1$ and $\sigma_2$ relevant to coil pair #4 and setting $V_m/V_0$ to 0.4.

Power is actually transferred to the EV only if $I_{r,out}>0$; from (5.3) $I_{r,out}$ results proportional to $I_p$ so that, by (5.14), power transfer surely takes place in the [$-x_m$, 0] space interval. In the symmetric space interval [0, $x_m$], the third of (5.14) maintains the same expression and is positive, while the sign of the first term in the second one must be changed, as explained above, so that $I_p(x)$ results positive in the interval [$\sigma_1$, $x_m$] only if

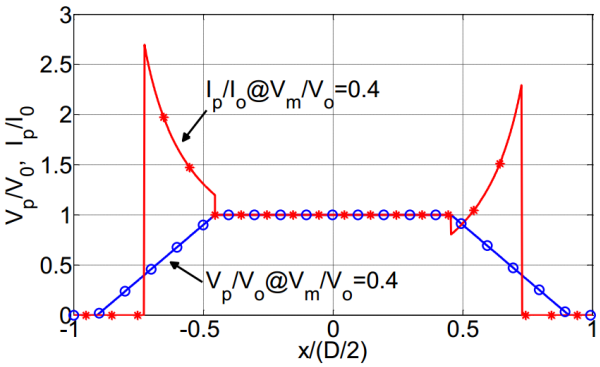


Fig. 5.12. Qualitative waveform of $I_p$ under SFC and OFC$_1$.

$$2\frac{P_{ch,out}}{V_0}\frac{(\sigma_2-\sigma_1)}{(x+\sigma_2)} > V_0\frac{\pi^2}{8}C_{dc}\frac{U}{(\sigma_2-\sigma_1)}, \qquad x \in [\sigma_1, x_m] \qquad (5.15)$$

From (5.15), the maximum value of $C_{dc}$ compatible with the described operations of the DWC system is

$$C_{dc} < \frac{16}{\pi^2}\frac{P_{ch,out}}{V_0^2 U}\frac{(\sigma_2-\sigma_1)^2}{(x_m+\sigma_2)} \qquad (5.16)$$

If (5.16) holds, the energy transferred to the EV while it moves along the interval [$-D/2$, $0$] is equal to

$$E_{SFC} = \frac{x_m}{U}P_{ch,out} \qquad (5.17)$$

Being in SFC, transferred energy does not depend on the track coils distance because each coil operates independently from the others; from this point of view, $E_{SFC}$ could be identified with half of the energy transferred by a single track coil while the EV moves on it.

*5.3.2 Voltage and current analysis under OFC ($D-\sigma_1>\sigma_2>D/2$)*

Under OFC, $V_p$ is originated from the simultaneous contribution of two track coils and takes the profile sketched in Fig. 5.13. Expression of $V_p$ in the interval [$-D/2$, $0$] is given by (5.18)

$$\begin{cases} V_p(x) = \frac{V_0}{\sigma_2-\sigma_1}(2\sigma_2 - D), & x \in \left[-\frac{D}{2}, -D+\sigma_2\right] \\ V_p(x) = \frac{V_0}{\sigma_2-\sigma_1}(x+\sigma_2), & x \in [-D+\sigma_2, -\sigma_1] \\ V_p(x) = V_0, & x \in [-\sigma_1, 0] \end{cases} \quad (5.18)$$

Two subcases can be recognized in OFC, depending on whether $V_m$ is higher or lower than the value taken by $V_p$ while the profiles of $M_a$ and $M_b$ are overlapped, i.e. in the interval [$-\sigma_2$, $-D+\sigma_2$] of Fig. 5.13. In the first case, denoted as $OFC_1$, pickup current is still given by (5.14) and from it, the same expression as (5.17) is obtained for the transferred energy. In the second case, denoted as $OFC_2$, where $V_p$ exceeds $V_m$ along the full interval [$-D/2$, 0], as represented in Fig. 5.13, and power transfer is performed continuously. This condition is reached if $V_p$ at position $x=-D+\sigma_2$ is equal or higher than $V_m$, i.e. if

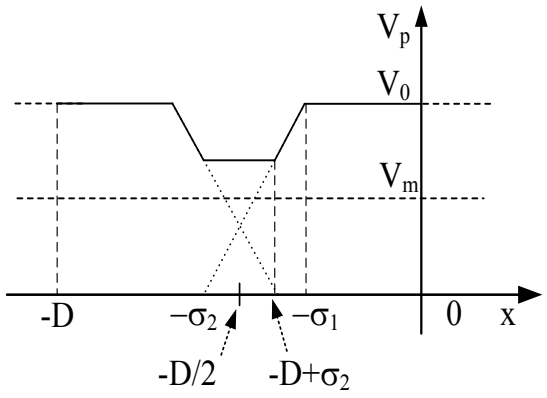


Fig. 5.13. Waveform of $V_p$ under $OFC_2$.

$$2\sigma_2 - D \geq \frac{V_m}{V_0}(\sigma_2 - \sigma_1) \quad (5.19)$$

Relation (5.19) is equivalent to requiring $x_m$ to be higher than ($D-\sigma_2$) so that, by (5.13), (5.19) can be rewritten in the form

$$X_t \geq \frac{D}{\left(\lambda+1-\frac{V_m}{V_0}\right)} \quad (5.20)$$

When $x_m$ is slightly lower than the boundary value ($D-\sigma_2$), power transfer is discontinuous in the interval [$-D/2$, $0$] and the transferred energy is given by (5.17). As soon as $x_m$ exceeds the boundary value, power transfer becomes continuous and the transferred energy steeply increases up to

$$E_{OFC} = \frac{D}{2U} P_{ch,out} \quad (5.21)$$

and results independent from the coils parameters $X_t$ and $\lambda$. The discontinuity in the transferred energy arises from the hypothesis of having continuous conduction of the diode rectifier as soon as $V_p$ exceeds $V_m$. In a real DWC system, conduction of diode rectifier passes through discontinuous mode when position $x_m$ is reached so that there is a smooth transition between the SFC and OFC$_1$ operating conditions and those of OFC$_2$.

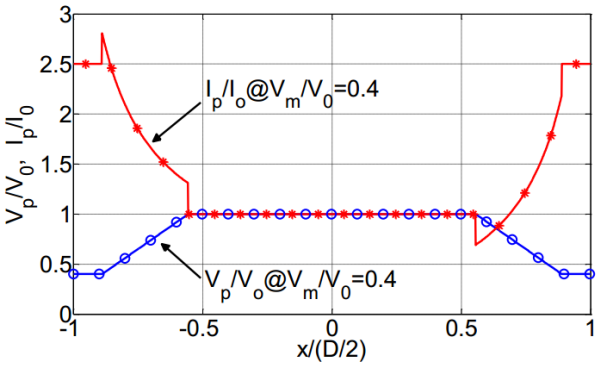

Fig. 5.14. Qualitative waveform of $I_p$ (red) and $V_p$ (blue) in OFC$_2$.

In OFC$_2$, pickup current is given by

$$\begin{cases} I_p(x) = 2\frac{P_{ch,out}}{V_0}\frac{(\sigma_2-\sigma_1)}{(2\sigma_2-D)}, & x \in \left[-\frac{D}{2}, -D+\sigma_2\right] \\ I_p(x) = V_0\frac{\pi^2}{8}C_{dc}\frac{U}{(\sigma_2-\sigma_1)} + 2\frac{P_{ch,out}}{V_0}\frac{(\sigma_2-\sigma_1)}{(x+\sigma_2)}, & x \in [-D+\sigma_2, -\sigma_1] \\ I_p\left(\frac{x}{D}\right) = 2\frac{P_{ch,out}}{V_0}, & x \in [-\sigma_1, 0] \end{cases} \quad (5.22)$$

By comparison with (5.14), (5.22) highligh that $I_p$ is always higher than zero and depends only on the coils layout, through $D$, $\sigma_1$ and $\sigma_2$, but not on $V_m$ and $V_0$ as it happened in SFC and OFC$_1$.

A qualitative waveform of $I_p$ is shown in Fig. 5.14, where $\sigma_1$ and $\sigma_2$ have been set to the values relevant to coil pair #4 and $V_m/V_0$ has been set to 0.4 to satisfy (5.19).

Like in SFC and OFC$_1$, requirement of having $I_{r,out}>0$ reflects on the maximum capacitance of $C_{dc}$. In this case it results independent from $x_m$ being expressed by

$$C_{dc} < \frac{16}{\pi^2}\frac{P_{ch,out}}{V_0^2 U}\frac{(\sigma_2-\sigma_1)^2}{D} \quad (5.23)$$

## 5.4 DWC system sizing procedure

A sizing procedure is developed for the coils of a DWC system aimed to both maintain the battery state of charge, i.e. of operating in CSM, and to charge it, if needed, while the EV runs at its maximum speed. This requires to size the coils to be able to supply the EV with the sum of the maximum power $P_{b,M}$ needed to charge the battery and the maximum power $P_{EV,M}$ needed to propel the EV.

The actual average power $P_p$ harvested by the pickup is

$$P_p = P_{ch,out} + P_{dc} \qquad (5.24)$$

where $P_{dc}$ is the power entering $C_{dc}$; it is positive while $V_{dc}$ is increasing and negative while $V_{dc}$ decreases. Average value of $P_{dc}$ over the [-$D$/2, $D$/2] interval is zero so that it does not contribute in supplying the EV and is not considered in designing the geometry of the coils set; instead, its contribution to the coils current must be considered in sizing the coils windings, the supply inverter and the diode rectifier.

### *5.4.1 Sizing of the DWC system under SFC and OFC1*

A DWC systems in SFC or $OFC_1$ operates in CSM when the net energy injected in the battery during the [-$x_m$, *0*] interval replaces the energy supplied by the battery to the propulsion drive in the interval [-$D$/2, -$x_m$]; by considering the worst case, i.e. the propulsion drive operating at maximum power, this condition is expressed by (5.25), where equality holds for CSM and inequality for battery charging.

$$\frac{x_m}{U} P_{b,M} \geq \frac{\left(\frac{D}{2} - x_m\right)}{U} P_{EV,M} \qquad (5.25)$$

From (5.25), a lower limit for $x_m$ is found as

$$x_m \geq \frac{D}{2} \frac{1}{1+\frac{P_{b,M}}{P_{EV,M}}} \qquad (5.26)$$

where the power ratio $P_{b,M}/P_{EV,M}$ is a characteristic of the EV and is considered as a constant.

Analysis of (5.25) in some particular cases gives somewhat obvious but worth to be mentioned results:

i) If the EV is not endowed with a battery, $P_{b,M}$=0 and from (5.25) it correctly results $x_m$=$D$/2 because the EV needs to be supplied along the whole [-$D$/2, 0] interval with the power $P_{EV,M}$.

ii) If the battery could be charged with the same power it supplies to the propulsion drive, i.e. $P_{b,M}$=$P_{EV,M}$, it is enough to charge it along half of the [-$D$/2, *0*] interval, but a power equal to twice $P_{EV,M}$ must be transferred on the EV.

iii) In general, the availability of batteries with higher maximum charging power allows to shorten the charging interval at the expenses of increasing the transferred power.

By substituting (5.13) in (5.26) and remembering that SFC and $OFC_1$ are considered, by (5.20) the following boundaries are obtained for $X_t$

$$\frac{D}{2}\frac{2}{\left(\lambda+1-\frac{V_m}{V_0}\right)} \geq X_t \geq \frac{D}{2}\frac{1}{\left(1+\frac{P_{b,M}}{P_{EV,M}}\right)\left(\frac{\lambda+1}{2}-\frac{V_m}{V_0}\right)} \qquad (5.27)$$

The boundaries given by (5.27) are met simultaneously only if (5.28) holds

$$\frac{V_m}{V_0} \leq \frac{\lambda+1}{2}\frac{\frac{P_{b,M}}{P_{EV,M}}}{\frac{1}{2}+\frac{P_{b,M}}{P_{EV,M}}} \qquad (5.28)$$

Setting an upper limit to $V_m/V_0$. Requirement (5.27) and (5.28) are somewhat conflicting: if the voltage ratio is set to the maximum, $X_t$ should be equal to $D/2$, entailing the deployment of a very expensive track having the coils covering half of its length. On the other hand, shortening of coils length requires to decrease $V_m/V_0$ thus exposing the components of the DWC system to higher voltage and current stress.

Fig. 5.15 reports some sizing characteristics of the considered DWC system; they represents the minimum value of $X_t/(D/2)$ satisfying (5.27) as a function of the $V_m/V_0$ ratio. From top to bottom, the blue solid lines are the loci of the ($V_m/V_0$, $X_t/(D/2)$) pairs relevant to a DD coil set, obtained with $\lambda$=1 and setting $P_{b,M}/P_{EV,M}$ respectively to 0.1, 1 and 5, values that range from the capability of lead acid batteries to that of lithium-ion ones.

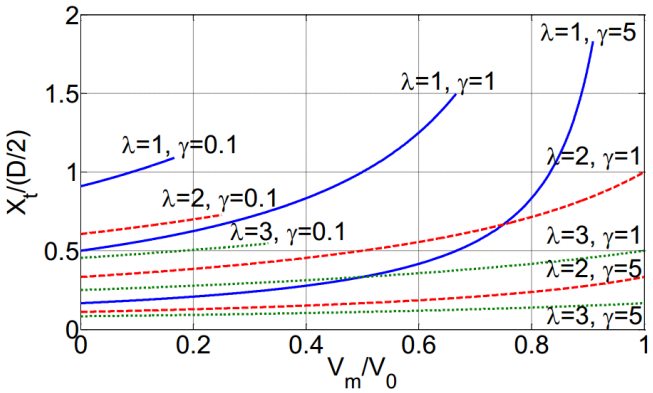

Fig. 5.15. Sizing characteristics of DWC with under SFC and OFC1.

The red dashed lines of Fig. 5.15 are the sizing characteristics obtained with an UDD coil pair having $\lambda$=2 and considering the same values of $P_{b,M}/P_{EV,M}$. As expected, the use of UDD coils allows the DWC system to achieve the required performance using shorter track coils and higher $V_m/V_0$ ratio; these effects are stronger if $\lambda$ is further increased, as shown by the green dotted characteristics, obtained setting $\lambda$=3.

The reported characteristic can be used both to size a DWC system devoted to CSM or to battery charging: if a ($V_m/V_0$, $X_t/(D/2)$) pair laying on a characteristic is chosen, the DWC system will operate in CSM; if an higher $X_t/(D/2)$ is selected for the same $V_m/V_0$ ratio, the resulting DWC system will be able to perform battery charging as well. In any case, the $X_t/(D/2)$ ratio

must not exceed the maximum value reached at the end of its relevant characteristic, otherwise the first of (5.27) will not be met and $OFC_2$ will be enforced.

Inspection of Fig. 5.15 shows that:

- In sizing the DWC system, a trade-off must be found between the cost of the track itself, proportional to $X_t/(D/2)$ and that of the power electronics installed onboard the EVs, which is inversely proportional to $V_m/V_0$. Smaller $X_t/(D/2)$ corresponds to the track design having more distant coils, and higher $V_m/V_0$ corresponds to better utilization of the system rating.
- The selection of the optimal sizing parameters is strongly affected by the battery characteristic through the $P_{b,M}/P_{EV,M}$ ratio. A battery with higher $P_{b,M}$ make $X_t/(D/2)$ lower and $V_m/V_0$ higher.

### *5.4.2 Sizing of the DWC system under $OFC_2$*

Under $OFC_2$ condition (5.25) does not apply because power is continuously transferred to the EV and battery can be charged, if necessary, along the full travel of EV over the track coils; consequently, charging capability of the DWC system does not depend on the ratio $P_{b,M}/P_{EV,M}$ and shifting between CSM and battery charging is performed by a suitable regulation of $I_{ch,out}$ made by the chopper.

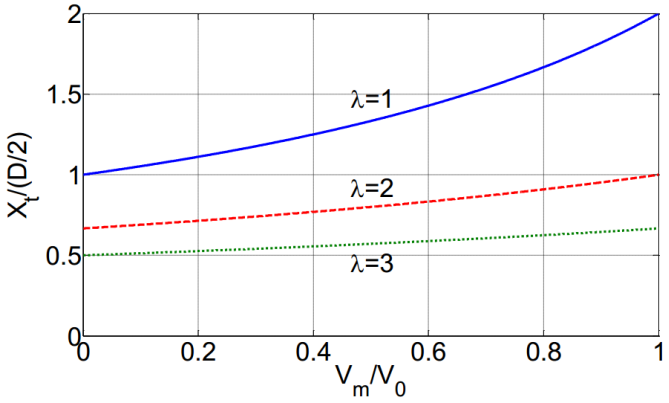

Fig. 5.16. Sizing characteristics of DWC with UDD coils under $OFC_2$.

By (5.9) and (5.20), $OFC_2$ takes place if

$$\frac{D}{2}\frac{2}{\left(\lambda+1-\frac{V_m}{V_0}\right)} \leq X_t \leq \frac{D}{2}\frac{2}{\lambda} \qquad (5.29)$$

The sizing characteristics of the DWC system in OFC for $\lambda$=1, 2, and 3 are reported in Fig. 5.16. The minimum value of $X_t$ satisfying (5.29), normalized to $D/2$ has been drawn; it corresponds to the maximum of $X_t$ that satisfies (5.27).

As it happened under SFC and $OFC_1$, the use of coil pair with $\lambda$>1 allows to design a DWC system with shorter track coils and higher $V_m/V_0$ ratio.

## 5.5 Case study and Simulation results

Performance of DD and UDD coils are compared considering a case study application where the DWC system is sized to supply the electric mini car whose parameters are reported in Table 5.1.

### *5.5.1 System Design*

The mechanical power needed to run a vehicle at constant speed $U$ on a horizontal road is

$$P = (F_d + F_{roll})U \qquad (5.30)$$

being $F_d$ the air drag force and $F_{roll}$ the rolling resistance force.

Force $F_d$ is expressed in (5.31) and results proportional to the air drag coefficient $C_d$ of the vehicle, to its front area $A_f$, and to the air density $\rho_{air}$, set at 1.167 kg/m$^3$.

$$F_d = \frac{1}{2} C_d \rho_{air} A_f U^2 \qquad (5.31)$$

The rolling resistance force is given by

$$F_{roll} = K_{rf} mg \qquad (5.32)$$

where $K_{rf}$ is the rolling friction coefficient of the tires , $m$ is the mass of the vehicle and $g$ is the gravitational acceleration.

From (5.30), the mechanical power required to move the case study EV at the maximum speed results is 1.78 kW. Taking into account the powertrain efficiency, the power $P_{EV,M}$ supplied to the propulsion drive is about 2.29 kW. From Tab. I the maximum battery charging power results in $P_{b,M}=V_{b,M}I_{b,M}$=560 W and hence maximum power required at the chopper output is about 2.85 kW while the power ratio $P_{b,M}/P_{EV,M}$ results in

$$\frac{P_{b,M}}{P_{EV,M}} \approx 0.244 \qquad (5.33)$$

Inspection of Figs. 5.15 and 5.16 shows that selecting high values for $\lambda$ allows to operate with higher $V_m/V_0$ and lower $X_t/D$; on the other side, if $\lambda$ increases the coupling coefficient between the coils decreases thus reducing the efficiency of the DWC system. For this reason, $\lambda$=3 has been set for the case study application. Using this value for $\lambda$ and 0.244 for the power ratio, the left half of Fig. 5.17 has been drawn. As a comparison, in the right part of the figure, the characteristics relevant to a DD coil set are reported, computed with $\lambda$=1.

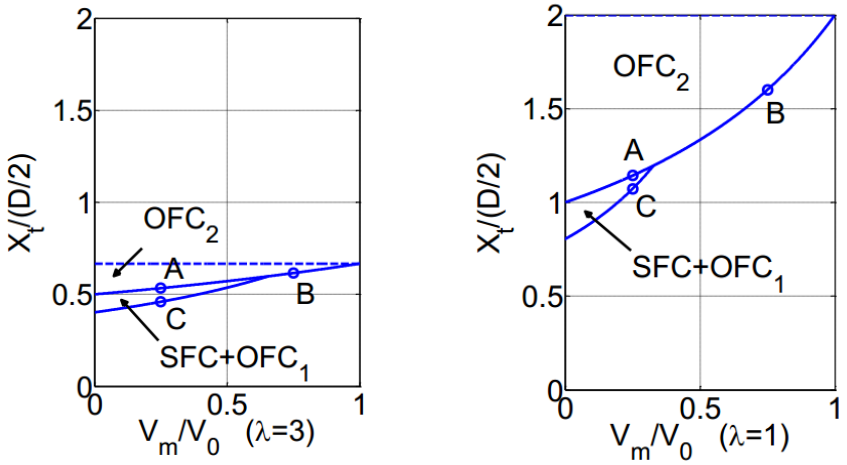


Fig. 5.17. Sizing characteristics of the case study DWC with DD coils (right) and UDD coils (left).

Fig. 5.17 shows that both with DD and UDD coils functioning is possible in SFC, $OFC_1$ and $OFC_2$ provided that the pair ($X_t$/(D/2), $V_m/V_0$) lays in the proper regions; but whichever functioning is selected, the graphs confirm that the use of UDD coils allows to operate with higher $V_m/V_0$ and shorter track coils.

Sizing procedure has been applied to UDD and DD coils operating at the working points highlighted by circles in Fig. 5.17. They correspond to the boundary of $OFC_2$ with $V_m/V_0$ equal to 0.25 (A) and 0.75 (B) and to the boundary of SFC+$OFC_1$ with voltage ratio equal to 0.25 (C). In the first point CSM and battery charging is possible while in the second and the third only CSM can be performed.

Pickup coil length has been set to 1.2 m, which is the maximum compatible with the case study EV dimension, with a track coil length $X_t$ of 0.4 m for UDD coils and 1.2 m for DD coils. Equations (5.27) or (5.29) have been used to find the ratio $X_t/(D/2)$ for each working point and

Table 5.3

Case study coil sizing results

| | UDD | | DD | |
|---|---|---|---|---|
| | $D$ [m] | $X_t/D$ [%] | $D$ [m] | $X_t/D$ [%] |
| A | 1.5 | 27 | 2.1 | 57 |
| B | 1.3 | 31 | 1.5 | 80 |
| C | 1.7 | 23 | 2.2 | 54 |

from it, being $X_t$ known, $D$ has been computed; finally, the ratio $X_t/D$ has been worked out. This later parameter is a good indicator of the cost of the track because it corresponds to the percentage of the track length than must be populated by coils to reach the requested

performance. The obtained results, summarized in Table 5.3, confirms that the use of UDD coils reduce the cost of the track to less than half without impairing the performances of the DWC system and affecting the cost of the power electronics installed onboard the EV

### *5.5.2 Simulation Results*

The schematic of Fig. 5.3 has been modeled in the PSIM environment to obtain realistic waveforms of the quantities involved in the functioning of the case study DWC system. A controlled voltage generator operating at 85 kHz has been used to model $V_p$ and its variation as a function of the time caused by the EV motion; the parasitic resistance of the pickup coil and the voltage drops across the power devices composing the diode rectifier and the chopper have been considered in the simulation. The chopper has the conventional buck topology with an inductor at the output side.

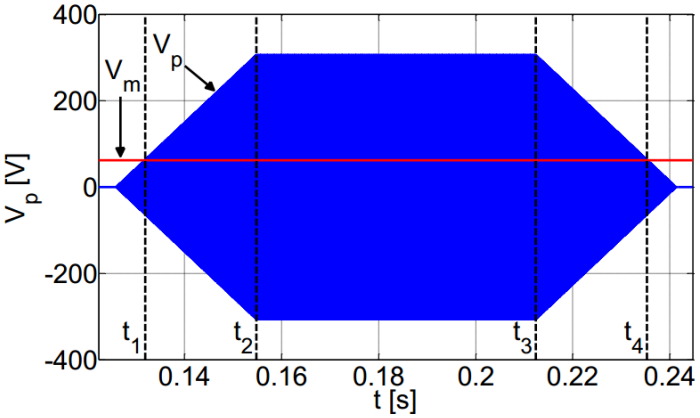


Fig. 5.18. Pickup voltage.

Simulations relevant to the three working points A, B and C have been performed obtaining results in good agreement with the theoretical findings described through the chapter. As an example, the waveforms of the quantities relevant to working point C are plotted in the following figures. The time axis of the graphs extends over the time interval $[T_D, 2T_D]$, where $T_D=D/U\approx0.1224$ s is the time taken by the EV to travel between two track coils.

Interval $T_D$ encompasses about $10^4$ supply periods so that the plot of induced voltage $V_p$ shown in Fig. 5.18 appears as a solid trapezoidal shape. The constant value $V_m$ is also drawn with a red line in order to recognize the time instants $t_1$ and $t_4$ where, according to the drawing of Fig. 5.12, current $I_p$ should start and stop flowing. At time instants $t_2$ and $t_3$ the current should have two steep variation due respectively to the end

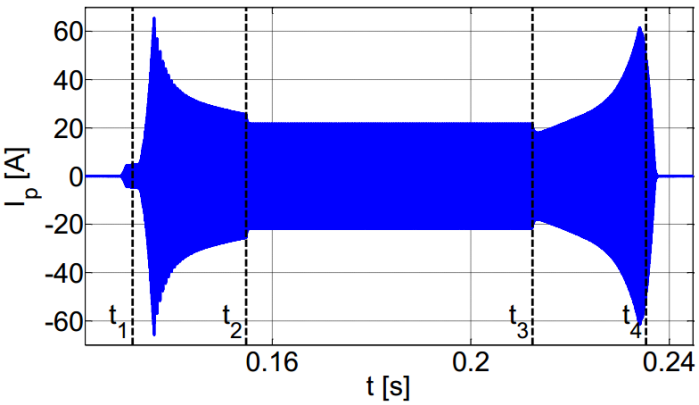


Fig. 5.19. Pickup current.

of charge and to the beginning of discharge of capacitor $C_{dc}$.

Graph of the pickup coil current is reported in Fig. 5.19. Its amplitude waveform is in good agreement with that sketched in in Fig. 5.12 and the small differences between them are easily explained. Current does not reach immediately its maximum value because just after $t_1$ the diode rectifier conduction is discontinuous and a short time interval is required before continuous conduction is reached. At $t_2$ and $t_3$ current variations happen as expected. At $t_4$ current does not vanish because the output inductance of the chopper forces $I_{ch,in}$ to keep flowing and to discharge the $C_{dc}$ to a voltage lower than $V_m$, thus protracting the conduction of the diode rectifier. This phenomenon also explains why in Fig. 5.19 a small current starts flowing when $V_p$ is still lower than $V_m$. Extension of current flow after $t_4$ partially compensates the delayed beginning of the continuous conduction of the diode rectifier at $t_1$. Indeed, while the diode rectifier is conducting the power at the chopper output is constant and, as shown in Fig. 5.20, power contribution lost at $t_1$ is almost completely recovered at $t_4$. As a result, the net energy supplied by the battery to the traction drive in the $T_D$ interval results in 7.75 J, being only 3% of the energy consumed to move the EV, which results in 280.3 J, so that CSM operation expected at this working point is nearly reached.

A number of FEM analysis has been performed on the pickup and track coils considering different $x$ positions to check if the proposed DWC system complies with the directive 2013/35/EU, which limits the exposure of operators to rms magnetic flux density lower than 100 μT [28].

Analysis has been performed setting the amplitudes and the relative phase of the coil currents to the values derived from the simulation. Contour plots of rms magnetic flux density relevant to three positions are reported in Figs. 21a, 21b and 21c. In the first of them the pickup is perfectly aligned with track coil *b*; according to the segmentation technique, only this track coil is supplied while track coil *a* is turned off. In the second figure the pickup coil is leaving the track coil *b* but the subsequent track coil *a* is not yet powered. In the last figure the pickup coil lays exactly between the track

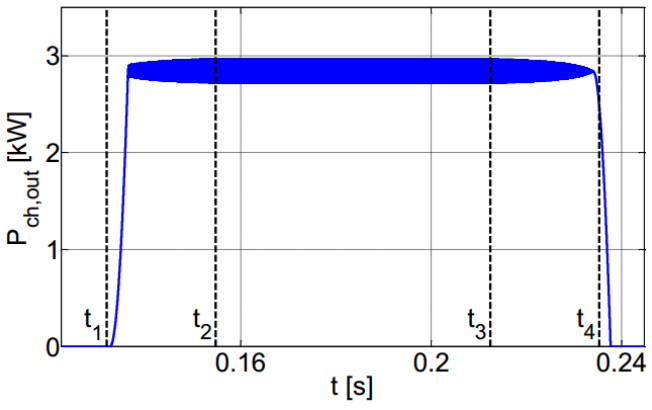


Fig. 5.20. Power at the chopper output.

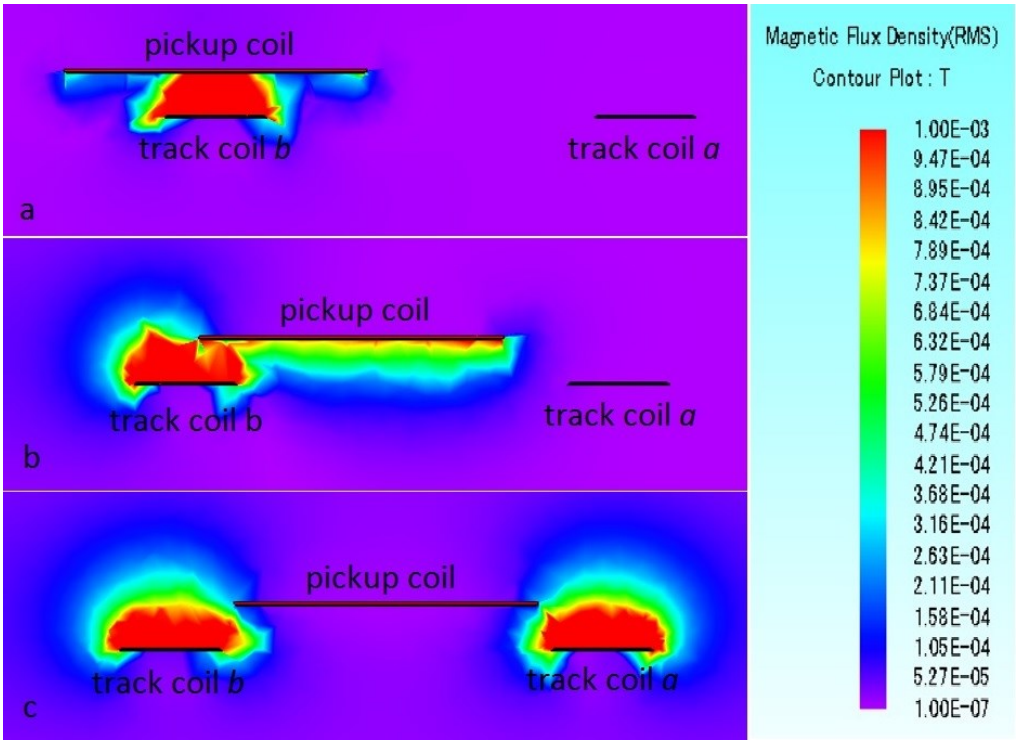


Fig. 5.21. Magnetic flux density contour plot.

coils *a* and *b*; here the worst situation from the point of view of leakage flux is depicted because coil *a* has been supplied before turning off coil *b*. At this position, both mutual inductances $M_a(x)$ and $M_b(x)$ are equal to 0 so that no current flows in the pickup coil. Inspection of the figures shows that in any case the rms magnetic flux density exceeds the 100μT limit only in a space region confined under the pickup coil and not exceeding the longitudinal dimension of the EV so that pedestrians moving near the track will not be subjected to harmful radiations.

## 5.6 Conclusion

This chapter dealt with a novel coil configuration derived from DD coils and denoted as UDD coils. The uneven lengths of track and pickup coils gives a flat-top profile to their mutual inductance that helps to reduce the gap between peak and average voltage induced across the pickup coil and lengthens the fraction of the distance between two track coils available to transfer power to the EV. Analytical expressions for induced voltage and current in the pickup coil are obtained and used to develop a sizing procedure that helps in defining the geometrical parameters of the track and pickup coils as a function of the EV battery and of the propulsion drive characteristics. The outcomes of a case study showed how the use of UDD coils could lead to a drastic reduction of the cost of the track. Theoretical findings have been checked against the results of FEM analysis and computer aided circuital analysis of a case study DWC system.

## References


[1] E. A. Grunditz and T. Thiringer, "Performance Analysis of Current BEVs Based on a Comprehensive Review of Specifications," *IEEE Transactions on Transportation Electrification*, Vol. 2, No. 3, pp. 270-289, Sept. 2016.

[2] B. Bilgin, P. Magne, P. Malysz, Y. Yang, V. Pantelic, M. Preindl, A. Korobkine, W. Jiang, M. Lawford, and A. Emadi, "Making the Case for Electrified Transportation," *IEEE Transactions on Transportation Electrification*, Vol. 1, No. 1, pp. 4-17, June 2015.

[3] H. Chaudhry and T. Bohn, "A V2G Application Using DC Fast Charging and its Impact on the Grid," *in proc. of IEEE Transportation Electrification Conference and Expo (ITEC)*, Dearborn, MI, 2012, pp. 1-6.

[4] J.M. Miller and A. Daga, "Elements of Wireless Power Transfer Essential to High Power Charging of Heavy Duty Vehicles," *IEEE Transactions on Transportation Electrification*, Vol. 1, No. 1, pp. 26-39, June 2015.

[5] M. Kabalo, F. Berthold, B. Blunier, D. Bouquain, S. Williamson and A. Miraoui, "Efficiency comparison of wire and wireless battery charging: Based on connection probability analysis," *in proc. of IEEE Transportation Electrification Conference and Expo (ITEC),* Dearborn, MI, 2014, pp. 1-6.

[6] G.A.Covic and J.T.Boys, "Inductive Power Transfer," *IEEE Proceedings*, vol. 101, nº 6, pp. 1276-1289, 2013.

[7] G.A. Covic and J.T. Boys, "Modern Trends in Inductive Power Transfer for Transportation Applications," *IEEE Journal of Emerging and Selected Topics in Power Electronics*, vol.1, nº 1, pp. 28-41, 2013.

[8] S.Y. Choi, B.W. Gu, S.Y. Jeong, and C.T. Rim, "Advances in Wireless Power Transfer Systems for Roadway-Powered Electric Vehicles," *IEEE Journal of Emerging and Selected Topics in Power Electronics*, vol.3, nº.1, pp.18-36, March 2015.

[9] J. Heo, D. S. Lee, S. J. Jeon, and N. H. Kim, "Furtive charging system for electric yard tractor," in proc. of *IEEE Transportation Electrification Conference and Expo*, Asia-Pacific (ITEC Asia-Pacific), Busan, 2016, pp. 666-670.

[10] J. Shin, S. Shin, Y. Kim, S. Ahn, S. Lee, G. Jung, S.-J. Jeon, and D.-H. Cho, "Design and implementation of shaped magnetic-resonance-based wireless power transfer system for roadway-powered moving electric vehicles," *IEEE Transactions on Industrial Electronics*, vol. 61, nº 3, pp. 1179-1192, 2014.

[11] J.T. Boys and G.A. Covic, "The Inductive Power Transfer Story at the University of Auckland," *IEEE Circuits and Systems Magazine*, vol. 15, nº 2, pp.6-27, 2015.

[12] W. Zhang, S.C. Wong, C.K. Tse, and Q. Chen, "An Optimized Track Length in Roadway Inductive Power Transfer Systems," *IEEE Journal of Emerging and Selected Topics in Power Electronics*, vol.2, nº 3, pp. 598-608, 2014.

[13] G.R Nagendra, G.A. Covic, and J.T Boys, "Determining the Physical Size of Inductive Couplers for IPT EV Systems," *IEEE Journal of Emerging and Selected Topics in Power Electronics*, vol. 2, nº 3, pp. 571-583, 2014.

[14] S. Bandyopadhyay, V. Prasanth, P. Bauer and J. A. Ferreira, "Multi-objective optimisation of a 1-kW wireless IPT systems for charging of electric vehicles," *in proc. of IEEE Transportation Electrification Conference and Expo (ITEC)*, Dearborn, MI, 2016, pp. 1-7.

[15] T.D. Nguyen, S. Li, W. Li, and C.C. Mi, "Feasibility study on bipolar pads for efficient wireless power chargers," in Proc. IEEE Applied Power Electronics Conference and Exposition (APEC), 2014, pp. 1676-1682.

[16] V. Prasanth and P. Bauer, "Distributed IPT Systems for Dynamic Powering: Misalignment Analysis," *IEEE Transactions on Industrial Electronics*, vol. 61, nº 11, pp. 6013-6021, 2014.

[17] Q. Zhu, Y. Guo, L. Wang, C. Liao, and F. Li "Improving the Misalignment Tolerance of Wireless Charging System by Optimizing the Compensate Capacitor, "*IEEE Transactions on Industrial Electronics*, vol. 62, nº 8, pp. 4832-4836, 2015.

[18] 12 S. Raabe and G.A. Covic, "Practical Design Considerations for Contactless Power Transfer Quadrature Pick-Ups," *IEEE Transactions on Industrial Electronics*, vol.60, nº 1, pp. 400-409, 2013.

[19] J. P. K. Sampath, D. M. Vilathgamuwa and A. Alphones, "Efficiency Enhancement for Dynamic Wireless Power Transfer System With Segmented Transmitter Array," *IEEE Transactions on Transportation Electrification*, Vol. 2, No. 1, pp. 76-85, March 2016.

[20] M. Budhia, J.T. Boys, G.A. Covic, and C.Y. Huang, "Development of a Single-Sided Flux Magnetic Coupler for Electric Vehicle IPT Charging Systems," *IEEE Transactions on Industrial Electronics*, vol. 60, nº 1, pp. 318-328, 2013.

[21] A. Zaheer, H. Hao, G.A. Covic, and D. Kacprzak, "Investigation of Multiple Decoupled Coil Primary Pad

Topologies in Lumped IPT System for interoperable electric vehicle charging," *IEEE Transactions on Industrial Electronics*, vol. 30, nº 4, pp. 1937-1955, 2015.

[22] 17 J. Deng, W. Li, T.D. Nguyen, S. Li, and C.C. Mi, "Compact and Efficient Bipolar Coupler for Wireless Power Chargers: Design and Analysis," *IEEE Transactions on Power Electronics*, vol. 30, nº 11, pp. 6130-6140, 2015.

[23] M. McDonough and B. Fahimi, "A study on the effects of motion in inductively coupled vehicular charging applications," *in proc. of IEEE Transportation Electrification Conference and Expo* (ITEC), Dearborn, MI, 2012, pp. 1-5.

[24] M. Bertoluzzo, G. Buja and, and H. K. Dashora, "Lumped Track Layout Design for Dynamic Wireless Charging of Electric Vehicles," *IEEE Transactions on Industrial Electronics*, vol.63, no.10, pp.6631-6640, 2016.

[25] W. Li, H. Zhao, S. Li, J. Deng, T. Kan, and C.C. Mi, "Integrated Compensation Topology for Wireless Charger in Electric and Plug-in Electric Vehicles," *IEEE Transactions on Industrial Electronics*, vol. 62, nº 7, pp. 4215-4225, 2015

[26] L. Chen, S. Liu, Y.C. Zhou, and T.J. Cui, "An optimizable circuit structure for high-efficiency wireless power transfer," *IEEE Transactions on Industrial Electronics*, vol. 60, no 1, pp. 339-349, 2013.

[27] G. Buja, M. Bertoluzzo, and K. N. Mude, "Design and Experimentation of a WPT Charger for Electric City Car," *IEEE Transactions on Industrial Electronics*, vol. 62, n. 12, pp. 7436-7447, 2015.

[28] Pinto R., Bertoluzzo M., Lopresto V., Mancini S., Merla C., Pede G., Genovese A., and Buja G, "Exposure assessment of stray electromagnetic fields generated by a wireless power transfer system," in Proc. IEEE 9th European Conference on Antennas and Propagation (EuCAP), pp. 1-4, 2015.

# Chapter 6

# Design Validation with FEM Co-simulation

Over the past 100 years, we have become increasingly dependent on our cars for meeting life's most basic needs. In most of the world, getting to and from work and holidays, bringing food home from the grocery store, or going to the doctor means using one's car. This reliance on the automobile and on the petroleum-powered internal combustion engine in particular, comes with significant costs. Our dependence on oil makes our overall economy and household budgets highly vulnerable to volatile oil prices. The pollutant emissions from our vehicles contribute to unhealthy air and global climate change.

## 6.1 Finite Element Analysis

The finite element method (FEM) is a numerical technique for finding approximate solutions to boundary value problems for partial differential equations. It is also referred to as finite element analysis (FEA). It subdivides a large problem into smaller, simpler parts that are called finite elements. The simple equations that model these finite elements are then assembled into a larger system of equations that models the entire problem. FEM then uses variational methods from the calculus of variations to approximate a solution by minimizing an associated error function.

### *6.1.1 Basic Concept*

The subdivision of a whole domain into simpler parts has several advantages:

- Accurate representation of complex geometry.
- Inclusion of dissimilar material properties.
- Easy representation of the total solution.
- Capture of local effects.

A typical work out of the method involves two steps. First step is to divide the domain of the problem into a collection of subdomains, with each subdomain represented by a set of element equations to the original problem. Second step comprises systematically recombining all sets of element equations into a global system of equations for the final calculation. The global system of equations has known solution techniques, and can be calculated from the initial values of the original problem to obtain a numerical answer.

In the first step above, the element equations are simple equations that locally approximate the original complex equations to be studied, where the original equations are often partial differential equations (PDE). To explain the approximation in this process, FEM is commonly introduced as a special case of Galerkin method. The process, in mathematical language, is to construct an integral of the inner product of the residual and the weight functions and set the integral to zero. In simple terms, it is a procedure that minimizes the error of approximation by fitting trial functions into the PDE. The residual is the error caused by the trial functions, and the weight functions are polynomial approximation functions that project the residual. The process eliminates all the spatial derivatives from the PDE, thus approximating the PDE locally with

- A set of algebraic equations for steady state problems,
- A set of ordinary differential equations for transient problems.

These equation sets are the element equations. They are linear if the underlying PDE is linear, and vice versa. Algebraic equation sets that arise in the steady state problems are solved using numerical linear algebra methods, while ordinary differential equation sets that arise in the transient problems are solved by numerical integration using standard techniques such as Euler's method or the Runge-Kutta method.

In the second step mentioned above, a global system of equations is generated from the element equations through a transformation of coordinates from the subdomains' local nodes to the domain's global nodes. This spatial transformation includes appropriate orientation adjustments as applied in relation to the reference coordinate system. The process is often carried out by FEM software using coordinate data generated from the subdomains.

FEM is best understood from its practical application, known as finite element analysis (FEA). FEA as applied in engineering is a computational tool for performing engineering analysis. It includes the use of mesh generation techniques for dividing a complex problem into small elements, as well as the use of software program coded with FEM algorithm. In applying FEA, the complex problem is usually a physical system with the underlying physics such as the Euler-Bernoulli beam equation, the heat equation, or the Navier-Stokes equations expressed in either PDE or integral equations, while the divided small elements of the complex problem represent different areas in the physical system.

FEA is a good choice for analyzing problems over complicated domains (like cars and oil pipelines), when the domain changes (as during a solid state reaction with a moving boundary),

when the desired precision varies over the entire domain, or when the solution lacks smoothness. For instance, in a frontal crash simulation it is possible to increase prediction accuracy in "important" areas like the front of the car and reduce it in its rear (thus reducing cost of the simulation). Another example would be in numerical weather prediction, where it is more important to have accurate predictions over developing highly nonlinear phenomena (such as tropical cyclones in the atmosphere, or eddies in the ocean) rather than relatively calm areas.

### *6.1.2 FEM Tools*

There are numerous software packages available that implement the finite element method for solving partial differential equations. These software are dedicated to perform various kind of analysis like electromagnetic, thermal, material structures, flued-dynamic analysis etc., amongst them our interest is electromagnetic analysis. In this way, COMSOL Multiphysics and JMAG-Designer are two tools have been used in the research work of this thesis. The former one has been used initially to evaluate inductances of coupled coils, which facilitates coil design in 2D and 3D with quite complex geometry. This tool is also good in analyzing results generating required plots, but in case of co-simulation with PSIM, a power electronic circuit simulator, this shows limitation.

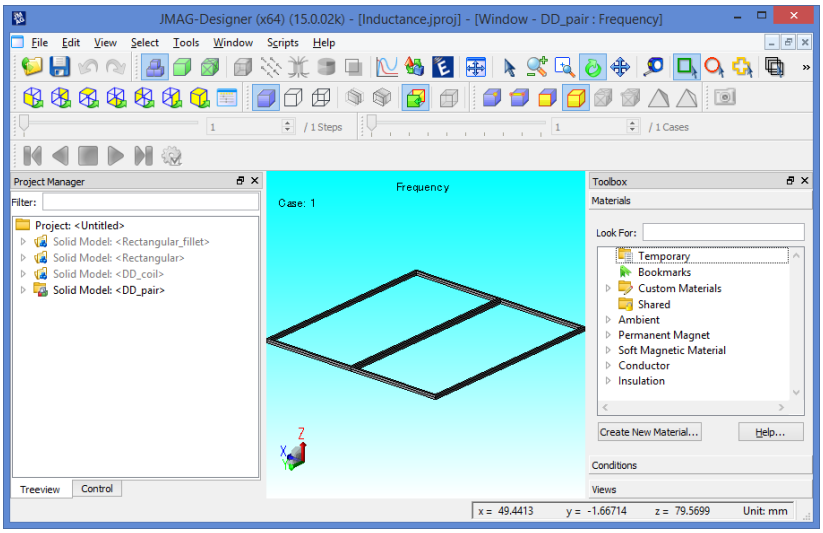


Fig. 6.1. JMAG-Designer.

Later, JMAG-Designer has been considered for further analysis and used extensively in research work summarized in this thesis. JMAG incorporates simulation technology to accurately analyze a wide range of physical phenomenon that includes complicated geometry, various material properties, and the heat and structure at the center of electromagnetic fields. JMAG has an interface capable of linking to third-party software and a portion of the JMAG analysis functions can also be executed from many of the major CAD and CAE systems.

## 6.2 Coil Model in JMAG-Designer

In wireless power transfer two planner coils face each other and power transfer occurs using magnetic coupling. They can be used for various applications, such as moving or rotating devices, or devices sealed inside enclosed spaces. As mentioned in chapter 3, the coil shape and pattern can be of various types but the spiral wound DD coil is the best choice for DWC system. Because the primary and secondary sides do not touch, the power transmission efficiency and leakage flux vary depending on their positions relative to each other. Therefore, it is important at the design stage to understand how properties change according to their placement. Thus, coil design using JMAG-Designer, to realize two identical DD coils in FEM environment is elaborated in this section, which allows precise modeling of the geometry of the parts and their relative positions, and makes it possible to visualize the leakage in the magnetic flux that is generated in the primary side and transmitted to the secondary side.

A panel FEM tool JMAG-Designer is shown in Fig. 6.1, where the left most column is project manager and center space is the display of the model. The right most column is a tool box that includes material and condition settings. The FEM code to model a pair of WPT coils incorporates the major steps: create geometry, import geometry & create study, apply material, apply test conditions, create circuit and link the components, set study properties, and run the study.

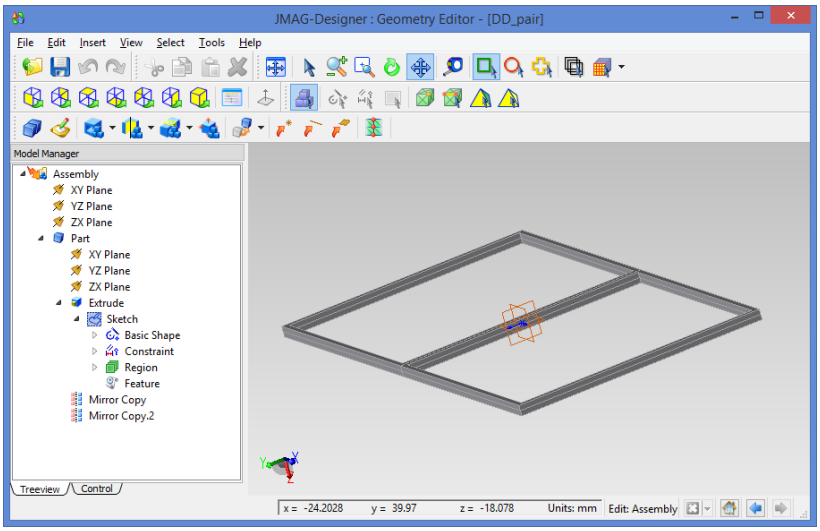


Fig. 6.2. JMAG Geometry Editor.

To create a geometry, an additional tool 'Geometry Editor' is used which can be launched from the JMAG-Designer window. Fig. 6.2 shows a screen shot of Geometry Editor where the left column is model manager and right side is design space. A physical structure of any part is designed by drawing a basic sketch and later by employing associated other functions like extrude, revolve, fillet, mirror copy etc., various geometries in 2D and 3D are obtained. This tool also allows to edit the geometries created by other CAD tools and available in the compatible file format. If the geometry model has got axis or mirror symmetry then only a

section of the symmetrical model can be adequate, which can be later considered complete in JMAG simulation. The full or partially created geometry is imported by JMAG from the Geometry Editor to use in FEM analysis.

In second stage, the geometry is imported into the project manager of JMAG-Designer and an FEM analysis is performed. There various types of FEM analysis can be performed on the imported model like magnetic, electric, thermal, structural etc., however, for this thesis, the

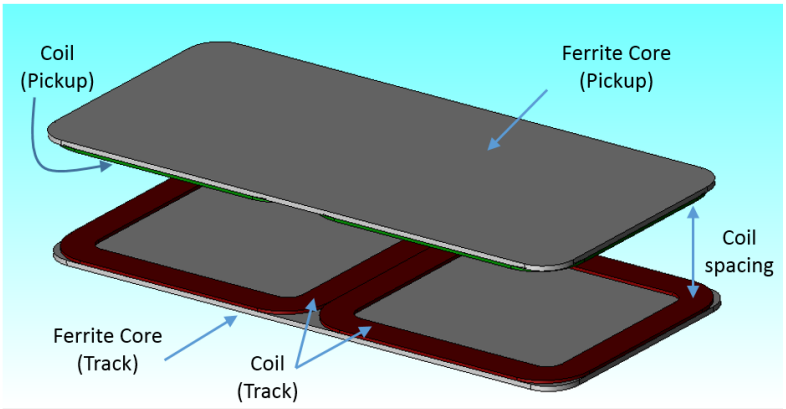


Fig. 6.3. JMAG Model of a pair of DD coils.

magnetic study of a WPT system is main important. In the allotted analysis study, materials are allocated to the every part of the geometry model to realize the actual system in FEM environment. There are various material categories including conducting, magnetic, insulating materials, as well as user defined materials. Later, test conditions are assigned to necessary parts to realize electric or magnetic components, also to enforce symmetricity to the sectional models for completion.

An electrical circuit can be created or imported as an important input for an analysis. There is a circuit editor in JMAG that provides an electrical simulation environment to the parts defined as electrical components in the test condition and need power supply, connections and ground. The circuit components must be linked with the test conditions of the model. In the circuit editor, there are some passive components like resistance, capacitor, inductor etc. available which make JMAG an independent simulation environment.

Following the necessary analysis procedure, a setup of DD coils is created in JMAG as shown in Fig. 6.3. One DD coil is basically built with a series connection of two square coils laid in a same plane and on a same Ferrite plate. The specifications of the assumptions, components, material, and test conditions used for this analysis are shown below.

*Components*

There are two DD coils as shown in Fig. 6.3, which are supported with two Ferrite plates for the purpose of core. This geometry is first created in the Geometry Editor and imported to JMAG, names of each component are depicted in the same figure.

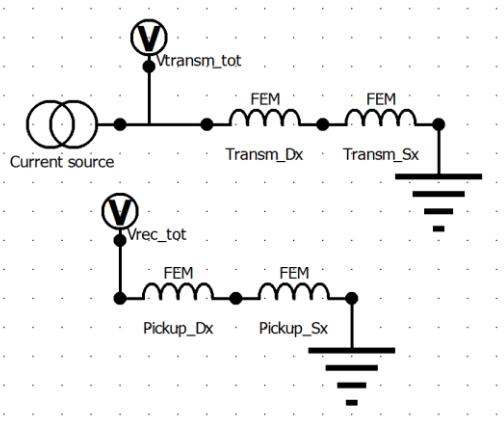


Fig. 6.4. Electrical schematic in JMAG Circuit Editor.

*Materials*

This model is a simple one where only two materials are used as mentioned in Table 6.1.

*Test Conditions and Circuit*

Both the coils shown in Fig. 6.3 are assigned as FEM coils in the condition selection, where the direction of current is choses such that each coil-half contains opposite magnetic polarity at the same coil face. These FEM coil conditions appears as inductors in the JMAG circuit editor as shown in Fig. 6.4, where each half section of a DD coil is represented as an individual inductor.

Table 6.1

| **Part** | **Material** | **Material Property** |
|---|---|---|
| Coil<br>(Track and pickup) | Copper | Resistivity= $1.673 \times 10^{-08}$<br>Relative permeability= 1 |
| Core<br>(Track and pickup) | Ferrite<br>TDK PC40_25deg | B-H curve |

In JMAG magnetic study, there are three types of analysis options available: static, transient and frequency analysis. In order to evaluate the magnetic properties of the pair like self and mutual inductances (*L* and *M*), flux density, current density etc., the frequency analysis is employed. In this example, the circuit is supplied by a current source of 1 A, 85 kHz, and voltage across the coils are measured; and L and M are computed using the obtained data.

## 6.3 PSIM model

*Powersim* or PSIM is specialized in electrical engineering simulation and design tools for research and product development in power supplies, motor drives, and power conversion and control systems.

A DWC system is composed of several active and passive electric components integrated that can be effectively simulated using PSIM. The components are mainly the WPT coils which

are basically two coupled inductors, high frequency inverter, rectifier and compensation topologies which includes various combinations of capacitor. Fig. 6.5 shows the schematic of the system which is simulated in PSIM.

The left most side is power supply system which draws power from the grid and provides high frequency current to the transmitting coil. This power conversion consists of a set of power electronic converters like rectifier, power factor correction circuit, and inverter. Second stage of the system is the WPT coils which are represented as inductors. The coil parameters can be set manually as well as imported from JMAG or any other compatible FEM tool. In the latter case, parameter variations can be accounted while change in geometry and position of the coils; this is called co-simulation and is discussed in detail in the next section. Both the WPT coils are supported with some compensation capacitor, as shown in the same figure, to improve system performance. The final stage of wireless charging is in receiving side where the high frequency pickup voltage is rectified, regulated and supplied to the vehicle battery. Thus a diode bridge rectifier and a chopper are deployed in the PSIM model.

## 6.4 PSIM-JMAG co-simulation

The WPT system organization discussed in the previous section can effectively and more preciously simulated using the coupled operation of two different simulation environments. Here in the specific case magnetic and power electronic systems need to be analyzed simultaneously. In this way, a special circuit block, which named ‘MagCoupler’, is employed

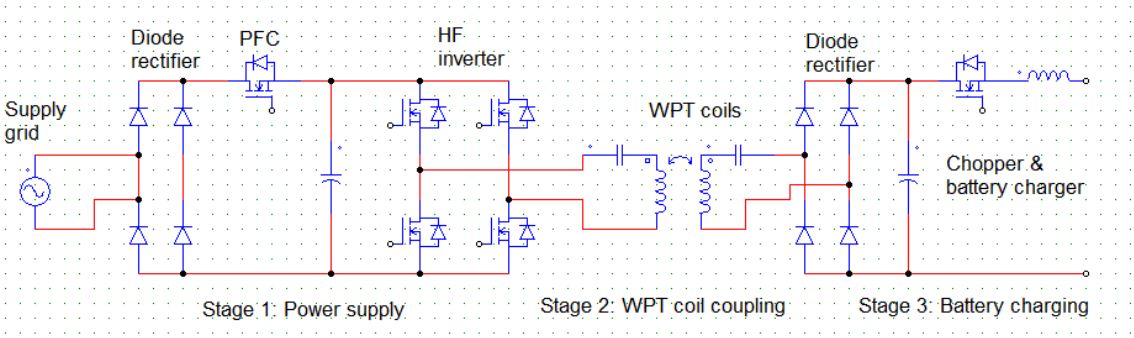


Fig. 6.5. Complete wireless charging circuit in PSIM.

in PSIM model to obtained JMAG environment. The MagCoupler Module is an add-on module to the PSIM software. It provides the dynamic link for PSIM and JMAG co-simulation, so that the power converter and control part of a system can be implemented and simulated in PSIM, and WPT coils and other magnetic devices can be implemented and solved in JMAG.

With the MagCoupler Module, coil manufacturers can interface and test their design with the intended power converters and control schemes, and optimize the design based on performance, size, and cost. On the other hand, the MagCoupler Module expands PSIM's capability to finite element analysis. A direct benefit is that one can simulate coil coupling based on the definition of the coil dimension, structure, and materials, thus eliminating the need to extract or derive coil parameters. This gives more accurate results that take into account

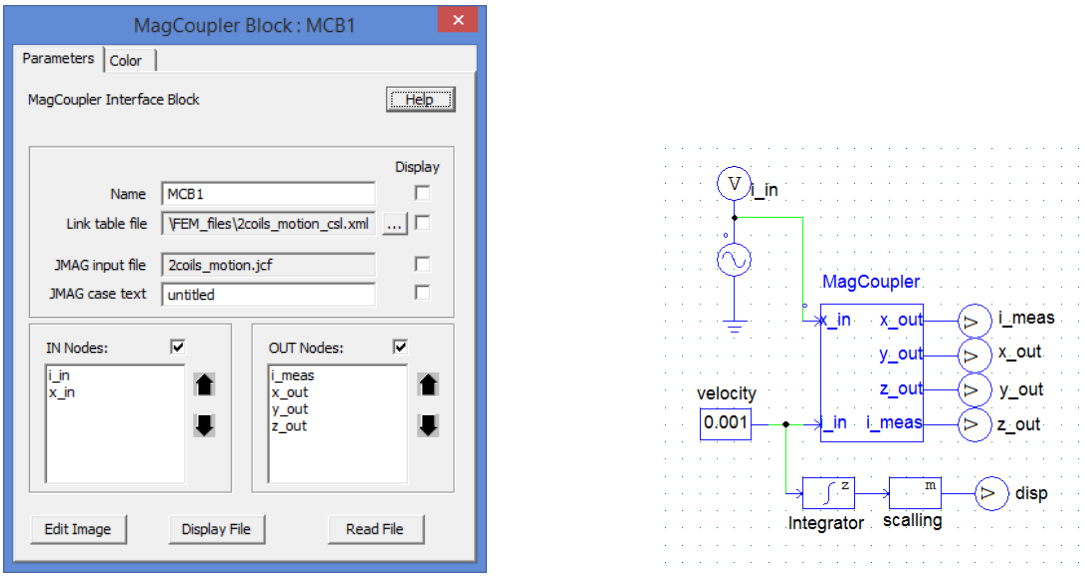


Fig. 6.6. MagCoupler block and its use in PSIM.

magnetic saturation and losses, time harmonics and space harmonics, and other nonlinear effects that would be difficult to consider otherwise. In addition, since PSIM links to MATLAB Simulink through the SimCoupler Module, one can run all three software together by having the control in Simulink, the power converter in PSIM, and the physical coil structure in JMAG.

Talking about the MagCoupler Block, it need to be configured in PSIM and appropriate inputs need to be provided. To run the MagCoupler Module, the path of the JMAG directory must be included in PSIM so that PSIM can load JMAG DLL files. To set the JMAG directory path in PSIM, go to Options -> Set Path, and click on 'Add Folder' to include the JMAG directory.

The MagCoupler block accepts voltages, currents, and positions as inputs, and it provides voltages, currents, positions, torques and force as the outputs. In PSIM, the MagCoupler block is a power circuit element. The way it interfaces with the rest of the circuit is that both the inputs and outputs are voltage signals (no electric current flows into the input nodes). To convert a current into a voltage signal, or vice versa, one can use a current-controlled voltage source, or voltage-controlled current source.

There is a Link Table File which defines the input/output interface nodes and their functions in JMAG. This file is in XML format, and is generated automatically by JMAG. This file can be located by clicking on the "Browser…" button at the right of the edit field. The main JMAG Input File is the JCF input data file that is read by the JMAG solver. The name is defined in the Link Table File.

An important note is that the JCF input file .jcf must be placed in the same directory as the .xml. If any material database is used in JMAG, it should also be placed in the directory of the .xml file. Also, the .xml file does not have to be in the same directory as the schematic file. The JMAG Case Text is a text identifying the specific JMAG circuit. It can be any text describing the JMAG circuit.

The IN Nodes and OUT Nodes are the nodes through which PSIM passes/receives the values to/from JMAG. On the MagCoupler block image, the order of the input/output nodes is from the top to the bottom. The order can be changed by highlighting the node and click on the upper or down arrow.

By clicking on the Edit Image button, one can edit and customize the image of the MagCoupler block. Clicking on the Display File button will display the Link Table File in the Microsoft Internet Explorer environment, and clicking on the Read File button will read or re-load the Link Table File.

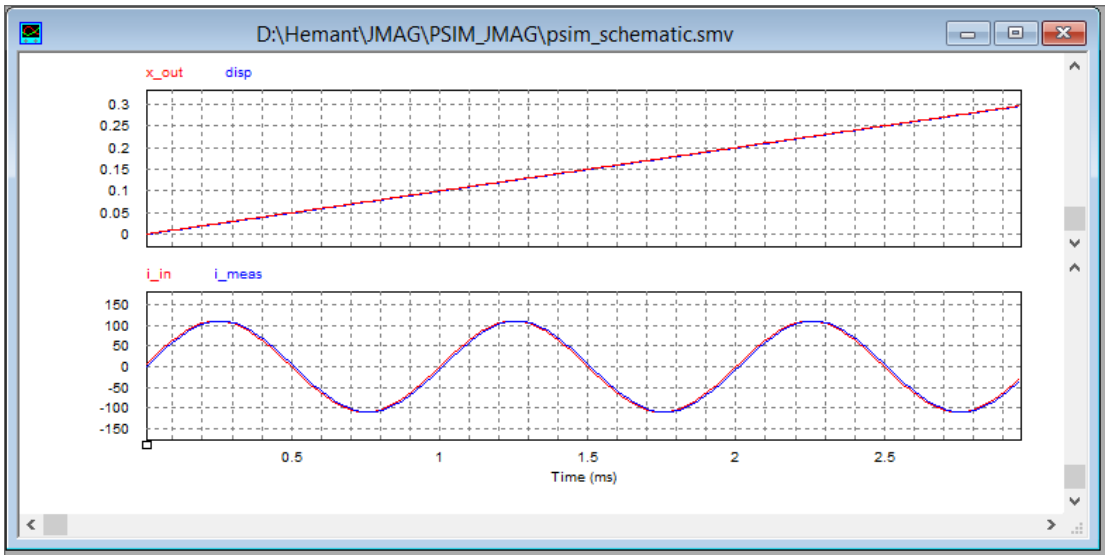


Fig. 6.7. Validation of JMAG-PSIM co-simulation.

## 6.5 Results and discussion

To test the JMAG-PSIM co-simulation, a simple circuit schematic is created as shown in Fig. 6.6, considering a system of two circular coils placed with a distance to transfer power

wirelessly. One coil is stationary and supplied by a current (value is decided in PSIM), and another coil is moving in the parallel plane of the first coil. There are two inputs to MagCoupler block (theoretically to the FEM model): supply current and velocity. The MagCoupler block provides output like measured current and displacement in x, y and direction. The verification of the PSIM-JMAG link can be done by comparing the given inputs in PSIM and observed response from JMAG as shown in Fig. 6.7.

Observing Fig. 6.7, the commended and measured values of current and displacement are expectedly matching. There is a small delay also observed in two waveforms, which is a delay of one simulation time step because The input value to JMAG is shifted 1 step against input value of JMAG Block in PSIM.

**References**


[1] J.N. Reddy, "An Introduction to the Finite Element Method" (Third edition). McGraw-Hill. 2006.

[2] O.C. Zienkiewicz, Z.R.L. Taylor, and J.Z. Zhu, "The finite element method: its basis and fundamentals", 7th Edition. Elsevier-2013.

[3] Gérard Meunier, "The Finite Element Method for Electromagnetic Modeling," Publication: John Wiley & Sons, 2010.

# Chapter 7

# Reflexive Segmentation and Compensation Topologies

The DWC track can be made with various arrangements. As discussed in chapter 4 & 5, they are classified in two categories: stretched coil track with a single elongated coil along the road [6], and lumped coil track with a series of multiple coils [7], [8]. In both the arrangements, the track coils are supplied by a high-frequency AC source to induce in the pickup an emf of convenient magnitude. In case if all the track is supplied at a time, is not good for safety and efficiency purpose, therefore the track is divided in segments of suitable length and each segment is operated individually; this strategy is called track segmentation. Considering a lumped coil track arrangement, this chapter is going to deal with an automatic way to implement segmentation in a DWC track.

## 7.1 Introduction

Let us consider an IPT with a lumped track and that all the track coils are supplied. They generate a magnetic flux but only that one generated by the track coil linked with the pickup, transfers electric power and charges the EV battery. Transferred power is proportional to the magnetic flux density so that effectiveness of the dynamic charging increases with it; on the other hand, exposition of living beings to high-intensity magnetic field is harmful [9] and safety limits must be fulfilled [10]. For both safety and efficiency reasons, the track coils are supplied selectively; this means that only the track coil coupled with the pickup is supplied whilst the other ones are left inactive. The technique of supplying only a specific coil of a lumped IPT track is called segmentation.

The straightforward method to implement segmentation is to supply each coil with an individual AC source, turned on or off according to the presence or the absence of a pickup

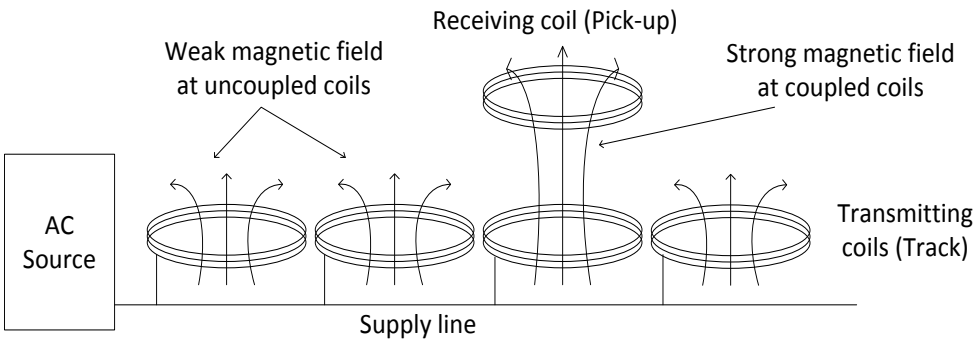


Fig. 7.1. Conceptual layout of the reflexive method.

above the coil, or to use a multi-output AC source that supplies one coil at a time. Both these approaches require the intervention of a control system that senses the presence of a pickup and activates the proper AC source.

A different method has been proposed in [8] to implement segmentation, where the track coils are connected in parallel to a supply line and a single AC source feeds the line, as illustrated in Fig. 7.1. This method exploits the fact that the reactance of the track coils not coupled with the pickup is so high that the magnitude of the current flowing into them is very low while the opposite occurs for the reactance of the track coil coupled with a pickup. As a matter of fact, the reflected reactance of a pickup with a properly designed circuit can compensate for the track coil reactance, thus enabling a substantial flow of current in the track coil and, from it, to the pickup one. This method of implementing the segmentation is termed reflexive. It executes an automatic selection of the coupled track coil without needing to detect the pickup and tampering with the command of the AC source.

This chapter analyzes the reflexive properties of a segmented IPT track for different topologies of the pickup circuit, some of them introduced in this chapter, and discusses the performance of the resultant IPT system. Description of the symbols and abbreviations used in the chapter for analysis purpose are listed in Table 7.1.

Table 7.1

Symbols & abbreviation

| Symbols & abbreviations | Description |
|---|---|
| $V_{track}$ | Supply voltage of the track. |
| $L_t$, $L_p$ | Self-inductance of track pickup coils, respectively. |
| $I_t$, $I_p$ | Current in track and pickup coils, respectively. |
| $Z_t$, $Z_p$ | Impedance of track and pickup circuits in uncoupled conditions. |
| $k$, $M$ | Coupling coefficient and mutual inductance between coupled track and pickup coils. |
| $Z_r$ | Reflected pickup impedance to track coil. |
| $Z_{r,x}$ | Reflected impedance with p or x compensation topology, where p stands for parallel and x for either CCsp or CCps or LCsp or CLsp. |
| *CCsp* | Pickup coil with series and parallel capacitors. |
| *CCps* | Pickup coil with parallel and series capacitors. |
| *LCsp* | Pickup coil with series inductor and parallel capacitor. |
| *CLsp* | Pickup coil with series capacitor and parallel inductor. |

## 7.2 Series/Parallel Resonant Compensation

Hereafter, coupling between one of the track coils and the pickup is examined by disregarding a possible, concurrent coupling of the pickup with two or three track coils; this assumption is reasonable as the track coils are distant each from the other much more than the pickup size. Moreover, the resistances of both the track and pickup coils are neglected. Lastly, the supply line is fed by an AC sinusoidal voltage source of peak magnitude $V_{track}$ and angular frequency $\omega=2\pi f$, where $f$ has a value of many tens of kHz.

The circuit schematics of a track coil and a pickup is drawn in Fig. 7.2, where $L_t$ and $L_p$ are the self-inductances of the track and pickup coils, $M$ is their mutual inductance, and $I_t$ and $I_p$ are the track coil and pickup currents. A consequential parameter of the circuit is the coupling coefficient $k$ between the track coil and the pickup, given by

$$k = \frac{M}{\sqrt{L_t L_p}} \qquad (7.1)$$

Two situations are envisaged: i) the track coil is uncoupled from the pickup, and ii) the track coil is fully coupled with the pickup. In the first situation $M$, and hence $k$, is zero whilst in the other situation $k$ is greater than zero but somewhat smaller than 1 due to the large airgap.

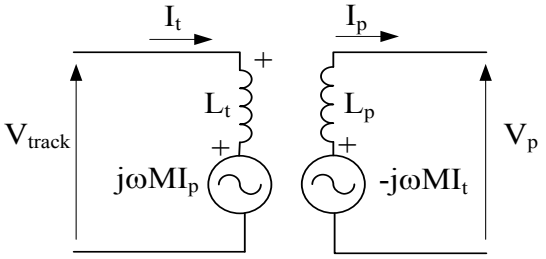


Fig. 7.2. Circuit schematics of the coupling between a track coil and a pickup.

When the track coil is uncoupled from a pickup coil, the current flow in the track coil is

$$I_t = \frac{V_{track}}{j\omega L_t} \qquad (7.2)$$

The magnitude of the current in (7.2) is low due to the high values of both the track coil inductance and the supply frequency.

When the track coil is coupled to a pickup coil, its impedance is modified by the reflected impedance of the pickup circuit. The latter impedance can be found from Fig. 7.2 and results in

$$Z_r = \frac{j\omega M I_p}{I_t} = \frac{-j\omega M j\omega M I_t}{I_t Z_p} = \frac{\omega^2 M^2}{Z_p} \qquad (7.3)$$

As (7.3) points out, the reflected impedance is a function of the pickup impedance that includes, besides the pickup coil reactance, the load resistance and the impedance of possible other components inserted in the pickup circuit.

IPT system for stationary EV battery charging utilizes capacitors connected either in series or in parallel to both the transmitting coil and the receiving coil to compensate for their reactive power with the end of maximizing the power transfer efficiency [5]. Full reactive power compensation is achieved by making the LC meshes resonating. In an IPT system for the dynamic EV battery charging, the transmitting coil is substituted for by the track and the receiving coil by the pickup. Then, a preliminary analysis of the reflexive properties carried out by leaving uncompensated the track coil and by inserting a resonating capacitor in series or in parallel to the pickup coil appears of interest. The circuit schematics becomes as in Fig. 7.3, where $R_{eq}$ is the equivalent resistance at the output terminals of the pickup and is representative of the battery load and the in-between power conversions, commonly constituted by a diode rectification and a DC-DC chopping.

Series capacitor compensation makes pickup reactance zero at resonance and therefore it reflects only the real part of the pickup impedance [11]. Then it does have a minor reflexive property.

Parallel capacitor compensation reflects both real and reactive parts of the pickup impedance and hence it has some reflexive property. By (7.3), the expression of the reflected impedance of the pickup becomes

$$Z_{r,p} = \frac{\omega M^2}{L_p}\left(\frac{R_{eq}}{\omega L_p} - j\right) \qquad (7.4)$$

According to (7.4), the reflected reactance is negative and then compensates for the track coil reactance. For a full compensation, its modulus must be equal to that of track coil, i.e.

$$\frac{\omega M^2}{L_p} = \omega L_t \qquad (7.5)$$

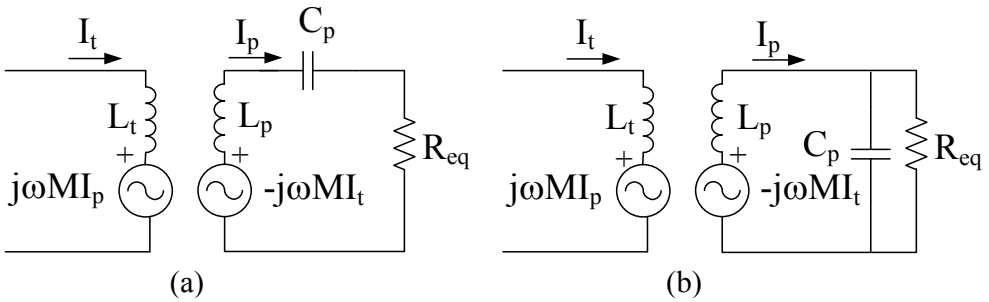


Fig. 7.3. Pickup coil series and parallel resonant topologies.

and, from it,

$$\frac{M^2}{L_p} = L_t \qquad (7.6)$$

This relationship is satisfied when the coupling coefficient is unity, which is not realistic in loosely coupled applications like the EV battery charging. Therefore, as it can be derived from (7.4), only the fraction *k* of the track coil reactance can be compensated for by the pickup, which is a quite small compensation.

As a result, series and parallel resonant topologies are not able to compensate effectively for the track coil reactance. Therefore, different topologies of the pickup circuit are investigated for a feasible reflexive segmentation.

## 7.3 Two-Component Compensation

Using two reactive components that maybe a combination of capacitors or inductors or both, this type compensation has been investigated in this section. Four two-component topologies are analysed to compensate for the track coil reactance to achieve reflexive segmentation. The topologies are denoted as CCsp, CCps, LCsp and CLsp, where the two upper-case letters represent the two components of the pickup circuit, and the two lower-case letters their connection type (s stands for series and p for parallel). The CCsp topology has been proposed in [9] whilst the other three are here introduced.

### *7.3.1 CCsp topology*

The CCsp topology is drawn in Fig. 7.4 (a). It inserts a capacitor $C_1$ in series to the pickup coil and the other capacitor $C_2$ in parallel to the series of $L_t$ and $C_1$. Capacitors $C_1$ and $C_2$ are chosen according to (7.7) for the pickup circuit to resonate at $\omega$.

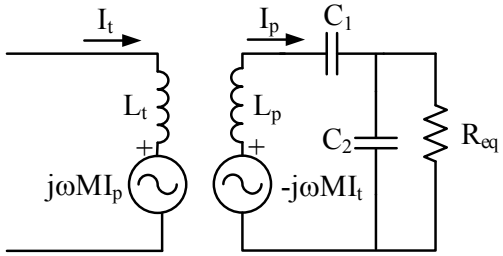

Fig. 7.4. Track coil compensation CCsp.

$$\omega = \frac{1}{\sqrt{L_p \frac{C_1 C_2}{C_1 + C_2}}} \qquad (7.7)$$

The pickup impedance results in

$$Z_p = j\omega L_p + \frac{1}{j\omega C_1} + \frac{1}{j\omega C_2 + \frac{1}{R_{eq}}} \qquad (7.8)$$

and the reflected impedance, calculated by (7.3), is

$$Z_{r,CCsp} = \frac{\omega^2 M^2}{\left(\omega L_p - \frac{1}{\omega C_1}\right)}\left(\omega C_2 R_{eq} - j\right) \qquad (7.9)$$

According to (7.9), the reflected reactance is negative and then can compensate for the track coil reactance. For a full compensation, it should be equal to that of the track coil, i.e.

$$\frac{\omega^2 M^2}{\left(\omega L_p - \frac{1}{\omega C_1}\right)} = \omega L_t \qquad (7.10)$$

By (7.1), (7.7) and (7.10), under full compensation the values of the pickup capacitors stays in the ratio of

$$\frac{C_1}{C_2} = \frac{k^2}{1-k^2} \qquad (7.11)$$

To assess the convenience of this topology, the reflected equivalent resistance is also evaluated. By (7.7) and (7.9), it can be expressed as

$$R_{r,CCsp} = \left[\frac{\omega^2 M^2}{\left(\omega L_p - \frac{1}{\omega C_1}\right)} \frac{C_1 + C_2}{C_1 \omega L_p}\right] R_{eq} \qquad (7.12)$$

An effective implementation of the reflexive segmentation requires that (7.12) must be a small fraction of the uncoupled track coil reactance $\omega L_t$.

If $R_{eq}$ is a small fraction of $\omega L_t$, the following constraint enables a reflexive segmentation:

$$\frac{\omega^2 M^2}{\left(\omega L_p - \frac{1}{\omega C_1}\right)} \frac{C_1 + C_2}{C_1 \omega L_p} \leq 1 \qquad (7.13)$$

Eq. (7.13) is fulfilled when the following relationship holds between $C_1$ and $C_2$

$$C_2 \leq \left(\frac{L_p}{k^2 L_t} - 1\right) C_1 - \frac{1}{\omega^2 k^2 L_t} \qquad (7.14)$$

The capacitor pairs belonging to the first quadrant of the plane $C_1$-$C_2$ of Fig. 7.5, and placed below the red solid line do not amplify the reflected equivalent resistance with respect to $R_{eq}$. On the other hand, relationship (7.11), represented by the blue dashed line in Fig.5, must be fulfilled to have full compensation; con sequently, the capacitor pairs must be selected in order that their values stay on the blue dashed line, at the right side of its intersection with the red solid one.

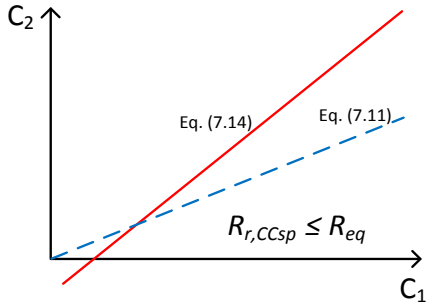


Fig. 7.5. Region of $C_1$, $C_2$ selection.

If, instead, $R_{eq}$ has a value comparable with $\omega L_t$, the reflexive segmentation is not achieved by (7.14). Under this circumstance, (7.13) must be modified by introducing a reduction factor $\alpha \leq 1$, i.e.

$$\frac{\omega^2 M^2}{\left(\omega L_p - \frac{1}{\omega C_1}\right)} \frac{C_1 + C_2}{C_1 \omega L_p} = \alpha \qquad (7.15)$$

By (7.11) and (7.15), the values of $C_1$ and $C_2$ are given by

$$C_1 = \frac{\alpha}{\omega^2(\alpha L_p - L_t)} \qquad (7.16)$$

$$C_2 = \frac{\alpha}{\omega^2 L_t} \qquad (7.17)$$

Further to (7.11), (7.16) and (7.17), the following relationship is found between the inductances of the track and pickup coils:

$$L_p = \frac{1}{\alpha k^2} L_t \qquad (7.18)$$

Both the quantities $\alpha$ and $k$ are smaller (or much smaller) than 1; therefore, eq. (7.18) states that the inductance of the pickup coil must be much higher than the track coil to achieve a satisfactory reflexive segmentation.

### *7.3.2 CCps topology*

Using a combination of two capacitors in the pickup circuit, the CCps topology is realized as shown in Fig. 7.6. Unlike CCsp, this topology inserts a capacitor $C_1$ in parallel to the pickup coil and the other capacitor $C_2$ in series to the parallel of $L_p$ and $C_1$.

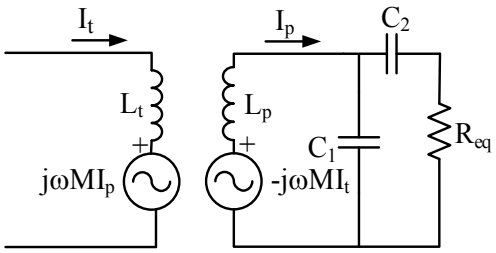

Fig. 7.6. Track coil compensation CCps.

The impedance of the pickup circuit results in

$$Z_p = j\omega L_p + \frac{1}{j\omega C_1 + \frac{1}{R_{eq} + \frac{1}{j\omega C_2}}} \qquad (7.19)$$

It can be rewritten as

$$Z_p = \frac{1 - \omega^2 L_p (C_1 + C_2) + j\omega R_{eq} C_2 (1 - \omega^2 L_p C_1)}{j\omega (C_1 + C_2) - \omega^2 C_1 C_2 R_{eq}} \qquad (7.20)$$

and the reflected impedance can be expressed as

$$Z_{r,CCps} = \frac{\omega^2 M^2 [j\omega(C_1+C_2) - \omega^2 C_1 C_2 R_{eq}]}{1-\omega^2 L_{pc}(C_1+C_2) + j\omega R_{eq} C_2 (1-\omega^2 L_p C_1)} \qquad (7.21)$$

By (7.21), there are two resonance conditions. If $C_1$ and $C_2$ are selected according to

$$\omega^2 L_p (C_1 + C_2) = 1 \qquad (7.22)$$

the reflected impedance is

$$Z_{r,CCps,1} = M^2 \left( \frac{C_1+C_2}{R_{eq} L_p C_2^2} + j \frac{\omega C_1}{L_p C_2} \right) \qquad (7.23)$$

The reactance of (7.23) is positive and hence the above selection of the values for the capacitors does not enable the compensation of the track coil reactance.

Instead, if $C_1$ is such that

$$\omega^2 L_p C_1 = 1 \qquad (7.24)$$

The reflected impedance, given by

$$Z_{r,CCps,2} = \frac{\omega M^2}{L_p} \left( \omega C_1 R_{eq} - j \frac{C_1+C_2}{C_2} \right) \qquad (7.25)$$

has a negative reactance and can compensate for the track coil reactance. Full compensation is obtained for

$$\frac{\omega M^2}{L_p} \frac{C_1+C_2}{C_2} = \omega L_t \qquad (7.26)$$

that leads to the following relationship between the capacitor values:

$$\frac{C_1}{C_2} = \frac{1-k^2}{k^2} \qquad (7.27)$$

By (7.24) and (7.25), the reflected equivalent resistance results in

$$Re(Z_{r,CCps,2}) = k^2 \frac{L_t}{L_p} R_{eq} \qquad (7.28)$$

Being $k$ much smaller than 1 and the ratio $L_t/L_p$ usually near to 1, eq. (7.28) indicates that the reflected equivalent resistance is substantially less than $R_{eq}$, which helps in improving the reflexive property of the pickup circuit. However, by considering the ratio (7.27) between $C_1$ and $C_2$, and the corresponding current flow in the pickup circuit of Fig. 7.6, it can be inferred that most of the pickup current is drawn by $C_1$ while the current in the series $C_2$-$R_{eq}$ will be somewhat low. This situation decreases the power transferred to the load, adversely affecting the overall efficiency of the IPT system.

### 7.3.3 LCsp topology

This topology provides compensation using a combination of an inductor and a capacitor the LCsp topology is drawn in Fig. 7.7. By this topology, an inductor $L_1$ is connected in series to the pickup coil and a capacitor $C$ in parallel to the series of $L_p$ and $L_1$. With this circuit, the components $L_1$ and $C$ are selected according to

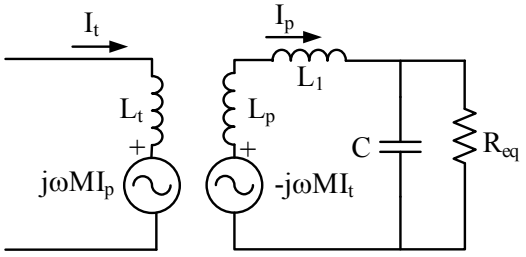


Fig. 7.7. Track coil compensation LCsp.

$$\omega = \frac{1}{\sqrt{(L_p+L_1)C}} \tag{7.29}$$

The impedance of the pickup circuit is

$$Z_p = j\omega L_p + j\omega L_1 + \frac{1}{j\omega C+\frac{1}{R_{eq}}} \tag{7.30}$$

and the reflected impedance can be expressed as

$$Z_{r,LCsp} = \frac{\omega M^2}{(L_p+L_1)}\left[\frac{R_{eq}}{\omega(L_p+L_1)} - j\right] \tag{7.31}$$

By (7.31), the reflected reactance is negative and fully compensates for the track coil reactance if

$$\frac{\omega M^2}{(L_p+L_1)} = \omega L_t \tag{7.32}$$

From (7.32), the inductance $L_1$ is given by

$$L_1 = -(1-k^2)L_p \tag{7.33}$$

Being $k<1$, eq. (7.33) leads to a negative value of the inductance $L_1$. This means that the compensation can not be achieved with this topology. Note that the required negative reflected reactance can be obtained by using a capacitor in place of the inductance, going back to the previously analyzed CCsp topology.

### 7.3.4 CLsp topology

The CLsp topology is drawn in Fig. 7.8. Unlike CLsp, this topology inserts the capacitor $C$ in series to the pickup coil and the inductor $L_1$ in parallel to the series of $L_p$ and $C$.

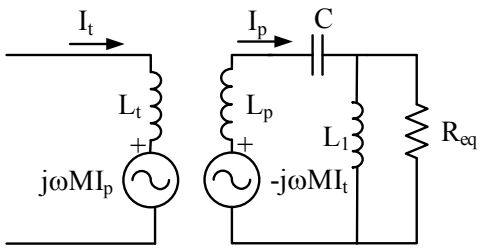


Fig. 7.8. Track coil compensation CLsp.

The impedance of the pickup circuit results in

$$Z_p = j\omega L_p + \frac{1}{j\omega C} + \frac{j\omega L_1 R_{eq}}{R_{eq}+j\omega L_1} \qquad (7.34)$$

and the reflected reactance in

$$Z_{r,CLsp} = \frac{\omega^2 M^2 \omega C\left(R_{eq}+j\omega L_1\right)}{\omega L_1\left(1-\omega^2 L_p C\right)+jR\left\{\omega^2\left(L_p+L_1\right)C-1\right\}} \qquad (7.35)$$

Like for the CCps topology, there are two resonance conditions. If $L_1$ and $C$ are selected according to

$$\omega = \frac{1}{\sqrt{(L_p+L_1)C}} \qquad (7.36)$$

the expression of the reflected impedance in (7.35) simplifies in

$$Z_{r,CLsp,1} = \frac{M^2}{L_1^2}\left(R_{eq} + j\omega L_1\right) \qquad (7.37)$$

The reactance of (7.37) is positive and again the above selection of the values for the inductor and the capacitor does not enable the compensation of the track coil reactance.

Instead, if $C$ is such that

$$\omega = \frac{1}{\sqrt{L_p C}} \qquad (7.38)$$

the reflected impedance, given by

$$Z_{r,CLsp,2} = \frac{\omega M^2}{L_1}\left(\frac{\omega L_1}{R_{eq}} - j\right) \qquad (7.39)$$

has a negative reactance that compensates for the track coil reactance. Full compensation is obtained for

$$\frac{\omega M^2}{L_1} = \omega L_t \qquad (7.40)$$

that yields the following value for the inductor:

$$L_1 = k^2 L_p \qquad (7.41)$$

The value of the capacitor, calculated from (7.38), is

$$C = \frac{1}{\omega^2 L_p} \qquad (7.42)$$

By (7.39), the reflected equivalent resistance is

$$Re\left(Z_{r,CLsp,2}\right) = \frac{\omega^2 M^2}{R_{eq}} \qquad (7.43)$$

Eq. (7.43) indicates that the reflected equivalent resistance is inversely proportional to the equivalent resistance. This means that, for a changing load, the reflexive segmentation may be impaired when the equivalent resistance is low, i.e. at high loads.

## 7.4 Discussion

The outcomes in terms of reflected impedance and reflected equivalent load for the different pickup circuit topologies are summarized in Table 7.2.

The CCsp topology can provide full compensation for the track coil reactance but it could amplify the reflected equivalent resistance up to impair the reflexive segmentation. The capacitors of the topology can be sized to account for this effect but the reflexive segmentation is achieved at the cost of a pickup inductance much greater than the track coil.

The other two-capacitor topology, CCps, exhibits good reflexive properties so that it could be used to enforce segmentation; on the other hand, most of the pickup current does not flow into the equivalent resistance since the parallel branch formed by $C_1$ has a lower impedance. This situation reduces the overall efficiency of the IPT system.

The LCsp topology cannot be used as it would require a negative inductance. Compared to CCsp, the CLsp topology has the advantage of allowing full compensation of the track coil reactance by means of a pickup coil having an inductance comparable with the track coil. However, the reflexive properties are weak for high loads.

From the above considerations, it appears that it is not possible to identify the most convenient topology that joins good reflexive properties with good performance for the IPT system. This suggests that the pickup circuit topology must be tailored on the application.

Table 7.2
Summary of reflected quantities with various topologies.

| Topology | Reflected reactance | Reflected equivalent resistance | Comments |
|---|---|---|---|
| CCsp | $\frac{-\omega^2 M^2}{\left(\omega L_p - \frac{1}{\omega C_1}\right)}$ | $\frac{\omega^3 M^2 C_2}{\left(\omega L_p - \frac{1}{\omega C_1}\right)} R_{eq}$ | Very big pickup coil inductance |
| CCps | $\frac{-\omega M^2}{L_p}\left(\frac{C_1 + C_2}{C_2}\right)$ | $\frac{\omega^2 M^2 C_1}{L_p} R_{eq}$ | Current drawn by $C_1$ reduces efficiency |
| LCsp | $\frac{-\omega M^2}{(L_p + L_1)}$ | $\frac{M^2}{(L_p + L_1)^2} R_{eq}$ | Negative $L_1$ required |
| CLsp | $\frac{-\omega M^2}{L_1}$ | $\frac{\omega^2 M^2}{R_{eq}}$ | High reflected equivalent resistance at high loads |

As an example, the study case of an IPT system reported in Table 7.3 is evaluated, where the equivalent resistance represents an EV battery load. It changes from a minimum to a maximum value during charging [12]. The requirements are to fully compensate for the track coil reactance and, at the same time, to make notably different the track current in coupled and uncoupled conditions. Parameters of the topology components are calculated according to the equations found above. The track coil impedance, i.e. its uncoupled impedance, is

Table 7.3
Circuit parameters.

| Component | Symbol | Value |
|---|---|---|
| Track coil inductance | $L_{tc}$ | 128 µH |
| Coupling coefficient | $k$ | 0.224 |
| Supply frequency | $f$ | 85 kHz |
| Minimum equivalent resistance | $R_{eq,min}$ | 5 Ω |
| Maximum equivalent resistance | $R_{eq,max}$ | 200 Ω |
| Supply voltage of the track coil | $V_{track}$ | 320V |

$$Z_{p,uncoupled} = 0 + j68.36 \qquad (7.44)$$

For a pickup circuit topology able to fully compensate for the track coil reactance, the track coil impedance is given only by the reflected equivalent resistance. The results reported in Table 7.4 show that the CCps topology has the best reflexive properties at high loads. A similar trend is exhibited by the CCsp topology, even if it has a worse behaviour than the CCps topology over the examined range of the equivalent resistance. On the contrary, the CLsp topology has the best reflexive properties at low loads. The relationships between the reflected equivalent resistance and the equivalent resistance are traced in Fig. 7.9 for the different pickup circuit topologies.

Table 7.4
Comparison of reflected equivalent resistance.

| Equivalent resistance (Ω) | Reflected equivalent resistance (Ω) | | | |
|---|---|---|---|---|
| | CCsp | CCps | LCsp | CLsp |
| 5 | 1+j0 | 0.26+j0 | - | 49.44+j0 |
| 10 | 2+j0 | 0.53+j0 | - | 24.72+j0 |
| 50 | 10+j0 | 2.64+j0 | - | 4.94+j0 |
| 100 | 20+j0 | 5.29+j0 | - | 2.47+j0 |
| 200 | 40+j0 | 10.58+j0 | - | 1.24+j0 |

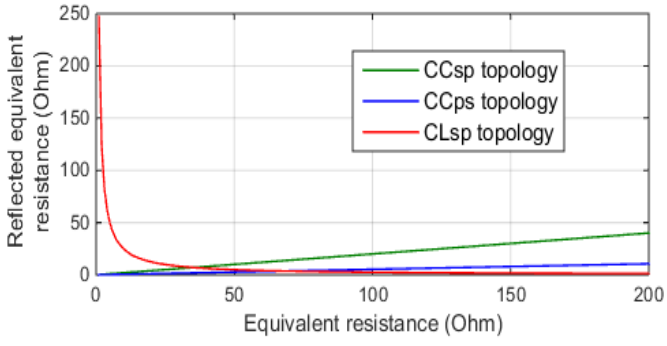


Fig. 7.9. Reflected equivalent resistance vs. equivalent resistance.

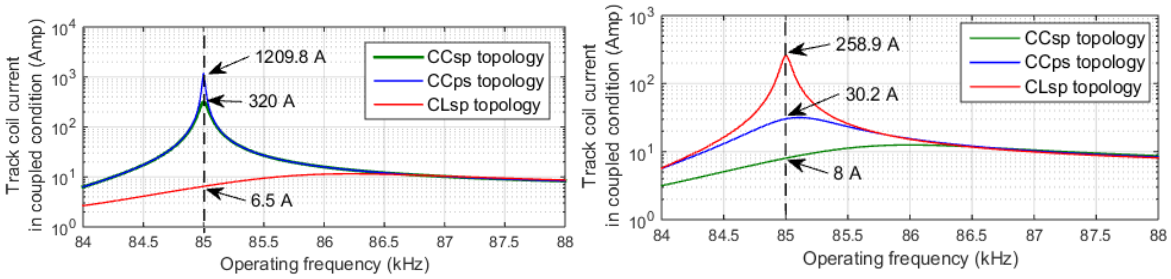


(a) (b)

Fig. 7.10. Coupled track coil current for different pickup circuit topologies a) $R_{eq}$=5Ω and b) $R_{eq}$=200Ω.

Figs. 7.10 (a) and (b) give the track coil current as a function of the supply frequency for the extreme values of the equivalent resistance range, i.e. for 5 and 200 Ω, respectively. In an uncoupled track coil, the current is 3.98 A. In the coupled track coil, the figures confirm the previous findings as the maximum current is attained with the CCps topology at high loads and with the CLsp topology at light loads. Moreover, from Figs. 7.10 (a) and (b), it comes out also that

i) The topologies with the highest reflexive properties are more sensitive to variations in the supply frequency.

ii) Their reflexive properties are significantly reduced if the supply frequency varies of a few percent around the established value.

## 7.5 Conclusion

The chapter has dealt with the issue of implementing the segmentation in a distributed IPT system using the reflexive method. Different two-component topologies for the pickup circuit have been studied and compared with the aim of examining their reflexive properties. Expressions for the capacitive and/or inductive components used in the topologies have been worked out. Impact of the different topologies on the efficiency performance of the IPT system has been also argued.

It has been found that each topology has merits and limits by considering both the reflexive properties and the ensuing efficiency performance. As a result, the most convenient topology has to be tailored on the application. Further to this, a study-case has been considered and the different topologies has been compared, finding out that the CCsp topology prevails at light loads and the CLsp one at high loads.

## References


[1] G.A. Covic and J.T. Boys, “Inductive power transfer”, Proc. of IEEE, vol. 101, no. 6, pp.1276-1289, June 2013.

[2] S. Lukic and Z. Pantic, “Cutting the Cord: static and dynamic inductive wireless charging of electric vehicles”, Proc. of IEEE Electrification Magazine, vol. 1, no. 1, 2013, pp. 57- 64.

[3] J. Li, Q. Yang, H. Chen and J. Wang, “Study and application of contact-less electrical energy transmission system,” Proc. of IEEE Conf. on Vehicle Power and Propulsion, 2008, pp. 1-4.

[4] K.N. Mude, H.K. Dashora, M. Bertoluzzo, and G. Buja, “From Wired to In-Moving Charging of the Electric Vehicles”, Proc. of WSEAS Int. Conf. on Development, Energy, Environment, Economics (DEEE), 2014, pp. 33-42.

[5] S.Y. Choi, B.W. Gu, S.Y. Jeong, and C.T. Rim, “Advances in Wireless Power Transfer Systems for Roadway-powered Electric Vehicles,” IEEE Journal of Emerging and Selected Topics in Power Electronics, Vol. 3, No. 1, pp. 18-36, 2015.

[6] S. Lee, J. Huh, C. Park, N. S. Choi, G. H. Cho, and C. T. Rim, “On-line electric vehicle using inductive power transfer system”, Proc. of IEEE Energy Conversion Congress and Exposition (ECCE), 2010, pp. 1598 – 1601.

[7] J.A. Russer, M. Dionigi, M. Mongiardo, and P. Russer, “A moving field inductive power transfer system for electric vehicles”, Proc. of European Microwave Conference (EuMC), 2013, pp. 519 - 522.

[8] K. Lee, Z. Pantic, and S.M. Lukic, “Reflexive Field Containment in Dynamic Inductive Power Transfer Systems”, *IEEE Transactions on Power Electronics*, vol. 29, no. 9, pp. 4592 – 4602, 2014.

[9] H. Jiang, P. Brazis, M. Tabaddor, and J. Bablo, “Safety considerations of wireless charger for electric vehicles - a review paper,” Proc. of IEEE Symposium on Product Compliance Engineering (ISPCE), 2012, pp. 1-6.

[10] International Commission on Non-Ionizing Radiation Protection (ICNIRP) Guidelines [Online]. Available: www.icnirp.de/documents/emfgdl.pdf

[11] C.S. Wang, O.H. Stielau, and G.A. Covic, “Design Considerations for a Contactless Electric Vehicle Battery Charger,” *IEEE Transactions on Industrial Electronics*, Vol. 52, No. 5, pp. 1308-1314, October 2005.

[12] K.N. Mude, M. Bertoluzzo, and G. Buja, “Design of contactless battery charger for electric vehicle,” Proc. of IEEE AFRICON, 2013, pp. 1099-1104.

# Chapter 8

# Performance Analysis of Reflexive Segmentation Topologies

Track segmentation of the dynamic wireless charging (DWC) systems for electric vehicles is mandatory for efficiency and magnetic field containment purposes. This chapter is concerned with some advanced aspects of the reflexive segmentation of a lumped track, obtained by inserting a compensation network in the pickup. After defining performance figures for the reflexive segmentation, namely segmentation ratio and power transfer efficiency of the WBC system, the limits of the elemental topologies made of one-capacitor compensation networks are reviewed. Then, two enhanced topologies based on dual-capacitor compensation networks are analyzed. It is found that these topologies increase the segmentation ratio but at the price of a low power transfer efficiency just in the range of the load resistance where the segmentation ratio is higher.

## 8.1 Introduction

There are basically two methods to accomplish the segmentation, as exemplified in Figs. 8.1 (a) and (b). One method, designated as centralized, consists in supplying a power line with a single high-frequency (HF) inverter and in connecting a track coil to the line through a switch, turned on when the coupling with a pickup coil is detected. The other method, designated as distributed, consists in supplying each track coil with a distinct HF inverter, turned on when the coupling with a pickup coil is detected. Both these methods have specific shortcomings, the

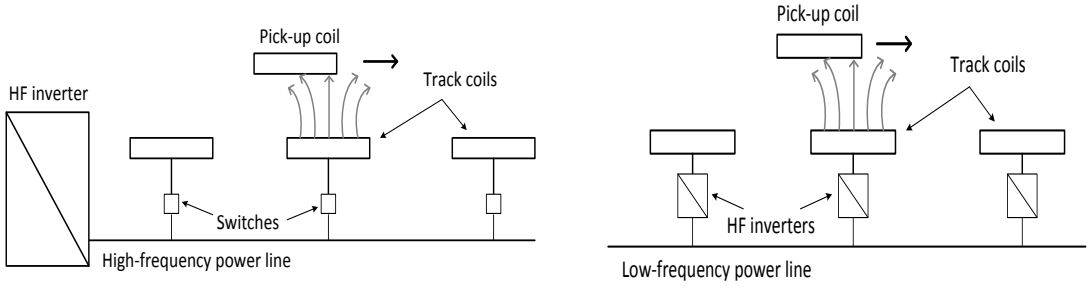


Fig. 8.1. Segmentation methods: a) centralized, b) distributed.

main one is that they require sensors to detect the pickup coil.

An alternative, recently proposed method exploits the fact that the impedance seen from the terminals of a track coil changes due to the reflection of the pickup coil circuit to the track coil. If the impedance is high under uncoupling situations and low under coupling situations, a

partial but satisfactory segmentation is achieved [7]. This method to accomplish segmentation is termed reflexive and utilizes a layout similar to the centralized segmentation method, where the differences are in the absence of any switch to connect the track coil to the line as well as of any sensor to detect the pickup coil. Instead, it makes use of a compensation network inserted in the pickup to maximize the difference in the magnitude of the track coil currents in the two extreme situations of coupled/uncoupled pickup coil.

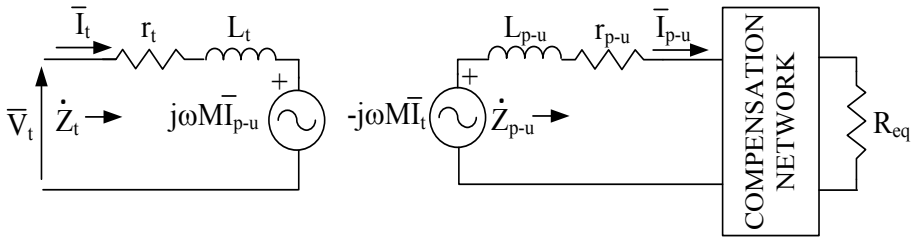


Fig. 8.2. Circuital scheme of coupling between track and pickup coils in a DWC system.

A lumped track made of a number of coils is considered. Each track coil is assumed to be identical to the others and placed at a distance from the other track coils such that their mutual coupling is negligible; moreover, it is assumed that a pickup coil is coupled only with one track coil at a time. Under these assumptions, the circuital scheme of the coupling between a track coil and the pickup coil with compensation network is represented by the circuital scheme of Fig. 8.2, where $\bar{V}_t$ is the sinusoidal voltage supply of the track coil, $L_t$ and $L_{p\text{-}u}$ are the self-inductances of the track and pickup coils, $r_t$ and $r_{p\text{-}u}$ are their parasitic resistances, $\bar{I}_t$ and $\bar{I}_{p-u}$ are the currents flowing through the coils, and $R_{eq}$ is the equivalent load resistance, i.e. the battery voltage/current ratio modified by the operation of the diode rectifier and the chopper, if any, interposed between the compensator network and the battery [9]. The angular frequency of $\bar{V}_t$ is $\omega=2\pi f$, with $f$ of some tens of kHz. In order not to impair the efficiency of the DWC system, only compensation networks of reactive type are used.

When a pickup coil is coupled to one of the track coils, the impedance of the pickup coil reflects into the track coil. Induced voltage in both coils depends on their mutual inductance $M$

$$M = k\sqrt{L_t L_{p-u}} \qquad (8.1)$$

where $k$ is the coupling coefficient. While EV is moving over a track coil, $k$ changes from 0 (uncoupled conditions) to $k_M$ (fully coupled conditions); note that $k_M$ is much smaller than 1 due to the large airgap existing between the two coils.

The current flowing in a track coil is

$$\bar{I}_t = \frac{\bar{V}_t}{\dot{Z}_t} \qquad (8.2)$$

where $\dot{Z}_t$ is the impedance seen from the track coil terminals. In uncoupling conditions, $\dot{Z}_t$ is equal to $r_t + j\omega L_t$ and the relevant track coil current is denoted with $\bar{I}_{t,nc}$. In coupling conditions, $\dot{Z}_t$ is modified by the reflected impedance $\dot{Z}_{ref}$ of the pickup coil, given by

$$\dot{Z}_{ref} \triangleq R_{ref} + jX_{ref} = \frac{\omega^2 M^2}{\dot{Z}_{p-u}} \qquad (8.3)$$

where $\dot{Z}_{p-u}$ is the pickup impedance and encompasses the coil impedance, the reactance of the compensation network and the equivalent load resistance. Then, $\dot{Z}_t$ becomes

$$\dot{Z}_t = r_t + j\omega L_t + \dot{Z}_{ref} \qquad (8.4)$$

and the relevant track coil current is denoted with $\bar{I}_{t,c}$.

## 8.2 Performance figures

The segmentation ratio *SR* of the DWC system is defined as

$$SR \triangleq \frac{|\bar{I}_{t,c}|}{|\bar{I}_{t,nc}|} \qquad (8.5)$$

By (8.2) and (8.3), it can expressed as

$$SR = \frac{|r_t + j\omega L_t|}{|r_t + j\omega L_t + \dot{Z}_{ref}|} \cong \frac{\omega L_t}{|r_t + j\omega L_t + \dot{Z}_{ref}|} \qquad (8.6)$$

where the last approximation is quite accurate since, in practice, it is $r_t \ll \omega L_t$ To obtain a satisfactory segmentation, *SR* must be somewhat higher than 1. From (8.6) it emerges that a condition to reach this objective consists in fully compensating for the track coil reactance by means of $X_{ref}$.

For the purpose of this analysis, efficiency of the power transfer of the DWC system is considered. It is denoted with $\eta_{pt}$ and is defined as

$$\eta_{pt} = \frac{P_{p-u}}{P_s} \qquad (8.7)$$

where $P_{p\text{-}u}$ is the power transferred from the track to pickup coil and $P_s$ is the power supplied to the track coil. In terms of circuit quantities, (8.7) is expressed as

$$\eta_{pt} = \frac{R_{ref}}{r_t + R_{ref}} \qquad (8.8)$$

## 8.3 Elemental compensation networks

Elemental compensation networks for the pickup coil as discussed in the previous chapter, are made of one capacitor connected either in parallel or in series to $R_{eq}$, as drawn in Figs. 7.3(a) and (b) in chapter 7 and [10]-[12].

Parallel capacitor Let parallel capacitor $C_p$ in Fig. 7.3(a) be sized to resonate with $L_{p\text{-}u}$ at the supply angular frequency $\omega$. The reflected impedance of the pickup circuit, calculated by neglecting $r_{p\text{-}u}$, is

$$\dot{Z}_{ref,p} = \frac{M^2}{L_{p-u}^2} R_{eq} - j\frac{\omega M^2}{L_{p-u}} \qquad (8.9)$$

Eq. (8.9) shows that the reactive part is negative and independent of $R_{eq}$; therefore it can fully compensate for the track coil reactance if

$$\frac{M^2}{L_{p-u}} = L_t \qquad (8.10)$$

Eq. (8.10) is satisfied only for $k$=1, circumstance that is far from being met in a loosely coupling application like the DWC systems.

Series capacitor Let series capacitor $C_s$ in Fig. 8.3(b) be sized to resonate with $L_{p\text{-}u}$ at the supply angular frequency $\omega$. The pickup reactance becomes zero and, hence, there is no chance to compensate for the track coil reactance.

As a result, the one-capacitor compensation networks are not suitable for the reflexive segmentation. Hence, there is the need of evaluating compensation networks with enhanced topology made of two capacitors connected either in series-parallel (SP) or in parallel-series (PS) to $R_{eq}$. They give rise to the SP and PS topology, respectively. As a recap, four compensation networks have been discussed in the previous chapter, and two out of them are dual capacitor topologies. The SP and PS topologies basically resemble CCsp and CCps topologies out of them, which are more analyzed in this chapter with their performance figures.

## 8.4 SP topology

This section evaluates the performance of the SP topology, at first by neglecting $r_{p\text{-}u}$ to appreciate separately the effect of each parasitic resistance on the performance figures.

The circuital scheme of the SP topology is drawn in Fig. 8.3. Let capacitor $C_p$ resonate with the fraction $L'_{p-u}$ of $L_{p\text{-}u}$ and capacitor $C_s$ with the remaining fraction of $L_{p\text{-}u}$. Eq. (8.10) becomes.

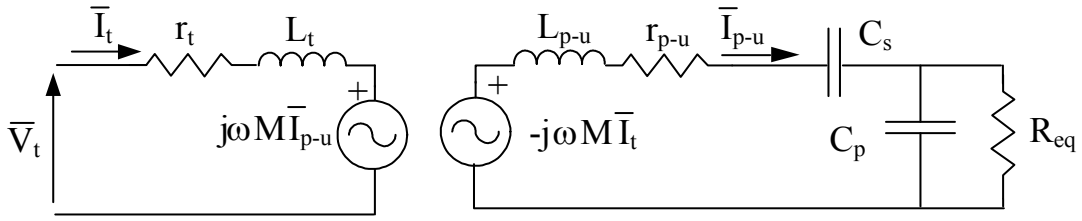


Fig. 8.3. SP topology for the pickup compensation network.

$$\frac{M^2}{L'_{p-u}} = L_t \qquad (8.11)$$

and the track coil reactance is fully compensated, provided that

$$L'_{p-u} = k_0^2 L_{p-u} \qquad (8.12)$$

where $k_0$ is the coupling coefficient around which the DWC system is designed. Settings above are achieved by selecting $C_p$ and $C_s$ as follows:

$$\omega^2 L'_{p-u} C_\mathrm{p} = 1 \;\rightarrow\; C_p = \frac{1}{\omega^2 k_0^2 L_{p-u}} \qquad (8.13)$$

$$\omega^2 \left(L_{p-u} - L'_{p-u}\right) C_\mathrm{s} = 1 \;\rightarrow\; C_s = \frac{1}{\omega^2 \left(1-k_0^2\right) L_{p-u}} \qquad (8.14)$$

An interesting side result of the capacitor selection in (8.13) and (8.14) is

$$\frac{C_p C_s}{C_p + C_s} = \frac{1}{\omega^2 L_{p-u}} \qquad (8.15)$$

which means that $L_{p-u}$ resonates with the series of $C_p$ and $C_s$.

Neglecting $r_{p-u}$ The reflected impedance of the pickup circuit is

$$\dot{Z}_{ref,sp} = \frac{\omega^2 M^2 j\omega C_s \left(1 + j\omega C_p R_{eq}\right)}{1 - \omega^2 L_{p-u} C_s + j\omega R_{eq}\left(C_p + C_s - \omega^2 L_{p-u} C_p C_s\right)} \qquad (8.16)$$

By (8.13) and (8.14), eq. (8.16) can be rewritten as

$$\dot{Z}_{ref,sp} = \left(\frac{1}{k_0^2}\frac{L_t}{L_{p-u}}\right) R_{eq} - j\omega L_t \qquad (8.17)$$

Eq. (8.17) points out that the SP topology amplifies the equivalent load resistance as seen from the track coil terminals since $k_0$ is much lower than 1. According to (8.6) and (8.8), this effect helps reaching a higher efficiency at the cost of a lower segmentation ratio.

The graphs of *SR* and $\eta_{pt}$ are traced in Fig. 8.4 as a function of $R_{eq}$ normalized to $\omega L_{p-u}$ ($R_{eq,n}$), for $k_0$=0.25 and for three values of $r_t$ normalized to $\omega L_t$ ($r_{t,n}$). Note that the normalized

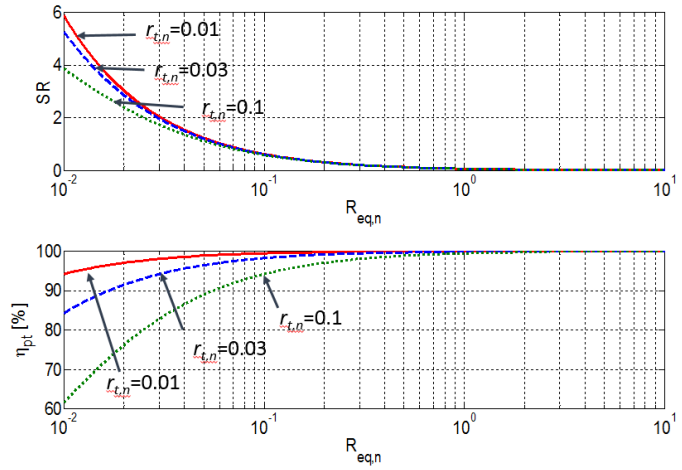


Fig. 8.4. *SR* and $\eta_{pt}$ vs. $R_{eq,n}$ for SP topology for $r_{t,n}$=0.01 (solid red line), $r_{t,n}$=0.03 (dashed blue line) and $r_{t,n}$=0.1 (dotted green line).

quantities are the inverse of the quality factors of the track and pickup coils and, usually, are quite less than 1. The interval 0.01-10 is taken for the horizontal axis as it includes the typical ranges of variation of $R_{eq,n}$. The graphs confirm that reaching high values of $\eta_{pt}$ opposes to the achievement of high values of *SR* and underline that both the performance figures are negatively affected by an increase in $r_{t,n}$. Moreover, the graphs show that, in most of the $R_{eq,n}$ interval, *SR* is lower than 1, which does not allow for any segmentation. Only if $R_{eq,n}$ is lower than about 0.03, *SR* exceeds 2, which is anyway a poor segmentation ratio. For low values of $R_{eq,n}$, the power transfer efficiency is rather sensitive to $r_{t,n}$, decreasing from 98% to about 82% for $R_{eq,n}$=0.03.

Including $r_{p\text{-}u}$ The reflected impedance takes on the following, more complex expression:

$$\dot{Z}_{ref,sp} = \frac{\omega^2 M^2 j\omega C_s(1+j\omega C_p R_{eq})}{1-\omega C_s(\omega L_{p-u}-jr_{p-u})+j\omega R_{eq}[C_p+C_s-\omega C_p C_s(\omega L_{p-u}-jr_{p-u})]} \qquad (8.18)$$

By substituting (8.13) and (8.14) for $C_p$ and $C_s$, the reflected impedance of the pickup circuit becomes

$$\dot{Z}_{ref,sp} = \frac{\frac{R_{eq}}{k_0^2}\frac{L_t}{L_{p-u}}\left[1+\frac{r_{p-u}}{(\omega L_{p-u})^2}\frac{R_{eq}}{k_0^4}+\frac{r_{p-u}}{R_{eq}}\right]-j\omega L_t}{\left[1+\frac{r_{p-u}}{(\omega L_{p-u})^2}\frac{R_{eq}}{k_0^4}\right]^2+\left(\frac{r_{p-u}}{k_0^2\omega L_{p-u}}\right)^2} \qquad (8.19)$$

Inspection of (8.19) reveals that, differently from (8.17), the resistive component of $\dot{Z}_{ref,sp}$ is no more linearly dependent on $R_{eq}$ and the reactive component is no more independent on $R_{eq}$, both the effects being due to the product $r_{p\text{-}u}R_{eq}$ in the denominator. Fig. 8.5 explicates

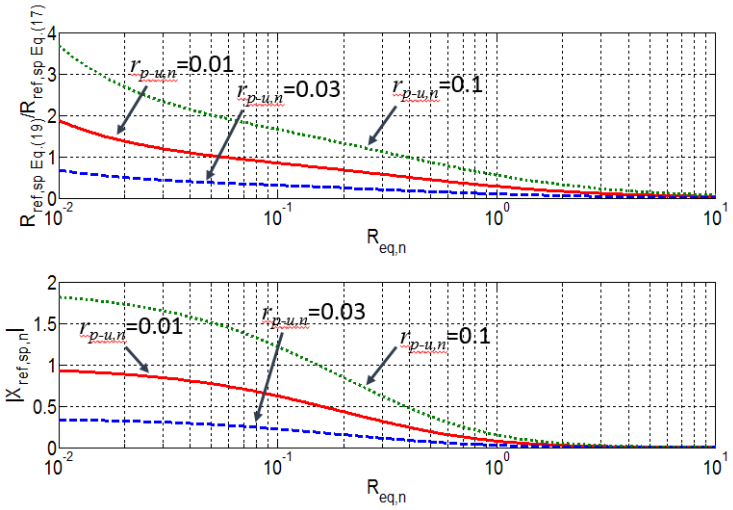


Fig. 8.5. $R_{ref,sp,n}$ ratio and $|X_{ref,sp,n}|$ vs. $R_{eq,n}$ for SP topology with $r_{pu,n}$=0.01 (solid red line), $r_{pu,n}$=0.03 (dashed blue line) and $r_{pu,n}$=0.1 (dotted green line).

the dependences. The upper diagram reports the reflected resistance ratio (*RRR*), given by the ratio between the reflected resistance in (8.19) and that one in (8.17). The graphs, drawn for $k_0$=0.25, show that RRR turns out to be much smaller than in the case of neglecting $r_{p\text{-}u}$, especially for the highest values of both $R_{eq,n}$ and $r_{p\text{-}u,n}$. According to (8.6) and (8.8), this decrease leads to an increase in SR and to a decrease of $\eta_{pt}$. On the contrary, for low values of $R_{eq,n}$, non-small values of $r_{p\text{-}u,n}$ increase RRR so that an higher $\eta_{pt}$ is achieved at the expenses of a lower SR. The lower diagram of Fig. 8.5 reports the absolute value of the reflected reactance normalized to $\omega_{Lt}$. This quantity, denoted as $X_{ref,sp,n}$, is lower than 1 for higher values of $R_{eq,n}$ where the RRR is low, so that the condition of the full compensation for the track coil reactance cannot be achieved.

Impact of $r_{p\text{-}u}$ on *SR* and $\eta_{pt}$ is illustrated in Fig. 8.6, where equal normalized values are taken for both $r_{p\text{-}u}$ and $r_t$. The upper diagram shows that, for low values of $R_{eq,n}$, *SR* is one half than in Fig. 8.4; this is a consequence of the fact that the RRR in Fig. 8.5 exceeds 1. For high values of $R_{eq,n}$, RRR is smaller than 1 but the reflected reactance decreases substantially so that an effective segmentation cannot be achieved. The lower diagram of Fig. 8.6 shows that the impact of $r_{p\text{-}u,n}$ on $\eta_{pt}$ is the opposite of that on *SR*: when $R_{eq,n}$ is high, $\eta_{pt}$ becomes lower than in Fig. 8.4 and decreases as $r_{p\text{-}u}$ increases; when $R_{eq,n}$ is low, $\eta_{pt}$ becomes higher and higher as $r_{p\text{-}u}$ increases. Fig. 8.6 outlines that the SP topology does not allow the simultaneous achievement of high values for both SR and $\eta_{pt}$.

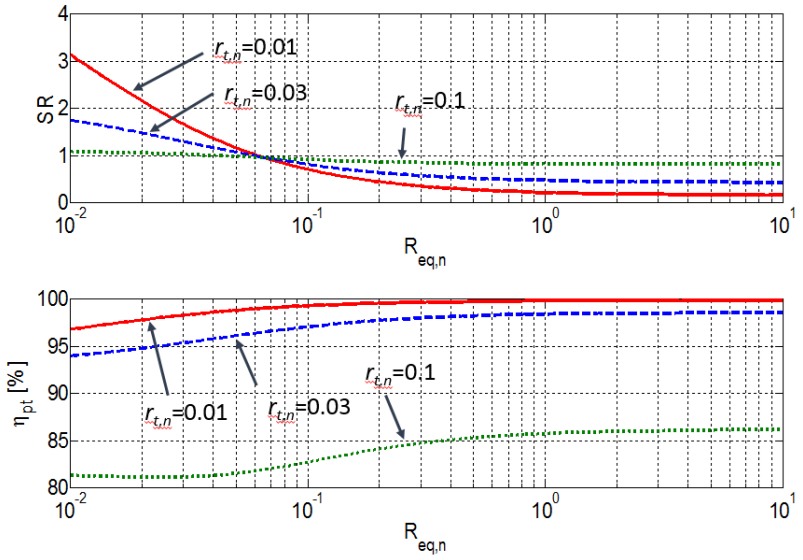


Fig. 8.6. *SR* and $\eta_{pt}$ vs. $R_{eq,n}$ for SP topology with $r_{p\text{-}u,n} = r_{t,n}$ =0.01 (solid red line), $r_{p\text{-}u,n} = r_{t,n}$ =0.03 (dashed blue line) and $r_{p\text{-}u,n} = r_{t,n}$ =0.1 (dotted green line).

## 8.5 PS topology

This Section derives the performance of the PS topology. Its circuital scheme, drawn in Fig. 8.7, shows that now capacitor $C_p$ is connected in parallel to the $C_s$-$R_{eq}$ branch.

Neglecting $r_{p\text{-}u}$ The impedance reflected to the track coil is

$$\dot{Z}_{ref,ps} = \frac{\omega^2 M^2 [j\omega(C_p+C_s)-\omega^2 C_p C_s R_{eq}]}{1-\omega^2 L_{p-u}(C_p+C_s)+j\omega R_{eq} C_s (1-\omega^2 L_{p-u} C_p)} \quad (8.20)$$

Reflected reactance is made independent from $R_{eq}$ by selecting $C_p$ so that it resonates with the pickup coil inductance at the supply frequency, i.e.

$$\omega^2 L_{p-u} C_p = 1 \rightarrow C_p = \frac{1}{\omega^2 L_{p-u}} \quad (8.21)$$

Under this condition, the reflected impedance results in

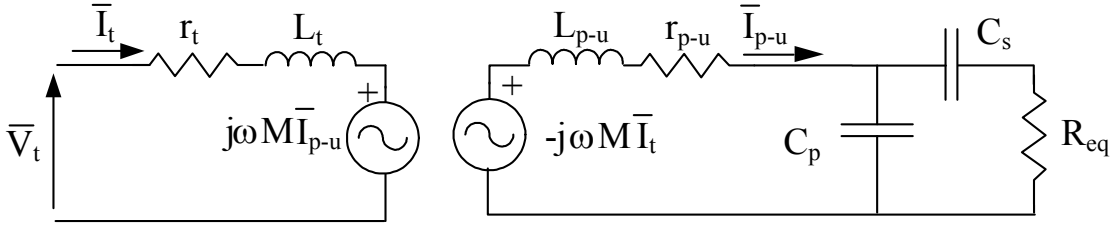


Fig. 8.7. PS topology for the pickup compensation network.

$$\dot{Z}_{ref,ps} = \left(k_0^2 \frac{L_t}{L_{p-u}}\right) R_{eq} - j\omega L_t k_0^2 \left(\frac{1+\omega^2 L_{p-u} C_s}{\omega^2 L_{p-u} C_s}\right) \qquad (8.22)$$

The impedance has a negative reactance that fully compensates for the track coil reactance if

$$k_0^2 \left(\frac{1+\omega^2 L_{p-u} C_s}{\omega^2 L_{p-u} C_s}\right) = 1 \;\rightarrow\; C_s = \frac{1}{\omega^2 L_{p-u}} \frac{k_0^2}{1-k_0^2} \qquad (8.23)$$

It is worth to notice that the ratio of $C_s$ to $C_p$, as obtained from (8.21) and (8.23) and given in (8.24), is the same that comes out from (8.13) and (8.14).

$$\frac{C_s}{C_p} = \frac{k_0^2}{1-k_0^2} \qquad (8.24)$$

Eq. (8.22) shows that the PS topology exerts an attenuation of the reflected resistive component. For low values of $R_{eq}$ this attenuation helps in reaching high values of SR but concurrently reduces $\eta_{pt}$, as shown in Fig. 8.8. For instance, let us compare the performance of the two compensation topologies at $R_{eq,n}$=0.1: by the SP topology, $\eta_{pt}$ exceeds 99% while SR is only 0.6, i.e. no reflexive segmentation is achieved; instead, by the PS topology, $\eta_{pt}$ is only 39% while SR reaches 61.

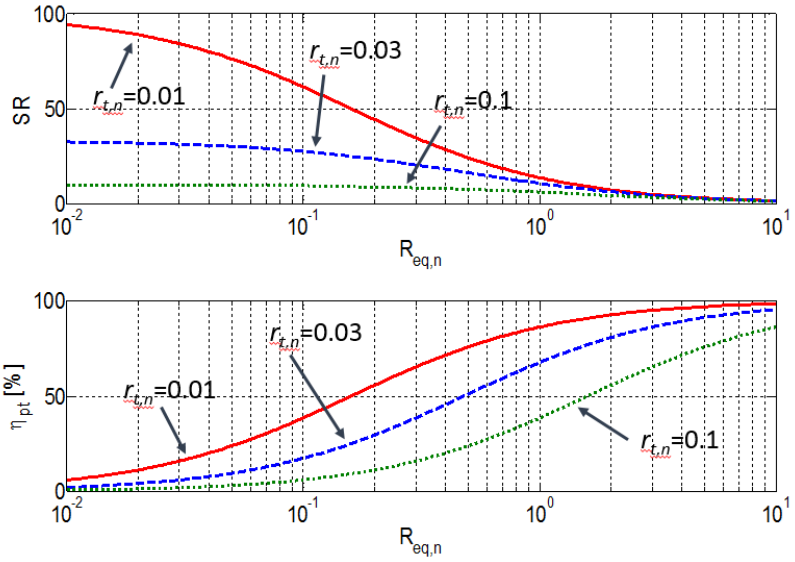


Fig. 8.8. *SR* and $\eta_{pt}$ vs. $R_{eq,n}$ for PS topology with $r_{t,n}$=0.01 (solid red line), $r_{t,n}$=0.03 (dashed blue line) and $r_{t,n}$=0.1 (dotted green line).

Including $r_{p-u}$ The reflected impedance of the pickup circuit is

$$\dot{Z}_{ref,ps} = \frac{\omega^2 M^2 [j\omega(C_p+C_s) - \omega^2 C_p C_s R_{eq}]}{1-\omega(C_p+C_s)(\omega L_{p-u} 1 - j r_{p-u}) + j\omega R_{eq} C_s [1-\omega C_p(\omega L_{p-u} - j r_{p-u})]} \qquad (8.25)$$

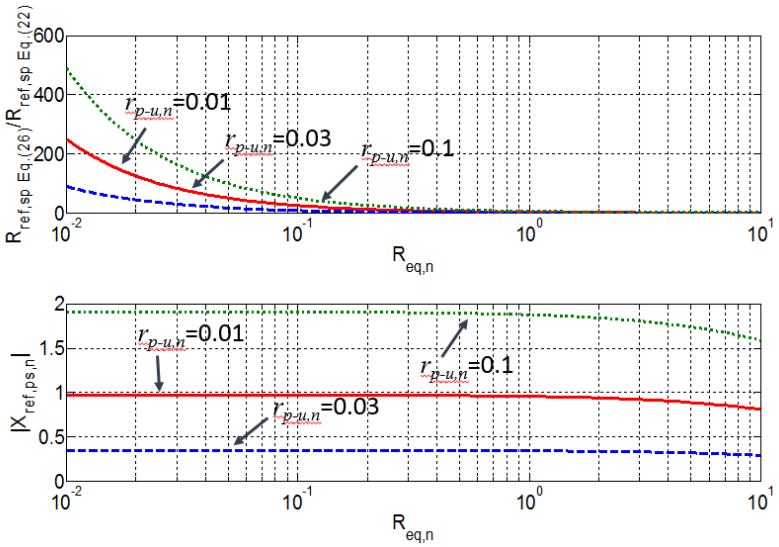


Fig. 8.9. $R_{ref,ps,n}$ and of $|X_{ref,ps,n}|$ vs. $R_{eq,n}$ for PS topology with $r_{pu,n}$=0.01 (solid red line), $r_{pu,n}$=0.03 (dashed blue line) and $r_{pu,n}$=0.1 (dotted green line).

By substituting (8.21) and (8.23) for $C_p$ and $C_s$, the reflected impedance of the pickup circuit becomes

$$\dot{Z}_{ref,ps} = \frac{k_0^2 R_{eq} \frac{L_t}{L_{p-u}} \left[1+\frac{r_{p-u} R_{eq}}{(\omega L_{p-u})^2}+\frac{r_{p-u}}{k_0^4 R_{eq}}\right] - j\omega L_t}{\left[1+\frac{r_{p-u} R_{eq}}{(\omega L_{p-u})^2}\right]^2 + \left(\frac{r_{p-u}}{k_0^2 \omega L_{p-u}}\right)^2} \qquad (8.26)$$

Effect of $r_{p\text{-}u}$ on resistance and modulus of the reactance of the reflected impedance is illustrated in Fig. 8.9. The graphs show that the reflected resistance with the PS topology is very sensitive to the presence of $r_{p\text{-}u}$. Indeed, for low values of $R_{eq}$, even for $r_{p\text{-}u,n}$=0.01, RRR is more than 200 times higher than when $r_{p\text{-}u}$ was neglected; in the same conditions, RRR was less than 2 with the SP topology. On the contrary, the presence of $r_{p\text{-}u}$ has a limited effect on the reflected reactance; for example, for $r_{p\text{-}u,n}$=0.01, the reflected reactance is nearly unaffected by $r_{p\text{-}u}$, being about 95% of $\omega L_t$ up to $R_{eq,n}$=1 while with the SP topology it was dropped at 8% of $\omega L_t$.

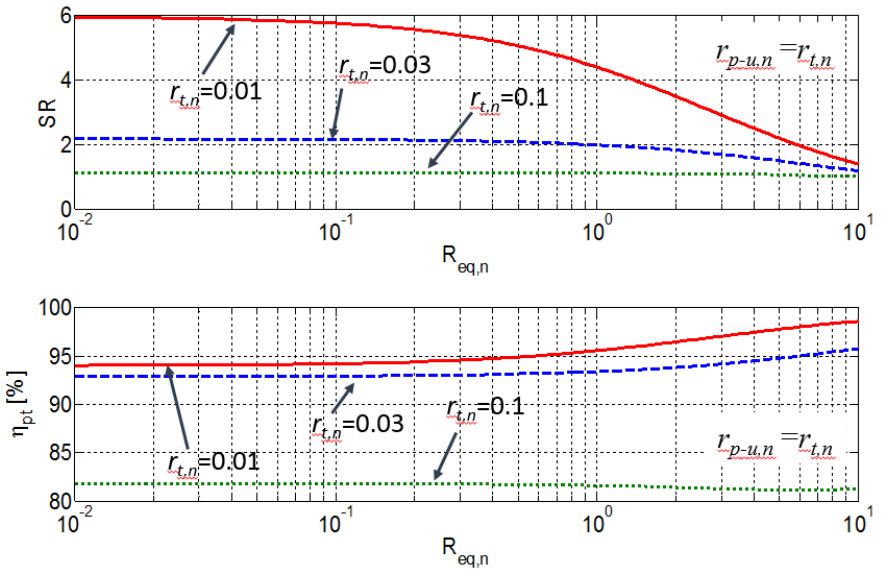


Fig. 8.10. *SR* and $\eta_{pt}$ vs. $R_{eq,n}$ for PS topology with $r_{p\text{-}u,n}$= $r_{t,n}$=0.01 (solid red line), $r_{p\text{-}u,n}$=$r_{t,n}$=0.03 (dashed blue line) and $r_{p\text{-}u,n}$= $r_{t,n}$ =0.1 (dotted green line).

Impact of $r_{p\text{-}u}$ on SR and $\eta_{pt}$ is illustrated in Fig. 8.10, where equal normalized values are taken for both $r_{p\text{-}u}$ and $r_t$. The graphs show that $r_{p\text{-}u}$ has a noticeable impact on SR, which is reduced to a few units all along the interval of $R_{eq,n}$. Instead, for low values of $R_{eq,n}$, quantity $\eta_{pt}$ increases when considering $r_{p-u}$. It worth to note that this does not mean that the total efficiency of the DWC system increases. Indeed, $\eta_{pt}$ does not include the pickup efficiency, i.e. the ratio between the power delivered to $R_{eq}$ and the power transferred to the pickup coil, which clearly is impaired by $r_{p-u}$. Fig. 8.10 outlines that also the PS topology does not allow the simultaneous achievement of high values for both SR and $\eta_{pt}$.

## 8.6 Coupling coefficient variation

Coupling coefficient $k$ depends on the relative position of the track and pickup coils and has a periodical behavior while the vehicle moves along the track. As a consequence, since $C_p$ and $C_s$ have been designed for a given value of $k_0$, SR and $\eta_{pt}$ change along the track.

The reflected impedances of the pickup with either SP or PS topology for a generic value of $k$ are proportional to (8.19) and (8.26), according to

$$\dot{Z}_{ref,sp} = \frac{k^2}{k_0^2} \frac{\frac{R_{eq}}{k_0^2}\frac{L_t}{L_{p-u}}\left[1+\frac{r_{p-u}}{(\omega L_{p-u})^2}\frac{R_{eq}}{k_0^4}+\frac{r_{p-u}}{R_{eq}}\right]-j\omega L_t}{\left[1+\frac{r_{p-u}}{(\omega L_{p-u})^2}\frac{R_{eq}}{k_0^4}\right]^2+\left(\frac{r_{p-u}}{k_0^2\omega L_{p-u}}\right)^2} \qquad (8.27)$$

$$\dot{Z}_{ref,ps} = \frac{k^2}{k_0^2} \frac{k_0^2 R_{eq} \frac{L_t}{L_{p-u}} \left[1 + \frac{r_{p-u}}{(\omega L_{p-u})^2} R_{eq} + \frac{r_{p-u}}{k_0^4 R_{eq}}\right] - j\omega L_t}{\left[1 + \frac{r_{p-u}}{(\omega L_{p-u})^2} R_{eq}\right]^2 + \left(\frac{r_{p-u}}{k_0^2 \omega L_{p-u}}\right)^2} \qquad (8.28)$$

Eqs. (8.28) and (8.28) point out that the track coil is over-compensated when the actual value of $k$ is greater than $k_0$ so that the reactance seen at the track coil terminals is capacitive; instead, when the actual value of $k$ is lower than $k_0$, compensation is not complete and the reactance is inductive.

The change of impedance affects $SR$ and $\eta_{pt}$ of both the SP and PS topologies, as shown in Figs. 8.11 and 8.12, respectively. The graphs are plotted by setting $r_{t,n}$=$r_{p\text{-}u,n}$=0.01 and by designing $C_p$ and $C_s$ for $k_0$=0.25; then two different values have been taken for $k$, namely 0.15 and 0.35. SR of the two topologies is adversely affected by both the increase and the decrease of $k$ since in both the cases the reactance of the track coil is not exactly compensated. On the contrary, $\eta_{pt}$ is not influenced by the reactive component of the reflected impedance whilst, for $k>k_0$, it takes advantage of the increased reflected resistance, reaching higher values; the opposite occurs for $k<k_0$.

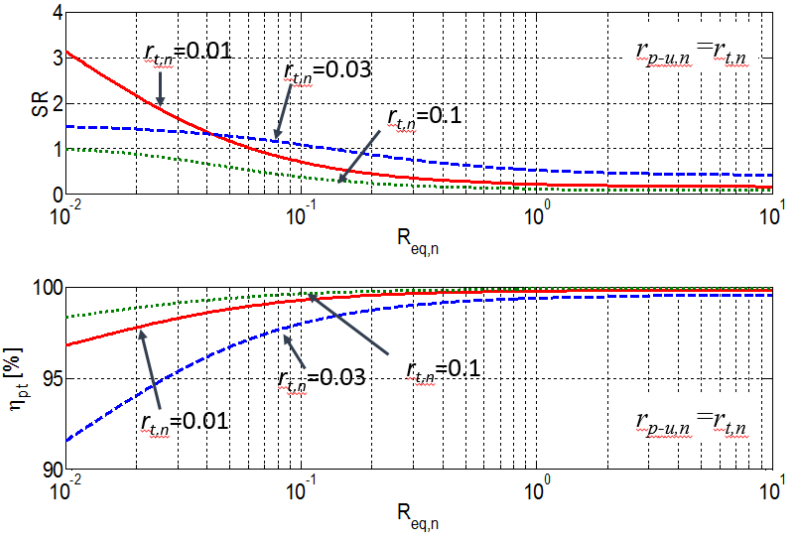


Fig. 8.11. $SR$ and $\eta_{pt}$ vs. $R_{eq,n}$ for SP topology with $r_{p\text{-}u,n}$ =$r_{t,n}$ =0.01 and $k$= 0.25(solid red line), $k$=0.15 (dashed blue line) and $k$=0.35 (dotted green line).

Examination of (8.27) and (8.28) reveals that the expression of the reflected impedance for the SP and PS topologies is exactly the same, provided that $k_0^2 R_{eq,n}$ is substituted for by $R_{eq,n}/k_0^2$. In other terms, the following relations holds:

$$SR_{ps}(R_{eq,n}) = SR_{sp}(k_0^4 R_{eq,n}) \qquad (8.29)$$

$$\eta_{pt,ps}(R_{eq,n}) = \eta_{pt,sp}(k_0^4 R_{eq,n}) \qquad (8.30)$$

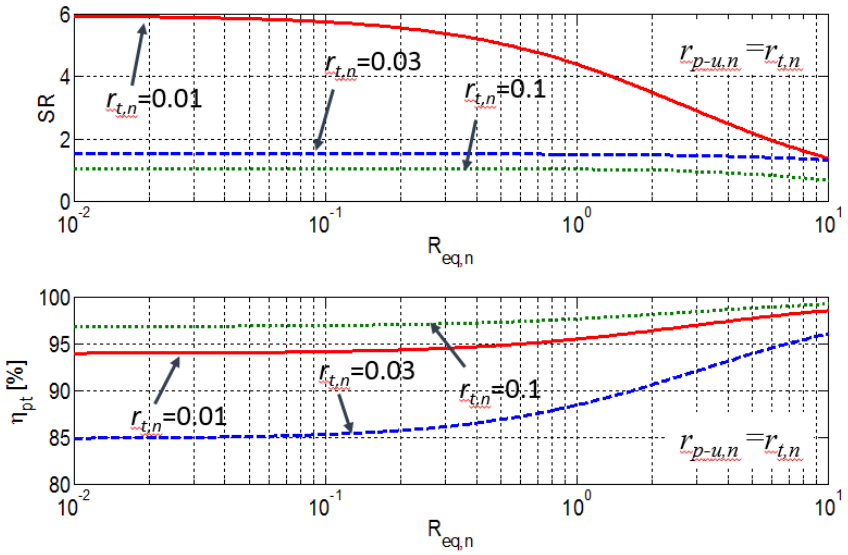


Fig. 8.12. *SR* and $\eta_{pt}$ vs. $R_{eq,n}$ for PS topology with $r_{p\text{-}u,n}$ =$r_{t,n}$=0.01 and $k$= 0.25 (solid red line), $k$=0.15 (dashed blue line) and $k$=0.35 (dotted green line).

The two relations are exemplified in Fig. 8.13, where the interval of $R_{eq,n}$ is extended from $10^{-4}$ to $10^{2}$ to highlight this outcome. From the figure, it clearly appears that SR and $\eta_{pt}$ relevant to one topology are obtained by translating along the $R_{eq,n}$ axis the corresponding quantities relevant to the other topology. As $k_0$ increases, the graphs shift closer each other up to merge when $k_0$=1. This result is easily explained by observing that, when $k_0$ approaches unity, according to (8.14) and (8.23), capacitor $C_s$ behaves like a short circuit and both the SP and PS topologies come down to the parallel compensation drawn in Fig. 7.3(b).

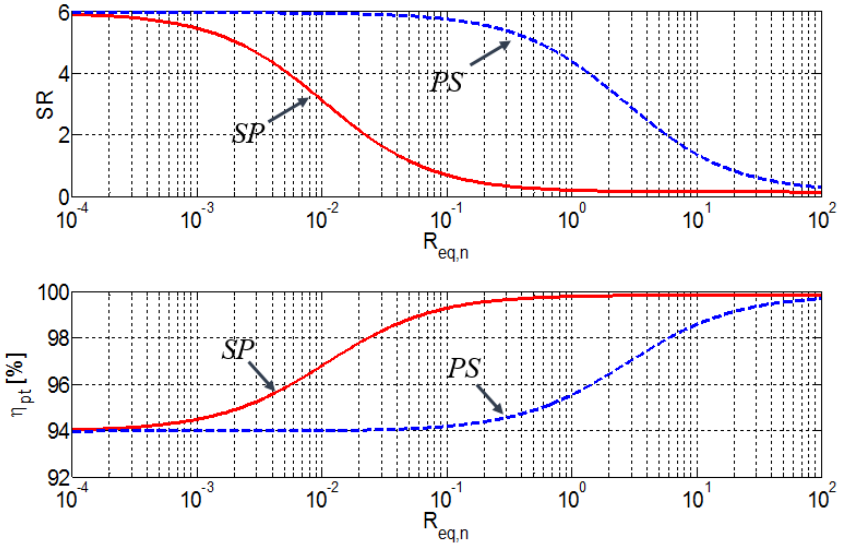


Fig. 8.13. *SR* and $\eta_{pt}$ vs. $R_{eq,n}$ for SP (solid red line) and PS (dashed blue line) topology with $r_{p\text{-}u,n}$=$r_{t,n}$=0.01 and $k$=0.25.

## 8.7 Three Element Compensation

Performance analysis of two element compensation topologies has been illustrated about which indicates inadequacy to achieve reflexive segmentation with a desired ebullition. Therefore a scope to accomplish it, needs to be explored with three or more element compensation. Fig. 8.14 reports two topologies which employ an extra inductor with SP and PS topologies discussed above, and can be called CCL topology.

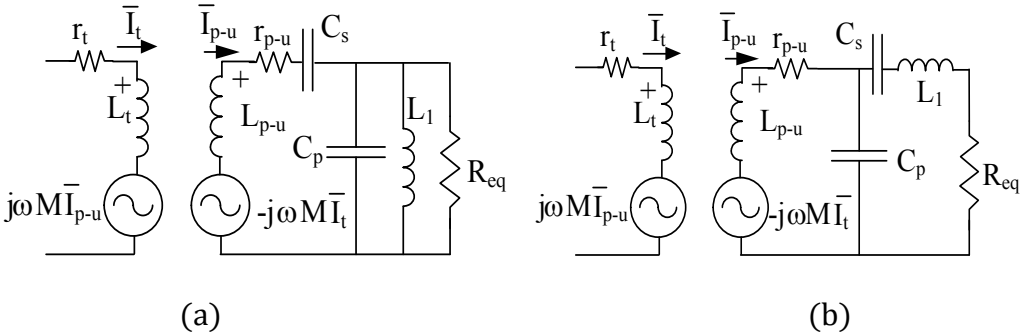


Fig. 8.14. Three element compensation topologies.

Looking at Fig. 8.14(b), it can be observed that the branch having a series combination of $C_s$ and $L_1$, holds a reactance. Based on sign of reactance it simply resembles to a $CC_{ps}$ or $CL_{sp}$ topology discussed in Chapter 7. Thus the circuits shown in Fig. 8.14(b) is not being discussed here. The pickup circuit shown in Fig. 8.14(a) is composed with a three element compensation topology where a capacitor $C_s$ is connected in series with the pickup coil and a parallel connected pair of capacitor, inductor is connected in parallel with the battery equivalent resistance $R_{eq}$.

Let's consider a situation when $C_s$ is designed to resonate with the coil inductance $L_{eq}$ then

$$\omega^2 L_{p\_u} C_s = 1 \qquad (8.31)$$

where ω is supply frequency. In that case, while neglecting the coil resistance, pickup impedance can be written as

$$Z_{p\_u} = \frac{j\omega L_1 R_{eq}}{R_{eq}(1-\omega^2 L_1 C_p)+j\omega L_1} \qquad (8.32)$$

and reflected impedance in the coupled track coil would be

$$Z_{ref} = \frac{\omega^2 M^2}{R_{eq}} - \frac{\omega M^2}{L_1}(1-\omega^2 L_1 C_p) \qquad (8.33)$$

Here in (8.33), one thing can be observed if $C_p$ and $L_1$ resonate with each other, then their branch impedance becomes infinity and only real part of the reflected impedance appear

in the track circuit. This is the same situation when an elementary series compensated pickup is coupled with a track coil.

Full compensation of the track reactance with this circuit can be achieved if

$$\frac{\omega M^2}{L_1}\left(1-\omega^2 L_1 C_p\right)=\omega L_t$$

which leads to a relation

$$L_1=\left(\frac{k^2}{1+k^2\omega^2 L_{p\_u} C_p}\right)L_{p\_u} \qquad (8.34)$$

and if $C_p$ is also tuned such that $\omega^2 L_{p\text{-}u} C_p$=1, then

$$L_1=\left(\frac{k^2}{1+k^2}\right)L_{p\_u} \qquad (8.35)$$

The value of extra inductor is very small in comparison of a pickup coil, therefore copper losses in $L_1$ can be also assumed small enough to be neglected. For better evaluation of the topology, the same performance figures SR and efficiency have been plotted in Fig. 8.15, neglecting the parasitic resistance of pickup coil.

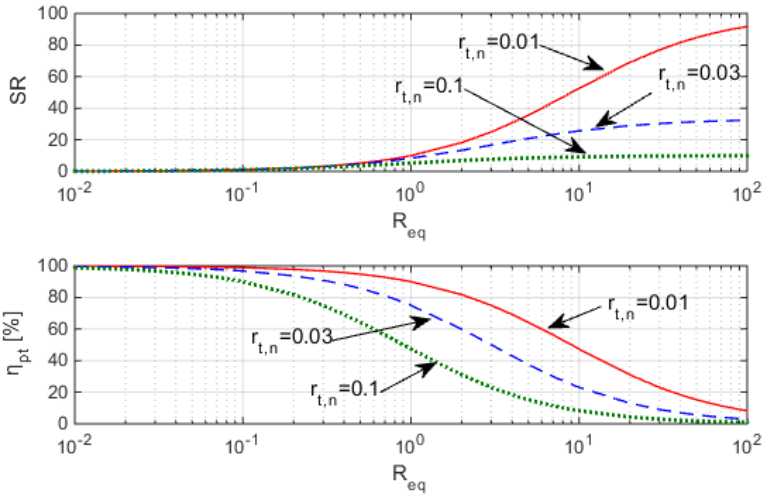


Fig. 8.15. *SR* and $\eta_{pt}$ vs. $R_{eq,n}$ for CCL topology with $r_{t,n}$=0.01 (solid red line), $r_{t,n}$=0.03 (dashed blue line) and $r_{t,n}$=0.1 (dotted green line).

Fig. 8.15 depicts that CCL topology cause very good efficiency at lower values of $R_{eq}$ but SR is too low to be accepted, and for higher values of $R_{eq}$ the properties of $\eta_{pt}$ and SR are reversed which is also not acceptable. In the next step, to evaluate the performance figures in consideration of coil resistance Fig. 8.16 has created for SR and $\eta_{pt}$ vs. $R_{eq}$. Here, three curves for each quantity are plotted for different values of coil resistance, considering same parasitic resistance in both the coils.

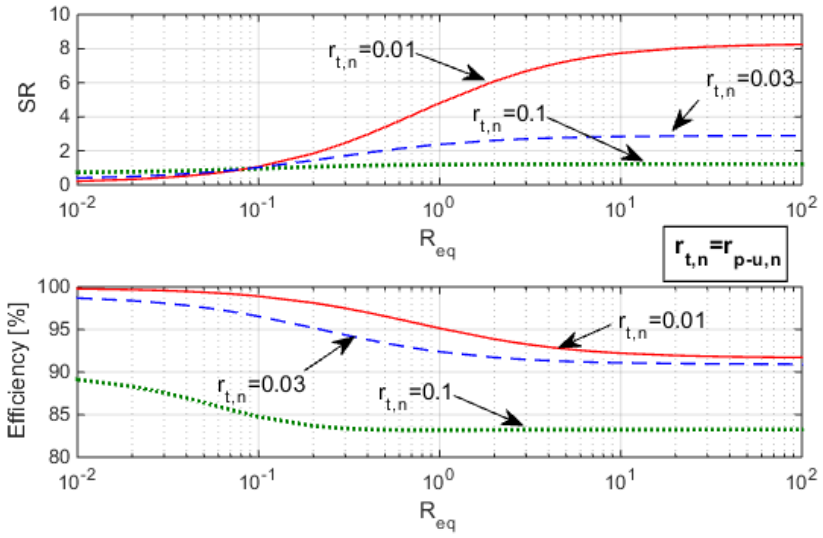


Fig. 8.16. *SR* and $\eta_{pt}$ vs. $R_{eq,n}$ for CCL topology with $r_{p\text{-}u,n} = r_{t,n}$ =0.01 (solid red line), $r_{p\text{-}u,n} = r_{t,n}$ =0.03 (dashed blue line) and $r_{p\text{-}u,n} = r_{t,n}$ =0.1 (dotted green line).

Fig. 8.16, indicates that SR is affected very badly in presence of coil resistance as observed in PS topology in this chapter above. SR is very poor at the lower values of $R_{eq}$ but $\eta_{pt}$ is very good in contrast. Here an interesting behavior can be observed that with increase in $R_{eq}$, $\eta_{pt}$ doesn't fall significantly and SR gets improved gradually. The characteristic of CCL topology is quite similar to the PS topology, however a little improvement in SR has been noticed.

## 8.8 Generalized Analysis of Pickup Compensation

The basic idea of reflexive segmentation is to enhance current in track coil for power transfer when it gets coupled with a pickup and rest of time the current is low enough to ensure safety. The reflected impedance of the pickup into a track coil is the key factor to achieve the required current enhancement or current gain. The behavior of reflected impedance depends upon the circuit deployed in pickup side. Considering a generalized situation as shown in Fig. 8.17, the pickup impedance seen by the induced voltage source can be written in real-imaginary form as in (8.36)

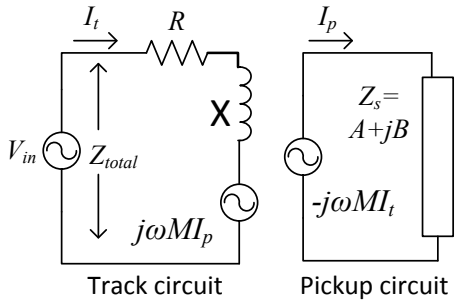


Fig. 8.17. Basic circuit schematic of IPT.

$$Z_s = A + jB \tag{8.36}$$

Reflexive impedance in the coupled track coil is

$$Z_r = \frac{\omega^2 M^2}{A+jB} \quad (8.37)$$

$$Z_r = \frac{\omega^2 M^2}{A^2+B^2}(A - jB) \quad (8.38)$$

The term $\omega^2M^2$ is constant for a pair of coupled coils so it can be represented as $\delta$ then real and imaginary parts of the reflected impedance are

$$Z_r = \frac{A\delta}{A^2+B^2} - j\frac{B\delta}{A^2+B^2} \quad (8.39)$$

Let's suppose a track coil has some impedance in uncoupled condition which can be written as

$$Z_t = R + jX \quad (8.40)$$

Where $R$ is resistance of track coil and $X$ is reactance. Now in coupled condition the total impedance of a track coil is

$$Z_{total} = \left(R + \frac{A\delta}{A^2+B^2}\right) + j\left(X - \frac{B\delta}{A^2+B^2}\right) \quad (8.41)$$

The basic idea of reflexive segmentation is to enhance current in the coupled track coil when a pickup gets interacted with it, therefore the total impedance should be minimum in that condition. This is possible when the imaginary part is essentially zero, which yields

$$A = \sqrt{\frac{\delta}{X}B - B^2} \quad (8.42)$$

Being zero of the imaginary part shows full compensation of the track coil reactance in reflexive manner. Even though the coil reactance is compensated but for achieving segmentation mechanism in this way the real part of impedance should also be minimum. Since this is resistance term which can't be cancelled out by any means therefore the condition of $min(Z_{total})$ is obtained when

$$\frac{A\delta}{A^2+B^2} = 0$$

$$A = 0 \quad (8.43)$$

Looking at (8.42) and (8.43), there are two values of $B$ for minimum impedance point

$$B = 0, \frac{\delta}{X} \quad (8.44)$$

There are two possibilities of minimum track impedance

*Case1: A=0 and B=0*

In this case pickup coil is not coupled or open circuit.

*Case2:* $A \rightarrow 0,\ B = \delta/X$

In this case the reactance of the track coil is fully compensated and reflected resistance is also minimum. A contour plot is displayed in Fig. 8.17, this shows current gain in coupled condition with variation in $A$ and $B$. The minimum value is obtained at

$$B = \frac{\delta}{X} = \frac{\omega^2 M^2}{\omega L_t} = k^2 X \qquad (8.45)$$

where $k$ is coupling coefficient. Thus it can be mentioned that when equivalent pickup reactance is $k^2$ times of the track coil reactance and resistance tends to be zero then segmentation can be good. In this situation when resistance is very low, efficiency doesn't stay good

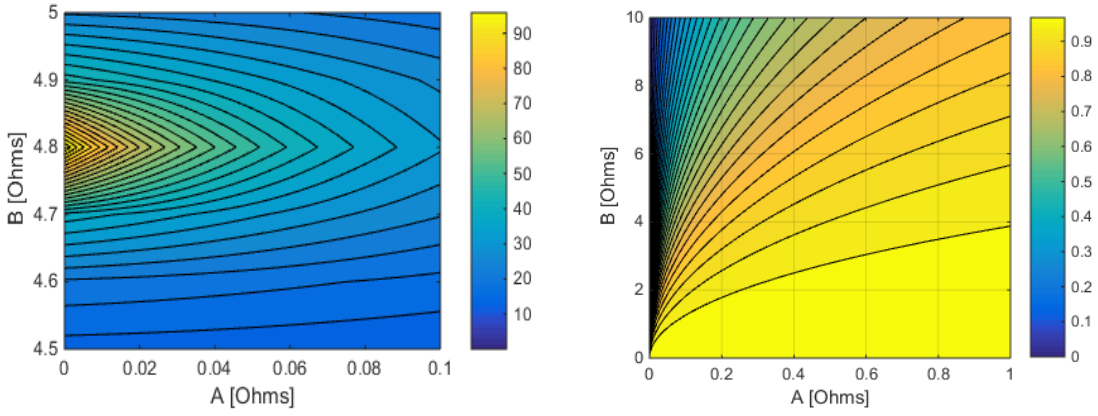


(a) (b)

Fig. 8.18. SR and $\eta_{PT}$ contours for generalized case of pickup compensation.

Assuming a coil pair which has 100 $\mu$H inductance in each coil and coupling coefficient between them is 0.3, where the track coil is supplied with 85 kHz and its normalized coil resistance is 0.01 w.r.t. its reactance $X$. contour plot of SR and $\eta_{pt}$ have been reported in Fig. 8.18 (a) and (b) respectively. As stated earlier that maximum SR can occur when $B$ is chosen according to (8.45); thus $A$=0 and $B$=4.8 is the condition for maximum SR. Regarding power transfer efficiency, $\eta_{pt}$ is higher for higher value of $A$ as shown in the contours of Fig. 8.18(b). Both SR and $\eta_{pt}$ cannot be achieved together.

## 8.9 Conclusions

The chapter has dealt with the reflexive segmentation of a DWC system. Two enhanced topologies based on pickup dual-capacitor compensation networks have been discussed to quantify their capabilities in executing the reflexive segmentation and, at the same time,

exhibiting a good efficiency in transferring the power from the track to the pickup coil. An accurate analysis, carried out by taking into account the parasitic resistances of the track and pickup coils, has outlined that the capabilities of segmentation and power transfer efficiency of a DWC system are significantly deteriorated by such resistances. Introduction of higher order compensation has been discussed which is also not found effective to improve the performance. Later, a generalized study of pickup compensation has been done to investigate possibility to achieve both SR and efficiency in good state, however in result, found that both the quantities cannot be obtained together.

That being the results, future works will be directed in evaluating either the insertion of compensation networks in the track and/or the use of more complex compensation networks in the pickup.

### References


[1] G. A. Covic and J. T. Boys, "Inductive power transfer", *Proceedings of IEEE*, vol. 101, no. 6, pp.1276-1289, June 2013.

[2] I. S. Suh and J. Kim, "Electric vehicle on-road dynamic charging system with wireless power transfer technology" Proc. of IEEE Int. Electric Machines & Drives Conf. (IEMDC), pp. 234 – 240, 2013.

[3] J.Li, Q.Yang, H.Chen and J.Wang, "Study and application of contact-less electrical energy transmission system," Proc. of IEEE Conf. on Vehicle Power and Propulsion (VPP), 2008, pp. 1-4.

[4] S. Y. Choi, B. W. Gu, S. Y. Jeong, and C. T. Rim, "Advances in Wireless Power Transfer Systems for Roadway-powered Electric Vehicles," *IEEE Journal of Emerging and Selected Topics in Power Electronics*, Vol. 3, No. 1, pp. 18-36, March 2015.

[5] H. Jiang, P. Brazis, M. Tabaddor, and J. Bablo, "Safety considerations of wireless charger for electric vehicles - a review paper," Proc. of IEEE Symp. on Product Compliance Engineering (ISPCE), 2012, pp. 1-6.

[6] International Commission on Non-Ionizing Radiation Protection (ICNIRP) Guidelines [Online]. Available: www.icnirp.de/documents/emfgdl.pdf

[7] K. Lee, Z. Pantic, and S. M. Lukic, "Reflexive Field Containment in Dynamic Inductive Power Transfer Systems", *IEEE Transactions on Power Electronics*, Vol. 29, No. 9, pp. 4592 – 4602, Sept. 2014.

[8] Z. Wei, J.C. White, A.M. Abraham, and C.C. Mi, "Loosely Coupled Transformer Structure and Interoperability Study for EV Wireless Charging Systems," *IEEE Transactions on Power Electronics*, Vol. 30, n° 11, pp. 6356-6367, 2015.

[9] C. S. Wang, O. H. Stielau, and G. A. Covic, "Design Considerations for a Contactless Electric Vehicle Battery Charger," *IEEE Transactions on Industrial Electronics*, Vol. 52, No. 5, pp. 1308-1314, Oct. 2005.

[10] Z. Pantic, S. Bai, and S. M. Lukic, "ZCS LCC-Compensated Resonant Inverter for Inductive-Power-Transfer Application," IEEE Transactions on Industrial Electronics, Vol. 58, No. 8, pp. 3500-3510, Aug. 2011.

[11] H. Dashora, M. Bertoluzzo, and G. Buja,"Reflexive properties for different pick-up circuit topologies in a segmented IPT track", Proc. of IEEE Int. Conf. on Industrial Informatics (INDIN), 2015, pp. 69-75.

[12] J. Deng, F. Lu, W. Li, R. Ma, C. Mi, "ZVS double-side LCC compensated resonant inverter with magnetic integration for electric vehicle wireless charger," IEEE Applied Power Electronics Conf. and Exp. (APEC), pp. 1131-1136, 2015.

# Chapter 9

# DWPT Power Supply

The discussion so far, in previous chapters, was mainly focused on wireless power transfer between two dedicated coils, considering sinusoidal voltage and current supply. In the complete power flow of wireless charging system (from grid to battery) there is a set of power converters in both track and pickup side, which regulate the power in appropriate form. This chapter contains a general overview of power supply for wireless power transfer and associated power converters. Different sections of the chapter will go through high frequency (HF) inverter, power factor correction, some advanced compensation topologies for the track and pickup side converters to charge the battery.

## 9.1 High Frequency Supply

Efficiency of power transfer as well as power transfer between two loosely coupled magnetic coils depends upon the supply frequency as mentioned in chapter 2. The supply frequency required for vehicular application is few kHz and the most properly it's adopted as 85 kHz [1]-[2]. Main source of the power supply is grid in any kind of EV charging, where the supply frequency is 50 to 60 Hz. The grid supply can be either single phase or three phase but that need to be converted into a single phase supply. Basically this is an AC to AC conversion (low to high frequency) and the most used topology is DC link converters. The grid voltage needs to be rectified to feed a high frequency inverter that produces HF AC supply. The arrangement converters to feed WPT track from the power grid consists of a rectifier to convert AC to DC, power factor correction circuit to impose unity power factor at the rectifier input, and an inverter to produce AC supply of desired frequency [3]-[4]. Separating into two: AC to DC conversion and DC to AC conversion, converters are discussed below.

### *9.1.1 Grid Rectifier and Power Factor Correction (PFC)*

For charging an EV, electric power is obtained normally from power grid which is available as low frequency voltage, either single or three phase. The AC supply is converted into DC voltage with an appropriate rectifier circuit. Mostly for this, full bridge diode rectifier is equipped which output is DC but contains ripple. To smoothen the DC voltage, filters can be used which again affects the rectifier input, especially power factor.[5] The grid supply is supposed to be cleaned and free from high voltage spikes and current harmonics, in order to ensure good quality. Discontinuous input current that exists on the grid caused by the non-linearity of the rectification process which further cause reduction of power factor. In order to

increase power factor of the system, a boost chopper is added to diode rectifier to minimize the reactive power demand from the utility grid and maximizes the current waveform quality by reducing the distortions. SiC diodes can be employed for high frequency operation as they have a very low reverse recovery current and short commutation time but their forward bias voltage drop is quite significant and thereby increases the conduction losses.

Among the three basic choppers buck, boost, buck-boost the boost chopper is the most suitable for use in implementing PFC [5]. Fig. 9.1 shows the arrangement of rectifier and PFC where input is grid and output is DC link. The PFC circuit requires one inductor, a diode and a switching element, typically a MOSFET. The output voltage of the boost converter is higher than the input. To maintain constant DC link voltage, the PFC boosts the rectified and pulsating DC voltage. A typical boost PFC is designed such that the regulated output voltage of the converter is higher than the peak of the highest input voltage. This allows the boost PFC circuit to achieve an input current waveform that has the same shape as the input voltage waveform for most of the operating input voltage range.

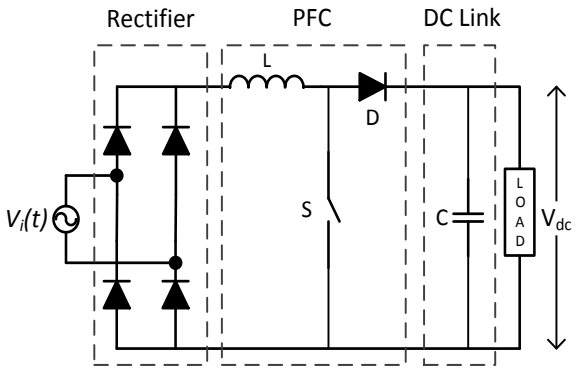


Fig. 9.1. Power factor correction circuit.

### *9.1.2 High Frequency Inverter*

The second stage is a conversion of voltage from DC to AC, where inverters are widely used for medium to large power transfer applications [4]. Such inverter employs semiconductor

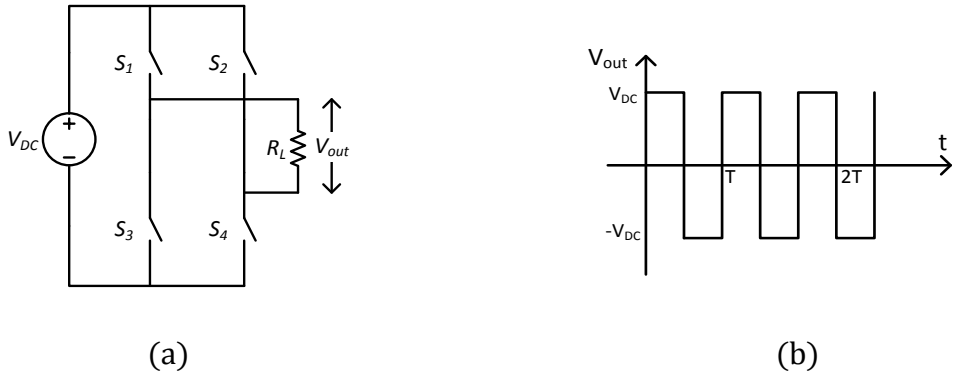


(a) (b)

Fig. 9.2 Static wireless charging.

switches like IGBTs which operate only in saturation and cut-off region. Among switch mode converters, single phase, H-bridge is the most common configuration of the inverter.

Fig. 9.2(a) represents a generalized DC/AC single-phase bridge inverter that consists two legs [6]. Upper and lower switch in each leg are complementary switches which do not get turn on together and there is a time gap between turning off of a switch and turning on of another. This delay is called dead time which is very important to avoid shoot through problem that may cause short circuit of the DC source. In the circuit shown switch $S_1$, $S_4$ are closed simultaneously for first half of the AC output waveform and in the next half period switches $S_2$, $S_3$ are closed. Fig. 9.2(b) shows the resulting AC waveform when mentioned pair of switches operate alternately at a duty ratio $D$ = 0.5. The output is a square wave with a period $T$, which corresponds to an AC fundamental frequency as:

$$f = \frac{1}{T}\ Hz \qquad (9.1)$$

The obtained square wave shape contains a fundamental frequency wave and numerous harmonics. To understand the behaviour of harmonics and efforts to eliminate them, Fourier series analysis is required. A general Fourier series is written as

$$f(t) = \frac{1}{2}a_0 + \sum_{n=1}^{\infty}(a_n \cos n\theta + b_n \sin n\theta) \qquad (9.2)$$

where *f(t)* is a time varying function to represent the waveform shown in Fig. 9.2(b) and $\theta=\omega t$. Coefficients are

$$a_0 = \frac{1}{\pi}\int_0^{2\pi} f(t)\, d\theta \qquad (9.3)$$

$$a_\mathrm{n} = \frac{1}{\pi}\int_0^{2\pi} f(t)\cos(n\theta)\, d\theta \qquad (9.4)$$

$$b_\mathrm{n} = \frac{1}{\pi}\int_0^{2\pi} f(t)\sin(n\theta)\, d\theta \qquad (9.5)$$

Solving the coefficients, values of $a_0$ and $a_n$ are found zero due to alternating shape and odd symmetry of the waveform respectively. The coefficient $b_n$ is obtained as

$$b_\mathrm{n} = \frac{2V_{dc}}{n\pi}(1 - \cos n\pi) \qquad (9.6)$$

where $V_{dc}$ is DC voltage in the input side of the inverter and in waveform this is represented as maximum voltage. Looking at (9.6) it is concluded, when $n$ is even then $b_n$ is zero due to the half wave symmetry and when $n$ is odd then

$$b_{\mathrm{n}} = \frac{4V_{dc}}{n\pi} \qquad (9.7)$$

Rewriting (9.2), the output voltage of the inverter can be written as

$$V_{out} = \frac{4V_{dc}}{\pi} \sum_{n=1,3,5\ldots}^{\infty} \frac{1}{n} \sin n\omega t \qquad (9.8)$$

Equation (9.8) represents an AC voltage which is a set of several sinusoidal voltages with different frequencies and amplitudes. The voltage waveform for n=1 is called fundamental component and rest of the series is harmonics of multiplied frequencies with *n*. A harmonic spectrum is shown in Fig. 9.3 that demonstrates that amplitude of a harmonic decreases when frequency ($n\omega$) increases. Since the even harmonics are not present then the nearest harmonics are 3rd and 5th harmonics which are significant in amplitude, thus their elimination becomes important. In order to remove the unwanted harmonics from inverter output, voltage phase-shift and multilevel inverters are used in many applications.

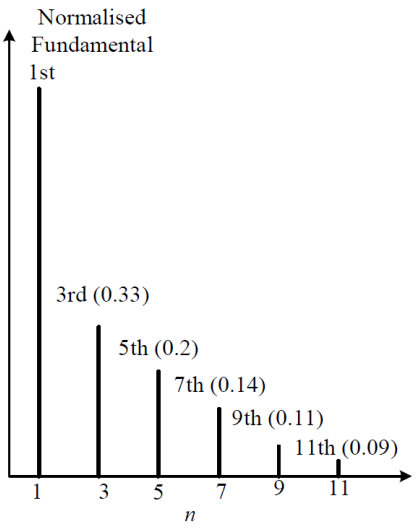

Fig. 9.3 Harmonic spectra of inverter output.

The voltage phase-shift inverter is also called quasi square wave inverter which outputs a particular wave shape as shown in Fig. 9.4. The angle $\alpha$ is phase shift and this is an important parameter to control output voltage. Here due to odd symmetry, half wave symmetry and absence of DC offset $a_0$=0 and $a_n$=0 in equation (9.2); and

$$b_{\mathrm{n}} = \frac{2}{\pi} \int_{\alpha}^{\pi-\alpha} V_{dc} \sin(n\theta)\, d\theta$$

$$= \frac{2V_{dc}}{n\pi} [\cos(n\alpha) - \cos n(\pi - \alpha)]$$

Further solving, the expression becomes

$$b_n = \frac{2V_{dc}}{n\pi} \cos(n\alpha)\, [1 - \cos n\pi] \qquad (9.9)$$

If *n* is even; $b_n = 0$

If *n* is odd; $b_n = \frac{4V_{dc}}{n\pi} \cos(n\alpha)$

Again looking at the resulting voltage expression including all harmonics

$$V_{out} = \frac{4V_{dc}}{\pi}\sum_{n=1,3,5\ldots}^{\infty}\frac{1}{n}\sin(n\omega t)\cos(n\alpha) \qquad (9.10)$$

It can be observed from (9.10) that the output voltage, with its all the harmonics, is affected by the phase shift angle. Thus, exploiting this property of quasi square, amplitude of the fundamental frequency voltage is controlled with the angle α in WPT application.

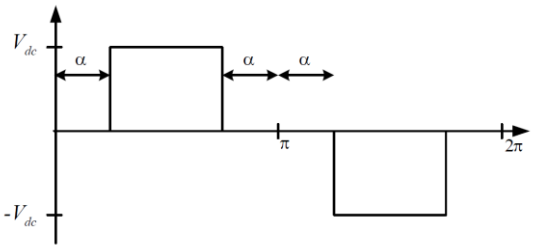

Fig. 9.4 Quasi square waveform.

Voltage waveform shown in Fig. 9.4 and represented by (9.10) can be obtained with the basic inverter circuit shown in Fig. 9.1(a), which is simply called two level inverter. Using quasi square wave operation, the amplitude of output voltage is regulated, but creating more steps of appropriate width in the voltage waveform can also help to eliminate harmonics of inverter output [6]-[10]. In this way multilevel inverters are being developed for power supply applications.

A multilevel converter uses more than two DC voltage levels to synthesize multiple steps in the output voltage. This includes an array of semiconductor switches and capacitor voltage sources, the output of which generate voltages with stepped waveforms. The commutation of the switches permits the addition of the capacitor voltages, which reach high voltage at the output, while the power semiconductors must withstand only reduced voltages [8], [9]. Fig. 9.5 shows a schematic diagram of one phase leg of inverters with different numbers of levels, for which the action of the power semiconductors is represented by an ideal switch with several positions. A two-level inverter generates an output voltage with two values (levels) with respect to the negative terminal of the capacitor [see Fig. 9.5(a)], while the three-level inverter generates three voltages, and so on. There are basically three topologies have been proposed by researchers to realize multilevel inverter: diode-

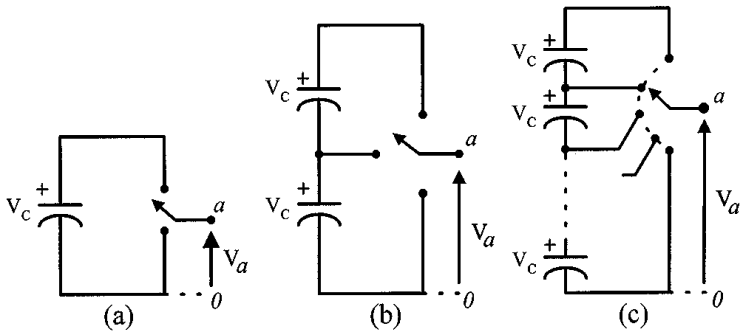

Fig. 9.5. One phase leg of an inverter with (a) two levels, (b) three levels, and (c) n levels.

clamped (neutral-clamped), capacitor-clamped (flying capacitors), and cascaded multi-cell with separate dc sources.

By increasing the number of levels in the inverter, the output voltages have more steps generating a staircase waveform, which has a reduced harmonic distortion. However, a high number of levels increases the control complexity. The control of the multilevel converter is to choose a series of switching angles to synthesize a desired sinusoidal voltage waveform. A Fourier series expression of the output voltage of *a* multilevel inverter can be written as

$$V_{out} = \frac{4V_{dc}}{\pi}\sum_{n=1,3,5\ldots}^{\infty}\frac{1}{n}\sin(n\omega t)\{\cos(n\alpha_1) + \cos(n\alpha_2) + \cdots + \cos(n\alpha_s)\} \quad (9.11)$$

where *s* is number of capacitor sources. Considering a 3-level inverter, the output voltage waveform generated by fundamental frequency switching scheme is shown in Fig. 9.6. Ideally,

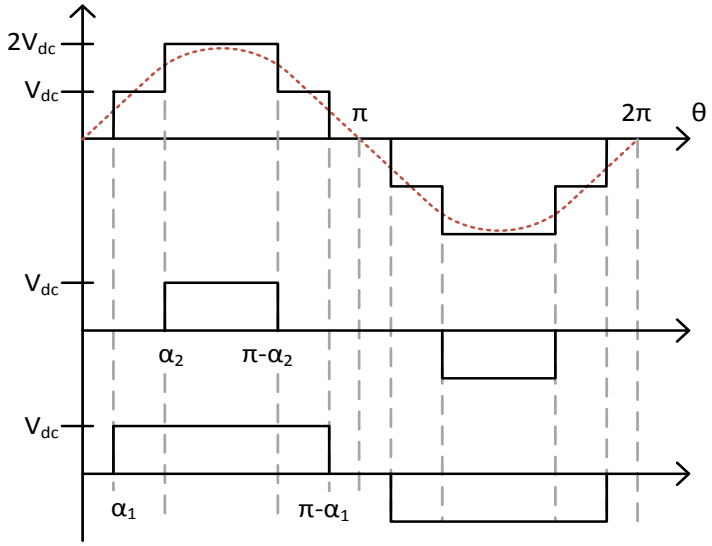


Fig. 9.6. Multilevel (3-level) inverter waveform.

given a desired fundamental voltage $V_1$, one wants to determine the switching angles $\alpha_1$ and $\alpha_2$ so that $V(\omega t) = V_1 sin(\omega t)$, and specific higher harmonics of $V(n\omega t)$ are equal to zero. In a three-level inverter, to keep desired fundamental voltage along with the elimination of 3rd harmonic, following relations are obtained in terms of the phase shift angles:

$$\cos(\alpha_1) + \cos(\alpha_2) = m \quad (9.12)$$

$$\cos(3\alpha_1) + \cos(3\alpha_2) = 0 \quad (9.13)$$

where the modulation index m is defined as $m=\pi V_1/(4V_{dc})$. Introducing more steps in the voltage waveform, with appropriate angle, helps to eliminate more number of harmonics [6]. Since the equations (9.12)-(9.13) are non-linear equations which can be solved by numerical methods

like Newton-Raphson method. The most attractive features of multilevel inverters are as follows.

- They can generate output voltages with extremely low distortion and lower dv/dt.
- They draw input current with very low distortion.
- They can operate with a lower switching frequency.

## 9.2 Compensation for Track

To obtain higher coupling between two coils, compensation of leakage inductance is required. This further helps to operate at resonance frequency so that impedance is purely resistive in nature. The compensation can be performed by inserting one or more capacitors with the track or/and pickup inductances. To compensate coil inductance and achieve a greater energy transfer, there are four fundamental topologies that can be set up for resonance: series-series (SS), series-parallel (SP), parallel-series (PS) and parallel-parallel (PP). Most of the WPT systems practically demonstrated by various researcher, adopt the basic series-series compensation topology, and in these systems, a constant supply current [11] needs to be maintained. Thus, meticulous control and tuning of the inverter is necessary since the load varies violently as the receive coil moves with the online EV. This adds to the control complexity and may reduce systematic reliability. Recently, a new compensation topology called LCL compensation network [12] has been successfully utilized in stationary wireless charging. Its advantages of facilitating zero voltage switch (ZVS) or zero current switch (ZCS) [12] of the inverter, increasing lateral misalignment tolerance, and improving WPT efficiency [13] have been demonstrated. The LCL basically forms a symmetrical T-network which has a special feature to transform constant voltage source to constant current source and vice versa. Such property of T-network is briefly discussed below.

### *9.2.1 Symmetrical T-type Network*

T-type compensation network is an arrangement of pure reactive elements which has been introduced to WPT systems recently. As shown in Fig. 9.7, an ideal symmetrical T-type compensation network consists of three ideal inductive or capacitive hands. Particularly, the left hand and the right hand have the same pure inductive reactance of $jX$, while the down hand is pure capacitive with reactance of $-jX$.

For a given impedance of $Z_o$, when such symmetrical T-type compensation network is applied as shown in Fig. 9.7, the overall impedance seen from the input side becomes:

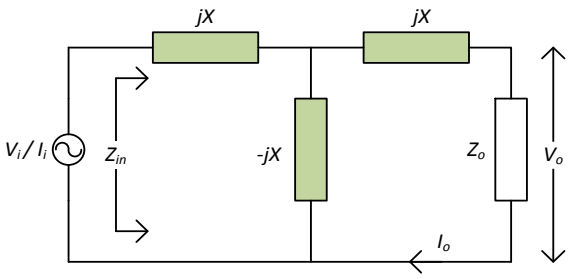

Fig. 9.7. Symmetrical T-network.

$$Z_i = jX + (jX + Z_o)||(-jX)$$

$$= jX + \frac{-jX(jX+Z_o)}{-jX+jX+Z_o} = \frac{X^2}{Z_o} \qquad (9.14)$$

If the circuit were supplied by a constant voltage source $V_i$, with the symmetrical T-type compensation network, then the output current flowing in $Z_o$ can be derived as:

$$I_o = \frac{V_i}{Z_i}\frac{(jX+Z_o)||(-jX)}{(jX+Z_o)}$$

$$= \frac{-jX(jX+Z_o)}{(jX+Z_o)Z_o}\frac{V_i}{\left(X^2/Z_o\right)}$$

Finally

$$I_o = \frac{V_i}{jX} \qquad (9.15)$$

Alternately, if the circuit were supplied by a constant current source Ii, with the symmetrical T-type compensation network, then the output voltage of $Z_o$ can be calculated as:

$$V_o = \frac{Z_o}{jX+Z_o} I_i (jX + Z_o)||(-jX)$$

Which yields

$$V_o = -jXI_i \qquad (9.16)$$

Equation (9.16) clearly shows that the symmetrical T-type compensation network provides a reciprocal transformation of the applied impedance. On the other hand, (9.18) and (9.19) indicate that this symmetrical network transforms voltage source and current source alternately, besides, constant current source or constant voltage source is achieved regardless of the impedance of the load. These two characteristics make the symmetrical T-type network considerably practical in WPT applications because of the impedance matching needs, and also for the reason that voltage source inverter is dominant but constant-current exciting the track coil is often preferred.

*9.2.2 LCL Compensation for Track*

There are many variants of T-type compensation network, among them an LCL compensation network is a fundamental but practical one. As its name suggests, an LCL compensation network is composed of an inductor serving as the left hand, a lumped capacitor acting as the down hand, and another inductor in the right hand is a WPT track coil itself. Fig. 9.8 shows two situations of track circuit: one is when the track coil is uncoupled with any pickup and another is when track and pickup are coupled. In the circuit shown, $L_T$ is track inductance and $L_1$ is an additional inductor of equal inductance of the track coil, to form in a symmetrical T-network. Here, the capacitor $C_T$ has equal and negative reactance of the track coil, so that it establishes resonance.

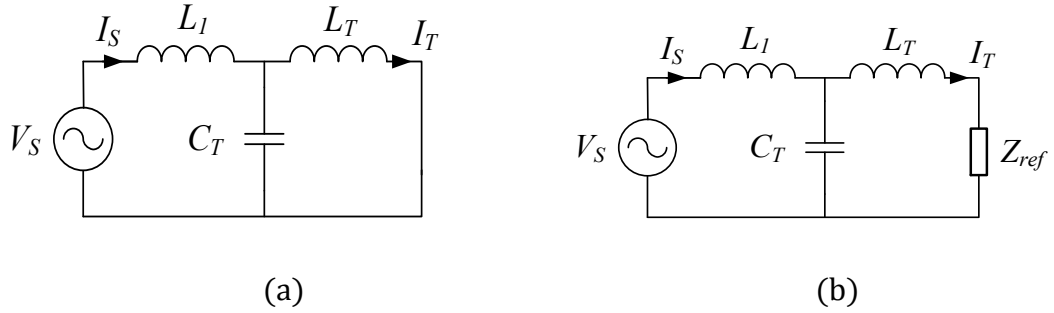


Fig. 9.8. LCL compensated track circuit (a) uncoupled condition and (b) Coupled with a pickup.

Looking at Fig. 9.8(a) and applying KVL, input current is

$$I_s = \frac{V_s}{j\omega_0 L_1 + j\omega_0 L_T\left(\frac{1}{1-\omega_0^2 L_T C_T}\right)} \qquad (9.17)$$

where $\omega_0$ is resonance frequency and given by

$$\omega_0 = \frac{1}{\sqrt{L_T C_T}} = \frac{1}{\sqrt{L_1 C_T}} \qquad (9.18)$$

The supply current $I_s$ according to (9.17) is zero when the track coil is not coupled. In this situation the voltage across capacitor $C_T$ is $V_s$ then current in the track coil will be

$$I_T = \frac{V_s}{j\omega_0 L_T} \qquad (9.19)$$

In this situation, track coil and $C_T$ are in resonance and this pair shows infinite impedance to the source. Subsequently, supply current is zero but there is current in the track coil which is decided by the reactance of one hand of the LCL network.

Another situation when a pickup is coupled with the track coil, it reflects the pickup impedance into the track coil. As shown in Fig. 9.8(b), $Z_{ref}$ is the reflected impedance, then by applying KVL supply current is written as

$$I_s = \frac{(1-\omega_0^2 L_T C_T + j\omega C_T Z_{ref})V_s}{j\omega L_1 + (j\omega L_T + Z_{ref})(1-\omega_0^2 L_1 C_T)} \qquad (9.20)$$

Since the capacitor is chosen that it can resonate with either of the inductors therefore (9.20) is written as

$$I_s = Z_{ref} \frac{V_s}{(L_1/C_T)} \qquad (9.21)$$

Track coil current can be calculated by $I_s$, using current division rule in two parallel branches, which yields

$$I_T = \frac{V_s}{j\omega_0 L_T} \qquad (9.22)$$

Note that (9.19) and (9.22) are same and independent of $Z_{ref}$, hence the LCL network maintains constant current in the track. The supply current given by (9.21) is no longer zero in coupled condition and that is directly proportional to $Z_{ref}$.

Apart of the features of the LCL network to provide compensation to the track coil and constant current supply, this network is also helpful to impose soft switching in the supply inverter. Since the overall impedance of an inverter should be somewhat inductive to achieve ZVS, perfectly symmetrical network is not the best solution at the track side. Certain variation [13] on the hands is needed. Thus, a little deviation of reactance is introduced in the left, right and central branch of the LCC-T network. In this situation the WPT system work near resonant frequency.

### *9.2.3 LCC Compensation for Track*

Exploiting the current/voltage source transformation phenomenon of the T-network, an LCC network is derived for WPT applications. Using an additional inductor of the same value of the track inductance in the LCL network can be a bulky arrangement. Thus partially compensating the track inductance of the LCL network, by

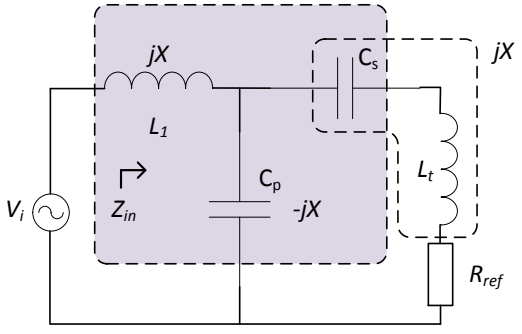


Fig. 9.9. Schematic of an LCC compensated track circuit.

introducing a capacitor, can optimize the system size. Moreover, as observed with earlier analysis and with (9.15) the reactance of an arm of T-network decides the constant output current. Therefore a smaller value of reactance is also preferred for high power application. An LCC compensation topology as shown in Fig. 9.9 consists of one inductor and two capacitors, and together with the track coil, it basically forms a structure similar to an LCL network. In this arrangement, two capacitors are there for compensation and an additional inductor is employed to form a T-network. The additional inductor can be independent or coupled with the track coil. In a configuration when the additional coil and the track coil are integrated or coupled together, and additional space for additional inductors is not needed. This integrated structure can also transfer the same amount of power with smaller additional inductances, compared with one that is not integrated. For the simplicity of coupling between the additional inductor and the coil can be avoided.

## 9.3 Pickup side Power Converters

In a WPT system pickup coil captures AC power with the same frequency as the supply one. The captured power fed to the battery after passing through high-frequency rectifier, and a non-isolated dc/dc converter. Fig. 9.10 shows a basic schematic of pickup side circuit for battery charging. In a dynamic WPT system with lumped coil track, coupling coefficient does not remain constant rather it varies periodically. Therefore voltage induced across pickup coil terminals also varies periodically. In such situation, power conditioning for charging a battery as well as propelling the vehicle simultaneously is more challenging than a stationary wireless charging.

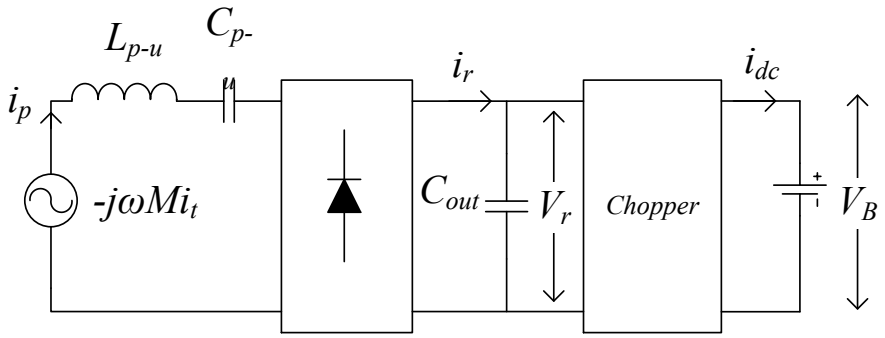


Fig. 9.10. Pickup side circuit for battery charging.

As shown in Fig. 9.10 an electrolytic capacitor $C_{out}$ is placed at the output of the rectifier that works as voltage buffer. Since the rectified DC voltage varies as vehicle moves over the WPT track then there exist a range of capacitor voltage. The capacitor $C_{out}$ acts as a supply source for the chopper depicted in the same figure which is responsible for charging the battery

and keeping its voltage constant. Clearly the chopper voltage is variable in a range and the output voltage remains constant. Thus the applicable chopper in such place should be a buck-boost chopper but considering a single ground in the vehicle, the chopper should be non-inverting.

The vehicle load is directly fed by the battery and that is fixed for a fix vehicle speed. Considering the power split at the output of chopper, the copper is operated such that it meets battery charging characteristic as well as load demand. A brief introduction of power conditioning and charging system mentioned in this section.

### *9.3.1 Rectifier*

This is a power electronic converter which converter AC voltage to DC voltage. A rectifier can be single phase or three phase, but in the pickup circuit of wireless power transfer, single phase rectifier is used. The simplest and mostly used configuration is full bridge diode rectifier which is compact and robust. The output of a single phase rectifier has very high amount of voltage ripple which need to be eliminated using filters. To smoothen the rectified DC voltage, an electrolytic capacitor is provided as shown in Fig. 9.10. For the sake of power continuity, the capacitor $C_{out}$ can be a super-capacitor especially in dynamic wireless charging from lumped coil track.

### *9.3.2 Chopper*

Chopper is a static power electronic device which makes variation in the input DC voltage level. This is also called DC to DC converter that basically performs step-up or step-down operation on the applied voltage. Based on voltage conversion ability, there are three basic choppers: buck, boost and buck-boost converter. Buck converter steps-down the input voltage, boot converter steps-up the input voltage and the buck-boost converter is adept to both step-up and down the input voltage according to its control, but unlike other two choppers it produces output with reverse polarity.

All the DC-DC converter consists of one or more semiconductor switch/s which is/are operated in pulse width modulation (PWM) pattern to control the output. PWM switching frequency is decided by career wave and pulse width by a controlled reference signal. High switching frequency is good for the continuity of the output current therefore adequate high frequency is adopted and kept fixed. The measure of pulse width is duty-ratio, which is the key parameter to control a chopper and step up/down the voltage.

As mentioned above, the DWC pickup needs a buck-boost chopper which can produce output voltage with the same polarity as input, so that the ground can be the same. To realize a non-inverter buck-boost chopper a combination of buck and boost converter is discussed in [14]-[16]. This chopper is also called cascaded buck-boost converter which has basic three modes of operations: buck mode, boost mode and buck-boost mode. A simple schematic of power circuit is shown in Fig. 9.11, where the circuit contains two controlled switches $S_1$, $S_2$ and two diodes $D_1$, $D_2$. The switches go under switching solely or simultaneously based on the desired operation mode. Diode $D_2$ works for reverse current blocking and diode $D_1$ as freewheeling in buck mode. There is a common inductor for both buck and boost operations, it acts as filter for buck mode and as an energy storage for boost mode.

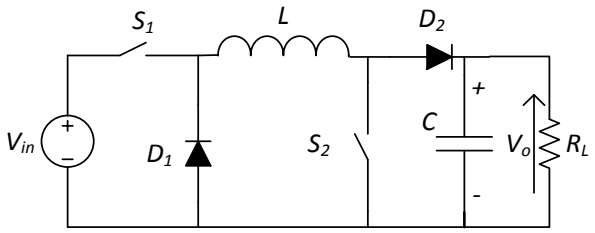


Fig. 9.11. Non-inverter buck-boost chopper.

There are some step-up and down converter topologies which employ single switch, for example inverting buck-boost, SEPIC, and Cuk converter. Apart of the merits of single switch, they have disadvantages of reverse output polarity and relatively high voltage and current stresses on the switch comparing to the buck and boost converter topologies. In contrast, the combination of two switches in the cascaded buck-boost configuration, is advantageous to achieve low switching stresses by splitting voltage and current in two active switches, and results in low energy storage requirement and high performance efficiency operating independently in buck or boost mode [15].

The working principle of the non-inverting buck-boost chopper is understood in three different modes that are mentioned above. Table 9.1 outlines the switch operation plan according to the converter output requirement.

Table 9.1 Operational modes of the chopper.

| **Mode** | **Voltage** | **S1** | **S2** |
|---|---|---|---|
| Buck | $V_o < V_i$ | Switching | Open |
| Boost | $V_o > V_i$ | Close | Switching |
| Buck-boost | $V_o < V_i$ *or* $> V_i$ | Switching | Switching |

*Buck-mode*: Switch $S_2$ remains open and switch $S_1$ has PWM switching then the circuit looks like a conventional buck converter where diode $D_1$ provides freewheeling path and $D_2$ is always conducting. In this mode the output voltage at steady state and with continuous conduction, follow the relation (9.23) where $\delta$ is duty ratio of $S_1$ switching. For a duty ratio $\delta$, at steady state, the relations of input-output voltage is

$$V_{o,buck} = \delta V_i \qquad (9.23)$$

*Boost-mode*: Switch $S_1$ is kept always close in this mode and switch $S_2$ operates with PWM pulses. Considering inductor $L$ as energy storage device and including diodes $D_1$, $D_2$ the converter behaves like a conventional boost converter. Then the output voltage is

$$V_{o,boost} = \frac{V_i}{1-\delta} \qquad (9.24)$$

*Buck-boost mode*: This is a mode when both the switches $S_1$, $S_2$ are operated with the PWM frequency. Subsequently, it behaves like normal buck-boost converter but the beauty of the circuit is that the output is non-inverting. When both the switches are closed, energy is stored in the inductor and the stored energy transferred to the load while $S_2$ is off. In this mode of operation the duty ratio of $S_1$, $S_2$ switching can be different according to control algorithm. In this mode when both the switches operate together then the output voltage is

$$V_{o,buck-boost} = \frac{\delta V_i}{1-\delta} \qquad (9.25)$$

The PWM switching and voltage control is carried out by comparing career and reference signal as usual control of basic converters. However, involvement of two switches and smooth transition of modes makes it challenging. There are two possibilities of generating PWM pulses for two switches: using one reference with two career signals as shown in Fig. 9.12 (a), and

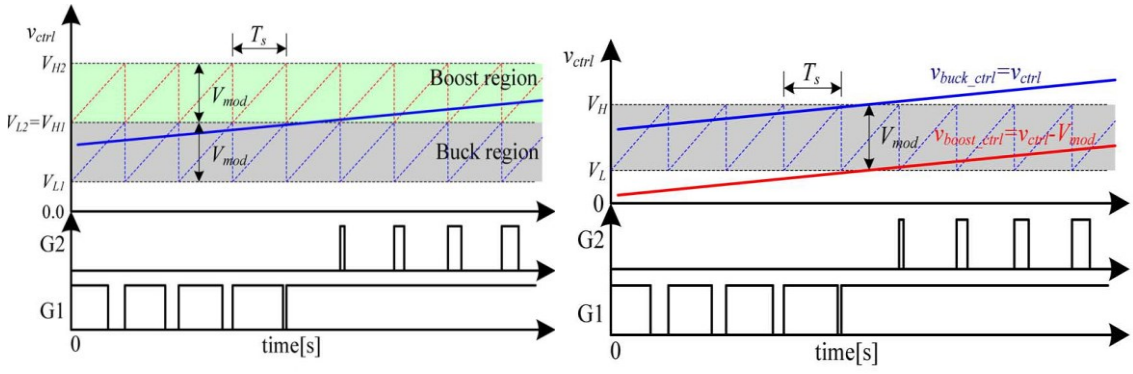


(a) (b)

Fig. 9.12. PWM pulse generation for $S_1$ and $S_2$: (a) One reference and two career, (b) Two reference and one

using two reference with one career signal as shown in Fig. 9.12 (b). Here the operation modes shown are only buck and boost, but due to some practical issues in smooth mode transition, control is modified. In that situation buck-boost mode is introduces between the mentioned two modes.

## References


[1] M.K. Uddin, G. Ramasamy, S. Mekhilef, K. Ramar, and Y. C. Lau, "A review on high frequency resonant inverter technologies for wireless power transfer using magnetic resonance coupling," proc. of IEEE Conference on Energy Conversion (CENCON), 2014, pp. 412-417.

[2] K.N. Mude, M. Bertoluzzo, and G. Buja "Design of contactless battery charger for electric vehicle", Proc. of IEEE AFRICON, 2013, pp.1099-1104.

[3] H. Abe, H. Sakamoto, and K. Harada, "A noncontact charger using a resonant converter with parallel capacitor of the secondary coil," Proc. of Applied Power Electronics Conference and Exposition Fukuoka, Japan, 1998, pp. 136-141.

[4] J.M. Barnard, J.A. Ferreira and J.D. VanWyk, "Linear contactless power transmission systems for harsh environments," Proc. of IEEE AFRICON, 1996, pp.711-714.

[5] R.W. Erickson and D. Maksimovic, "Fundamental of Power Electronics," Second edition, Springer International Edition.

[6] M.H. Rashid, "Power Electronics: Circuits Devices and Applications," Third edition, Pearson Education International publication.

[7] J. Rodriguez, J.S. Lai, and F.Z. Peng, "Multilevel inverters: a survey of topologies, controls, and applications," in *IEEE Transactions on Industrial Electronics*, vol. 49, no. 4, pp. 724-738, Aug 2002.

[8] M. Malinowski, K. Gopakumar, J. Rodriguez, and M.A. Perez, "A Survey on Cascaded Multilevel Inverters," *IEEE Transactions on Industrial Electronics*, vol. 57, no. 7, pp. 2197-2206, July 2010.

[9] Z. Du, L.M. Tolbert, and J.N. Chiasson, "Harmonic elimination for multilevel converter with programmed PWM method," proc. of IEEE Industry Applications Conference, 2004, vol.4, pp. 2210-2215.

[10] B.X. Nguyen, D.M. Vilathgamuwa, G. Foo, P. Wang, and A. Ong, "A modified cascaded multilevel converter topology for high power bidirectional inductive power transfer systems with the reduction of switching devices and power losses," proc. of IEEE International Conference on Power Electronics and Drive Systems, 2015, pp. 93-97.

[11] Q. Zhu; L. Wang, Y. Guo, C. Liao, and F. Li, "Applying LCC Compensation Network to Dynamic Wireless EV Charging System," *IEEE Transactions on Industrial Electronics*, vol. PP, no. 99, pp. 1-1, 2016.

[12] X. Qu, Y. Jing, H. Han, S. C. Wong, and C. K. Tse, "Higher Order Compensation for Inductive-Power-Transfer Converters With Constant-Voltage or Constant-Current Output Combating Transformer Parameter Constraints," *IEEE Transactions on Power Electronics*, vol. PP, no. 99, pp.1-1, 2016.

[13] Z. Pantic, S. Bai and S. M. Lukic, "ZCS LCC -Compensated Resonant Inverter for Inductive-Power-Transfer Application," *IEEE Transactions on Industrial Electronics*, vol. 58, no. 8, pp. 3500-3510, Aug. 2011.

[14] J. Chen, D. Maksimovic, and R. Erickson, "Buck-boost PWM converters having two independently controlled switches," Power Electronics Specialists Conference, 2001. PESC. 2001 IEEE 32nd Annual, Vancouver, BC, 2001, pp. 736-741 vol.2.

[15] Y.J. Lee, A. Khaligh, and A. Emadi, "A Compensation Technique for Smooth Transitions in a Noninverting Buck–Boost Converter," *IEEE Transactions on Power Electronics*, vol. 24, no. 4, pp. 1002-1015, April 2009.

[16] K. Colak, M. Bojarski, E. Asa, and D. Czarkowski, "A constant resistance analysis and control of cascaded buck and boost converter for wireless EV chargers," proc. of IEEE Applied Power Electronics Conference and Exposition (APEC), 2015, pp. 3157-3161.

# Chapter 10

# Case Study: DWC System Design

Dynamic wireless charging (DWC) is implemented on a road where one or more EVs get interacted with the WPT track. For vehicle movement over the track it's important to analyze the requisite energy transferred to the vehicle per unit distance and a WPT track is designed according to power and energy requirement. The per-kilometer requisite energy can be computed in two parts: one part of energy is required for propelling the vehicle at a constant speed and another part is the energy used to charge the battery or auxiliaries. Considering an example vehicle for a case study, a lumped coil track is designed in this chapter. The design process basically includes coil design as an individual segment of the track and the placement of the coil one the road.

## 10.1 Subject Electric Vehicle

A battery electric vehicle has been chosen for the experimental implementation of the DWC system. Fig. 10.1 shows the image of the candidate vehicle for the case study which is built by ENEA, an Italian national agency for new technologies, energy and sustainable

Fig. 10.1 Electric car ENEA Urbe.

economic development; and the name of the vehicle is Urbe. This is a prototype for the development of transport in urban use that is being researched in Vehicles Laboratory for Low Environmental Impact at the Research Centre ENEA in Rome. This is a four wheeler, two seater

compact car where its wheelbase and track width are wide. More images of the vehicle in different views are shown in Fig. 10.2.

Fig. 10.2 Electric car Urbe.

As regards the traction, the original vehicle is a series hybrid, the type of hybrid in which the energy flows in series through the components, that is, from the fuel-tank to IC engine, the alternator, the drive motor with the electric storage, finally, that intervenes when necessary, both in acceleration and in regenerative braking. Special feature of this car is the super capacitor instead of a traditional battery, offering efficiency and durability advantages.

As regards the components, Urbe is equipped with a green petrol fuelled IC engine of 250 cc, by an alternator (permanent magnet), 4 groups of supercapacitors from 16 volts and 500 Farads, a liquid cooled permanent magnet motor drive, and suitably programmed electronic management system. From the point of view of performance, this is suitable for use in town: maximum speed is 70 km/h, greater than what is allowed but dictated by safety concerns; satisfactory acceleration, regenerative braking, driving in electric only mode (though limited to less than a km) to the traits congested or protected areas such as parking garages, hospital complex, crowded areas. The small size of the car also ensure excellent manoeuvrability thus ensuring a reduction in city traffic.

Table 10.1
Vehicle parameters

| Quantity | Symbol | Values |
|---|---|---|
| Mass | $m$ | 756 kg |
| Maximum vehicle speed | $U$ | 50 km/h |
| Air drag coefficient | $C_d$ | 0.28 |
| Front area | $A_f$ | 2.1 m$^2$ |
| Rolling friction coefficient | $K_{rf}$ | 0.01 |
| Powertrain efficiency (DC link to wheel) | $\eta_{PT}$ | 0.82 |
| Under body width | $b$ | 1150 mm |
| Under body length | $l$ | 1450 mm |
| Ground clearance | $C_g$ | 170 mm |

Availability of DWC system in such vehicle can improve the usability

and demand in the market. In order to implement the concept of wireless charging discussed in previous chapters, this chapter elaborates a case study which focusses to design a DWC system to meet the vehicle propulsion requirements. For this purpose, required and available vehicle parameters are mentioned in Table 10.1.

## 10.2 Power and Energy Consideration

The required tractive power to propel a vehicle at constant speed is calculated by (1) and for the vehicle parameters mentioned in Table 10.1 is 1.95 kW. Taking powertrain efficiency in account and an electrical power $P_{aux}$ (equal to 500W) for the consumption of the electric auxiliaries such as lights, fan etc., the power supplied by the battery or DC link can be written as

$$P_{DC} = \frac{P_{tract}}{\eta_{PT}} + P_{aux} \qquad (10.1)$$

Calculating the power using (10.1) the power requirement at the DC bus is 2.88 kw for moving vehicle. Now considering the vehicle travel for a certain distance i.e. 1 km for simplicity, required tractive energy can be computed by

$$E_{tract} = \frac{1000\, P_{tract}}{U} \qquad (10.2)$$

where $U$ is vehicle speed and maximum vehicle speed is 207 kJ. The energy calculated by (10.2) is the per km energy required by an electric vehicle while moving on a WPT road without battery drain. This energy is required when vehicle moves at maximum speed, but for slower speed the residual energy can be stored into the battery.

The pickup power is maximum when the pickup is perfectly aligned with a track coil, so the peak mutual inductance ($M_0$) should be according to the power rating of the system. The pickup power can be expressed by (10.3) if the self-inductance of the pickup coil is compensated by a series capacitor.

$$P_{pickup} = \frac{\omega_s^2 I_t^2 M_0^2}{R_L} \qquad (10.3)$$

where $R_L$ is battery equivalent resistance.

The average power is the one which fulfills the per km energy requirement if constantly transferred. Since the lumped coil track transfers the power to the moving vehicle in periodic fluctuations therefore the peak power over the face of a track coil should be higher than the average power. The peak power depends upon the mutual inductance but an average power also

varies according to $\sigma$. In other words the average power depends upon the distance between two track coils. Considering linear approximation of mutual inductance profile of a DD couple, power transfer for SFC track arrangement, as discussed in chapter 4, can be written as

$$\begin{cases} P_{L,SFC}\left(\frac{x}{D}\right) = KM_0^2\left(1-\frac{1}{\sigma}\frac{x}{D}\right)^2, & \frac{x}{D}\in[0,\sigma] \\ P_{L,SFC}\left(\frac{x}{D}\right) = 0, & \frac{x}{D}\in[\sigma,(1-\sigma)] \\ P_{L,SFC}\left(\frac{x}{D}\right) = KM_0^2\left[1+\frac{1}{\sigma}\left(\frac{x}{D}-1\right)\right]^2, & \frac{x}{D}\in[(1-\sigma),1] \end{cases} \quad (10.4)$$

where $x$ is the distance from the center of the first coil and variable

$$K \triangleq \frac{1}{2}\frac{\omega_s^2 I_t^2}{R_L}$$

where $\omega_s$ is supply frequency in rad/sec, $I_t$ is peak to peak supply current and $R_L$ is equivalent load resistance as shown in Fig. 3. All these terms are kept fixed for the design process.

### 10.3 Coil Placement and Mutual Inductance

The pickup power is maximum when the pickup is perfectly aligned with a track coil, so the peak mutual inductance ($M_0$) should be according to the power rating of the system. The average power is the one which fulfills the per km energy requirement if constantly transferred. Since the lumped coil track transfers the power to the moving vehicle in periodic-spikes pattern therefore the peak power over the face of a track coil should be higher than the average power. The peak power depends upon the mutual inductance and track current but an average power also varies with the distance between track coils. Considering linear approximation of mutual inductance profile of a DD couple, the average power between two consecutive track-coils can be given in the form of the peak power for SFC track design is

$$P_0 = \frac{3P_{av}}{2\sigma} \quad (10.5)$$

The boundary condition for SFC track arrangement can be defined for σ=0.5; then peak power is 3 times higher than the average power. In simple way, it can be stated that if power ratio is below 3 then OFC arrangement is required to meet the power requirement. According to (10.4) when pickup is perfectly aligned with a track then peak power is

$$P_0 = \frac{\omega_s^2 I_t^2 M_0^2}{2R_L} \quad (10.6)$$

Using (10.5), $\sigma$ can be computed for SFC track design, but according to power ratio if OFC track configuration is required then σ can be obtained using energy equation from chapter 4

$$E_{OFC} = 2\sigma D\left(\frac{5}{3} + \frac{1}{\sigma^2} - \frac{1}{6\sigma^3} - \frac{2}{\sigma}\right)\frac{KM_0^2}{U} \quad (10.10)$$

This is the energy captured in D distance therefore average power can be obtained by just dividing with travel time D/U; then this relation can be modified and written as

$$10\sigma^3 - 3\left(\frac{P_{av}}{P_0} + 4\right)\sigma^2 + 6\sigma - 1 = 0 \quad (10.7)$$

There are three solutions of this cubic equation; two solutions are always complex conjugate which are not the feasible value of $\sigma$ but one solution among them is real number. In this way the value of can be identified using (10.5) and (10.7) based on the power ratio.

In the design problem for URBE car, the average power is 2.88 kw and the peak power is considered 5 kw. Here in this case the peak power is below the thrice of the average power so OFC track arrangement is applicable. According to equation (10.7) the value of $\sigma$ is 0.7508. The peak mutual inductance $M_0$ can be computed by (10.9) considering supply current 100 A at 85 kHz frequency and load resistance can be evaluated by (10.8) considering 48V battery voltage then

$$R_L = \frac{8}{\pi^2}\frac{V_B^2}{P_{av}} \cong 0.65\Omega \quad (10.8)$$

and then

$$M_0 = 1.508\ \mu H \quad (10.9)$$

For the computed value of peak mutual inductance, pair of DD coil is designed with the help of FEM tool and that is discussed in the next section.

## 10.4 Coil Sizing

For the defined values of $M_0$. $R_L$, and $\sigma$, a WPT track can be designed. Considering the DD coils are suitable for WPT coupler, a DD coil pair is modeled in JMAG to achieve the desired mutual inductance. The available space under body of the car is 1.45x1.15 $m^2$ where the pickup coil can be attached. Bigger Y dimension of the DD coil is better for lateral misalignment tolerance of the vehicle. Therefore the width of the vehicle after subtracting 10 cm margin from both side is considered for the Y-dimension of the vehicle as shown in Fig. 10.3. Keeping the

mentioned airgap and fixed Y-dimension of the coil various coils with different number of turns are proposed which are mentioned in Table 10.2. These coils are designed for the defined peak power which means all the coils are designed for a desired mutual inductance. It is obvious that for a fixed $M_0$, coil size would be smaller with more number of turns and smaller coil area is beneficial for the cost of the core material.

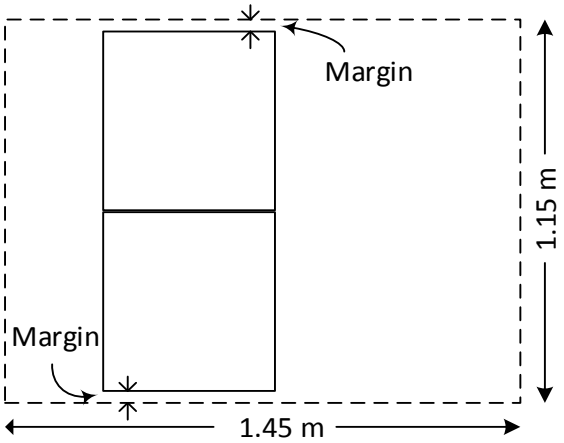


Fig. 10.3. Illustration of dimension of the car and DD coils.

In the same table, last two columns show the total required wire and core for the construction of a WPT track of 1 km. By increasing number of turns, coil size can be chosen smaller for the same amount of peak power but it increases required wire length. Its noticeable here that total area of required core material for 1 km is almost independent of coil size and number of turns. According to this results, three turns coil has been chosen for further design.

Table 10.2

DD coils with various number of turns

| **No. of Turns, N** | **X (mm)** | **Y (mm)** | **L (µH)** | **$M_0$ (µH)** | **k** | **No. of coils per-km** | **Winding wire per-km (in km)** | **Core area per-km (in $m^2$)** |
|---|---|---|---|---|---|---|---|---|
| 1 | 1450 | 950 | 19,66 | 8,91 | 0,45 | N/A | N/A | N/A |
| 2 | 820 | 950 | 41.53 | 15.11 | 0.36 | 916 | 4.75 | 713,56 |
| **3** | **415** | **950** | **49.33** | **15.15** | **0.31** | **1810** | **12.81** | **713,59** |
| 4 | 275 | 950 | 59.24 | 15.15 | 0.26 | 2731 | 24.36 | 713,47 |
| 5 | 211 | 950 | 70.45 | 15.11 | 0.21 | 3559 | 38.64 | 713,40 |

## 10.5 Core Consideration and Selection

Magnetic materials have been so extensively used in a diverse range of applications, that the advancement and optimal utilization of magnetic materials have been significantly improved. Magnetic materials are basically classified in two types based on their magnetic properties: soft magnetic material and hard magnetic material (Appendix A). The former one gets easily magnetized and demagnetized, whereas the later one is difficult to demagnetize then it is also referred as permanent magnets. The soft magnetic material, due to its property, is usually implemented to create magnetic path in alternating flux situation. This technique is also

used in wireless power transfer to improve magnetic coupling between two distant coils. Fig. 10.4 shows a side view of DD coils to depict the flux linking in presence of two magnetic cores in top and bottom.

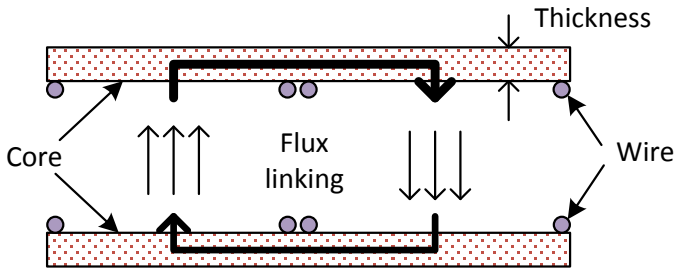


Fig. 10.4. Demonstration of the assistance of core in flux linking.

For a core, Ferrite materials have been developed for high-frequency applications most of the time because of their high electrical resistivity and low eddy current losses. The wide range of possible geometries, the continuing improvements in the material characteristics and their relative cost-effectiveness make ferrite components the choice for both conventional and innovative applications [2], [3]. Ferrites have a paramount advantage over other types of magnetic materials: high electrical resistivity and resultant low eddy current losses over a wide frequency range. Additional characteristics such as high temperature stability have expanded ferrite uses into quality filter circuits, high frequency transformers, wide band transformers, adjustable inductors, delay lines, and other high frequency electronic circuitry. As the high frequency performance of other circuit components continues to be improved, ferrites are routinely designed into magnetic circuits for both low and high power applications. For the most favorable combination of low cost, high $Q$, high stability, and lowest volume, ferrites are the best core material choice for frequencies from 10 kHz to 50 MHz. Ferrites offer an unmatched flexibility in magnetic and mechanical parameters.

*10.5.1 Core Plate Design*

Fig. 10.4 shows a side view of DD coils to depict the flux linking in presence of two magnetic cores in top and bottom. Simply, two ferrite plates of certain thickness can be used as cores for both track and pickup. The plate thickness can be adopted such that the magnetic flux

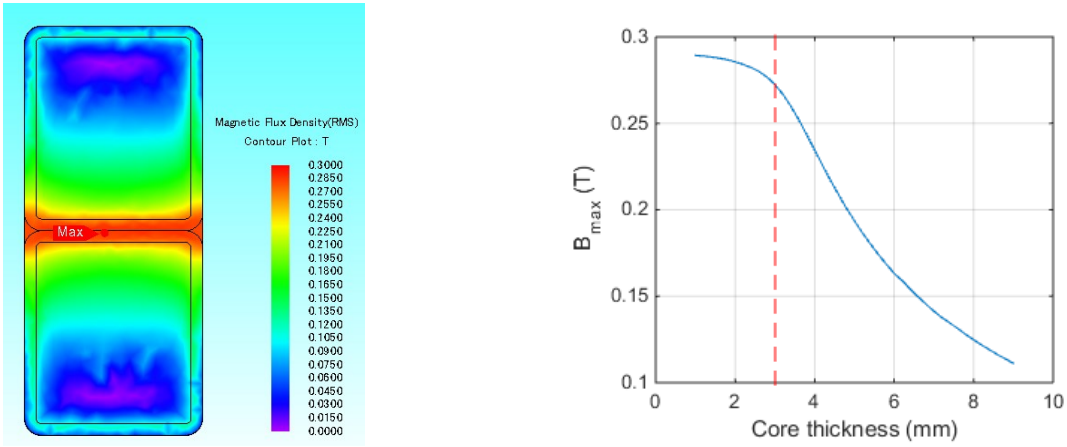


Fig. 10.5. Flux density distribution (left) and variation of $B_{max}$ with core thickness.

density ($B$) should be under limit and core does not get saturated. For ferrite material the limit is generally $B_{max}$= 0.3 T at ambient temperature 25°c.

Core design and optimization is carried out using multiple FEM simulations ran with different core dimensions. Choosing a coil from the Table 2, having three turns, two identical cores are designed for both the track and the pickup coils. First of all core thickness has been designed so that the core is not saturated. For this, value of maximum flux density ($B_{max}$) in a core is computed using FEM code, considering maximum current in a DD coil. Since the equivalent load resistance is obtained in (10.8) appears in series with the pickup coil and consumes 5 kw of peak power, thus the DD coil and core must be designed with taking this in account. The current in the pickup coil is

$$I_p = \sqrt{\frac{P_0}{R_L}} \cong 87.8 \text{ A} \qquad (10.10)$$

Eq. (10.10) provides the maximum value of current in the pickup coil, however keeping a margin and having a good number, 100 A at 85 kHz frequency is decided to calculate the core thickness. The flux density in the core varies with the change in its area of cross section, therefore to know the saturation property of the core, a graph of $B_{max}$ vs. core thickness is plotted in Fig. 10.5. It evident that for the design value of $B_{max}$, core thickness should be 3 mm. Fig.

10.5 also illustrates the contours of the flux density, which is maximum at the side common to the two sub coils and falls towards the lateral extremities.

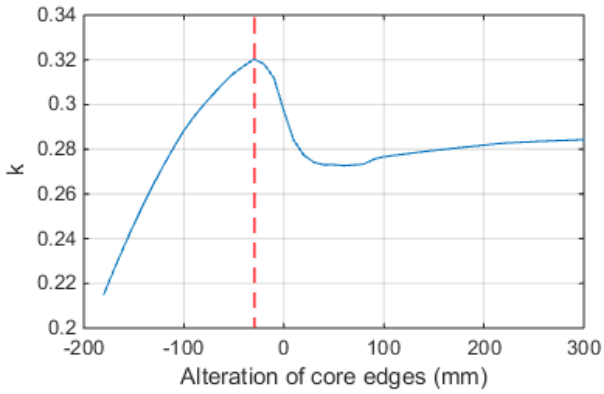


Fig. 10.6. Effect on coupling with variation in core area.

Keeping a fix thickness of the core which is adequate to avoid saturation, variation of the area of core plate has been studied. In the previous study, both the plate cores (for track and pickup each) are adopted with the same dimensions of a coil. Now the study focuses on the effect of limiting and increasing the boundaries of the plate core. Considering the coil dimensions as reference, same variations in core X-dimension and Y-dimension is introduced and change in coupling behavior has been observed. Fig. 10.6 shows a graph of coupling coefficient ($k$) w.r.t. the variation in the core dimension. The situation when the plate core fully covers a DD coil, per unit dimension is unity; expansion in core dimension is represented by dimension >1 and reduction is by <1 value.

For the smaller core dimension the coupling is worse and larger core area improves the coupling, but interesting behavior is noticed at unit dimension. The coupling coefficient is found maximum for the dimension obtained after eliminating the winding area of the coil from the coil area. In simple way, the core which covers inner area of the DD coil, causes maximum $k$. This phenomenon can be verified by individually varying X and Y dimension of the core plates. For this analysis, the same three turn coil has been considered which has 9 mm wire diameter (including insulation) then winding span is 27 mm. Taking coil dimensions for reference, the dimension difference between coil and core are represented as ΔX and ΔY for X

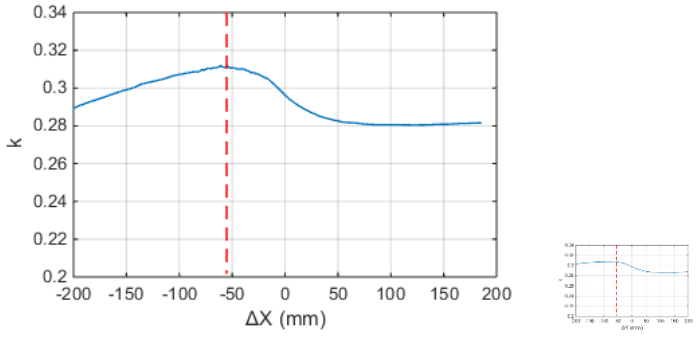


Fig. 10.7. Variation in core X-dimension (left) and variation in core Y-dimension (right).

and Y dimensions respectively. First, keeping core Y-dimension fixed, core X-dimension is varied and k vs. ΔX is plotted in Fig. 10.7 (left). The coupling is found better when core is little smaller than the coil, and in this particular case, the value is 54 mm which is winding span in both extremities. Similarly, keeping ΔX fixed to zero, Y-dimension is varied and found that maximum coupling is possible when the plate core confined to the inner boundaries of the DD coil. One more thing can be observed in Fig. 10.7 that variation in k is more with ΔX in comparison of ΔY, this can be explained by the flux density contours shown above.

For the smaller core dimension the coupling is worse and larger core area improves the coupling, but interesting behavior is noticed at unit dimension. The coupling coefficient is found maximum for the dimension obtained after eliminating the winding area of the coil from the coil area. In simple way, the core which covers inner area of the DD coil, causes maximum *k*. This phenomenon can be verified by individually varying X and Y dimension of the core plates. For this analysis, the same three turn coil has been considered which has 9 mm wire diameter (including insulation) then winding span is 27 mm. Taking coil dimensions for reference, the dimension difference between coil and core are represented as ΔX and ΔY for X and Y dimensions respectively. First, keeping core Y-dimension fixed, core X-dimension is varied and *k* vs. ΔX is plotted in Fig. 10.7 (left). The coupling is found better when core is little smaller than the coil, and in this particular case, the value is 54 mm which is winding span in both extremities. Similarly, keeping ΔX fixed to zero, Y-dimension is varied and found that maximum coupling is possible when the plate core confined to the inner boundaries of the DD coil. One more thing can be observed in Fig. 10.7 that variation in *k* is more with ΔX in comparison of ΔY, this can be explained by the flux density contours shown above.

*10.5.2 Core Optimization*

The magnetic core greatly improves the coupling properties between two coils but it also causes cost, therefore appropriate and optimized dimensions of a plate core are selected. Another way of material saving is by replacing the core plate by strips or bars of Ferrite. As shown in Fig. 10.8, the bars can provide flux path to the associated coil. Since the bars are placed with certain distance from each other, then bars-assembled

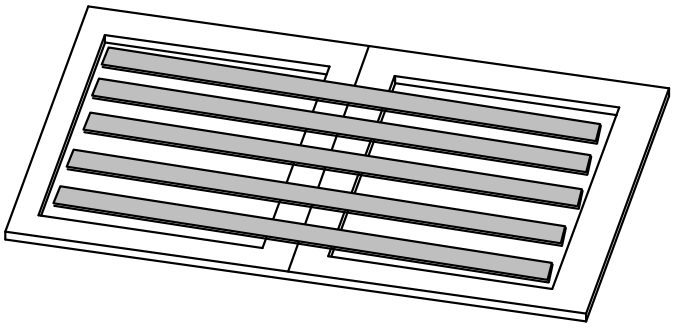

Fig. 10.8. Bars assembled core.

(BA) core is not as effective as a plate core, due to increase in leakage flux.

To understand the difference in coupling with plate and BA core, coupling coefficient with varying core material is analyzed. A FEM model is created in JMAG where a plate core is divided in 12 bars such that each bar has length equal to core Y-dimension, width is $12^{th}$ part of core X-dimension and height is same as core thickness. The core X and Y-dimensions are obtained from the previous section. In such arrangement when there are 12 bars, the core behaves like a plate core because all the bars are attached to each other and a negligible leakage flux exists beyond the core. In order to save core material, less number of bars are employed and coupling coefficient is observed. Fig. 10.9 shows the variation of *k* when bars are removed one by one and uniform distance is kept between two neighbor bars. In this study bar dimensions remain same, thus reducing the number of bars actually saves material.

## References

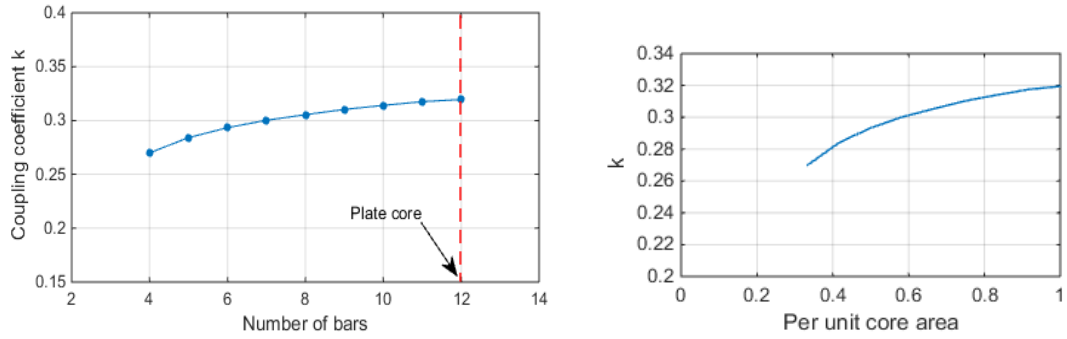


Fig. 10.9. Effect on coupling with number of bars.


[1] J. Dai and D.C. Ludois, "A Survey of Wireless Power Transfer and a Critical Comparison of Inductive and Capacitive Coupling for Small Gap Applications," *IEEE Transactions on Power Electronics*, vol. 30, no. 11, pp. 6017-6029, Nov. 2015.

[2] X.C. Wei, E.P. Li, Y.L. Guan, and Y.H. Chong, "Simulation and Experimental Comparison of Different Coupling Mechanisms for the Wireless Electricity Transfer" Journal of Electromagnetic Waves and Applications, Vol. 23, No. 7, pp. 925-934, 2009.

[3] S.S. Mohan, M. Hershenson, S.P. Boyd and T.H. Lee, "Simple Accurate Expressions for Planar Spiral Inductances," IEEE Journal of Solid-State Circuits, Vol. 34, No. 10, pp. 1419-24, Oct. 1999.

[4] S. Bandyopadhyay, V. Prasanth, P. Bauer, and J.A. Ferreira, "Multi-objective optimization of a 1-kW wireless IPT systems for charging of electric vehicles," in proc. of IEEE Transportation Electrification Conference and Expo (ITEC), 2016, pp. 1-7.

[5] S.K. Burke, R.J. Ditchburn, and T.P. Theodoulidis, "Impedance of curved rectangular spiral coils around a conductive cylinder," *Journal of Applied. Physics*, vol. 104, no. 1, pp. 0141912-1–0141912-11, Jul. 2008.

[6] K.N. Mude, M. Bertoluzzo, G. Buja, and R. Pinto, "Design and experimentation of two-coil coupling for electric city-car WPT charging" Journal Of Electromagnetic Waves And Applications, Vol. 30, No. 1, pp. 70-88, 2016.

[7] C. Mi; G. Buja; S.Y. Choi; C.T. Rim, "Modern Advances in Wireless Power Transfer Systems for Roadway Powered Electric Vehicles," *IEEE Transactions on Industrial Electronics*, to be published, DOI: 0.1109/TIE.2016.2574993.

[8] S. Chopra and P. Bauer, "Analysis and design considerations for a contactless power transfer system," IEEE International Telecommunications Energy Conference (INTELEC), 2011, pp. 1-6.

[9] X. Shi, C. Qi, M. Qu, S. Ye, G. Wang, L. Sun, and Z. Yu, "Effects of coil shapes on wireless power transfer via magnetic resonance coupling," Journal Of Electromagnetic Waves And Applications, Vol. 28, No. 11, pp. 1316–1324, May 2014.

[10] D. Ongayo and M. Hanif, "Comparison of circular and rectangular coil transformer parameters for wireless Power Transfer based on Finite Element Analysis," IEEE Brazilian Power Electronics Conference and Southern Power Electronics Conference (COBEP/SPEC), 2015, pp. 1-6.

[11] S. Mohan, M. Hershenson, S.P. Boyd, and T.H. Lee, "Simple accurate expressions for planar spiral inductances," IEEE Journal of Solid State Circuits, Vol. 34, pp. 1419-1424, 1999.

[12] K. N. Mude, M. Bertoluzzo, and G. Buja, "Inductive characteristics of different coupling setups for wireless charging of an electric city-car," IEEE International Electric Vehicle Conference (IEVC), 2014, pp. 1-7.

[13] X. Zhang, Z. Yuan, Q. Yang, Y. Li, J. Zhu, and Y. Li, "Coil Design and Efficiency Analysis for Dynamic Wireless Charging System for Electric Vehicles," *IEEE Transactions on Magnetics*, vol. 52, no. 7, pp. 1-4, July 2016.

[14] S. Bhattacharya and Y.K. Tan, "Design of static wireless charging coils for integration into electric vehicle," IEEE International Conference on Sustainable Energy Technologies (ICSET), 2012, pp. 146-151.

[15] Z. Dang and J.A.A. Qahouq, "Range and misalignment tolerance comparisons between two-coil and four-coil wireless power transfer systems," IEEE Applied Power Electronics Conference and Exposition (APEC), 2015, pp. 1234-1240.

[16] S. Bhuyan, K. Sivanand, and S.K. Panda, "Effect of design parameters on resonant wireless energy transfer system," Journal of Electromagnetic Waves and Applications Vol. 27, No. 3, pp. 288-298, 2013.

[17] Y. Kim and S. Lim, "Compact magnetic coupled resonator with high efficiency during misaligned wireless power transmission" Journal Of Electromagnetic Waves And Applications Vol. 27 , No. 15, pp. 1942-1948, 2013

[18] M. Budhia, J.T. Boys, G.A. Covic, and C.Y. Huang, "Development of a Single-Sided Flux Magnetic Coupler for Electric Vehicle IPT Charging Systems," *IEEE Transactions on Industrial Electronics*, vol. 60, no. 1, pp. 318-328, Jan. 2013.

[19] J. Deng, W. Li, T.D. Nguyen, S. Li, and C.C. Mi, "Compact and Efficient Bipolar Coupler for Wireless Power Chargers: Design and Analysis," *IEEE Transactions on Power Electronics*, vol. 30, no. 11, pp. 6130-6140, Nov. 2015.

[20] A. Zaheer, G. A. Covic, and D. Kacprzak, "A Bipolar Pad in a 10-kHz 300-W Distributed IPT System for AGV Applications," *IEEE Transactions on Industrial Electronics*, vol. 61, no. 7, pp. 3288-3301, July 2014.

[21] M. Bertoluzzo, G. Buja, and H.K. Dashora, "Lumped Track Layout Design for Dynamic Wireless Charging of Electric Vehicles," *IEEE Transactions on Industrial Electronics*, Vol. 63, No. 10, pp. 6631 - 6640, Oct. 2016.

# Chapter 11

# Testing and Validation of Design

Performance of a wireless charging system mainly depends upon the coil structure, power supply and compensation network. This thesis has mostly been dealing with all these topics at analytical aspects with simulation support. Having prime focus on the DD coil set, this chapter elaborates the coil construction and observation of their coupling properties during misalignment.

## 11.1 Development of Coil Setup

As discussed earlier in chapter 4 that a pair of polarized coils shows different coupling profile while misalignment in longitudinal and lateral direction. Considering linear mutual inductance variation of DD coil set with the longitudinal displacement as observed with FEM analysis, track layout design and coil design have been discussed in former chapters. In this way, there are two polarized coil structures have been discussed: DD coils in chapter 4 and UDD in chapter 5. Thus, experimental development of such coils has been performed in this section.

### *11.1.1 Construction of DD coil-set*

To design a pair of DD coils of identical shape and size which can completely cover each other while they are perfectly aligned, have been developed in the lab with a single turn of strained wire. The dimensions of the coils are scaled down size of the coil pair #1 considered in chapter 4, where the reduction ratio of 6.25. Then, the original coil dimensions 2.5x1.5 $m^2$ and coil distance 20 cm are set at 0.4x0.24 $m^2$ and 3.2 cm, respectively. Each coil lays on the core and the core-coil structure is covered on the two sides by plates for protection purposes.

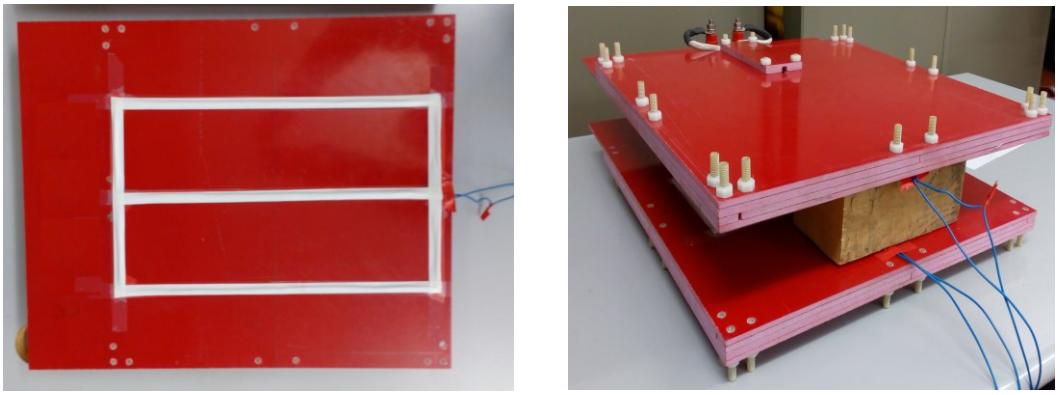

Fig. 11.1 DD coil setup with Ferrite plate core.

The cores are made up of 16 square planar elements with dimensions 100mm × 100mm × 6mm, placed side by side to form a square with a side of 0.4 m. The core elements are manufactured by Ferroxcube Company with part number BLK/100/100/6-3C95.

*11.1.2 Construction of UDD coil-set*

The UDD coil set is a special configuration of DD coil set where the pickup coil is longer in size than the track coil. The UDD coil is deliberated more in chapter 5 in detail, which illustrates that their mutual inductance varies with trapezoidal behavior during longitudinal displacement. To experimentally validate this behavior, the largest coil pair #4 from chapter 5 has been chosen to create the coil setup in the lab. The original size of pickup coil is 1.2x0.7 $m^2$, and track coil is 0.4x0.95 $m^2$, where the value before cross is length and the value after

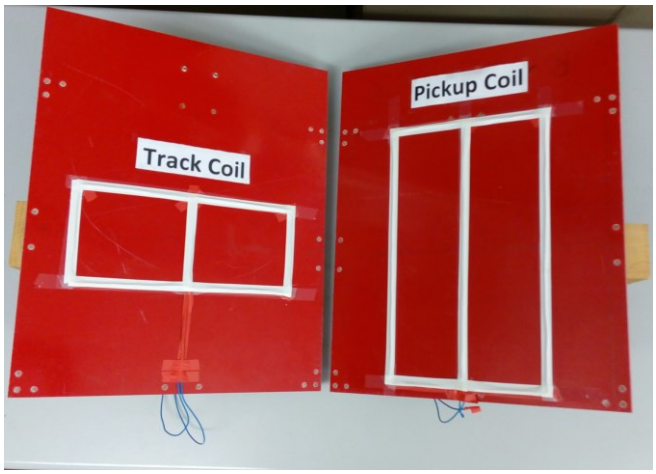


Fig. 11.2 Experimental setup of a UDD coil set.

cross is width of a coil. These two DD coils of unequal dimensions are realized on the surface of two Ferrite plate mentioned above with a scaling factor 1/3. Thus, the dimensions of the experimental coils are 13.3x31.6 cm2 and 40.0x23.3 cm2 for the track and pickup coils respectively, and their appearance with single turn is shown in Fig. 11.2. In experimental situation, both the coils face each other with a distance of 5.7 cm which is a scaled down value of 0.17 m, the original one.

## 11.2 Observation of Misalignment

Misalignment is inevitable situation in dynamic wireless power transfer, therefore observation of coupling properties in misaligned coils is important in system design. Finding the longitudinal coupling profile the most suitable in case of DD and UDD coils, misalignment in this direction has been experimentally studied in this section. To obtain the mutual inductance

between two coupled inductors, there can be two ways: open circuit test or series connection. In the first method, one inductor is supplied with a certain amount of alternating current $I_1$ and voltage across the second inductor $V_2$ (i.e. open circuited) is measured, than the mutual inductance between them can be computed as

$$M = \frac{V_2}{j\omega I_1} \qquad (11.1)$$

where ω is the supply frequency.

Another method is by connecting two inductors in series with two different connections, one is with same polarity and other one with opposite polarity. Assuming $L_1$, $L_2$ the self-inductances and $M$ is mutual inductance of two coils then the equivalent inductance of their series combination can be written as

$$L_{eq1} = L_1 + L_2 + M \qquad (11.2)$$

$$L_{eq2} = L_1 + L_2 - M \qquad (11.3)$$

Then the mutual inductance of the pair can be simply obtained as

$$M = \frac{L_{eq1} - L_{eq2}}{2} \qquad (11.4)$$

The first method requires a power supply that can provide sufficient current at desired frequency. Since the coil setup is developed with single turn, therefore the inductance values are very small, which can be clearly observed with open circuit test if supply current and frequency are quite high. Because of that the second method is adopted to calculate mutual inductance of two coils developed in the lab. The inductive parameters of the coil-coupling setup have been measured by an LCR meter of InSTEK Co., model LCR-819. For the measurement, the instrument applies sinusoidal voltage of amplitude 1V (RMS) and frequency within a predefined set to the coil. Since the selection of 85kHz frequency is not available in the instrument, the inductive parameters of the coils have been measured at the frequencies of 66 kHz and 100 kHz, obtaining almost equal values.

For the identical DD coils, measurements have been executed by increasing the longitudinal displacement from 0 to 0.4 m with steps of 0.01 m. The obtained results are reported by red circles in Fig. 11.3. As a comparison, the mutual inductance obtained by the FEM analysis and plotted in Fig. 4.4 is also reported here, after scaling down its maximum value and the longitudinal displacement in order that they match the scale of the experimental

prototype. The data of Fig. 11.13 confirm the almost linear decrease of the mutual inductance with the longitudinal displacement thus validating the analysis made based on the FEM data.

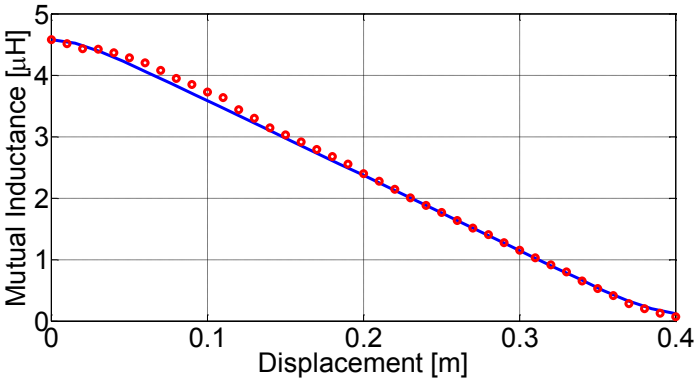


Fig. 11.3. Mutual inductance of the experimental DD coils pair vs. longitudinal displacement.

Similarly, mutual inductance profile of the developed UDD coil has been obtained and plotted in Fig. 11.4, where the red solid line represent scaled down FEM data and blue circles show the measured values.

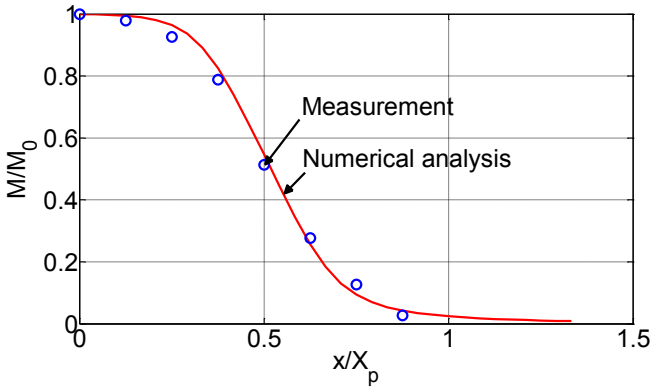


Fig. 11.4. Mutual inductance of UDD coils pair vs. longitudinal displacement.

# Conclusion

Dynamic wireless charging (DWC) or in-moving charging of electric vehicle (EV) makes possible to use smaller batteries, convenient EV charging, and unlimited driving range. The DWC has been discussed in this thesis, is based on the principle of inductive power transfer (IPT), where the power transfer occurs between two physically isolated coils one is buried in the road surface and another is under the vehicle body. Considering a lumped track where a series of inductive coils uniformly disseminated along the road, certain design aspects and DWC operation have been dealt in the research.

Beginning with concept building of IPT, a state of art about dynamic charging, critical system requirements, and primary configurations of the IPT track have been presented to enter into the subject. Later, identifying the importance of coil structure in an IPT arrangement for the sake of system performance; a detailed discussion has been included in the thesis about coupling properties of the coils and their utility for DWC. Since an EV keeps moving over a lumped track, therefore coupling of pickup with the coils in the track stays varying between zero and a maximum value. Considering the variable coupling profile, merits of a double-D shaped coils that is also called DD coil, have been explained over the ordinary coils used in stationary applications of wireless power transfer by numerical methods.

Based on the analysis of the mutual inductance profile of a DD coil set under misalignment, power and energy transfer from a track to pickup coil has been modelled mathematically. Using the relations of energy with coil dimensions and placement along the road, design procedure has got presented for an IPT track layout. Implementation of all the proposed hypothesis has been demonstrated with an example of compact-C car. Carrying forward the analysis of the track layout with DD coils, a special configuration of coils that is called unequal-DD (UDD) coils has been proposed, where the pickup coil is longer than a track coil in the direction of motion. Mutual inductance in employment of UDD coils varies with a trapezoidal nature that helps in the economy of track layout and lowering the system rating. Analytical expressions of power transfer and energy have been derived to obtain the sizing procedure for track layout and coils, with a case study. The outcomes of the case study showed how the use of UDD coils could lead to a drastic reduction of the cost of the track. Theoretical findings have been checked against the results of FEM analysis and computer aided circuital analysis.

This thesis has also dealt with the segmentation of a lumped coil track, which is very important DWC that allows track coils to be on/off based on the availability of a vehicle. An automatic technique has been deliberated for that, which exploits the properties of the impedance reflected into a track coil from a coupled pickup. Behaviour of the reflected impedance can be defined by the compensation in pickup circuit that can cause drastic rise in supply current to the coupled track coil which remains low while uncoupled. Thus, finding the regular one-capacitor compensation inadequate, four different compensation topologies that employ two reactive components have been investigated. Amongst them two topologies of dual capacitor have been found suitable to attain desired segmentation. Later, to deeply analyse the qualified topologies, their performance figures like segmentation ratio and efficiency have been examined. The outcomes evident that the parasitic resistance of the coils impairs the performance very much, therefore a compensation only in pickup cannot serve effectively to achieve the reflexive segmentation.

Talking about power converters, this thesis also includes some discussion about the complete arrangement of converters, both in track side and pickup side, which makes wireless charging possible. Specifically, an LCC compensation in track side is elaborated in brief which can produce constant current/voltage supply for the IPT track as desired. In pickup side, introducing the basic arrangement a non-inverting buck-boost converter has been discussed which is able to keep continuity in power to feed the battery.

Collecting all the research and analysis outcomes, a case study has been organized considering an electric vehicle: ENEA Urbe. This case study includes DD coil design and track layout that can fulfil the energy requirement to propel the vehicle in absence of the battery drain. All the designs have been carried out with FEM code which is later validated with experimentation of DD coil set.

## Appendix A

# Magnetic Materials

Magnetic materials are used to provide desired path to the employed magnetic flux, and they are also called rear earth materials. For the application which use high frequency oscillating magnetic field like wireless power transfer (WPT), Ferrite is extensively used.

Ferrite is a type of ceramic compound composed of iron-oxide ($Fe_2O_3$) combined chemically with one or more additional metallic elements. They are both electrically nonconductive and ferromagnetic, meaning they can be magnetized or attracted to a magnet. Ferrites can be divided into two families based on their magnetic coercivity, their resistance to being demagnetized. Hard ferrites have high coercivity, hence they are difficult to demagnetize. They are used to make magnets, for devices such as refrigerator magnets, loudspeakers and small electric motors. Soft ferrites have low coercivity. They are used in the electronics industry to make ferrite cores for inductors and transformers, and in also in WPT.

To build the experimental setup in the lab, I-type core of Ferrite 3C95 has been used which is manufactured by Ferroxcube Co. 3C95 is a low to medium frequency power material with low power losses from 25 to 100 °C for use in power transformers at frequencies up to 0.5 MHz. Especially suited for broad temperature range applications like automotive etc. Key specifications of the material are outlined in Table A.1.

Table: A.1

| Symbol | Conditions | Value | Unit |
|---|---|---|---|
| $\mu_i$ | 25 °C; ≤ 10 kHz, 0.25 mT | 3000±20% | |
| $\mu_a$ | 100 °C; 25 kHz, 200 mT | ≈ 5000 | |
| Bsat | 25 °C; 10 kHz, 1200 A/m | ≈ 530 | mT |
| | 100 °C; 10 kHz, 1200 A/m | ≈ 410 | |
| $P_V$ | 25 °C; 100 kHz; 200 mT | ≈ 350 | kW/m$^3$ |
| | 100 °C; 100 kHz; 200 mT | ≈ 290 | |
| ρ | DC; 25 °C | ≈ 5 | Ωm |
| $T_C$ | | ≥ 215 | °C |
| Density | | ≈ 4800 | kg/m$^3$ |

# Appendix B

## Organizations Involved in WBC Research

Wireless power transfer isn't a new concept in electrical engineering but after growing advancement in power electronics and other supporting technology, several researchers in various organizations are working on this field. Some of them are introduced below.

*KAIST and OLEV Technology*

Korean Advanced Institute of Science and Technology (KAIST) started working on roadway powered electric vehicles (RPEV) project which was begun in 1976 USA. Later, the RPEV is undertaken by a Korean research team as online electric vehicle (OLEV) project and developed a method for wirelessly transferring power to busses. This method consists of two parallel conductors under the road in segments, which are turned on/off based on the availability of a bus driving over them. The receiver coil is put under the bus and is located 20 cm above the road, whereas the power lines are placed 15 cm below the road surface, thus a total distance of 35 cm. Because of the distance pickup modules need to be quite large (width of 80 cm) and several modules are needed to be able to make the transfer of 100 kW possible. The system is single phase and runs a 200 A current with the frequency 20 kHz and has an 80 % efficiency. The OLEV project passed through various generations, and now they are working on $6^{th}$ generation of development.

*University of Auckland,*

University of Auckland is an acknowledged pioneer in wireless power transfer, which have significantly contributed in concept building of coil structure for both static and wireless power transfer.

*Oak Ride National Laboratories*

ORNL works both on motionless and in-moving wireless charging of electric vehicles. ORNL's power electronics team developed world's first 20 kw wireless charging system for a passenger cars by developing a unique architecture that included an ORNL-built inverter, isolation transformer, vehicle-side electronics and coupling technologies. For the demonstration, researchers integrated the single-converter system into an electric Toyota RAV4 equipped with an additional 10 kwH battery. Their next target is wireless charging at 50 kw, to realize commercially available plug-in quick chargers.

*Qualcomm Halo*

Qualcomm Halo-Wireless electric vehicle charging (WEVC) technology is based on internal investment along with decades of technical and commercial development by the University of Auckland. This technology enables license partners to build a charging system that meets requirements of automotive manufacturer, regardless of their coil architecture.

*WiTricity corp*

WiTricity Corporation is founded in 2007, to commercialize technology invented by a team of MIT physicists in 2006. This company designs, develops, manufactures, and markets patented technology for wireless energy transfer. In this way, they have developed WiT-3300 Deployment Kit that is a wireless "Park-and-Charge" self-charging system of 3.3 kw for electric vehicles.

*Delphi Wireless charging system*

Delphi initially started devolvement of the WPT system in 2011 with its own specification of 3.3 kW output power with an input voltage range between 85 V to 265 V AC, 60 Hz supply. Delphi Automotive has equipped several test vehicles in Munich. It has reached an agreement with WiTricity corp to develop automatic wireless charging products for hybrid and electric vehicles. The collaboration between the two companies will help establish a global infrastructure of safe and convenient charging options for EV.

*Bombardier PRIMOVE*

PRIMOVE is Bombardier's complete e-mobility portfolio allowing cities and the transportation industry to easily incorporate electric mobility. PRIMOVE team in working on static as well as dynamic wireless charging solutions for various vehicles like buses, cars and trams. It uses mix of static and dynamic charging works which benefits economy in the infrastructure and minimizes the need for batteries. PRIMOVE solution uses a three-phase system which is divided into segments to avoid unnecessary magnetic field around the roads and maximize its efficiency.

*TBD*

Siemens and BMW announced at Hannover 2011 that they will be testing a prototype that will use inductive energy charging to charge electric vehicles. EVs would be able to roll over charging stations and need not to plug in a cord, which would be ideal for service cars like taxi cabs because it works even during a short stop. The system therefore generates a magnetic field

whose strength in and around the vehicle is far below the internationally recommended limit of 6.25 microtesla.

*Plugless power*

Plugless Power is a USA based firm of Electric Vehicle Supply Equipment (EVSE) products, manufactured by Evatran Co. that enable inductive charging for electric vehicles (EV). This has been selling wireless chargers to use with the Nissan LEAF, Chevrolet Volt, Cadillac ELR and Tesla Model S.

*Stanford university wireless charging*

Researchers at Stanford University have developed a concept of road-based, high-efficiency, wireless charging system for electric vehicles. Using mathematical simulations they proved that by bending the copper coils at a 90 degree angle and attaching them to a metal plate, up to 10 kilowatts of electricity can be transferred at an efficiency of 97%. Based on this research, Highways England has announced that it plans for off-road (test track) trials with a view to carrying out subsequent on-road charging and increase the range of EVs.

## Publications


[1] M. Bertoluzzo, G. Buja, and H.K. Dashora, "Design of DWC System Track with Unequal DD Coil Set," *IEEE Trans. on Transportation Electrification*, DOI: 10.1109/TTE.2016.2646740.

[2] M. Bertoluzzo, G. Buja, and H.K. Dashora, "Lumped Track Layout Design for Dynamic Wireless Charging of Electric Vehicles," *IEEE Trans. on Industrial Electronics*, Vol. 63, No. 10, pp. 6631-6640, Oct. 2016.

[3] H.K. Dashora, S. Giacomuzzi, M. Bertoluzzo, and G. Buja, "Performance Analysis of Reflexive Segmentation Topologies in DWC systems", accepted for IEEE Industrial Electronics International Conference (IECON), 2016.

[4] H.K. Dashora, M. Bertoluzzo, G. Buja, "Reflexive properties for different pick-up circuit topologies in a distributed IPT track," In proc. of IEEE International Conference on Industrial Informatics (INDIN), 2015, pp. 69-75.

[5] K.N. Mude, H.K. Dashora, M. Bertoluzzo, and G. Buja, "From wired to in-moving charging of the electric vehicles," In Proc. of International Conference on Development, Energy, Environment and Economics, 2014, pp. 33-42.


■■■